Deep Earth volatile cycles as revealed by basalt chemistry

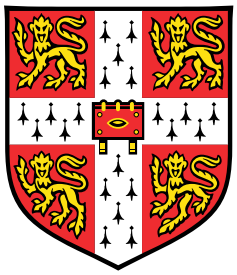

Simon William Matthews

Department of Earth Sciences
University of Cambridge

This dissertation is submitted for the degree of
Doctor of Philosophy

St Catharine's College

January 2019

Deep Earth volatile cycles as revealed by basalt chemistry

Simon William Matthews

Earth's volatiles (e.g. CO_2 and H_2O) are thought to be stored largely in the interior of the planet. The partitioning of these volatile elements between Earth's surface and interior controls the evolution of our atmosphere and oceans, acting as a regulator on our planet's long term climate. Basalt geochemistry is our most direct probe of Earth's convecting mantle, however the tendency of volatile elements to form vapour phases deep within volcanic systems obscures the mantle volatile signals inherited by basalts. This thesis explores the extent to which basalts may preserve mantle volatile signals, places new constraints on volatile heterogeneity within the Icelandic plume, and considers the role of mantle convection in establishing deep Earth volatile cycles.

Volatile- trace element systematics in suites of basaltic glass and melt inclusions have been widely used to infer volatile abundances in the depleted mantle, but have resulted in a large diversity of estimates. In this thesis a new statistical treatment of such datasets is developed, using simple numerical models for concurrent magma mixing and degassing. It is demonstrated that the role of magma degassing was previously underestimated, and the variability in apparent mantle volatile concentrations is largely a result of variability in magma mixing and degassing.

Using a large new dataset of Icelandic melt inclusions sampling diverse mantle components, alongside a compilation of existing suites, the gross structure of the global melt inclusion array is shown to be controlled by magma degassing and olivine decrepitation. By applying the new statistical treatment of the data developed here, the presence of at least three mantle components with distinct volatile chemistry are demonstrated to contribute Icelandic magmas. With a novel combination of geophysical and geochemical constraints, the thermal structure and mineralogy of the melting region beneath Iceland is constrained. The role of mineralogical heterogeneity in the long term storage of mantle volatiles is critically assessed.

Declaration

This dissertation is the result of my own work and includes nothing which is the outcome of work done in collaboration except as declared in the Preface and specified in the text.

It is not substantially the same as any that I have submitted, or, is being concurrently submitted for a degree or diploma or other qualification at the University of Cambridge or any other University or similar institution except as declared in the Preface and specified in the text. I further state that no substantial part of my dissertation has already been submitted, or, is being concurrently submitted for any such degree, diploma or other qualification at the University of Cambridge or any other University or similar institution except as declared in the Preface and specified in the text

It does not exceed the prescribed word limit for the relevant Degree Committee.

Material previously submitted for Part III Geological Sciences Tripos (University of Cambridge). The scientific question addressed in Chapter 3 is similar to that addressed in my Part III dissertation, and uses the same primary observations pertaining to crystallisation temperatures. However, Chapter 3 incorporates a re-analysis of the primary observations, and an entirely new approach to estimating mantle temperatures and lithology. Previously examined material is closely related to that included in Sections 2.1.1, 2.2.1, 2.3.1 and 3.1 only.

Simon William Matthews
January 2019

Acknowledgements

Firstly I must thank my supervisors, Oli Shorttle, John Maclennan and John Rudge. They have been unfailingly supportive and enthusiastic about my scientific endeavours.

I owe a huge thanks to the people who helped and taught me how to collect the data underpinning this thesis. Richard Hinton was a pleasure to work with at the Edinburgh Ion Probe and spent a large amount of time ensuring I could collect good data and indulging my many questions on SIMS. Iris Buisman not only taught me everything I know about EPMA analysis, but was also a extraordinarily calming influence at some of the most stressful stages of sample prep. Sèbastien Facq and David Neave were of great help getting me started with the Raman measurements. Advice from Ben Winpenny, Margaret Hartley and Lois Salem, was invaluable for making progress with, often fraught, melt inclusion preparation.

Some of my most treasured memories from my PhD are from the field season I spent in Iceland with Euan Mutch. I couldn't have chosen anyone better to have spent 'Ok-mas' day with. I have greatly enjoyed conversations about the mantle, igneous rocks, and everything else with many members of the Department. In particular, conversations with Helen Williams and Callum Reekie have not only helped shape the hypotheses developed in this thesis, but also my view of the Earth.

Throughout my PhD, I have gratefully received financial support from the NERC ESS DTP, NERC Deep Volatiles Consortium and the Deep Carbon Observatory.

Finally, I thank my family and friends who have been constantly supportive of my studies.

Table of contents

Chapter 1

Introduction

The mantle is the largest reservoir by mass in the Earth, and through volcanism and subduction it remains in continual chemical communication with Earth's atmosphere and oceans. The volatile elements, including carbon and hydrogen, are key components in this cycle, providing thermostatic control on Earth's climate via silicate weathering and carbonate subduction (Hayes and Waldbauer, 2006; Walker et al., 1981), and control the melting behaviour (e.g. Asimow et al., 2003; Dasgupta and Hirschmann, 2010) and rheology of the mantle (e.g. Hirth and Kohlstedt, 1996). Though the concentration of volatile elements in Earth's mantle are thought to be low (Cartigny et al., 2008; Javoy and Pineau, 1991; Le Voyer et al., 2017; Michael and Graham, 2015; Saal et al., 2002), the mantle volatile budget may greatly exceed that in any other reservoir (Cartigny et al., 2008; Dasgupta, 2013; Dasgupta and Hirschmann, 2010; Hirschmann and Dasgupta, 2009; Kelemen and Manning, 2015). Over the lifetime of the Earth the mass and chemistry of our oceans and atmosphere is likely to have been modulated by fluxes to and from the mantle (e.g. Dasgupta, 2013; McGovern and Schubert, 1989; Parai and Mukhopadhyay, 2012).

Heat loss from the interior of the Earth drives vigorous convection in Earth's mantle (Davies, 1977). Where this convective circulation brings portions of the mantle close to Earth's surface magmas are generated by decompression melting (McKenzie, 1984; McKenzie and Bickle, 1988), and inherit the majority of the mantle's volatile inventory (e.g. Aubaud et al., 2004; Rosenthal et al., 2015). The magma then rises towards the Earth's surface, transporting its volatile cargo until volcanic vapours are liberated from it (e.g. Dixon and Stolper, 1995). At subduction zones, oceanic crust is returned to the mantle along with the volatile inventory it acquired on the seafloor from serpentinisation (e.g. Alt et al., 2013), carbonate mineral precipitation (e.g. Kelemen et al., 2011), and accumulation of sediments (e.g. Plank, 2014). Much of the volatile inventory of the subducting slab is removed during metamorphic reactions beneath volcanic arcs before it reaches the deep mantle (e.g. Kerrick and Connolly, 2001).

Despite a growing understanding of the processes controlling volatile partitioning between the Earth's mantle and surface, the magnitudes of the fluxes remain largely uncertain (Dasgupta and Hirschmann, 2010; Kelemen and Manning, 2015). Figure 1.1 summarises the most recent estimates of carbon fluxes and their uncertainties. Much of the uncertainty arises from the difficulty in constraining the efficiency of volatile removal from subducting slabs in the mantle wedge (Hirschmann, 2018; Kelemen and Manning, 2015). Experimental work combined with thermal (Syracuse et al., 2010) and thermodynamic models (Holland and Powell, 1998; Sverjensky et al., 2014) suggests carbon and water should be almost entirely removed from most slabs (Kelemen and Manning, 2015). However, evidence from super-deep diamonds (Pearson et al., 2014; Stachel, 2001; Thomson et al., 2014; Walter et al., 2011) and observations from oceanic basalts (Dixon et al., 2017; Hauri et al., 2018; Hirschmann, 2018) have been used to argue for substantial volatile recycling beyond the mantle wedge.

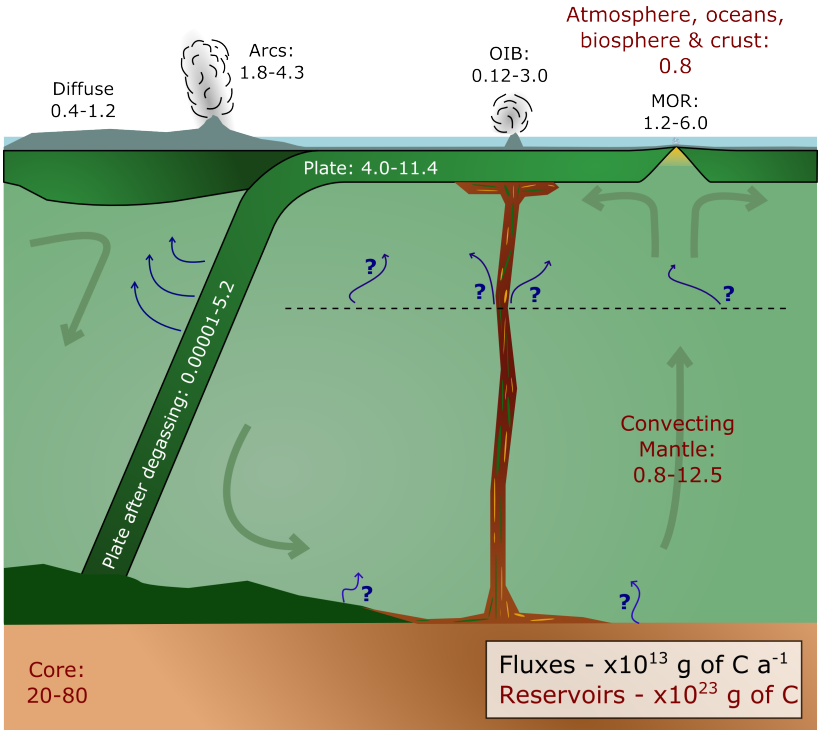

Figure 1.1: Summary of carbon budgets and fluxes throughout the Earth compiled from the reviews by Dasgupta and Hirschmann (2010) and Kelemen and Manning (2015). Blue arrows show potential fluxes of carbon-rich fluids, decoupled from the solid mantle flow (indicated by the larger green arrows). OIB: Ocean Island Basalt. MOR: Mid Ocean Ridges.

This thesis takes an observational approach to the problem, utilising Icelandic basalts to characterise the diverse history of volatile recycling recorded by the mantle upwelling beneath Iceland. Chapter 2 describes the collection of a new melt and mineral inclusion dataset acquired from a number of Icelandic eruptions. In Chapter 3 I use this dataset alongside a new thermal model of multi-lithological mantle melting to place new constraints on the temperature and mineralogy of the Icelandic plume, the primary physical properties controlling the mantle's convective circulation (Turcotte and Schubert,

2014). I develop a new statistical basis on which to interrogate volatile-trace element systematics of suites of basalts in Chapter 4. This new understanding of volatile-trace element systematics is combined with the new dataset and existing datasets to make the first comprehensive description of carbon and water heterogeneity (Chapters 6 and 7) in the Icelandic mantle. Chapter 8 discusses the implications of these new estimates of carbon and water mantle abundances for the global water and carbon cycle.

In the remainder of this chapter I review the progress in identifying carbon and water concentrations of different mantle reservoirs (Sections 1.1 and 1.2), the role of mantle convection in Earth's deep volatile cycles (Section 1.3), and how the physical properties primarily controlling mantle convection (mineralogy and temperature) may be inferred (Sections 1.3.1 and 1.3.2).

1.1 Estimates of mantle carbon concentrations

Progress in identifying mantle carbon concentrations has been limited by the tendency of carbon to exsolve from magmas to form CO_2 vapour prior to eruption (Dixon and Stolper, 1995). Decoupling of magma and vapour during transport then prevents reconstruction of the primary magmatic CO_2 concentration, in turn preventing extrapolation back to the mantle source. Studies of mantle carbon have therefore necessitated unique approaches, summarised here.

The carbon concentration in Earth's upper mantle was first estimated by Javoy et al. (1982), who took the mean carbon concentration found in mantle peridotites (400 ppmw), after filtering for primitive carbon isotope signatures. In order to reconcile the calculated flux of carbon from the mid-ocean ridge (MOR) system with the exosphere carbon inventory, Javoy et al. (1982) argued for significant carbon recycling into the mantle. However, more recent compilations of carbon contents of mantle xenoliths suggest the mean concentration is much lower (100 ppmw) and represents a highly heterogeneous population (Deines, 2002). Furthermore, mantle xenoliths are derived from the lithospheric mantle (Pearson et al., 2003), where carbon may be added by extensive metasomatism (e.g. Kelemen and Manning, 2015; Keller et al., 2017).

Hirschmann (2018) also argued for significant recycling of carbon into the mantle in order to reconcile exospheric and mantle carbon budgets. He compiled more recent estimates of upper mantle carbon concentrations and exosphere budgets, then compared them with Ba and Nb budgets of the same reservoirs. Ba and Nb both behave similarly to carbon during mantle melting (Rosenthal et al., 2015), but during recycling Ba is partitioned strongly into aqueous fluids (Kogiso et al., 1997; Stracke et al., 2003a), whilst Nb is largely immobile. The CO_2/Ba ratio of the exosphere is significantly lower than the upper mantle, whilst the exospheric CO_2/Nb ratio is larger, leading Hirschmann (2018) to argue

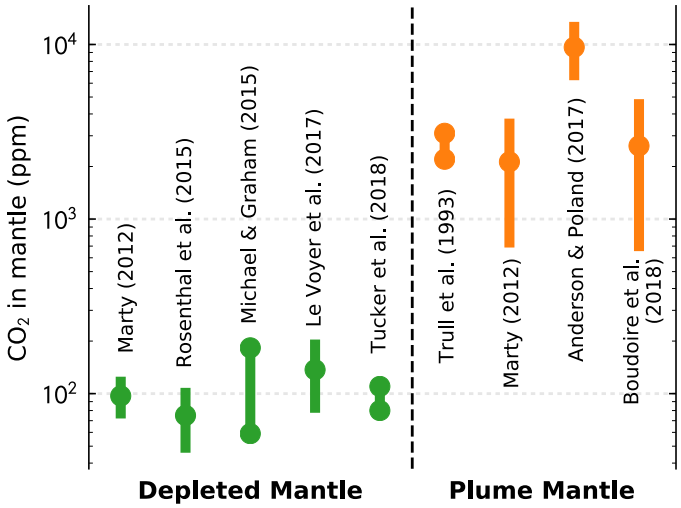

Figure 1.2: A selection of the most recent estimates of the CO_2 concentration in the depleted mantle, and all existing estimates of plume mantle CO_2 concentrations.

the behaviour of carbon during recycling is intermediate between the two, neither being efficiently retained or removed from the subducting slab.

The finding that significant carbon must be recycled into the mantle is at odds with the conclusions of Kelemen and Manning (2015) who argued that carbon should be efficiently removed from most subducting slabs, and the apparent discrepancy between the mantle and exosphere carbon budgets is due to a large carbon reservoir in the lithospheric mantle overlying the subduction plate. Hirschmann (2018) argued xenoliths derived from metasomatised lithosphere do not corroborate the high carbon concentrations Kelemen and Manning (2015) predict, though this might reflect decomposition of carbonates during exhumation (Canil, 1990; Sleep, 2009), though Hirschmann (2018) contests this.

The arguments for and against significant carbon recycling depend on arguments made on the basis of the expected outcomes of processes (Kelemen and Manning, 2015), or average carbon inventories of large reservoirs (Hirschmann, 2018; Javoy et al., 1982). Though convective stirring of the mantle is expected to provide efficient mechanical mixing of mantle heterogeneity introduced by recycling (e.g. Allègre and Turcotte, 1986; Hoffman and McKenzie, 1985), there is abundant geochemical evidence in both mid-ocean ridge basalt (MORB) and ocean-island basalt (OIB) that the identities of mantle heterogeneities are retained on a small scale (e.g. Maclennan, 2008b; Saal et al., 1998; Shorttle and Maclennan, 2011; Woodhead and McCulloch, 1989; Zindler et al., 1984). Additionally, studies of OIB isotope geochemistry demonstrate mantle plumes carry significant quantities of recycled material (e.g Allègre, 1987; Stracke et al., 2005), in addition to components of primordial mantle (e.g. Hart et al., 1992; Kurz et al., 1983) and depleted mantle (e.g. Fitton et al., 2003; Kerr et al., 1995; Skovgaard et al., 2001).

By estimating the volatile abundance in these separate mantle components, more direct estimates of the efficiency of volatile cycling may be made. The difference in volatile abundance between depleted

and primordial domains might reflect the efficiency with which carbon was extracted from the mantle during early Earth outgassing (Allègre et al., 1983; Porcelli and Ballentine, 2002), or continental and oceanic crust formation (Gast, 1968; O'Nions et al., 1977). Any quantity of carbon in recycled mantle components would reflect some amount of carbon recycling, and reference could be made to estimates of carbon abundance in oceanic lithosphere (e.g. Hirschmann, 2018; Kelemen and Manning, 2015) to quantify recycling efficiency.

Many estimates have been made for the carbon abundance in the depleted mantle, and some of the most recent are shown in Figure 1.2. A variety of techniques have been applied to samples from diverse locations, I critically evaluate these previous estimates in Section 1.1.1. A number of estimates have also been made of the bulk carbon content of plume mantle (summarised in Figure 1.2). Though there is significant variability in these estimates, they all suggest carbon concentrations in plumes are higher than that in the depleted mantle. It is unclear whether the high bulk plume carbon budgets reflect carbon enrichment in depleted, recycled or primordial plume components. In order to robustly constrain the efficiency of carbon recycling and early atmosphere formation, these separate contributions must be resolved. I review these bulk constraints in Section 1.1.2.

A note on terminology

Throughout this thesis I quantify mantle carbon concentrations as oxidised carbon, CO_2, in preference to its reduced form, C, more likely to prevalent in the deep mantle (e.g. Dasgupta and Hirschmann, 2010). When carbon concentrations are measured in this study, since they are made in lavas, the carbon is present as CO_2. Therefore the observed carbon concentrations are better represented as CO_2, and to maintain consistency throughout the text I describe mantle carbon budgets in terms of CO_2.

1.1.1 Depleted Mantle

Melting beneath the global mid-ocean ridge system predominantly samples the depleted mantle (Gale et al., 2013a). The submarine environment is advantageous for volatile studies, and much of the work in this field has been focussed on MORB for this reason. The high pressures of eruption allow lavas to retain a greater proportion of their volatile budget (Moore, 1979), and exsolved volatiles will reside in the ocean for a characteristic time period.

Since the only source of ^{3}He to the oceans is from magmatic degassing (Clarke et al., 1969), the inventory of ^{3}He in the oceans can be used to estimate the total flux of ^{3}He from the exsolved magmatic vapours of the mid-ocean ridge system (Bianchi et al., 2010; Craig et al., 1975; Farley et al., 1995). Though the solubilities of CO_2 and He differ in basaltic melts (Jambon et al., 1986; Stolper

and Holloway, 1988), which results in the $CO_2/^3He$ of magmatic fluids being progressively fractionated, this deviation from the mantle ratio can be corrected for by using the $^4He/^{40}Ar^*$ (radiogenic production) ratio to estimate the degree of fractionation (Marty, 1995). The corrected $CO_2/^3He$ ratios of hydrothermal fluids can then be combined with the estimated total flux of ^3He to calculate of the total MOR CO_2 flux, and further combined with estimates of total melt productivity to quantify the average CO_2 concentration of the depleted mantle (Marty, 2012; Marty and Tolstikhin, 1998). Using the most recent estimate of the ^3He flux derived from oceanographic measurements (Bianchi et al., 2010), the average CO_2 concentration in the depleted mantle is 97 ± 20 ppmw (Marty, 2012).

Though the average depleted mantle carbon budget may be robustly constrained by combining estimates of mantle $CO_2/^3He$ with the global ^3He flux derived from oceanographic measurements, this technique places little constraint on how heterogeneously CO_2 is distributed within the depleted mantle. Additionally, Ballentine et al. (2002) question how robust such calculations are given the time-integrated ^3He flux to the oceans represents only 1000 years of magmatic activity (Farley et al., 1995), yet oceanic crust production takes place on a timescale of tens of millions of years.

Heterogeneity in lithophile trace element abundances is substantially better constrained than ^3He heterogeneity in the depleted mantle (Salters and Stracke, 2004). Since CO_2 and Ba are thought to behave almost identically during mantle melting (Rosenthal et al., 2015), primary magmatic CO_2/Ba ratios should equal the CO_2/Ba ratio of the mantle source. Estimates of mantle CO_2/Ba ratios can then be combined with an estimate of the mantle Ba concentration to estimate the CO_2 concentration of the small volume of mantle that gave rise to the magma (Saal et al., 2002). Observations from MORB glasses, olivine-hosted melt inclusions and popping rocks have all been used to constrain mantle CO_2/Ba ratios, the results of which I summarise here.

Submarine Glasses

Rare ultra-depleted glasses are occasionally erupted on the ocean floor, often in fracture zones (Gale et al., 2013a). Many ultra-depleted glasses contain sufficiently low CO_2 concentrations that they must have been undersaturated in CO_2 vapour during eruption. The glasses CO_2 undersaturation led Michael and Graham (2015); Shimizu et al. (2016) to suggest they preserve mantle CO_2/Ba and CO_2/Nb ratios. Significant diversity of CO_2/Ba and CO_2/Nb ratios have been measured in these glasses (Figure 1.3), which do not correlate with isotope or trace element ratios (Michael and Graham, 2015). Extrapolating the average CO_2/Ba ratio of the ultra-depleted glasses (105 ± 9) to the rest of the depleted mantle, Michael and Graham (2015) estimated the depleted mantle CO_2 concentration ranges between 60 and 130 ppm. Whilst this observation might indicate source heterogeneity, in Chapter 4 I argue the diversity is likely to arise from concurrent magma degassing and mixing.

Whilst it is possible the CO_2 undersaturated glasses do record mantle mantle CO_2/Ba ratios, their extreme depletion might be taken as an indication they do not sample typical depleted mantle. An alternative approach is to use a more representative, though CO_2 saturated, sample of MORB glasses and attempt to correct for CO_2 degassing. Since degassing strongly fractionates the $^{13}C/^{12}C$ isotope ratio (Javoy et al., 1978), if the primary magmatic $^{13}C/^{12}C$ ratio is known, the amount of CO_2 lost by degassing may be calculated (Pineau and Javoy, 1983). Cartigny et al. (2008) apply this technique to a suite of glasses from the Mid-Atlantic ridge, and find highly variable CO_2/Ba and CO_2/Nb ratios (Figure 1.3).

Tucker et al. (2018) instead use the fractionated ratios of $^4He^*/^{40}Ar^*$ of $^4He^*/^{21}Ne^*$ measured in MORB glasses estimate the amount of CO_2 lost by degassing, additionally incorporating kinetic disequilibrium into their calculations. Whilst similar in principle to the approach adopted by Marty (1995) and Marty and Tolstikhin (1998), estimating primary magmatic CO_2 concentrations of individual samples offers the possibility of resolving heterogeneity in mantle carbon abundances. Tucker et al. (2018) reconstruct variable CO_2/Ba ratios for the primary melts, with an average of 103 ± 28, similar to the average of the CO_2 undersaturated glasses reported by Michael and Graham (2015). Tucker et al. (2018) also estimated the average depleted mantle $CO_2/^3He$ with their technique, which they combined with the global MOR ^3He flux estimate to calculate an average depleted mantle CO_2 concentration of 110 ppmw.

Popping Rocks

Popping rocks are seafloor lavas that have partially or completely retained exsolved vapour as vesicles (Hekinian et al., 1973). Noble gas systematics, vesicle-size distributions and high $\delta^{13}C$ values have been used to argue the volatiles contained in the vesicles were derived from the coexisting lava, and they represent the entirety of the primary magma's volatile budget (Cartigny et al., 2008; Sarda and Graham, 1990). Recent work by Jones et al. (2019) instead suggests that much of the vesicle population may reflect secondary addition of volatile exsolved from an external magma.

If the volatile content of the lava plus vesicles is assumed to reflect the primary magma volatile contents, the mantle source region must have had $\sim$300 ppmw carbon (Javoy and Pineau, 1991). Despite the very high inferred primary magmatic CO_2 concentrations, popping rocks show CO_2/Nb and CO_2/Ba ratios that are broadly similar to those inferred from undersaturated glasses and melt inclusion suites (Cartigny et al., 2008).

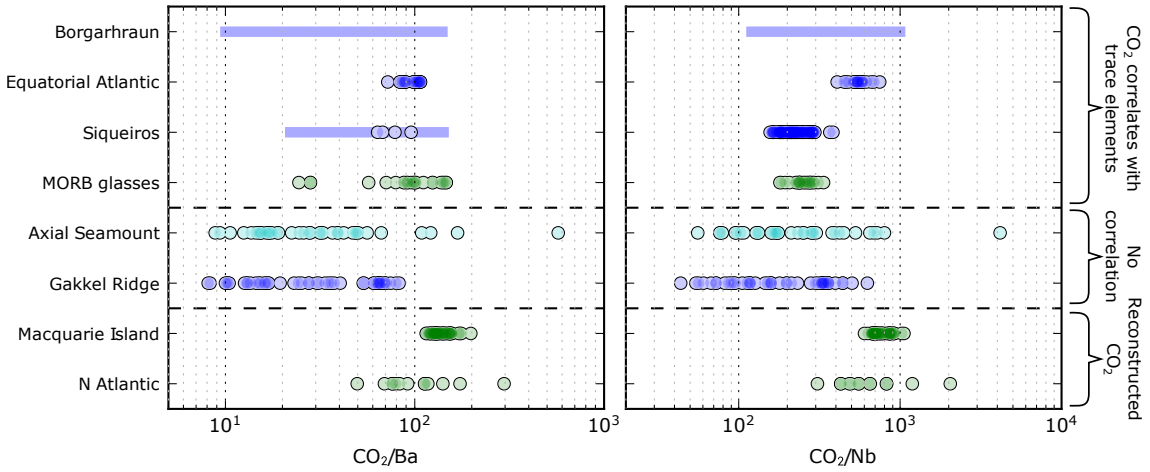

Figure 1.3: Compilation of published data used for estimating mantle CO_2/Ba and CO_2/Nb ratios. The data are separated into datasets that show a correlation between CO2 and trace elements (and have therefore been identified as undegassed on that basis), datasets that show no such correlation (and so have been inferred to be partially degassed), and datasets where the CO_2 concentration has been reconstructed from Cl concentrations or C-isotope fractionation. Green points indicate data obtained from glasses, cyan points indicate data obtained from plagioclase hosted melt inclusions, and green indicates data obtained from olivine hosted melt inclusions. Bars indicate unpublished data reported by Rosenthal et al. (2015). Data sources: Borgarhraun (Northern Iceland): unpublished data from Hauri et al., reported by Rosenthal et al. (2015); Equatorial Atlantic: Le Voyer et al. (2017); Siqueiros: Saal et al. (2002), unpublished Ba data from Saal et al. reported by Rosenthal et al. (2015); MORB (undersaturated) glasses: Michael and Graham (2015), Shimizu et al. (2016); Axial Seamount: Helo et al. (2011); Gakkel Ridge: Shaw et al. (2010), Wanless et al. (2014); Macquarie Island: Shimizu et al. (2016); N. Atlantic: Cartigny et al. (2008).

Melt Inclusions

As crystals grow within deep magma bodies droplets of their parental magma may become trapped, these isolated pockets of magma are known as melt inclusions. This deep crystal assemblage is often carried by magmas to the surface when they erupt (e.g Wanless and Shaw, 2012; Winpenny and Maclennan, 2011). Melt inclusion suites from individual eruptions often preserve a large diversity of trace element geochemistry (e.g Gurenko and Chaussidon, 1995; Maclennan, 2008a) and radiogenic isotope geochemistry (e.g. Maclennan, 2008b; Saal et al., 1998), interpreted to reflect partially mixed co-genetic fractional melts from one or more mantle components. When melt inclusions datasets are combined with models of mantle melting and magma evolution, the structure of the trace element geochemistry can be used to unravel the processes magmas experience prior to eruption (e.g. Gurenko et al., 1996; Maclennan et al., 2003a; Neave et al., 2014; Sobolev, 1996).

Melt inclusion suites are unique in that they can preserve melts at high pressure, where volatiles may remain largely undegassed, and simultaneously provide information on the magmatic processes the

magmas have experienced. The first MORB melt inclusion suite characterised both for trace and volatile elements was derived from ultra-depleted lavas from the Siqueiros Fracture Zone in the Pacific (Saal et al., 2002). The positive correlation between CO_2 and Nb concentrations led Saal et al. (2002) to suggest that CO_2 had behaved identically to Nb during both melting and magma evolution, and they had not been fractionated from each other by degassing. The average CO_2/Nb ratio possessed by the melt inclusions (239 ± 46) was therefore believed to represent the mantle source.

Le Voyer et al. (2017) also found a strong positive correlation between CO_2 and the most incompatible trace elements in a sample from the Equatorial Atlantic, but found these inclusions preserved a much higher CO_2/Nb ratio of 557 ± 79 Similarly, Hauri et al. (2018) found the same property in a melt inclusion dataset from Borgarhraun, a depleted eruption in the Northern Volcanic Zone of Iceland, which preserved an intermediate CO_2/Nb ratio of 391 ± 16 The observed variability in the apparent mantle CO_2/Nb ratios was interpreted by Hauri et al. (2018) to reflect the depleted mantle CO_2 concentration varying between 48–129 ppmw.

Hirschmann (2018) combined these results with the average CO_2/Nb and CO_2/Ba ratios from melt inclusion suites not possessing CO_2–trace element correlations. He argued that variability in the depleted mantle CO_2/Ba and CO_2/Nb ratios is not controlled by source enrichment, and that the depleted mantle is well characterised by an average CO_2/Ba ratio of 100 ± 20 Hirschmann (2018) acknowledges this average CO_2/Ba ratio may be an underestimate given the likelihood of partial degassing and mixing having affected these melts (Chapter 4). The implication of this result is heterogeneity in the depleted mantle CO_2 concentration largely co-varies with mantle trace-element enrichment and depletion.

In Chapter 4 I demonstrate that positive correlations between CO_2 and incompatible trace elements are a natural consequence of concurrent magma degassing and mixing. I argue that the average CO_2/Nb ratios recorded by melt inclusion suites are determined by the degree of mixing and extent of degassing prior to melt inclusion entrapment; and the existing melt inclusion datasets are consistent with a single CO_2/Ba (or CO_2/Nb) ratio in the depleted mantle. In Chapter 6 I demonstrate a new approach that may be taken to robustly account for the effects of magma degassing and mixing when identifying variability in mantle CO_2/Ba ratios.

1.1.2 Lower mantle

Whilst there is evidence that the depleted mantle volatile budget has been replenished by primordial and recycled components (Clarke et al., 1969; Hirschmann, 2018; Porcelli and Ballentine, 2002), these mantle components are most strongly expressed in plume derived basalts. The difference in mantle components sampled by ocean-ridge spreading and ocean-island volcanism has been understood as a

reflection of the advection of lower mantle components within buoyant mantle plumes (e.g Hart et al., 1992).

Using OIB to constrain the volatile abundance of its source region has proved more difficult than for MORB. The majority of OIB volcanism is sub-aerial, leading to comparatively low eruption pressures and more extensive volatile loss due to degassing. In addition, OIB is generally derived from smaller extents of melting than MORB (e.g. McKenzie and O'Nions, 1991); for the same mantle CO_2 concentration OIB primary magmas will inherit higher CO_2 concentrations than primary MORB magmas, making them more susceptible to degassing. Far fewer studies have attempted to quantify the CO_2 concentration of plume mantle than the depleted mantle (Figure 1.2), and none have attempted to resolve the carbon contents of individual mantle components. I review the existing constraints here.

In the absence of direct observations of the carbon content of the lower mantle, Marty (2012) estimates a 'bulk mantle' CO_2 content. This estimate reflects the average of both the depleted and lower mantle. By utilising the largely invariant C/N and N/^{40}Ar ratios in OIB and MORB related fluids (Marty and Dauphas, 2003; Marty and Zimmermann, 1999). Since the Earth's budget of ^{40}Ar is intimately linked to its ^{40}K budget, the total amount of ^{40}Ar remaining in the mantle can be estimated from the terrestrial K budget (Allègre et al., 1996). Marty (2012) then combined the ^{40}Ar budget with the largely invarient C/N and N/^{40}Ar ratios in OIB and MORB related fluids (Marty and Dauphas, 2003; Marty and Zimmermann, 1999) to estimate a bulk mantle carbon content of 580 ± 380 ppmw (Figure 1.2). This bulk mantle estimate is much higher than any estimates made for the depleted mantle, and suggests the lower mantle must be much richer in carbon.

Trull et al. (1993) estimate the carbon content of both the lower and upper mantle by utilising two-box models of mantle evolution. They constrain their model using the observed C/^{3}He and C/^{4}He ratios in MORB and OIB, and assume a primordial mantle concentrations of C and He and its ^{3}He/^{4}He ratio. Using a number of models, Trull et al. (1993) suggested a range between 2200–3100 ppmw C in the lower mantle (Figure 1.2).

By modelling magma supply rates and fitting geophysical observations and CO_2 and SO_2 Kilauea summit emissions, Anderson and Poland (2017) estimated the CO_2 content of primary Hawaiian magmas as 0.97 wt%. They then extrapolated this to the mantle source, assuming a melt fraction of 10%, to yield 960 ppmw CO_2 in the mantle melting beneath Hawaii. This analysis relies on the total magmatic CO_2 emissions to be adequately quantified. If extensive deep degassing takes place, as I argue is likely in Chapter 4, much of the CO_2 may be diffusely emitted away from the Kilauea summit (e.g Chiodini et al., 1998; Parks et al., 2013). Underestimating CO_2 emissions would result in the calculated mantle CO_2 content being an underestimate, however the calculated concentration is the highest mantle CO_2 estimate yet made. Furthermore, active upwelling of plume mantle and lateral transport of deep low-degree volatile-rich plume melts may complicate the relationship between the

melt fraction and the concentration of volatile and trace elements in magmas (Gibson and Richards, 2018; Maclennan et al., 2001a).

Using He–Ar–CO_2 systematics of fluid inclusions in crystals from Piton de la Fournaise, Boudoire et al. (2018) estimate magmas have degassed 94±5 % of their primary CO_2 budget. This extent of degassing implies the primary magmsa had 3.5±1.4 wt% CO_2, which they propagate to source carbon concentration of 716 ± 525 ppmw by assuming the mantle melt fraction. Their estimate of mantle CO_2 is comparable to the bulk mantle estimate made by Marty (2012), and may reflect a similar mixture of depleted, primordial and enriched mantle components.

1.2 Estimates of mantle water concentrations

The solubility of H_2O in basaltic melts is much greater than CO_2, and is only like to degas extensively during sub-aerial eruption (Dixon and Stolper, 1995). Submarine basaltic glasses therefore provide a much better record of their primary water concentrations than their carbon concentrations. Melt inclusions have been largely avoided in mantle water studies, as H^+ is known to rapidly diffuse through olivine, allowing melt inclusion H_2O concentrations to re-equilibrate with the surrounding melt (e.g. Hartley et al., 2015; Koleszar et al., 2009; Qin et al., 1992).

1.2.1 Constraints from oceanic basalts

Similarly to studies of mantle carbon, many mantle water studies are predicated upon estimating primary magmatic water concentrations. The most widely adopted approach is to use water contents measured in extremely primitive glasses that have undergone minimal crystal fractionation (e.g. Jambon and Zimmermann, 1990; Sobolev and Chaussidon, 1996), or to correct observed H_2O concentrations in moderately evolved glasses for crystal fractionation (e.g. Nichols et al., 2002; Simons et al., 2002). Assuming a mantle melt fraction then allows the mantle H_2O concentration to be estimated, much as applied in the studies of mantle plume carbon contents, with the same potential issues (Section 1.1.2). The mantle H_2O estimates derived using this methodology are shown by squares on Figure 1.4.

Other studies have utilised the large effect water has on the melting behaviour of the mantle and the chemistry of the magmas they produce (Asimow et al., 2004; Gibson and Richards, 2018). By modelling the variations in major element chemistry seen in fractionated MORB affected by the Azores hotspot, Asimow et al. (2004) demonstrated they were best matched by evolution of mixed magmas from a dry depleted and wet enriched mantle components. Gibson and Richards (2018) used

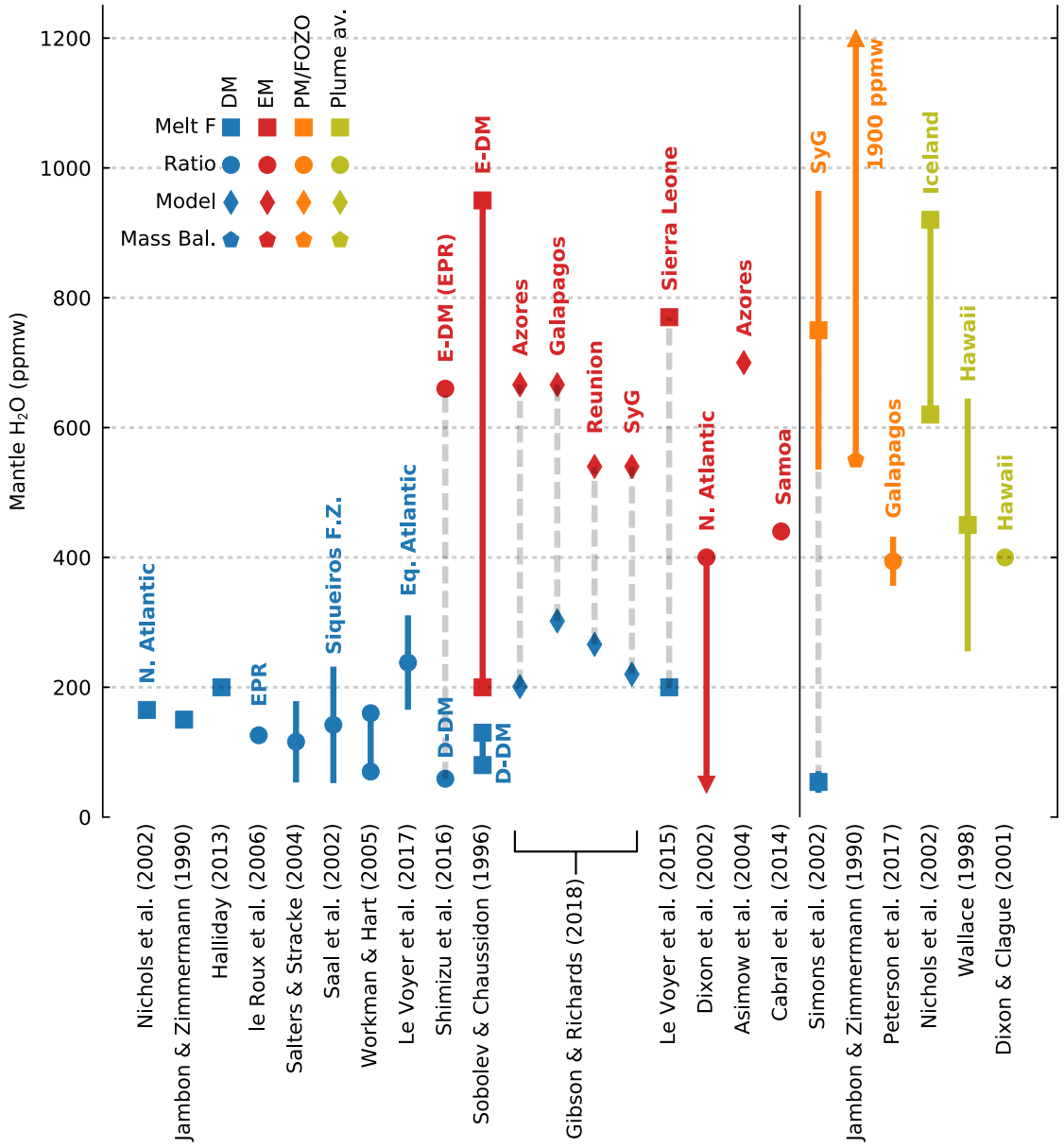

Figure 1.4: Compilation of mantle H_2O estimates from mid-ocean ridge basalts (left of figure) and ocean islands (right of figure). Where estimates apply to specific locations they are annotated. Symbols indicate the method used to calculate the estimate, and the colour indicates the mantle endmember they apply to. EM corresponds to any recycled mantle components, and PM/FOZO corresponds to high $^3He/^4He$ components.

a melting model to invert the trace element and water concentrations of glasses from a number of volcanic lineaments thought to arise from interactions between mantle plumes and mid-ocean ridges (e.g. Harpp and Geist, 2002). They found the lava chemistry could be matched best by contributions of melts from a comparatively dry depleted mantle source, and wet enriched mantle source.

Alternatively, consideration of the melting process may be avoided if magmatic H_2O concentrations are compared with the concentration of a trace element with similar behaviour during melting (e.g. Dixon and Clague, 2001; Dixon et al., 2002; Shimizu et al., 2016). In Chapter 4 I assess which trace element is most appropriate for the comparison, and argue that whilst Ce is most widely used, H_2O/La ratios are probably least fractionated from the source during melting. Figure 1.5 shows the range of H_2O/Ce values inferred for different mantle end-members. Though there is substantial variability, there is no consistent sense of offset between depleted and enriched mantle components.

Once the mantle H_2O/La or H_2O/Ce ratio has been identified, it may be combined with an estimate of the source La or Ce concentration (e.g. Stracke et al., 2003a; Workman and Hart, 2005) to calculate the mantle H_2O concentration. Mantle H_2O estimates derived using this technique are shown as circles on Figure 1.4. The elevated H_2O concentrations for the enriched mantle, compared with the depleted mantle, arise from the trace element enrichment assumed to be present in enriched mantle sources.

Cabral et al. (2014) use melt inclusions from Mangaia to constrain the H_2O/Ce ratio and H_2O content of the HIMU mantle component. They suggest the melt inclusions retain their primary H_2O/Ce ratios having not been affected by H^+ diffusion by looking for a correlation between melt inclusion H_2O concentration and inclusion size. This approach will only be sensitive to diffusive loss of water due to H^+ exchange with surrounding magma with low H_2O concentrations. Invariance of H_2O concentration with inclusion size could instead indicate re-equilibration of H_2O concentrations by both gain and loss of H^+ with surrounding magma containing an intermediate water content, as might be expected during magma storage (Hartley et al., 2015; Koleszar et al., 2009). In Chapter 4 I develop a new approach for utilising melt inclusion datasets to estimate pre-eruptive H_2O/Ce ratios when extensive degassing from the carrier lava has occurred during subaerial eruption.

1.2.2 Mantle water heterogeneity

Figure 1.4 demonstrates that whilst there's variability in the H_2O content estimated for similar mantle components, the depleted mantle is uniformly found to have lower H_2O concentrations than both enriched and primordial mantle components. Some of this variability might reflect uncertainty or systematic errors in the different techniques, but it is also likely that at least some of the signal represents real global variability (e.g Dixon et al., 2017).

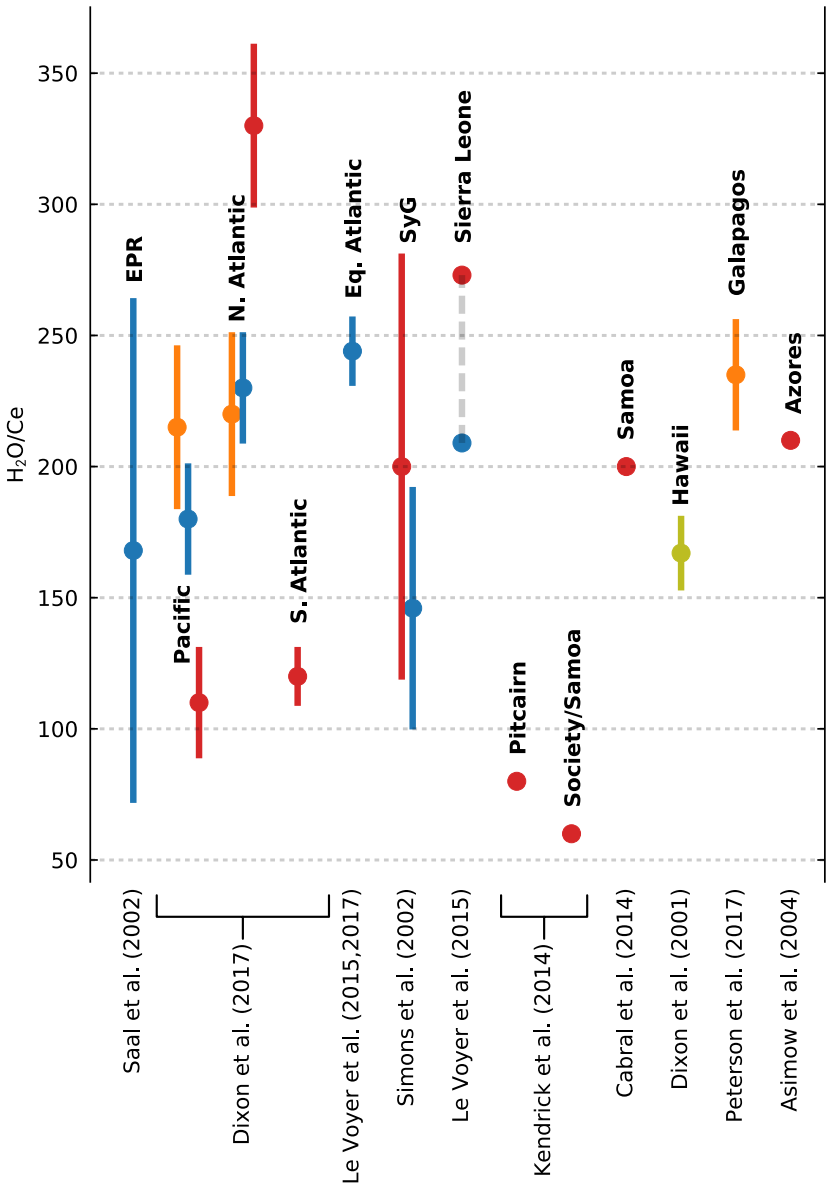

Figure 1.5: Compilation of literature H_2O/Ce ratios inferred for mantle components. See Figure 1.4 for a key to colours.

There is some inconsistency in how different authors have treated the mantle components associated with plumes. For example Dixon et al. (2002) used radiogenic Pb- and Sr-isotopes of their samples to explicitly consider the distinct contributions from 'EM'-like and 'FOZO' components, whilst the study by Gibson and Richards (2018) was chiefly concerned with the dynamics of plume derived melts and so did not require detailed consideration of different plume components. This inconsistency between different studies may therefore contribute to some of the variability in plume components summarised in Figure 1.4, but a robust observation is that both enriched and primordial plume components appear to be richer in water than the depleted mantle.

Dixon et al. (2017) undertook a global study of submarine glasses to provide a consistent view on global mantle H_2O variability. They combined H_2O/Ce and δD measurements to infer the relative dehydration of mantle components in the Pacific and Atlantic basins, arguing that the observed variations reflect different extents of fluid removal during subduction. An important conclusion of their study was enriched mantle components can have H_2O/Ce both lower and higher than the depleted or primordial mantle (Figure 1.5). Dixon et al. (2017) did not provide estimates of absolute H_2O concentrations in these mantle components, and so this study does not appear on Figure 1.4. It is likely that if estimates were made using the endmember H_2O/Ce ratios, they would coincide with the previous estimates shown on Figure 1.4.

In Chapter 7 I demonstrate substantial H_2O heterogeneity exists in the Icelandic mantle, and the recycled component has unusually low concentrations of water, likely even lower than the H_2O concentration in the Icelandic depleted mantle.

1.3 The role of mantle convection in Earth's volatile cycles

In the present day, fluxes of elements from the mantle are primarily controlled by movement of mantle material through the melting regions beneath ocean islands, mid-ocean ridges and volcanic arcs (e.g. Dasgupta and Hirschmann, 2010; Kelemen and Manning, 2015). The ability of the mantle to retain elements recycled in subducting plates depends on the fate of these dense slabs. Images from seismic tomography reveal slabs entering the lower mantle (e.g. Van der Hilst et al., 1997), where they might sequester their volatiles until it is entrained in a mantle plume and carried back into the upper mantle (e.g. Hart et al., 1992; Hofmann and White, 1982). Alternatively their volatile elements might be lost by carbonated melting in the transition zone (Thomson et al., 2016). Noble gas isotope ratios also require part of the mantle to have retained its volatile elements and remained isolated throughout the lifetime of the Earth, until being entrained in mantle plumes (e.g. Allègre et al., 1983; Harrison et al., 1999).

The convective circulation of the Earth is driven by density contrasts within the mantle. The density of mantle regions is determined its mineralogy (or lithology) and its temperature (Turcotte and Schubert, 2014). Additionally, the development of convective instabilities and the entrainment of mantle material depends on its rheological properties, a function of its temperature, mineralogy and water content (e.g Ballmer et al., 2017; Manga, 2010; Samuel and Farnetani, 2003; Tackley, 1998). A complete understanding of the Deep Earth carbon and water cycles therefore requires quantification not only of the mantle volatile inventory, but also the mantle lithologies which host them and their physical properties.

In Chapter 3 I place new bounds on the temperature and lithological heterogeneity present in the Icelandic mantle. I find that geophysical, geochemical and petrological constraints require the mantle to be considerably hotter than ambient mantle, and made of a mixture of lherzolite, pyroxenite and harzburgite. In Chapter **??** I consider the bearing these results have on the storage and transport of mantle volatiles. I review the techniques previously used to estimate mantle temperature and lithology here.

1.3.1 Estimating mantle temperature

Mantle temperature estimates invariably rely on relationships determined between variables indirectly sensitive to mantle temperature. Previous studies have utilised magma and crystal chemistry, magma flux estimates, trace-element geochemistry, seismic tomographic inversions, and mantle transition zone topography as imaged by receiver function analysis. These diverse techniques are broadly in agreement for the MORB mantle and the Iceland plume, the results of which are summarised in Figure 1.6. These techniques are reviewed here. In Chapter 3 I outline a new technique for combining petrological, geophysical and geochemical observations to simultaneously determine mantle temperature and lithology.

Petrological temperature estimates

Mantle potential temperature estimates based on petrological observations generally work by inferring primary magma compositions, followed either by fitting this to predicted accumulated mantle melt compositions (Herzberg and Asimow, 2015; Hole and Millett, 2016), or estimating the temperature of olivine saturation and extrapolating back to the solidus (Putirka, 2008a, 2016). Differences in olivine-melt equilibration temperatures have been observed as a function of tectonic setting (Coogan et al., 2014; Heinonen et al., 2015; Putirka, 2008a, 2016; Trela et al., 2017) and time (Putirka, 2016; Spice et al., 2016).

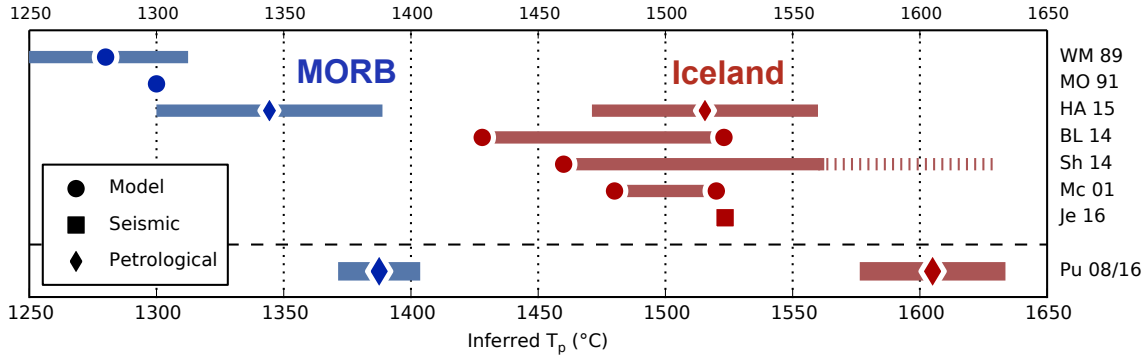

Figure 1.6: Previous T_p estimates for mid-ocean ridges (blue) and Iceland (red). Estimates of T_p derived from olivine-liquid equilibration temperatures by Putirka (2016, 2008b) (Pu 08/16) are shown below the dashed line. Jenkins et al. (2016) (JE 16) estimate a ΔT_p of 210 °C, shown here relative to the median T_p from the MORB inversion. Shorttle et al. (2014) (Sh 14) report a minimum bound, represented by the point and dashed line. The other estimates are BL14: Brown and Lesher (2014), HA 15: Herzberg and Asimow (2015), Mc 01: Maclennan et al. (2001a), MO 91: McKenzie and O'Nions (1991) and WM 89: White and McKenzie (1989). Where there are two symbols a range of estimates is reported; single symbols and bars indicate a single estimate and its reported uncertainty.

However, many of these studies do not apply a correction for the cooling associated with the melting process. Such a correction is applied by Putirka (2008a, 2016, 2005), where absolute potential temperatures are estimated from olivine-liquid equilibration temperatures. However, a discrepancy of $\sim$100 °C exists between the potential temperature estimates reported by Putirka (2016, 2008b) and those based on other methods (Figure 1.6).

A potential challenge in employing olivine-liquid equilibria to obtain mantle temperatures is that the composition of the magma in equilibrium with the most forsteritic olivine crystals must be known. In general, olivine crystals may be out of equilibrium with their carrier liquid (e.g. Helz and Thornber, 1987; Thomson and Maclennan, 2012), requiring that their parental liquid composition be estimated. Whilst this extrapolation is a straight-forward process if only one primary magma exists for any one eruption, fractional melt extraction from the mantle can generate multiple primary melts that are not fully mixed at the time of olivine saturation (Slater et al., 2001; Sobolev, 1996). Keiding et al. (2011) and Herzberg (2011) described how incomplete mixing of fractional melts can cause primary magma MgO and FeO concentrations to be overestimated, which propagates into higher crystallisation temperature estimates.

Melt productivity temperature estimates

The fraction of solid mantle converted to magma during melting depends on how far its solidus is overstepped (McKenzie, 1984). Magmas may be generated from solid peridotite by a reduction in pressure or an increase in temperature. If the melting behaviour of the mantle is known, and the effect of decompression is isolated, the melt fraction can be related to mantle temperature (McKenzie and Bickle, 1988).

One approach to estimating melt fraction compares total melt productivity with an estimate of the flux of mantle through the melting region. At mid-ocean ridges this comparison is straight forward; the mantle flow field is a direct consequence of plate spreading, crustal thickness is directly proportional to the mantle melt fraction (McKenzie, 1984). In order to apply this to ocean islands, assumptions must be made about plume dynamics (e.g. Watson and McKenzie, 1991). Applying this approach to the global mid-ocean ridge system, White and McKenzie (1989) estimated the MORB mantle potential temperature of $1280 \pm 30\,^{\circ}\mathrm{C}$.

To derive the relationship between melt fraction and mantle temperature a model for the melting behaviour of the mantle is required. A large number of experimental studies have sought to constrain this (e.g. Green and Ringwood, 1967; Hirose and Kushiro, 1993; Ito and Kennedy, 1967; Sarafian et al., 2017; Walter, 1998). The experimental observations are then used either to parameterise empirical functions (e.g. Hirschmann, 2000; Katz et al., 2003; McKenzie and Bickle, 1988), or to constrain the thermodynamic properties of the mineral phases and magmas (e.g. Ghiorso et al., 2002; Ghiorso and Sack, 1995; Holland et al., 2018; Jennings and Holland, 2015). However the melting behaviour of different mantle lithologies can differ markedly (e.g. Jennings et al., 2016; Pertermann and Hirschmann, 2003; Yasuda et al., 1994).

An alternative approach uses lava trace element concentrations to infer melt fraction. The batch and fractional melting equations (e.g. Zou, 2007) provide simple relationships between mantle and lava trace element concentrations, their partition coefficients during melting and melt fraction. If the mantle trace element concentrations are known it is straightforward to calculate the melt fraction. Using trace elements with depth dependent bulk partitioning behaviour allows a melt fraction vs depth curve to be inverted for (McKenzie and O'Nions, 1991).

Rare earth element inversions have been widely applied to both MORB and OIB (e.g. Gibson and Geist, 2010; Gibson et al., 1997; Klöcking et al., 2018a,b; Maclennan et al., 2001a; Watson, 1993), and the resulting temperature estimates agree well with other techniques (Figure 1.6). However, application of the technique is problematic when the mantle trace element concentrations are unknown. This is particularly problematic for estimating mantle plume temperatures, as plume mantle is extremely

heterogeneous (e.g. Allègre and Turcotte, 1986) and there's significant uncertainty in the trace element concentrations of enriched mantle components (Stracke et al., 2003a).

1.3.2 Estimating mantle lithology

Much of the diversity in radiogenic isotope geochemistry seen in OIB has been interpreted in terms of recycling oceanic crust (e.g. White and Hofmann, 1982). At high pressures oceanic crust will be transformed to eclogite, or pyroxenite if crust becomes mixed with peridotite (e.g. Holland et al., 2013). Episodes of extensive melt extraction leave residual harzburgite (e.g. Jennings and Holland, 2015). It has also been suggested early Earth magma ocean processes may have left lithological heterogeneity which could still be preserved in the modern Earth (e.g Ballmer et al., 2017). The material participating in mantle convection, and transporting volatiles through the deep Earth, is therefore extremely mineralogically heterogeneous.

Despite the expectation from radiogenic isotope geochemistry for the existance of eclogite in the melting regions beneath ocean islands, extensive experimental evidence shows that any melts derived from such a lithology should be silica-oversaturated (e.g. Pertermann and Hirschmann, 2003; Yasuda et al., 1994; Yaxley and Green, 1998). OIB melts are generally silica-undersaturated, and often nepheline-normative (e.g Gill, 2010). However, experiments on silica-deficient pyroxenites have demonstrated silica-saturated and silica-undersaturated melts may be generated (e.g. Hirschmann et al., 2003; Kogiso et al., 2004), and some pyroxenite derived melts may have major element chemistry indistinguishable from peridotite derived melts (Lambart et al., 2009). Such lithologies might be derived from subducted eclogite by mechanical mixing with lherzolite (e.g. Kogiso et al., 1998), or reaction between eclogite-derived melts and lherzolite (e.g. Mallik and Dasgupta, 2012; Yaxley and Green, 1998). Many studies have suggested the offset between the major element chemistry of MORB and OIB may, in part, be caused by the contribution of pyroxenitic lithologies in the source of OIB (e.g. Dasgupta et al., 2010; Gibson, 2002; Herzberg, 2010; Jennings et al., 2016; Kogiso et al., 2003; Shorttle and Maclennan, 2011).

Another approach taken to estimating mantle mineralogy is to exploit the difference in solid-melt partitioning of minor elements between pyroxenitic and lherzolitic lithologies. In particular, the compatibility of Ni is strongly controlled by the presence of olivine, being much more compatible in olivine than other mantle phases (Beattie, 1993; Beattie et al., 1991). If olivine is not present in the mantle source, Ni will behave more incompatibility than if olivine were present, yielding primary magmas with much higher Ni concentrations. Sobolev et al. (2005) argued that the extremely high NiO concentrations in Hawaiian olivine phenocrysts must be derived from high NiO concentrations in their parental melts, which in turn must have been derived from an olivine-free mantle source.

This methodology has been applied to ocean islands globally (e.g. Gurenko et al., 2009; Sobolev et al., 2007; Trela et al., 2015; Vidito et al., 2013) to estimate variable contributions from pyroxenitic mantle. However, recent experimental work (Matzen et al., 2013, 2017a) has demonstrated that the partitioning behaviour of Ni between olivine and melt depends strongly on melt composition, temperature and pressure. Combining the new experimental constraints with melting models has demonstrated that melts derived from an olivine-bearing source can explain enrichments in Ni seen in many OIB olivine phenocrysts (Matzen et al., 2017b). Though the presence of pyroxenitic mantle lithologies can't be ruled out, they are not required by these observations, and make it difficult to place quantitative constraints on the amount of pyroxenite in the mantle.

The partitioning of U-series elements are particularly sensitive to the presence of garnet during mantle melting (e.g. Blundy and Wood, 2003). The relatively short half-lives of many U-series isotopes allows secular equilibrium to be attained in the mantle, but the melting process can generate disequilibrium. The extent of disequilibrium is controlled by the degree of element fractionation, the porosity and the rate of magma generation (e.g. McKenzie, 1985, 2000). All of these parameters are sensitive to the relative proportion of pyroxenite in the melting region, and the presence of U-series disequilibria in lavas has been used to argue for the presence of pyroxenite in the mantle (e.g. Allègre and Condomines, 1982; Elkins et al., 2016; Koornneef et al., 2012; Prytulak and Elliott, 2009). However, the complexity in the interpretation of U-series equilibria may make it difficult to make quantitative estimates of mantle pyroxenite contents.

Harder still to constrain is the presence of lithologies that contribute little to melt production. Refractory residues from previous melting events may be a cryptic component of the mantle (Bizimis et al., 2007; Harvey et al., 2006; Liu et al., 2008; Stracke et al., 2011; Warren, 2016). Even if they do melt, their depletion in trace elements will prevent isotope and trace element geochemistry of basalts revealing their presence. Shorttle et al. (2014) proposed a novel technique for assessing the presence of such mantle domains. Whilst the presence of pyroxenite in the mantle can be constrained using a variety of techniques, its presence in all but the lowest quantities in mantle plumes is difficult to reconcile with the requirement that they are buoyant. Shorttle et al. (2014) suggest that plume buoyancy may be enhanced by the presence of substantial quantities of refractory and low-density harzburgite.

1.4 Iceland as a natural laboratory for mantle volatiles

Iceland is a region of anomalous melting situated on the Mid-Atlantic Ridge, where zero-age crustal thickness is 20 km at the coasts (Darbyshire et al., 2000; Jenkins et al., 2018), and rises to 40 km in central Iceland (Darbyshire et al., 1998; Jenkins et al., 2018). Most authors attribute the anomalously

high melt production to the coincidence of a mantle plume with the Mid-Atlantic ridge (e.g. Maclennan et al., 2001a; Vink, 1984; White et al., 1992).

Plate spreading takes place along its three rift zones: the Western Volcanic Zone, the Eastern Volcanic Zone and the Northern Volcanic zone (Sæmundsson, 1979). Immediately offshore, plate spreading takes place on the Reykjanes and Kolbeinsey Ridges (Gudmundsson, 1995). In addition to the volcanism within these rift zones, volcanism takes place in Iceland's flank zones: the Snaefellsness peninsula, an abandoned ridge segment (Hardarson et al., 1997) which experiences some amount of NS stretching owing to differential spreading rates in the main rift zones (Karson, 2017), Vestmannaeyjar, the propagating extension of the EVZ (Gudmundsson, 1995), and Snæfell and Öræfajökull, regions of incipient rifting (Thordarson and Höskuldsson, 2014). The dominant magma type is tholeiitic basalt, though alkaline basalt is more typical of the flank zones (Jakobsson, 1972).

Iceland offers an excellent opportunity for studying mantle volatile heterogeneity; a number of mantle components have been observed and primitive basaltic material is readily available. These properties of Icelandic volcanism are discussed here.

1.4.1 Mantle heterogeneity

Recycled mantle components

Considerable variability has been observed in the radiogenic isotope geochemistry of Icelandic basalts, interpreted to reflect mixing between three and five mantle end-member components (e.g. Hanan and Schilling, 1997; Kitagawa et al., 2008; Peate et al., 2009, 2010; Shorttle et al., 2013; Thirlwall et al., 2004).

A number of hypotheses have been presented to suggest the origin of these components. Chauvel and Hémond (2000) proposed the array of endmembers reflects different parts of a complete section of ancient recycled oceanic crust. However, Thirlwall et al. (2004) suggested the data could be better explained by mixing of subduction modified palaeozoic oceanic crust mixing with North Atlantic asthenosphere, with some additional contributions from an EM1-like source with and without recent melt depletion. Peate et al. (2010) suggested the enriched mantle components instead reflect FOZO- or C-like mantle, ubiquitous globally, with a possible origin from mantle wedge peridotites metasomatised by fluids from a subducting slab.

The major element chemistry of the enriched basalts fit best with experimental melts derived from a chemical mixture of MORB-like basalt and peridotite (Shorttle and Maclennan, 2011). This would lend support to the hypothesis of crustal recycling. Though the precise origin of the enriched material

is debated, it is clear that it represents recycling of some form and is potentially typical of much of the recycled material in Earth's mantle.

Primordial mantle components

The proto-Iceland plume is associated with the highest $^3He/^4He$ measured in basaltic material (Starkey et al., 2009; Stuart et al., 2003). Though more recent volcanism on Iceland does not produce as extreme $^3He/^4He$ ratios, the basaltic glasses, crystals and geothermal fluids still record some of the highest $^3He/^4He$ ratios observed on Earth (e.g. Hilton et al., 1990, 1998). Measured $^3He/^4He$ ratios also extend down to MORB values of $\sim$8 R_a and lower, where R_a is the atmospheric $^3He/^4He$ ratio (e.g. Condomines et al., 1983; Macpherson et al., 2005).

No co-variation between $^3He/^4He$ and the lithophile radiogenic isotope ratios is seen either in the proto-Iceland plume (Starkey et al., 2009) or modern-day Iceland (Condomines et al., 1983). However, there is spatial structure to the distribution of $^3He/^4He$ ratios, with the highest ratios being observed in central Iceland, perhaps demarcating the plume conduit (Breddam et al., 2000; Harðardóttir et al., 2018).

1.4.2 Preservation of primitive basaltic melts

As magmas evolve during crustal storage they may undergo extensive fractional crystallisation, crustal assimilation, mixing and degassing (e.g. Carmichael, 1964; Hemond et al., 1988; Maclennan, 2008a; Neave et al., 2014). All of these processes variably obscure mantle signals inherited by magmas as they were generated.

The high MgO content of many Icelandic lavas suggests they are extremely primitive (Shorttle and Maclennan, 2011), and often carry crystal cargoes derived from near-primary mantle melts (Thomson and Maclennan, 2012). Many melt inclusion suites have been observed to record some of the diversity of fractional melts, allowing melting and crustal processes to be better understood (Gurenko and Chaussidon, 1995; Maclennan, 2008a,b; Maclennan et al., 2003a; Neave et al., 2018).

Barometric studies based on crystal-melt equilibria has revealed much of the primitive crystal cargo formed at, or below, the MOHO (Maclennan, 2019; Maclennan et al., 2001b; Neave and Putirka, 2017; Winpenny and Maclennan, 2011). This suggests that the melt inclusions trapped by the crystals are unlikely to have had any influence from the crust (Gurenko and Chaussidon, 1995), but also that they were trapped at high pressure where degassing may be minimal (Hauri et al., 2018).

Chapter 2

Samples and Methods

2.1 Samples

In order to obtain a record of magma chemistry with as little influence of magmatic processing as possible, samples containing extremely forsteritic olivine crystals were targeted. Forsteritic olivine is the first phase to crystallise from Icelandic basaltic melts. The spinel inclusions and melt inclusions it traps are therefore likely to have experienced minimal crustal processing and offer the best chance of reconstructing the properties of primary mantle melts.

2.1.1 Eruptions used in estimating mantle temperature and mineralogy

Figure 2.1 shows the location of the eruptions from which co-existing olivine and spinel crystals were analysed for aluminium exchange thermometry (Chapter 3). The Theistareykir picrite is an extremely olivine-rich postglacial lava flow, situated near to the northern tip of the Northern Volcanic Zone (Elliott et al., 1991; Slater et al., 2001). Borgarhraun is an olivine, clinopyroxene- and plagioclase-phyric lava flow in the Theistareykir volcanic system (Maclennan et al., 2003b), and is also postglacial in age (Sæmundsson, 1991). Both the picrite and Borgarhraun samples were collected from lava flows as whole rocks. Herðubreiðartögl was formed during a subglacial eruption close to the end of the last glaciation (Werner et al., 1996). Samples were collected from the olivine- and plagioclase-phyric pillow lavas at the north of the mountain. Kistufell is a monogenetic table mountain located at the northern margin of the Vatnajökull ice cap and most likely formed towards the end of the last glaciation (Breddam, 2002). The samples were collected from the olivine-rich pillow lavas near the base of the mountain.

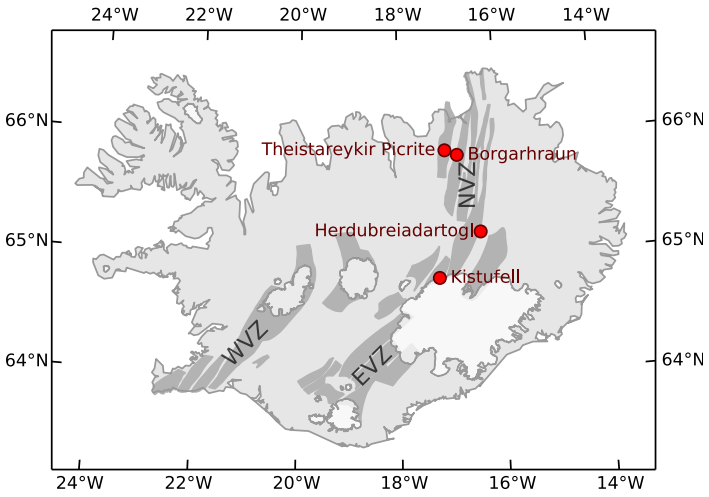

Figure 2.1: Map of Iceland showing the locations of the four eruptions for which crystallisation temperatures were estimated, with the neovolcanic zones marked in dark grey. NVZ, EVZ and WVZ are the Northern, Eastern and Western Volcanic Zones, respectively.

2.1.2 Eruptions analysed for melt inclusion volatiles

Samples were collected from four fresh primitive eruptions in Iceland (Figure 2.2) which represent diverse mantle sources, as indicated by their Sr-, Nd- and He-isotope ratios. Háleyjabunga and Stapafell are in close proximity on the Reykjanes Peninsula in the Western Rift Zone, but preferentially sample more depleted and enriched mantle components respectively (Thirlwall et al., 2004). Stapafell erupted sub-glacially between 70 and 14 ka (Saemundsson et al., 2010) forming basal pillow basalts, from which samples were taken near 63°54.585'N, 22°31.409'W. Háleyjabunga was erupted as a sub-aerial lava shield at ∼13 ka (Saemundsson et al., 2010), from which olivine-phyric lava flow samples were taken from the Eastern side of the vent near 63°48.978'N, 22°39.099'W. Berserkjahraun is an eruption younger than 11 ka in the Snæfellsnes flank zone (Hjartarson and Sæmundsson, 2014), and has extreme geochemical enrichment (Peate et al., 2010). Glassy olivine- and plagioclase-phyric scoria was collected from the crater at 64°95.915'N, 22°89.853'W. Heilagsdalsfjall is a lava flow erupted in the Northern Volcanic Zone with an age < 11.5 ka (Sæmundsson et al., 2012). Glassy olivine-phyric achneliths were collected from the crater at 65.49934°N, 16.70224°W.

2.2 Sample Preparation

2.2.1 Sample preparation for aluminium exchange thermometry

Fresh olivine crystals from Herðubreiðartögl and Kistufell were picked from crushed tephra and pillow glass respectively, cleaned, mounted in resin and then polished. For the Borgarhraun and Theistareykir picrite eruptions, 30 µm thick polished sections were prepared from whole-rock samples.

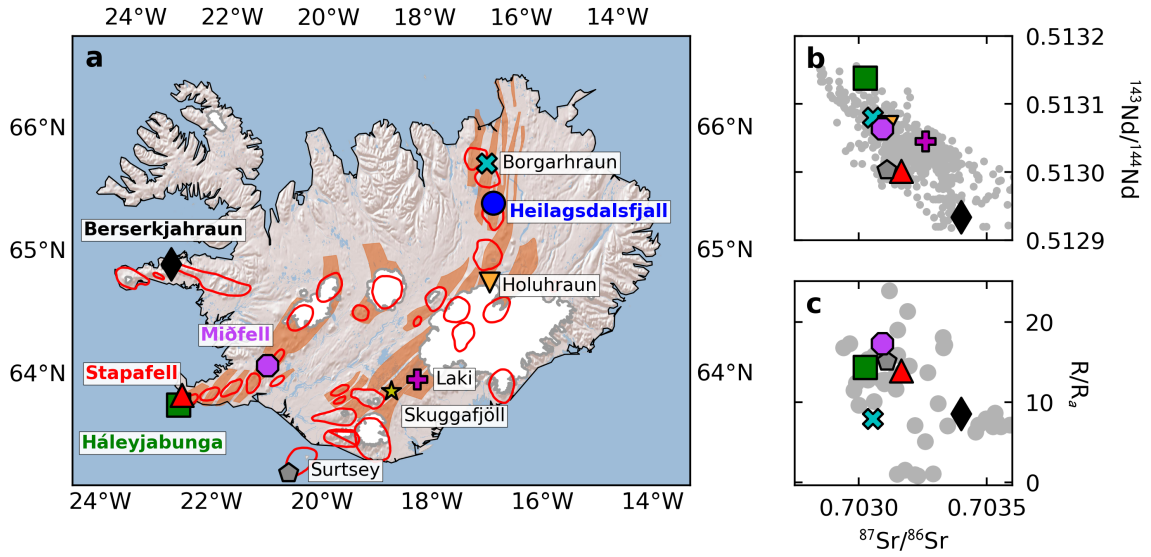

Figure 2.2: Panel a: Locations of the eruptions studied here (bold text and large symbols), and the locations of other Icelandic eruptions for which CO_2 and trace element measurements have been made on melt inclusions. Orange shading shows the active rift zones. Red outlines show active volcanic centres. Panel b: Sr and Nd isotope ratios of whole rocks from the same eruptions. Panel c: $^{3}He/^{4}He$ isotope ratio (R) normalised to the atmospheric value (R_a). Grey circles in panels b and c show data compiled for Iceland (sources given in Appendix B).

2.2.2 Sample preparation for melt inclusion analysis

Tephra (Berserkjahraun and Heilagsdalsfjall), and whole rock (Stapafell and Háleyjabunga) were crushed and crystals of olivine and clinopyroxene were picked out by hand under binocular microscope. Melt inclusions from Háleyjabunga were re-homogenised by heating in a gas-mixing furnace, following the methods of Maclennan (2008b). Crystals were individually mounted on glass slides in crystal-bond, and ground and polished on both sides using silicon-carbide paper in order to obtain a clear optical view into the crystals. Melt inclusions that contained bubbles were then analysed by Raman spectroscopy (Section 2.5). Melt inclusions were the exposed by grinding down using silicon-carbide paper. Crystals were then extracted from crystal bond, cleaned in acetone, and mounted in epo-thin epoxy resin. The epoxy stubs were then polished using 6 µm, 3 µm and 1 µm diamond suspension on felt pads, being cleaned with de-ionised water in a sonic bath after each stage. After polishing the mounts were cleaned again with iso-propanol and compressed air. Maps of each mount were made by Back-Scattered Electron-Microscopy under low-vacuum conditions, using the FEI QEMSCAN 650F in the Department of Earth Sciences, University of Cambridge. A final 60 s polish using alumina powder on a felt pad was used to create sufficient relief that the inclusions could be easily seen on the ion-probe's optical microscope. The mounts were then gold coated for Secondary-Ion Mass Spectrometry (Section 2.4). Following SIMS, the gold coat was

Eruption	Lat.	Lon.	Reference
Berserkjahraun	64.963	-22.971	This study
Háleyjabunga	63.817	-22.667	This study
Stapafell	63.9	-22.62	This study
Heilagsdalsfjall	65.498	-16.701	This study
Borgarhraun	65.825	-16.8	Hauri et al. (2018)
Laki	64.071	-18.238	Hartley et al. (2014)
Skuggafjöll	63.977	-18.723	Neave et al. (2014)
Holuhraun	64.85	-16.83	Bali et al. (2018)
Surtsey	63.3	-20.6	Schipper et al. (2016)
Miðfell	64.175	-21.049	Miller et al. (in review)

Table 2.1: The locations and references for the eruptions from which melt inclusions are discussed in this thesis.

removed by polishing with 1 µm diamond suspension on a felt pad, cleaned as described above, and then carbon-coated in preparation for Electron Probe Micro-Analysis to ascertain the major element concentrations of the inclusions and their host crystals (Section 2.3.2). Where inclusions were too small for EPMA analysis adjacent to the SIMS pit the mounts were ground down using silicon-carbide paper and polished with diamond suspension, before re-coating, as described above.

2.3 Electron Probe Micro-Analysis

2.3.1 Aluminium exchange thermometry

Olivine and spinel pairs were chosen for analysis such that the spinel was within the core of the olivine crystal. Both olivine and spinel were analysed for Al, Cr, Fe, Mn, Ni, Si, Mg, Ca, Ti and P with the Cameca SX-100 electron microprobe at the Department of Earth Sciences, University of Cambridge, over four sessions. Calibration was performed at the start of each session using natural and synthetic standards (Table 2.3). An acceleration voltage of 15 kV, and currents of 40 nA for spinel and 100 nA for olivine were used. Under these conditions, the detection limit for Al in olivine was 12 ppmw. A profile of points spaced $\sim$10 µm apart was collected in each olivine crystal oriented towards the spinel inclusion and approximately perpendicular to, the nearest olivine crystal edge (Figure 2.3). Similarly, a profile through the diameter of each spinel inclusion with a point spacing of $\sim$7 µm was collected in a direction parallel to the olivine profile (Figure 2.3). Estimates of measurement precision for each element used in the calculation were calculated from the scatter of points about their mean value in unzoned crystals. Where the uncertainty arising from this internal reproducibility is greater than the uncertainty calculated on the basis of counting statistics, it is used in preference.

Eruption	Ba/Nb	$^{143}Nd/^{144}Nd$	$^{87}Sr/^{86}Sr$	R/R_a	$^{206}Pb/^{204}Pb$	$^{207}Pb/^{204}Pb$	$^{208}Pb/^{204}Pb$	Refs.
Berserkjahraun	7.26	0.512934	0.7034	8.54	19.1335	15.5388	38.7567	Peate et al. (2010)
Háleyjabunga	8.17	0.513138	0.703026	14.3	18.28	15.463	38.003	Kokfelt et al. (2006), Füri et al. (2010)
Stapafell	5.87	0.513001	0.703166	13.9	18.895	15.518	38.486	Peate et al. (2009), Breddam et al. (2000)
Heilagsdalsfjall	7.93							
Borgarhraun	8.29	0.51308	0.703054	7.91	18.072	15.427	37.732	Kokfelt et al. (2006), Füri et al. (2010)
Laki	4.04	0.513045	0.703261		18.4763	15.4728	38.209	Thirlwall et al. (2004)
Skuggafjöll	5.17			16.9				Harðardóttir et al. (2018)
Holuhraun		0.513068	0.703115					Sigmarsson and Halldórsson (2015)
Surtsey	7.36	0.513003	0.703109	15.1	19.164	15.647	39.007	Chauvel and Hémond (2000), Hemond et al. (1993), Poreda et al. (1986)
Miðfell	8.32	0.513064	0.703092	17.3				Brandon et al. (2007), Debaille et al. (2009), Füri et al. (2010)

Table 2.2: Radiogenic isotope ratios of whole rock samples from the eruptions considered in this text. References for the whole-rock isotope ratios are given.

Table 2.3: Standard materials used for calibrating the Electron Micro-Probe.

Element	Standard
Si	Diopside
Fe	Fayalite
Mg	St Johns Olivine
Ca	Diopside
Ni	NiO
Mn	Mn metal
Cr	Cr metal
Ti	Rutile
Al	Corundum
P	Apatite
Na	Jadeite
K	K-Feldspar
Cl	Halite
S	Celestine

Table 2.4: Summary of uncertainties in parameters used in calculating olivine crystallisation temperatures. Precision calculated empirically from repeat measurements of unzoned crystals. Counting statistics are the minimum uncertainty given the number of counts during calibration and analysis.

Measurement	Empirical Precision	Counting Stats Error
Al_2O_3 in olivine	0.0038 wt%	2%
Fo in olivine	0.051 mol%	5%
Al_2O_3 in spinel	0.17 wt%	5%
Cr# of spinel	0.002	14%
Mg# of spinel	0.007	5%

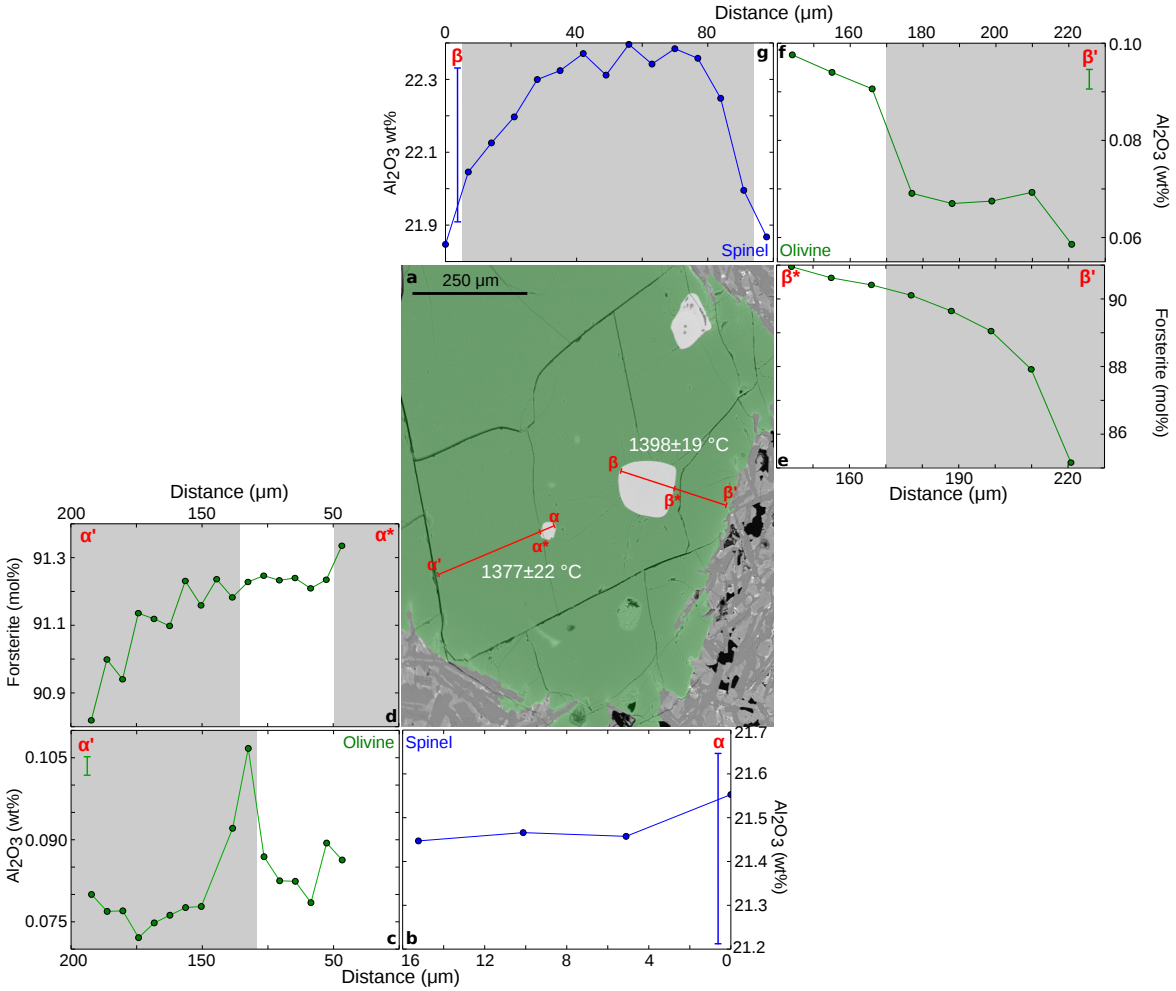

Figure 2.3: Back Scatter Electron Image (panel a) and chemical data for Borgarhraun olivine crystal BH47-1. The olivine macrocryst has been coloured green in the BSE image. Two profiles, α-α*-α' (panels b, c and d) and β-β*-β' (panels e, f and g), were measured by EPMA through both spinel and olivine as shown. The grey bars indicate points not included in the thermometry calculations. Representative one standard deviation analytical uncertainties are shown as green and blue bars. The temperature calculated for each profile and its uncertainty are shown on the BSE image.

Table 2.5: Crystals used and counting times for each element analysed in glass by electron microprobe. The elements were measured in the order shown.

Crystal	Elements (time /s)
LTAP	Na(10)
PET	Ca(40) Ti(60)
LPET	K(10) P(60) Cl(100) S(400/200)
TAP	Si(20) Mg(80) Al(80)
LIF	Fe(20) Cr(80) Mn(80) Ni(100)

Table 2.6: Crystals used and counting times for each element analysed in olivine by electron microprobe. The elements were measured in the order shown.

Crystal	Elements (time /s)
LTAP	Al(150)
PET	Ca(90) Ti(60)
LPET	P(150)
TAP	Si(20) Mg(30)
LIF	Fe(20) Cr(40) Mn(40) Ni(60)

2.3.2 Melt inclusions and their host crystals

Analyses were performed using the Cameca SX-100 microprobe at the Department of Earth Sciences, University of Cambridge, over 8 sessions. Natural and synthetic standards were used for calibration at the start of each session (Table 2.3). An accelerating Voltage of 15 kV and beam current of 6 nA focused to 5 µm was used for glass, and 20 nA focused to 1 µm for olivine and clinopyroxene. Count rates at the centre of the K-α peak were measured, and background counts were measured either side of the peaks with offsets chosen to minimise peak overlap. The crystals used and counting times are given in Tables 2.5, 2.6 and 2.7. Initial data reduction was performed using the in-built software with ZAF corrections. Accuracy, precision and instrumental drift were monitored with olivine, glass and pyroxene secondary standards. For all analytical sessions the combined accuracy and precision of SiO_2 measurements in glass was better than 3 % (one standard deviation), other elements are reported in Tables 2.8 and 2.9. Where sufficient material was available, a minimum of three analyses were made in each inclusion and host crystal, and their means taken. In order to avoid secondary fluorescence effects from olivine analysis near inclusion edges was avoided, and any anomalous data was discarded.

Table 2.7: Crystals used and counting times for each element analysed in clinopyroxene by electron microprobe. The elements were measured in the order shown.

Crystal	Elements (time /s)
LTAP	Na(30) Al(30)
PET	Ca(10) Ti(40)
LPET	K(30) P(100)
TAP	Si(20) Mg(30)
LIF	Fe(30) Ni (60) Cr(40) Mn(40)

Session		SiO_2	MgO	FeO	CaO	Al_2O_3	MnO	TiO_2	P_2O_5	Cr_2O_3	NiO	Total
	accepted values	40.81	49.42	9.55			0.14				0.37	100.29
1/18/18	average	40.53	48.42	9.69	0.13	0.04	0.15	0.01	0.01	0.02	0.38	99.38
	precision	0.70	0.92	0.16	0.05	0.02	0.03	0.01	0.01	0.02	0.03	1.53
	fractional precision	0.02	0.02	0.02	0.38	0.57	0.17	1.98	1.17	1.05	0.07	0.02
	accuracy	0.01	0.02	0.02			0.08				0.02	0.01
2/23/18	average	40.73	48.46	9.69	0.15	0.05	0.14	0.00	0.01	0.01	0.37	99.61
	precision	0.33	0.73	0.12	0.04	0.02	0.03	0.01	0.00	0.02	0.03	1.08
	fractional precision	0.01	0.02	0.01	0.29	0.34	0.23	1.71	0.64	1.17	0.07	0.01
	accuracy	0.00	0.02	0.01			0.03				0.00	0.01
5/15/17	average	40.80	48.65	9.72	0.11	0.05	0.13	0.00	0.01	0.01	0.36	99.84
	precision	0.21	0.17	0.13	0.01	0.04	0.02	0.01	0.00	0.02	0.03	0.28
	fractional precision	0.01	0.00	0.01	0.09	0.86	0.19	6.22	0.52	1.87	0.10	0.00
	accuracy	0.00	0.02	0.02			0.06				0.02	0.00
5/21/17	average	40.88	48.33	9.70	0.11	0.04	0.14	0.00	0.01	0.02	0.38	99.60
	precision	0.23	0.23	0.17	0.01	0.00	0.01	0.01	0.00	0.01	0.02	0.58
	fractional precision	0.01	0.00	0.02	0.05	0.09	0.09	2.91	0.73	0.85	0.05	0.01
	accuracy	0.00	0.02	0.02			0.01				0.02	0.01
6/22/17	average	41.05	48.99	9.83	0.10	0.04	0.14	0.01	0.00	0.02	0.37	100.55
	precision	0.19	0.29	0.16	0.01	0.00	0.02	0.01	0.00	0.01	0.03	0.33
	fractional precision	0.00	0.01	0.02	0.05	0.07	0.14	1.44	1.10	0.63	0.09	0.00
	accuracy	0.01	0.01	0.03			0.02				0.01	0.00
5/15/17	average	40.80	48.65	9.72	0.11	0.05	0.13	0.00	0.01	0.01	0.36	99.84
	precision	0.21	0.17	0.13	0.01	0.04	0.02	0.01	0.00	0.02	0.03	0.28
	fractional precision	0.01	0.00	0.01	0.09	0.86	0.19	6.22	0.52	1.87	0.10	0.00
	accuracy	0.00	0.02	0.02			0.06				0.02	0.00
6/7/16	average	40.81	48.74	9.76	0.11	0.04	0.15	0.01	0.01	0.03	0.39	100.04
	precision	0.18	0.33	0.15	0.00	0.00	0.03	0.01	0.01	0.01	0.01	0.46
	fractional precision	0.00	0.01	0.02	0.04	0.07	0.23	1.19	0.53	0.41	0.04	0.00
	accuracy	0.00	0.01	0.02			0.07				0.05	0.00
5/20/16	average	41.19	48.94	9.89	0.12	0.04	0.15	0.01	0.01	0.02	0.37	100.74
	precision	0.17	0.22	0.10	0.01	0.00	0.02	0.01	0.01	0.02	0.02	0.42
	fractional precision	0.00	0.00	0.01	0.07	0.09	0.15	0.89	0.54	0.96	0.06	0.00
	accuracy	0.01	0.01	0.04			0.09				0.01	0.00

Table 2.8: Statistics from repeat measurements of the olivine secondary standard NMNH 111312–44. All measurements in wt%. Where accuracy is quoted as 0.0, it is better than 0.5%.

Session		SiO_2	MgO	FeO	CaO	Al_2O_3	Na_2O	K_2O	MnO	TiO_2	P_2O_5	Cr_2O_3	NiO	SO_2	Cl	Total
	accepted values	50.81	6.95	11.83	11.12	14.06	2.62	0.19	0.22	1.85	0.20			0.28	0.03	100.10
1/18/18	average	50.29	6.88	11.89	10.95	13.70	2.69	0.21	0.23	1.92	0.23	0.02	0.00	0.30	0.03	99.34
	precision	0.81	0.12	0.33	0.19	0.29	0.09	0.04	0.04	0.07	0.03	0.03	0.02	0.01	0.01	1.68
	fractional precision	0.02	0.02	0.03	0.02	0.02	0.03	0.17	0.17	0.04	0.12	1.50	5.56	0.04	0.17	0.02
	accuracy	0.01	0.01	0.00	0.01	0.03	0.03	0.10	0.06	0.04	0.13			0.05	0.17	0.01
2/23/18	average	50.60	6.91	11.87	10.98	13.54	2.69	0.20	0.21	1.87	0.21	0.02	0.02	0.17	0.03	99.32
	precision	0.52	0.18	0.22	0.17	0.32	0.06	0.02	0.04	0.04	0.03	0.02	0.02	0.03	0.01	1.09
	fractional precision	0.01	0.03	0.02	0.02	0.02	0.02	0.10	0.18	0.02	0.13	0.68	1.47	0.17	0.19	0.01
	accuracy	0.00	0.01	0.00	0.01	0.04	0.03	0.04	0.03	0.01	0.03			0.38	0.19	0.01
5/15/17	average	51.18	7.02	11.80	10.83	13.73	2.71	0.20	0.21	1.98	0.23	0.01	0.00	0.15	0.03	100.07
	precision	0.17	0.06	0.23	0.01	0.05	0.09	0.04	0.05	0.04	0.03	0.01	0.01	0.02	0.00	0.42
	fractional precision	0.00	0.01	0.02	0.00	0.00	0.03	0.18	0.23	0.02	0.14	1.18	50.27	0.13	0.15	0.00
	accuracy	0.01	0.01	0.00	0.03	0.02	0.03	0.03	0.04	0.07	0.13			0.47	0.13	0.00
5/21/17	average	50.32	6.79	11.84	10.92	13.59	2.69	0.22	0.20	1.88	0.20	0.01	0.02	0.18		98.87
	precision	0.78	0.17	0.27	0.27	0.33	0.12	0.03	0.05	0.06	0.02	0.03	0.02	0.02		1.71
	fractional precision	0.02	0.02	0.02	0.03	0.02	0.05	0.12	0.25	0.03	0.08	2.81	1.37	0.12		0.02
	accuracy	0.01	0.02	0.00	0.02	0.03	0.03	0.16	0.08	0.02	0.00			0.35		0.01
6/22/17	average	51.06	6.92	12.04	10.86	13.83	2.74	0.22	0.25	1.94	0.23	0.01	0.02	0.19		100.29
	precision	1.00	0.19	0.20	0.15	0.24	0.13	0.03	0.05	0.01	0.01	0.03	0.04	0.01		1.73
	fractional precision	0.02	0.03	0.02	0.01	0.02	0.05	0.13	0.22	0.01	0.06	4.41	1.96	0.06		0.02
	accuracy	0.00	0.00	0.02	0.02	0.02	0.05	0.15	0.15	0.05	0.14			0.33		0.00
5/15/17	average	51.18	7.02	11.80	10.83	13.73	2.71	0.20	0.21	1.98	0.23	0.01	0.00	0.15	0.03	100.07
	precision	0.17	0.06	0.23	0.01	0.05	0.09	0.04	0.05	0.04	0.03	0.01	0.01	0.02	0.00	0.42
	fractional precision	0.00	0.01	0.02	0.00	0.00	0.03	0.18	0.23	0.02	0.14	1.18	50.27	0.13	0.15	0.00
	accuracy	0.01	0.01	0.00	0.03	0.02	0.03	0.03	0.04	0.07	0.13			0.47	0.13	0.00
6/7/16	average	49.99	6.91	11.62	10.90	13.93	2.63	0.20	0.23	1.96	0.21	0.01	0.02	0.29	0.03	98.95
	precision	0.33	0.10	0.21	0.11	0.17	0.09	0.02	0.02	0.06	0.01	0.02	0.01	0.01	0.01	0.76
	fractional precision	0.01	0.02	0.02	0.01	0.01	0.03	0.10	0.10	0.03	0.06	1.22	0.75	0.03	0.19	0.01
	accuracy	0.02	0.01	0.02	0.02	0.01	0.00	0.06	0.03	0.06	0.03			0.02	0.20	0.01
5/20/16	average	50.15	6.79	11.90	10.83	13.80	2.72	0.20	0.20	1.96	0.22	0.02	0.03	0.29	0.04	99.16
	precision	0.67	0.13	0.30	0.21	0.21	0.07	0.02	0.04	0.07	0.04	0.02	0.02	0.01	0.01	1.49
	fractional precision	0.01	0.02	0.02	0.02	0.02	0.02	0.09	0.21	0.03	0.17	0.85	0.77	0.04	0.23	0.01
	accuracy	0.01	0.02	0.01	0.03	0.02	0.04	0.03	0.08	0.06	0.11			0.04	0.30	0.01

Table 2.9: Statistics from repeat measurements of the glass secondary standard NMNH 111240–52. All measurements in wt%. Where accuracy is quoted as 0.0, it is better than 0.5%.

2.4 Secondary Ion Mass Spectrometry

SIMS analyses were performed over five sessions (one of which was a single repeat analysis) on the Cameca ims-4f ion microprobe at the NERC Ion Microprobe Facility at the University of Edinburgh, UK. Samples were allowed to outgas under vacuum overnight before analysis, and were retained under vacuum for the entire duration of each session (5 days).

2.4.1 ^{12}C analyses

Carbon analyses were performed prior to the trace elements and other volatiles, with the mass spectrometer configured in high-mass resolution mode in order to resolve the interference of $^{24}Mg^{2+}$ with $^{12}C^{+}$. The samples were bombarded with O^{-} primary ion beam with an accelerating voltage of 15 kV and beam current 5 ± 1 n focused to a spot size with a width of $\sim$20 µm. A secondary accelerating voltage of 4500 V with a 50 V offset and 25 µm image field. The ion beam was rastered over a $\sim$40 µm square area for 4 minutes prior to the analysis in order to remove surface contamination. Measurements were of the following species were made over 15 cycles, with counting times in seconds shown in brackets: $^{24}Mg^{2+}$ (5), ^{12}C (10), $^{40}Ca^{2+}$ (2) and ^{30}Si (2). The first 8 cycles were discarded to avoid the effects of surface contamination, all analyses were monitored to ensure ^{12}C counts had assymptoted by the 8th cycle. Background counts were estimated using the CO_2-free USGS standard glasses BIR-1G, GSD-1G and BCR-2G, and were subtracted from the raw analyses. Calibration curves were made using analyses of basaltic standard materials 17-2, s2-3 and s5-14. The accuracy for CO_2 concentration measurements was better than 3% for all sessions, and the precision over all sessions was 4% (Table 2.14).

2.4.2 Trace element, H, F and Cl analyses

Trace elements were analysed subsequently, alongside H_2O, F and Cl. Measurements were made in the same pits as the CO_2 analyses using similar beam conditions, apart from a secondary accelerating voltage of 4500 V was used with a 75 V offset. The following isotopes were measured over 8 cycles, for the time indicated in brackets: ^{1}H (5), ^{7}Li (5), ^{11}B (5), ^{16}O (2), ^{19}F (5), ^{30}Si (2), ^{35}Cl (5), ^{39}K (2), ^{42}Ca (2), ^{47}Ti (2), ^{88}Sr (3), ^{89}Y (3), ^{90}Zr (3), ^{93}Nb (3), atomic mass 130.5 (3) ^{138}Ba (3), ^{139}La (3), ^{140}Ce (3), ^{141}Pr (5), ^{143}Nd (5), ^{149}Sm (8), ^{151}Eu (8), ^{154}Gd (5), ^{156}Gd (4), ^{157}Gd (8), ^{159}Tb (5), ^{161}Dy (5), ^{165}Ho (5), ^{167}Er (8), ^{169}Tm (8), ^{171}Yb (10), and ^{175}Lu (10). Peak positions were verified whilst rastering the beam over the sample before every analysis. The background was checked by measuring mass 130.5, but was always sufficiently low to be ignored. Counts normalised to ^{30}Si were converted to absolute element concentrations with the JCION-6 software using analyses of GSD-1G

for calibration, accounting for oxide interferences. Accuracy and precision were checked by repeat analyses of matrix glasses and basaltic standards GSD-1G, T1G, BCR and NIST-610 (Tables 2.10, 2.11, 2.12 and 2.13). The accuracy of the GSD-1G analyses were better than 4% for most elements across all sessions. For the April 2016 session the accuracy of the T1G analyses was better than 15% for most elements and for the October 2016 session it was better than 8% for most elements. The accuracy of BCR analyses in the April 2017 and October 2017 sessions was better than 9% for most elements. The accuracy of the NIST-610 analyses in the October 2017 session was better than 12% for most elements. The precision across all sessions estimated from repeat analyses of GSD-1G ranges from 3% for the most abundant trace elements to 10% for the least abundant. The precision of Nb in the most depleted glasses is generally better than 10%. The estimated accuracy and precision for the H_2O analyses are summarised in Table 2.15.

2.5 Raman Spectroscopy

Micro-Raman spectroscopy was performed on the bubbles hosted in melt inclusions over 10 sessions using the Horiba LabRam instrument in the Department of Earth Sciences, University of Cambridge. A 532.05 nm (green) laser was used at 100 mW power, with a 25% filter, a 300 µm hole aperture, a 100 µm slit spacing, an 1800 grating, and a x50 LWD objective lens. The spectrometer was centered on 1350 cm^{-1}, and 20 accumulations of 8 s each were acquired. Calibration was performed on a Si-wafer using the auto-calibrate routine on the Horiba LabSpec software at the start of each session. Samples were positioned and focused using transmitted light. Optical images were taken of each bubble using the in-built confocal light microscope in order to estimate the volumes of the bubble and melt inclusion. The majority of the spectra were collected at room temperature ($\sim$20°C), though a small number of inclusions were measured on a heating stage at 40°C in order to move the inclusion beyond the triple point of CO_2, but no significant difference in the spectra were observed.

Spectra were processed by fitting a guassian curve to each peak of the Fermi diad and a baseline to account for noise (Figure 2.4). A least-squares fit was obtained with the SciPy optimize.curve_fit() function. The error on the fit was calculated as the standard deviation of the peak divided by square-root of the number of counts defining it. The CO_2 densimeter calibrated by Kawakami et al. (2003) was used to convert the Fermi diad separation into a CO_2 fluid density. I apply the same calculation as used by Hartley et al. (2014) to calculate the CO_2 content of the bubble relative to the mass of the inclusion in ppmw, $[CO_2]_{vb}$:

$$[CO_2]_{vb} = \left(\frac{M_{vb}^{CO_2}}{M_{gl}} \right) \times 10^6 \tag{2.1}$$

where $M_{vb}^{CO_2}$ is the CO_2 density in the vapour bubble multiplied by its volume, and M_{gl} is the volume of the inclusion multiplied by a density of 2750 kg m^{-3}. The volumes were determined by measuring

	Berserkjahraun (3)			Heilagsdalsfjall (8)			Stapafell (6)		
	mean	σ	σ/μ	mean	σ	σ/μ	mean	σ	σ/μ
H_2O	0.09	0.02	0.22	0.07	0.01	0.21	0.33	0.15	0.44
Li	3.86	2.31	0.60	3.29	0.38	0.12	3.62	0.81	0.22
B	2.61	0.38	0.15	0.18	0.14	0.77	0.62	0.26	0.42
F	3100	360	0.12	169	80	0.47	473	197	0.42
Cl	905	84	0.09	32.8	36.8	1.12	173	89	0.51
K	10030	1840	0.18	502	306	0.61	2039	821	0.40
Ca	82660	7280	0.09	91550	3830	0.04	89290	1420	0.02
Ti	16300	740	0.05	4240	1190	0.28	8690	2460	0.28
Sr	389	12	0.03	78.2	28.0	0.36	175.4	52.8	0.30
Y	31.63	0.94	0.03	16.53	1.74	0.11	21.45	2.78	0.13
Zr	218.05	10.01	0.05	23.37	13.54	0.58	80.47	30.86	0.38
Nb	51.20	3.67	0.07	1.17	0.15	0.13	14.06	0.56	0.04
Ba	353.95	23.74	0.07	9.87	0.65	0.07	76.34	0.73	0.01
La	37.35	2.72	0.07	1.72	1.08	0.63	8.83	3.81	0.43
Ce	78.57	4.91	0.06	4.13	2.58	0.63	20.40	8.61	0.42
Pr	9.43	0.26	0.03	0.65	0.38	0.59	2.86	1.21	0.42
Nd	42.24	2.15	0.05	3.75	2.17	0.58	13.96	5.62	0.40
Sm	7.53	0.52	0.07	1.45	0.55	0.38	3.57	1.21	0.34
Eu	2.34	0.17	0.07	0.59	0.18	0.31	1.19	0.35	0.29
Gd	6.96	0.30	0.04	2.04	0.72	0.35	3.61	1.03	0.29
Tb	0.99	0.06	0.06	0.39	0.07	0.17	0.65	0.19	0.29
Dy	6.30	0.08	0.01	2.88	0.25	0.09	4.16	0.78	0.19
Ho	1.18	0.07	0.06	0.65	0.10	0.15	0.84	0.12	0.14
Er	3.48	0.44	0.13	1.96	0.21	0.11	2.25	0.34	0.15
Tm	0.45	0.05	0.11	0.26	0.03	0.11	0.32	0.04	0.13
Yb	2.72	0.35	0.13	1.98	0.25	0.13	1.96	0.24	0.12
Lu	0.42	0.01	0.03	0.29	0.05	0.16	0.31	0.06	0.19

Table 2.10: Summary of the statistics from repeat analyses of the matrix glasses from Berserkjahraun, Heilagsdalsfjall and Stapafell during the same SIMS sessions as the melt inclusions were analysed. The number in brackets indicates the number of analyses made. One standard deviation, σ, and the fractional precision, σ/μ, are shown. H_2O measurements are in wt%, all other measurements are in ppmw.

	reference value	mean	σ	σ/μ	Apr 2016 accuracy	Oct 2016 accuracy
H_2O	0.0094	0.01	0.01	0.62	0.36	0.48
Li	19.9	17.64	8.66	0.49	0.08	0.04
B	4.1	1.69	1.28	0.76	0.58	0.40
F	320	420	190	0.45	0.60	0.48
Si	273500	233600	103000	0.44	0.00	0.00
Cl	113	127	59.0	0.46	0.42	0.23
K	16260	12530	5560	0.44	0.13	0.06
Ca	50710	37640	16610	0.44	0.14	0.12
Ti	4530	3400	1500	0.44	0.12	0.11
Sr	284	212.88	94.18	0.44	0.15	0.09
Y	23.9	18.88	8.34	0.44	0.09	0.06
Zr	144	117.11	51.75	0.44	0.06	0.03
Nb	8.87	6.64	2.95	0.44	0.13	0.12
Ba	388	287.83	127.67	0.44	0.16	0.10
La	70.4	54.95	24.26	0.44	0.09	0.08
Ce	127	97.20	43.04	0.44	0.12	0.08
Pr	12.4	9.46	4.19	0.44	0.10	0.11
Nd	41.4	34.41	15.40	0.45	0.07	0.02
Sm	6.57	5.13	2.31	0.45	0.13	0.04
Eu	1.21	0.68	0.35	0.52	0.48	0.20
Gd	5.31	4.32	2.31	0.54	0.15	0.06
Tb	0.773	0.58	0.27	0.46	0.17	0.06
Dy	4.5	3.51	1.58	0.45	0.12	0.04
Ho	0.86	0.69	0.31	0.44	0.07	0.04
Er	2.49	2.36	1.07	0.45	0.12	0.11
Tm	0.354	0.287	0.130	0.45	0.07	0.02
Yb	2.38	1.99	0.89	0.45	0.06	0.01
Lu	0.354	0.290	0.131	0.45	0.08	0.005

Table 2.11: Summary of statistics from 6 analyses of T1G standard material. One standard deviation, σ, the fractional precision across sessions, σ/μ, and the accuracy for the April 2016 and October 2016 sessions are shown. H_2O measurements are in wt%, all other measurements are in ppmw.

	reference value	mean	σ	σ/μ	Apr 2017 accuracy	Oct 2017 accuracy
H_2O		0.02	0.00	0.09		
Li	9	9.02	0.09	0.01	0.01	0.00
B	6	4.32	0.13	0.03	0.29	0.27
O		511468.80	2078.54	0.00		
F		451.80	50.84	0.11		
Si		254075.20	225.17	0.00		
Cl		63.18	16.63	0.26		
K	14900	14055.87	416.43	0.03	0.04	0.07
Ca		49145.50	283.27	0.01		
Ti	14100	13053.82	140.80	0.01	0.07	0.07
Sr	342	325.91	3.04	0.01	0.05	0.04
Y	35	33.19	0.30	0.01	0.05	0.05
Zr	184	177.60	3.02	0.02	0.05	0.02
Nb	12.5	11.37	0.42	0.04	0.06	0.12
Ba	683	626.81	9.38	0.01	0.09	0.08
La	24.7	23.92	0.24	0.01	0.02	0.04
Ce	53.3	49.53	0.23	0.00	0.07	0.07
Pr	6.7	6.06	0.14	0.02	0.10	0.09
Nd	28.9	28.60	1.07	0.04	0.03	0.01
Sm	6.59	6.29	0.22	0.04	0.02	0.07
Eu	1.97	2.32	0.32	0.14	0.33	0.03
Gd	6.71	7.64	0.52	0.07	0.08	0.20
Tb	1.02	1.06	0.05	0.05	0.01	0.07
Dy	6.44	6.538	0.589	0.090	0.07	0.04
Ho	1.27	1.301	0.073	0.056	0.01	0.04
Er	3.7	3.538	0.229	0.065	0.003	0.08
Tm	0.51	0.495	0.023	0.047	0.02	0.04
Yb	3.39	2.489	0.653	0.262	0.42	0.12
Lu	0.503	0.484	0.040	0.083	0.01	0.09

Table 2.12: Summary of statistics from 6 analyses of BCR standard material. One standard deviation, σ, the fractional precision across sessions, σ/μ, and the accuracy for the April 2017 and October 2017 sessions are shown. H_2O measurements are in wt%, all other measurements are in ppmw.

	s4-13 (3)			st1 (4)			st2 (5)			st6 (6)		
	mean	σ	σ/μ	mean	σ	σ/μ	mean	σ	σ/μ	mean	σ	σ/μ
H_2O	3.66	0.09	0.03	3.04	0.25	0.08	2.80	0.14	0.05	1.44	0.08	0.06
Li	8.82	0.09	0.01	5.31	0.07	0.01	5.37	0.08	0.02	5.40	0.10	0.02
B	28.5	1.2	0.04	6.55	0.20	0.03	6.57	0.02	0.004	6.60	0.15	0.02
F	2420	60	0.02	160	80	0.50	125	12	0.10	115	9	0.08
Cl	1670	160	0.10	60.9	12.8	0.21	38.1	7.4	0.19	38.7	5.2	0.13
K	15820	300	0.02	1780	60	0.03	1860	45	0.02	1850	60	0.03
Ca	79210	550	0.01	72090	1280	0.02	73830	550	0.01	73710	580	0.01
Ti	4810	30	0.01	4901	59	0.01	5002	54	0.01	4999	69	0.01
Sr	697	5	0.01	374	9.75	0.03	385	7.5	0.02	387	6	0.02
Y	24.0	0.2	0.01	16.1	0.6	0.04	16.5	0.2	0.01	16.1	0.4	0.02
Zr	137.9	3.2	0.02	44.4	0.77	0.02	44.6	1.0	0.02	44.4	0.3	0.01
Nb	18.5	0.3	0.02	1.05	0.06	0.06	1.22	0.21	0.17	1.09	0.08	0.07
Ba	856	10	0.01	104.0	4.5	0.04	107.2	3.9	0.04	108.7	4.8	0.05
La	46.4	0.6	0.01	3.90	0.17	0.04	4.07	0.06	0.02	4.04	0.21	0.05
Ce	92.5	2.7	0.03	10.24	0.68	0.07	10.76	0.44	0.04	10.19	0.41	0.04
Pr	10.57	0.25	0.02	1.59	0.07	0.05	1.71	0.15	0.09	1.56	0.06	0.04
Nd	44.2	0.6	0.01	8.39	0.53	0.06	9.03	0.71	0.08	8.69	0.54	0.06
Sm	8.15	0.27	0.03	2.50	0.31	0.12	2.48	0.28	0.11	2.46	0.24	0.10
Eu	1.03	0.21	0.21	0.72	0.106	0.148	0.763	0.17	0.223	0.821	0.151	0.18
Gd	6.82	1.81	0.27	2.51	0.25	0.10	2.45	0.53	0.22	2.85	0.26	0.09
Tb	0.935	0.161	0.17	0.420	0.088	0.21	0.469	0.063	0.14	0.448	0.036	0.08
Dy	5.11	0.43	0.08	2.685	0.319	0.12	3.04	0.30	0.10	2.91	0.58	0.20
Ho	0.958	0.049	0.05	0.632	0.065	0.10	0.681	0.061	0.09	0.624	0.069	0.11
Er	2.827	0.335	0.12	1.831	0.268	0.15	1.922	0.293	0.15	1.717	0.089	0.05
Tm	0.410	0.012	0.03	0.235	0.012	0.05	0.253	0.026	0.10	0.263	0.041	0.16
Yb	2.31	0.10	0.04	1.805	0.225	0.13	1.759	0.201	0.11	1.737	0.341	0.20
Lu	0.306	0.064	0.21	0.271	0.042	0.15	0.257	0.030	0.12	0.270	0.026	0.10

Table 2.13: Summary of the statistics from repeat analyses of the standard materials s4-13, st1, st2 and st6 during the same SIMS sessions as the melt inclusions were analysed. The number in brackets indicates the number of analyses made. One standard deviation, σ, and the fractional precision, σ/μ, are shown. H_2O measurements are in wt%, all other measurements are in ppmw.

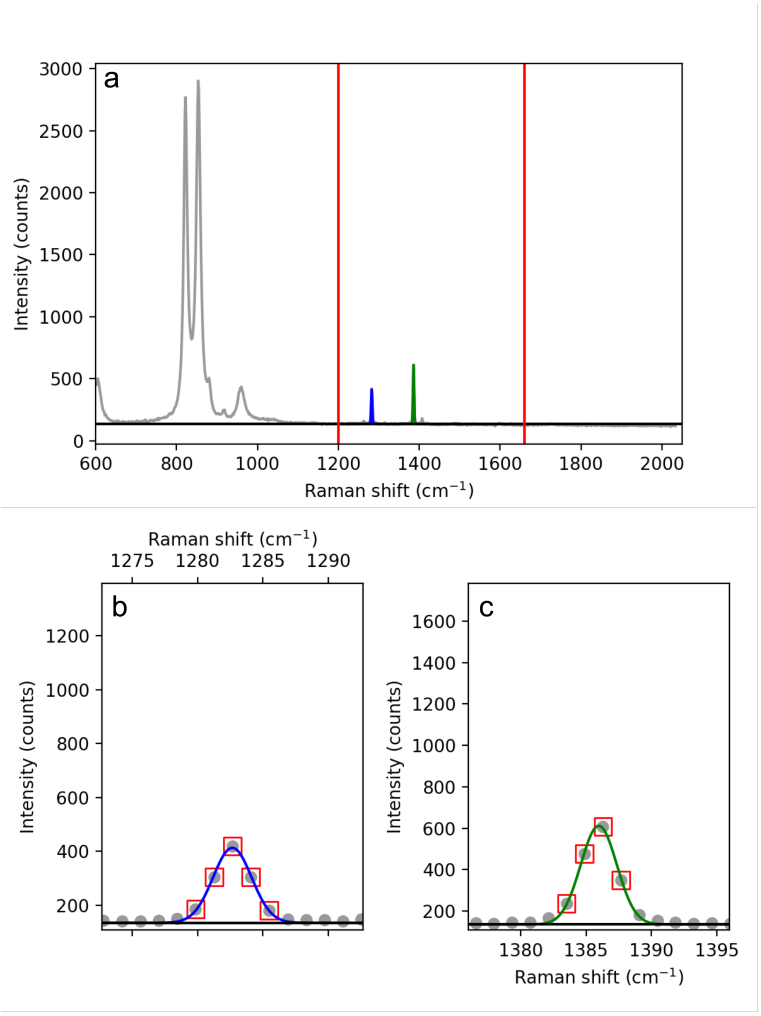

Figure 2.4: An example of a Raman spectrum collected from a bubble containing CO_2, and the result of the fitting routine. Panel a shows the complete spectrum (grey), with peaks associated with olivine between 600 and 1100 cm^{-1}. The two peaks of the Fermi diad have their fit overlaid in blue and green, the horizontal black line indicates the baseline arising from noise. The vertical red lines bound the range of the spectrum passed to the fitting routine. Panels b and c show a close up of the fits to the two diad peaks. The red boxes indicate the points used in calculation of the uncertainty on the calculated peak centre.

Table 2.14: Summary of the statistics from repeat CO_2 analyses of standard materials used for CO_2 calibration curves. One standard deviation, σ, the fractional precision, σ/μ, and the number of analyses, n, are shown. All quantities in ppmw.

material	mean	σ	σ/μ	n
17-2	2594	76	0.03	9
s2-3	576	55	0.10	5
s5-14	1279	39	0.03	9
s4-13	1101	44	0.04	4
st1	1320	240	0.18	4
st2	1045	22	0.02	4
st6	698	33	0.05	4
		average	0.04	

Table 2.15: Summary of the statistics from repeat H_2O analyses of standard materials (Shishkina et al., 2010). One standard deviation, σ, the fractional precision, σ/μ, the fractional accuracy, and the number of analyses, n, are shown. All quantities in wt%.

material	ref	mean	σ	σ/μ	accuracy	n
st1	2.96	3.04	0.25	0.08	0.03	4
st2	2.84	2.80	0.14	0.05	0.02	5
st6	1.48	1.44	0.08	0.05	0.03	6
			average	0.06	0.02	

the bubble diameter, melt inclusion length and melt inclusion width, using the ImageJ software (Schneider et al., 2012). Where the optical image did not have a sufficient field of view for the whole inclusion to be imaged, backscatter electron (BSE) images obtained using the electron probe were used instead. The volume of the inclusion was estimated by assuming it can be approximated as an ellipsoid of revolution (with rotational symmetry about its longest axis).

Chapter 3

The Temperature and Mineralogy of the Iceland Plume

Mantle temperature and lithology are the primary variables controlling the convective circulation in Earth's mantle (Section 1.3). Though a number of different constraints have been used to estimate the temperature of the Icelandic mantle (Section 1.3.1), the different techniques have produced widely varying results when applied individually, and often display trade-offs with mantle lithology. In this chapter I formally combine constraints from petrological thermometry, crustal thicknesses, and geochemistry to find a mantle temperature consistent with each independent constraint.

The petrological constraint on mantle temperature used here is derived from crystallisation temperatures of forsteritic olivine crystals. These temperatures are derived using the aluminium-spinel Al-exchange thermometer (Coogan et al., 2014; Wan et al., 2008). Using this thermometer is advantageous over olivine-liquid thermometry because it only requires assumptions about coexisting olivine and spinel being in equilibrium, rather than assumptions about equilibration pressure, or the composition of a melt that is no longer present. The crystallisation temperatures estimated using the Al-exchange thermometer are lower than those estimated using olivine-liquid equilibria (Coogan et al., 2014). In Section 3.3.6, the factors contributing to this discrepancy are discussed. The discrepancy in equilibration temperatures, and consequently mantle temperature, for Iceland arise from overestimation of primary FeO by Putirka (2008a) due to incomplete mixing of fractional melts (Table 3.7). For MORB the discrepancy derives from the assumption by Putirka (2008a) that melt and olivine equilibrated at mantle pressures, rather than crustal pressures as done here.

The samples and analytical techniques used are described in Sections 2.1.1 and 2.3.1. In Section 3.1 I present new determinations of crystallisation temperatures for four eruptions from the Northern Volcanic Zone of Iceland, and compare these to crystallisation temperatures at mid-ocean ridges

and estimates from elsewhere in Iceland. In Section 3.2 I use a thermal model to calculate how mantle temperature, mantle composition and melt source depth affect crystallisation temperature. By inverting this model and combining observations of crustal thickness and pyroxenite contributions to melt chemistry I show that the Icelandic mantle is at least 140 °C hotter than the MORB source mantle. In Section 3.3 I discuss the results and the validity of the assumptions. This approach not only integrates petrological, geochemical and geophysical observations, but additionally quantifies uncertainty arising from the trade-off between mantle temperature, composition and melt extraction processes.

3.1 Olivine-Spinel Al Exchange thermometry

Aluminum exchange between olivine and spinel was parameterized as a function of temperature by Coogan et al. (2014) using experimental data (Coogan et al., 2014; Wan et al., 2008):

$$T(\mathrm{K}) = \frac{10000}{0.575 + 0.884\mathrm{Cr\#} - 0.897\ln(k_d)} \tag{3.1}$$

where

$$k_d = \frac{\mathrm{Al_2O_3^{olivine}}}{\mathrm{Al_2O_3^{spinel}}} \tag{3.2}$$

$$\mathrm{Cr\#} = \left(\frac{\mathrm{Cr}}{\mathrm{Cr+Al}}\right)^{\mathrm{spinel}} \tag{3.3}$$

Uncertainties in each parameter are reported by Coogan et al. (2014), though I use an estimate of total uncertainty in temperature, as described in Section 3.1.2. The crystallisation temperatures calculated are shown in Table 3.3.

3.1.1 Petrography and Chemistry of the Olivine and Spinel

Collection of profiles in spinel and olivine allowed the effect of both diffusion and growth zoning to be identified if present. Experimental studies suggest Al is a very slow-diffusing species in olivine (Spandler and O'Neill, 2010); it is therefore likely that Al concentrations are primary and have not been reset. Sharp steps in Al concentration were observed along some olivine profiles, e.g. Figure 2.3f, most likely indicating multiple stages of crystal growth from magmas of different chemistry and temperature. Smooth variations in Al concentration and Cr# were seen in many of the profiles through the spinel inclusions, rising to a maximum in the centre in some cases, e.g. Figure 2.3g, and a minimum in others. If post-entrapment Al exchange between spinel and olivine was responsible for the zoning, very large changes in Al concentration in the olivine would be required in order to satisfy

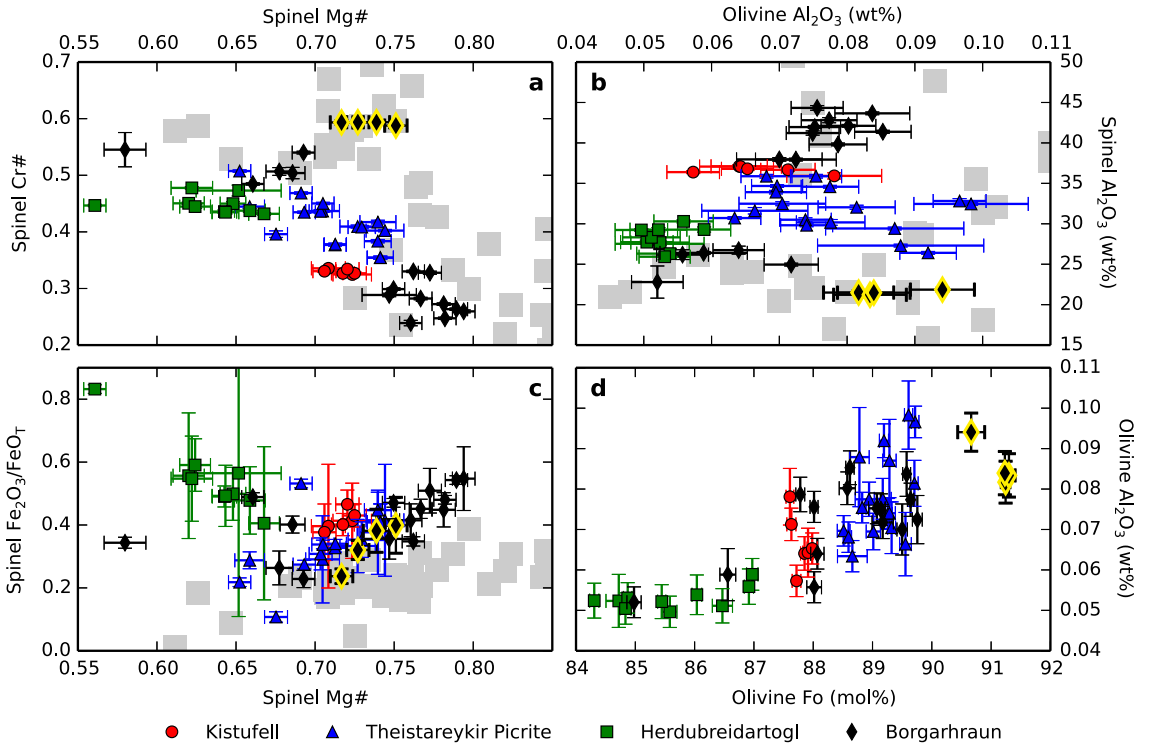

Figure 3.1: Olivine and spinel chemistry for the crystals used in this study. The grey squares are experimental data from Wan et al. (2008) and Coogan et al. (2014) used to calibrate the thermometer by Coogan et al. (2014). Spinel Mg# (panels a and c) is calculated using FeO derived from a charge balance calculation. Error bars indicate analytical precision and natural variability in the crystal. The Borgarhraun points with a yellow outline are the four high-temperature points used in the calculation of mantle temperature.

mass balance. No corresponding gradients in Al concentration were observed in adjacent olivine indicating that the spinel zoning does not arise from Al exchange with the olivine, and therefore formed prior to the spinel's trapping. The points at the spinel rims in contact with olivine are therefore the most likely to have been in Al equilibrium with the olivine that crystallised at the time of spinel trapping. I therefore use these measurements in the calculations.

Coogan et al. (2014) emphasise the importance of phosphorus in enhancing the uptake of Al in olivine, and recommend extrapolating Al_2O_3 concentration back to 0 wt% P_2O_5. The phosphorus concentration in all crystals analysed in this study was low, typically less than 100 ppmw P_2O_5 (Table 3.1), and showed no correlation with Al in the vast majority of crystals. Where there was a correlation, the average Al_2O_3 of the low-phosphorus points was within one standard deviation of the value obtained by a linear regression back to 0 wt% P_2O_5.

Table 3.1: Average measured composition for each olivine crystal. Samples beginning with 'BH' are from Borgarhraun, 'HBT' are Herðubreiðartögl, 'KS' from Kistufell and 'TP' from the Theistareykir Picrite. All measurements shown in wt%.

Sample	SiO_2	MgO	FeO	NiO	CaO	Al_2O_3	Total
BH22-1-1	40.86	47.05	10.19	0.28	0.37	0.072	99.25
BH22-2-1	40.69	46.41	11.21	0.30	0.37	0.064	99.44
BH22-3-1	40.07	44.50	14.02	0.23	0.38	0.052	99.71
BH22-4-1	40.20	46.80	11.36	0.28	0.33	0.076	99.30
BH38-1-1	40.33	47.74	9.71	0.29	0.38	0.072	98.77
BH38-2-1	40.75	48.54	8.30	0.35	0.40	0.082	98.72
BH38-2-2	40.83	48.62	8.26	0.35	0.40	0.083	98.86
BH47-1-1	40.76	48.45	8.90	0.35	0.36	0.094	99.26
BH47-1-2	40.99	48.97	8.39	0.35	0.36	0.084	99.45
BH62-1-1	39.91	47.36	10.36	0.30	0.39	0.075	98.63
BH62-1-2	40.91	47.89	9.86	0.30	0.40	0.077	99.72
BH62-1-3	40.78	47.67	9.97	0.30	0.40	0.070	99.46
BH62-1-4	40.85	47.81	9.92	0.30	0.41	0.084	99.63
BH62-2-1	40.37	46.59	11.31	0.29	0.34	0.056	99.42
BH62-3-1	40.52	47.02	10.81	0.30	0.35	0.080	99.37
BH62-3-2	40.46	46.97	10.75	0.30	0.34	0.085	99.17
BH62-4-1	40.43	46.54	11.55	0.29	0.32	0.079	99.46
BH62-5-1	39.82	45.39	12.57	0.25	0.38	0.059	98.83
BH70-2-1	40.61	47.26	10.26	0.31	0.33	0.075	99.10
HBT2-1-1	39.87	43.79	14.08	0.24	0.33	0.052	98.71
HBT2-1-2	39.74	43.43	14.41	0.24	0.32	0.052	98.52
HBT2-2-1	40.61	46.01	12.29	0.27	0.34	0.059	99.87
HBT2-6-1	40.43	45.73	12.27	0.28	0.34	0.056	99.43
HBT2-7-1	40.32	45.22	13.08	0.26	0.34	0.054	99.61
HBT2-8-1	39.98	44.27	14.07	0.24	0.32	0.053	99.25
HBT2-9-1	40.17	44.17	14.08	0.24	0.32	0.050	99.36
HBT2-10-1	40.14	45.58	12.72	0.25	0.34	0.051	99.39
HBT2-5-1	40.21	44.47	13.36	0.25	0.34	0.050	98.97
HBT2-5-2	40.15	44.49	13.51	0.25	0.33	0.052	99.09
KS01-2-1	38.92	45.85	11.30	0.30	0.33	0.064	97.00
KS01-4-1	39.62	45.80	11.23	0.31	0.32	0.064	97.60
KS01-5-1	38.98	45.49	11.08	0.31	0.32	0.065	96.51
KS02-1-1	39.45	45.66	11.52	0.28	0.36	0.078	97.66
KS02-1-2	38.04	44.76	11.26	0.29	0.33	0.071	95.03
KS02-2-1	39.14	45.55	11.37	0.30	0.33	0.057	97.00
TP01-3-1	39.82	46.87	10.06	0.33	0.36	0.074	97.81
TP01-3-2	38.99	46.12	9.98	0.34	0.35	0.078	96.16
TP01-4-1	39.42	46.47	10.47	0.31	0.39	0.088	97.56
TP01-7-1	40.40	47.76	9.76	0.31	0.38	0.097	98.98
TP01-7-2	40.12	47.39	9.80	0.31	0.38	0.098	98.41
TP01-7-3	40.71	47.80	9.78	0.31	0.38	0.081	99.37
TP01-8-1	39.97	46.43	10.59	0.30	0.39	0.063	98.02
TP01-8-2	39.74	47.01	10.06	0.32	0.38	0.087	97.90
TP01-9-1	32.16	43.33	9.01	0.32	0.35	0.066	85.53
TP02-1-1	40.27	47.54	10.13	0.31	0.39	0.070	99.04
TP02-2-1	40.52	46.83	10.83	0.30	0.37	0.070	99.22
TP02-2-2	40.84	47.59	10.47	0.30	0.38	0.070	99.99
TP02-3-1	40.23	46.97	10.41	0.31	0.38	0.077	98.72
TP02-4-1	40.47	47.40	10.14	0.29	0.38	0.074	99.07
TP02-5-1	40.15	46.94	10.14	0.31	0.38	0.092	98.31
TP02-7-1	39.99	46.95	10.53	0.30	0.37	0.075	98.50
TP02-7-2	42.53	30.29	9.18	0.18	5.18	0.068	98.21

Sample	MgO	$FeO_{(tot)}$	Cr_2O_3	Al_2O_3	Total	FeO	Fe_2O_3
BH22-1-1	15.48	14.76	43.68	24.95	99.60	12.24	2.80
BH22-2-1	15.25	16.02	40.94	26.74	99.71	12.95	3.41
BH22-3-1	12.81	21.67	40.63	22.79	99.39	16.55	5.69
BH22-4-1	18.42	14.21	20.75	44.33	98.43	10.35	4.29
BH38-1-1	17.98	13.14	27.88	37.94	97.79	10.00	3.48
BH38-2-1	15.60	13.34	46.76	21.50	98.00	10.99	2.61
BH38-2-2	15.75	13.58	46.22	21.22	97.59	10.54	3.38
BH47-1-1	16.65	13.37	46.46	21.86	99.10	9.84	3.93
BH47-1-2	16.33	13.82	46.79	21.48	99.16	10.29	3.93
BH62-1-1	18.82	13.33	22.37	41.96	97.13	8.95	4.86
BH62-1-2	19.23	13.28	22.37	42.81	98.39	8.89	4.87
BH62-1-3	18.32	14.02	27.59	37.96	98.61	9.61	4.89
BH62-1-4	18.94	13.47	21.39	43.66	98.18	9.41	4.52
BH62-2-1	15.32	17.03	39.64	26.18	98.94	12.51	5.02
BH62-3-1	18.74	13.13	23.50	42.11	98.15	9.35	4.19
BH62-3-2	18.38	14.02	24.26	41.38	98.75	9.97	4.50
BH62-4-1	17.87	15.14	25.31	39.81	98.88	10.64	5.00
BH62-5-1	14.69	19.37	37.01	26.40	98.39	13.45	6.58
BH70-2-1	17.87	14.25	24.92	41.22	98.94	10.80	3.84
HBT2-1-1	13.91	22.80	33.63	27.52	99.05	15.19	8.46
HBT2-1-2	13.63	33.30	33.30	27.68	98.41	19.04	15.84
HBT2-2-1	14.99	19.80	33.95	29.29	99.14	13.85	6.62
HBT2-6-1	15.35	18.59	34.34	30.30	99.85	13.62	5.52
HBT2-7-1	14.94	21.45	35.20	26.31	99.65	14.22	8.03
HBT2-8-1	13.94	22.54	35.34	25.93	99.03	15.10	8.26
HBT2-9-1	14.12	23.21	33.10	27.73	99.35	15.15	8.95
HBT2-10-1	14.66	20.56	34.53	28.32	99.21	14.19	7.08
HBT2-5-1	14.66	20.95	33.67	29.23	99.63	14.53	7.13
HBT2-5-2	14.63	20.88	33.55	29.27	99.42	14.47	7.13
KS01-2-1	16.77	15.68	26.61	37.11	97.00	11.43	4.72
KS01-4-1	16.87	15.83	26.84	37.07	97.47	11.41	4.91
KS01-5-1	16.55	15.81	26.61	36.80	96.63	11.61	4.66
KS02-1-1	16.38	16.30	27.05	35.92	96.77	12.02	4.76
KS02-1-2	16.25	16.17	26.99	36.68	96.99	12.07	4.55
KS02-2-1	16.74	16.43	27.24	36.39	97.67	11.58	5.39
TP01-3-1	15.81	14.90	35.27	30.50	97.27	11.81	3.43
TP01-3-2	15.60	14.97	34.82	30.17	96.38	11.72	3.61
TP01-4-1	15.27	18.00	35.88	27.30	97.23	12.17	6.47
TP01-7-1	17.05	14.35	32.92	32.82	97.87	10.45	4.34
TP01-7-2	16.54	14.40	33.54	32.46	97.66	11.08	3.69
TP01-7-3	16.92	14.21	34.20	32.04	98.07	10.61	4.00
TP01-8-1	15.55	15.30	35.20	30.71	97.48	12.27	3.36
TP01-8-2	15.70	15.28	35.91	29.42	97.08	11.71	3.96
TP01-9-1	14.23	13.37	30.89	31.61	90.77	12.20	1.31
TP02-1-1	16.70	14.55	33.43	32.48	97.96	11.04	3.90
TP02-2-1	16.44	15.31	31.27	34.68	98.47	11.83	3.87
TP02-2-2	17.03	14.99	31.46	33.91	98.13	10.69	4.78
TP02-3-1	16.47	15.46	31.35	34.58	98.61	11.83	4.03
TP02-4-1	14.69	17.09	35.59	29.82	97.94	13.58	3.91
TP02-5-1	14.36	16.33	40.56	26.41	98.38	13.65	2.98
TP02-7-1	17.18	14.62	29.37	35.88	97.73	10.69	4.37
TP02-7-2	17.18	14.62	29.37	35.88	97.73	10.69	4.37

Table 3.2: Average measured composition for each spinel crystal. Samples beginning with 'BH' are from Borgarhraun, 'HBT' are Herðubreiðartögl, 'KS' from Kistufell and 'TP' from the Theistareykir Picrite. All measurements shown in wt%.

Figure 3.1 shows that the majority of the crystals, particularly those recording the highest temperatures, are well within the bounds of the crystal compositions used in the experimental calibration of the thermometer. This includes the Mg# and Cr# of the spinel, olivine and spinel Al concentrations, and the estimated Fe_2O_3/FeO_T ratio calculated by charge balance (Tables 3.1 and 3.2). The Mg# is defined as:

$$\text{Mg\#} = \frac{\text{Mg}}{\text{Mg} + \text{Fe}^{2+}} \tag{3.4}$$

where each quantity is in mols. The spinel crystals that have higher Fe_2O_3/FeO_T ratios than the calibration have the lowest crystallisation temperatures. Since the lowest crystallisation temperatures are not used in the T_p inversion (justified in Section 3.1.3), these high Fe_2O_3/FeO_T ratios have no further consequence in this study.

3.1.2 Error Propagation

For each olivine-spinel pair, the olivine-spinel Al-exchange temperature and its uncertainty were calculated by applying a Monte Carlo error propagation. Values for each chemical parameter used in the thermometer (olivine and spinel Al_2O_3, and spinel Cr#) were selected at random from Gaussian distributions defined by the mean and standard deviation of the measurement. The analytical precision for Al_2O_3 was $1\sigma = 38$ ppmw in olivine, and $1\sigma = 0.17$ wt% in spinel, though a (1σ) relative error of 2.0 % based on EPMA counting statistics was used instead for Al_2O_3 in spinel. For spinel Cr#, the precision was $1\sigma = 0.0020$. Repeat analyses of olivine and spinel crystals were paired at random. The temperature calculated from the randomly picked chemical parameters was then used as the mean for the definition of a Gaussian distribution representing the calibration uncertainty. The standard deviation for the uncertainty in the thermometer calibration was taken to be 14 °C, obtained from the distribution of data around the empirical regression through the experimental data. This process was repeated 10,000 times for each olivine-spinel pair in order to obtain a distribution, from which a mean and standard deviation could be calculated. The propagated uncertainty in temperature estimate is typically $\sim$20 °C and is similar in magnitude to that reported by Spice et al. (2016) and Wan et al. (2008). Some crystals have a greater uncertainty, arising from their internal heterogeneity and the associated uncertainty in how to pair olivine and spinel analyses. Where single olivine crystals had multiple spinel inclusions, analyses pairing each spinel inclusion with the adjacent olivine gave temperature estimates within their mutual uncertainty.

3.1.3 Thermometry Results

Crystallisation temperature estimates for the Northern Volcanic Zone (NVZ) are shown in Figure 3.2. The histograms in Figure 3.2 show offsets and variable widths in crystallisation temperature

		Fo	Spinel				Fo	Spinel	
Sample	T_{crys} (°C)	(mol%)	Cr#	Mg#	Sample	T_{crys} (°C)	(mol%)	Cr#	Mg#
BH22-1-1	1320 ± 21	89.17	0.54	0.56	HBT2-10-1	1234 ± 23	86.47	0.45	0.51
BH22-2-1	1280 ± 20	88.07	0.51	0.54	HBT2-5-1	1223 ± 22	85.58	0.44	0.50
BH22-3-1	1263 ± 25	84.98	0.55	0.43	HBT2-5-2	1227 ± 23	85.45	0.43	0.50
BH22-4-1	1264 ± 18	88.01	0.24	0.66	KS01-2-1	1249 ± 20	87.85	0.32	0.60
BH38-1-1	1268 ± 23	89.76	0.33	0.65	KS01-4-1	1249 ± 25	87.91	0.33	0.60
BH38-2-1	1383 ± 27	91.24	0.59	0.58	KS01-5-1	1254 ± 19	87.98	0.33	0.59
BH38-2-2	1371 ± 22	91.30	0.59	0.59	KS02-1-1	1296 ± 25	87.61	0.34	0.58
BH47-1-1	1399 ± 20	90.66	0.59	0.62	KS02-1-2	1273 ± 19	87.63	0.33	0.58
BH47-1-2	1377 ± 22	91.23	0.59	0.61	KS02-2-1	1228 ± 20	87.72	0.33	0.60
BH62-1-1	1270 ± 18	89.07	0.26	0.69	TP01-3-1	1293 ± 24	89.26	0.44	0.57
BH62-1-2	1277 ± 20	89.64	0.26	0.70	TP01-3-2	1315 ± 32	89.17	0.44	0.57
BH62-1-3	1265 ± 23	89.50	0.33	0.67	TP01-4-1	1355 ± 37	88.78	0.47	0.55
BH62-1-4	1288 ± 21	89.58	0.25	0.68	TP01-7-1	1351 ± 18	89.72	0.40	0.62
BH62-2-1	1256 ± 21	88.02	0.50	0.55	TP01-7-2	1355 ± 26	89.61	0.41	0.60
BH62-3-1	1279 ± 19	88.57	0.27	0.68	TP01-7-3	1313 ± 22	89.71	0.42	0.62
BH62-3-2	1294 ± 20	88.62	0.28	0.66	TP01-8-1	1260 ± 21	88.66	0.43	0.56
BH62-4-1	1283 ± 19	87.78	0.30	0.64	TP01-8-2	1340 ± 30	89.29	0.45	0.57
BH62-5-1	1258 ± 33	86.56	0.48	0.52	TP01-9-1	1275 ± 27	89.56	0.40	0.52
BH70-2-1	1267 ± 19	89.14	0.29	0.64	TP02-1-1	1276 ± 31	89.32	0.41	0.61
HBT2-1-1	1238 ± 27	84.72	0.45	0.47	TP02-2-1	1270 ± 19	88.51	0.38	0.59
HBT2-1-2	1250 ± 22	84.31	0.45	0.43	TP02-2-2	1268 ± 22	89.01	0.38	0.62
HBT2-2-1	1258 ± 21	86.97	0.44	0.52	TP02-3-1	1284 ± 25	88.94	0.38	0.59
HBT2-6-1	1241 ± 22	86.92	0.43	0.53	TP02-4-1	1302 ± 19	89.28	0.44	0.52
HBT2-7-1	1251 ± 25	86.04	0.47	0.51	TP02-5-1	1347 ± 41	89.19	0.51	0.51
HBT2-8-1	1255 ± 21	84.87	0.48	0.48	TP02-7-1	1285 ± 19	88.83	0.35	0.62
HBT2-9-1	1236 ± 22	84.83	0.44	0.48	TP02-7-2	1308 ± 39	82.50	0.35	0.62

Table 3.3: Crystallisation temperatures estimated for each olivine and spinel pair. Samples beginning with 'BH' are from Borgarhraun, 'HBT' are Herðubreiðartögl, 'KS' from Kistufell and 'TP' from the Theistareykir Picrite. Crystallisation temperature uncertainties are 1 s.d.

distributions between each eruption. The scatter plot shows that the variation in crystallisation temperature between eruptions co-varies with their olivine forsterite content. Since the forsterite content of crystallising olivine decreases during fractional crystallisation it can be used as a proxy for melt evolution. The evolution of temperature during fractionation is shown in Figure 3.2 by solid blue and red lines, for KG1 and KR4003-derived melts respectively (Kogiso et al., 1998; Walter, 1998). The caption to Figure 3.2 describes this crystallisation calculation. These melts represent the end-member melt compositions entering the Icelandic NVZ crust (Shorttle et al., 2014). Much of the range in crystallisation temperature can be accounted for by the cooling associated with fractional crystallisation, and the deviations from this are consistent with the range of crystallisation temperatures that would arise from melts with variable composition (and therefore liquidus temperature) arriving from the mantle. Crystallisation temperatures recorded in the Borgarhraun crystals extend over much of the range of the dataset, and therefore the dataset does not resolve differences in mantle temperature within Iceland. The difference in position and shape of the histograms represents biased sampling of the history of fractional crystallisation by each eruption.

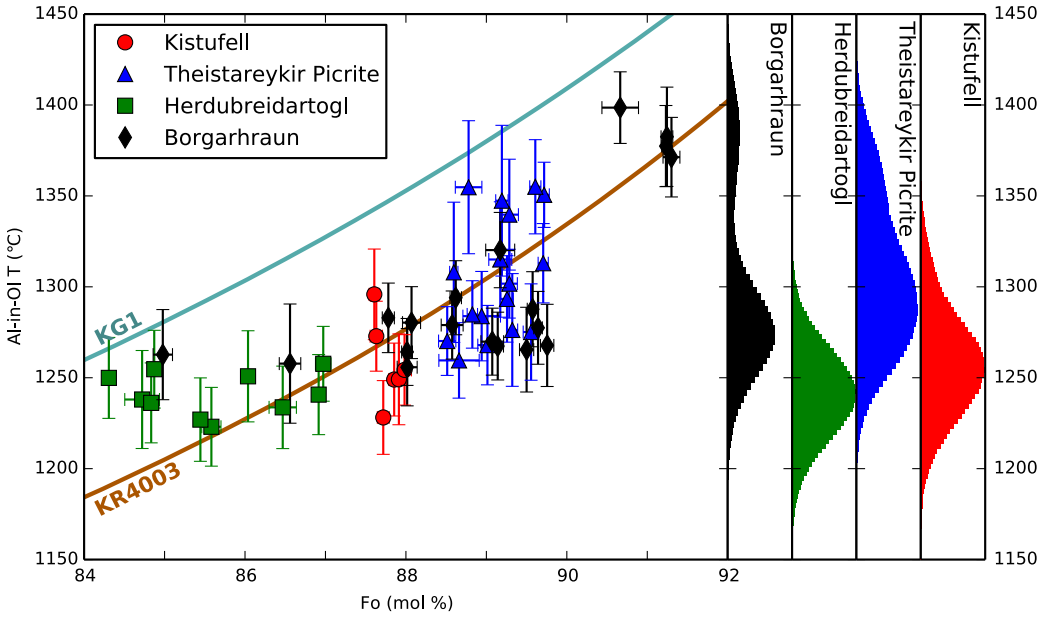

Figure 3.2: Olivine-spinel aluminium exchange temperatures for the new Iceland dataset. The distributions on the right show the summed Monte Carlo distributions for each eruption. The two lines show the evolution of olivine fractionation, calculated using Petrolog3 (Danyushevsky and Plechov, 2011) and the Beattie (1993) olivine partitioning model at 0.8 GPa, QFM. The starting compositions used were experimental liquids derived from KR4003 at 3.0 GPa, 1540 °C (Walter, 1998), and KG1 at 3.0 GPa, 1525 °C (Kogiso et al., 1998) (the two end-member melts identified as best describing primitive NVZ melts by Shorttle and Maclennan (2011)).

.

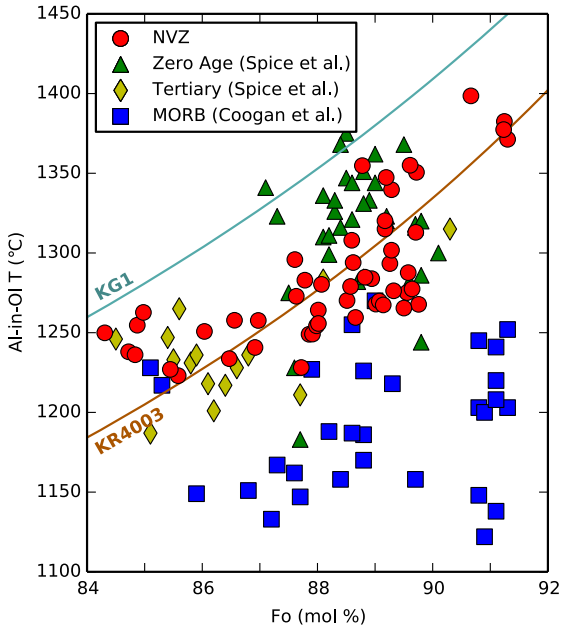

Figure 3.3: Comparison of the new olivine-spinel aluminum exchange temperatures for Iceland's NVZ with the olivine-spinel aluminum exchange temperatures for zero-age and Tertiary Iceland from Spice et al. (2016), and the dataset for MORB from Coogan et al. (2014). Uncertainty for the dataset presented here is shown in Figure 3.2, but is of a similar magnitude to the ± 22 °C uncertainty of the Spice et al. (2016) and Coogan et al. (2014) datasets. Lines show fractional crystallisation models as described in the caption to Figure 3.2.

3.1.4 Comparisons with Published Data and Relationship to Mantle Temperature

Figure 3.3 shows the same data compared with the crystallisation temperatures reported for Iceland by Spice et al. (2016) and those for MORB by Coogan et al. (2014). The Spice et al. (2016) zero age crystallisation temperatures are consistent with the range found in the new dataset. The range of temperatures at a given olivine composition in Figure 3.3 hint at spatial and temporal variability in the parameters controlling crystallisation temperature. The highest temperatures in the combined dataset are for $Fo_{>90}$ Borgarhraun crystals from this study, though there are no olivine crystals with a similar composition in the Spice et al. (2016) dataset. In addition to zero age eruptions, Spice et al. (2016) reported results from Tertiary flows, arguing that their offset in crystallisation temperature is consistent with a cooler mantle in the Tertiary, as indicated by other mantle temperature proxies. However, taking into account olivine forsterite content, the crystallisation temperatures for Tertiary Iceland overlie the range of temperatures reported from young Icelandic olivines in this paper. The temperature offset observed by Spice et al. (2016) could therefore be consistent with an undersampling of primitive, higher temperature olivine crystals in the Tertiary eruptions they studied, rather than being a signal of lower plume temperatures in the Tertiary. In contrast, a consistent offset to lower crystallisation temperatures is seen in the MORB dataset relative to Iceland at all olivine forsterite contents. In order to generate such an offset, the melt compositions, in particular the MgO and FeO concentrations, supplied from the mantle must be different. In Section 3.2 I consider the role of both lithology and temperature in accounting for this observation.

Using offsets in crystallisation temperature distribution as a proxy for mantle temperature, without controlling for differences in extent of fractional crystallisation, would lead to inferring mantle T_p both increases and decreases with distance along the NVZ away from the plume centre. By examining the relationship between crystallisation temperature and melt evolution, for which I use olivine forsterite content as a proxy (Figure 3.2), it is clear that the offset in position of the histograms shown on the right of Figure 3.2 are not controlled by variations in mantle temperature. A more robust observation to link to mantle T_p is the crystallisation temperature of primitive melts. Olivine crystals from Borgarhraun of Fo_{91} are assumed to be in equilibrium with mantle olivine and therefore the first crystals to have grown from mantle-derived melts. When inverting for mantle T_p (Section 3.2.5), I use the crystallisation temperatures of the most forsteritic crystals. For Iceland these forsteritic crystals are from Borgarhraun, for the MORB dataset of Coogan et al. (2014), the most forsteritic crystals are from the Siqueiros Fracture Zone.

3.2 Thermal Model

Since the highest crystallisation temperatures are observed in the most forsteritic olivine crystals, they likely reflect crystallisation of melts derived directly from the mantle. As discussed in Section 1.3.1, the diversity in melt inclusion chemistry seen in such crystals indicates fractional mantle melts are not completely homogenised before leaving the mantle. These fractional melts are derived at different pressure and temperature conditions, therefore their major element chemistry, including MgO and FeO concentrations, will also be diverse. Since the temperature of olivine saturation is a function of both MgO and FeO concentration (Roeder and Emslie, 1970), different melts derived from mantle of the same T_p will reach olivine saturation at different temperatures. I present a forward model to understand the uncertainty this process introduces into converting crystallisation temperatures into mantle T_p.

Olivine saturation is modelled here; however it is the co-saturation temperature of olivine and spinel that is recorded by the Al-exchange thermometer. Though experimental data suggests spinel may saturate before olivine (Maaløe and Jakobsson, 1980), the presence of spinel inclusions in the most forsteritic olivine crystals suggests spinel saturated before or very soon after olivine saturation. Therefore, it is very unlikely that the requirement for both olivine and spinel saturation in the melt requires a significant cooling (or differentiation) interval.

There are a number of steps in the process used to extract mantle temperature estimates, which are summarised sequentially:

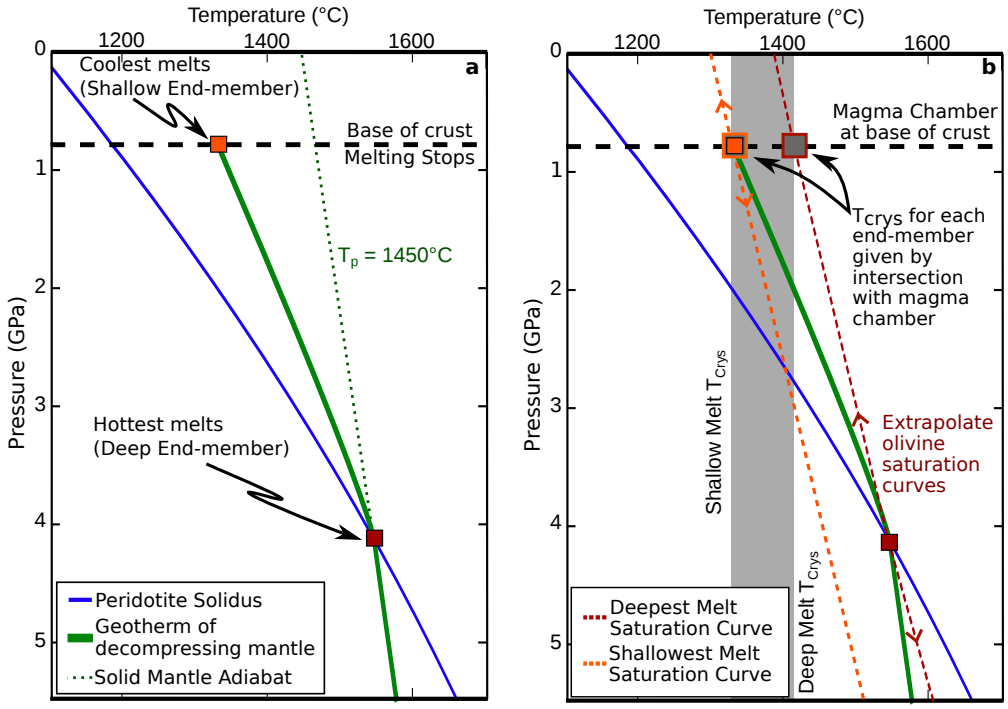

Figure 3.4: Schematic illustration of the thermal model in the simplest case of melting a 100% lherzolite mantle with T_p =1450 °C. Panel a shows how the end-member melts are selected, after calculating the geotherm. Panel b shows how olivine saturation curves are extrapolated from each of the points selected in Panel a. Finding the intersection of these curves with the base of the crust (assumed to be where crystallisation begins) allows estimation of the olivine saturation temperature of both end-member melts.

1. A multi-component melting model (described comprehensively by Shorttle et al. (2014), and more generally by Phipps Morgan (2001)) is used to calculate the thermal structure and melt fraction for many individual melting regions with variable mantle temperature (T_p) and differing proportions of pyroxenite and harzburgite (ϕ_{Px},ϕ_{Hz}). (Section 3.2.2 and Figures 3.4a, 3.5a and 3.5b).

2. Crustal thickness (t_c) is calculated from the melt fraction against depth curve, assuming mid-ocean ridge corner flow. Melting is stopped in the model once mantle upwells to the base of the crust.

3. The fraction of bulk crust (i.e. the fully mixed melt) derived from pyroxenite is calculated (F_{Px}).

4. Hypothetical end-member melts from the base and top of the melting region, representing absolute limits of fractional melt diversity, are considered from each melting region modelled (Figure 3.4a).The temperature at which each end-member melt is saturated in olivine at the base of the crust is estimated (T_{crys}), since I assume this is where the magma chamber resides (Section 3.2.1 and Figure 3.4b).

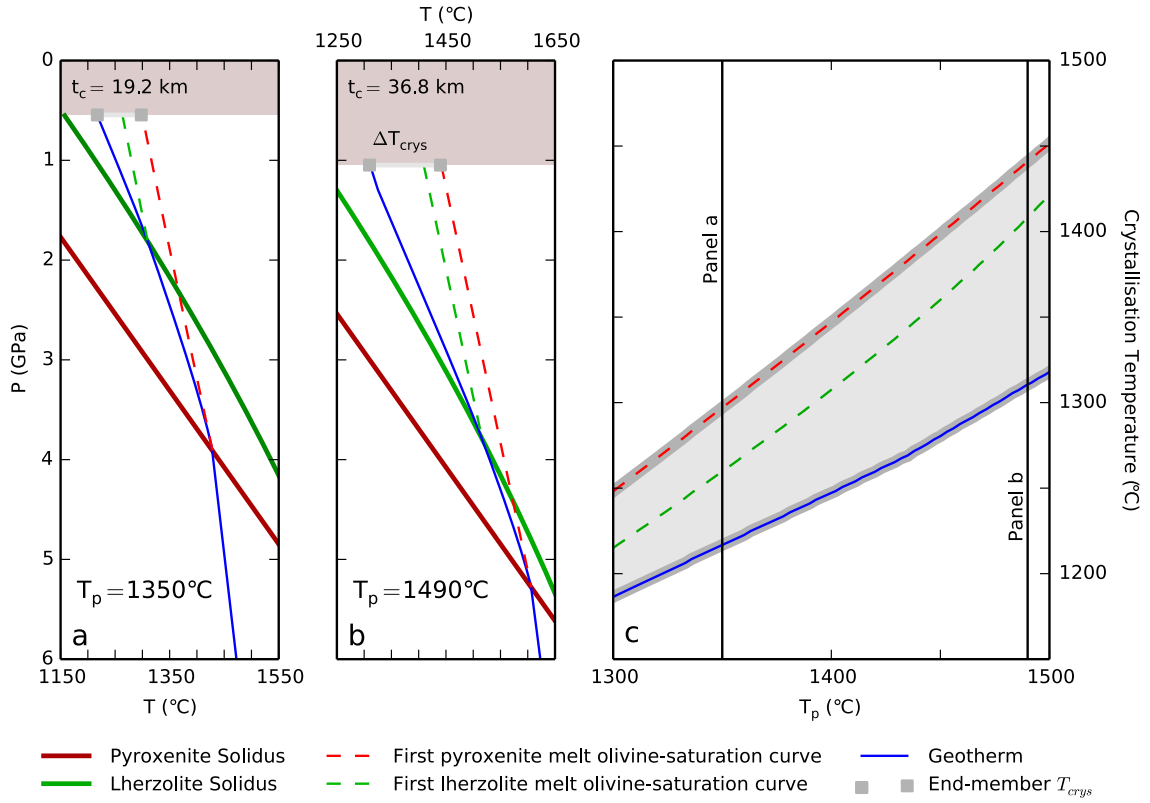

Figure 3.5: Panels a and b show the geotherms (blue) for adiabatically ascending mantle of 70% lherzolite and 30% pyroxenite undergoing melting for $T_p = 1350\,^{\circ}\mathrm{C}$ and $T_p = 1490\,^{\circ}\mathrm{C}$ respectively. The olivine-saturation curves for two deep melts (first pyroxenite and lherzolite melts) are shown by the dashed lines. The olivine saturation curves are omitted for the shallow melt bound since the olivine saturation temperature at the base of the crust coincides with the geotherm. The produced crustal thickness (t_c) is shown by the filled box. The range of olivine saturation temperatures of primitive melts generated by each model is shown by the small-, light-grey boxes. Panel c shows the range of olivine saturation temperatures of primitive melts for the same mantle composition as a function of T_p.

5. This set of modelled melting regions constitutes the forward model. When the results are plotted for fixed mantle T_p (Figure 3.6), two surfaces bound possible crystallisation temperatures of primary melts arriving from the mantle. One surface represents fractional melts with a deep origin; the other represents shallow fractional melts. Variable mixing of melts derived between these two end-members (or re-equilibration with the mantle) will result in an intermediate crystallisation temperature.

6. By finding the melting region which simultaneously satisfies t_c, F_{Px} and T_{crys}, the forward model is inverted to obtain T_p, ϕ_{Px} and ϕ_{Hz}. Since each melting region model has two end-member T_{crys} bounds, there are two solutions: one assuming the observed T_{crys} arose from a deep-originating fractional melt, and one assuming a shallow origin. The T_p inferred differs

for each solution due to the different magnitude of temperature correction required. A shallow melt has experienced significant cooling due to the latent heat of fusion, thus requiring a large temperature correction. A deep melt has experienced no such cooling, is intrinsically warmer and thus requires no temperature correction for melting, though will saturate in olivine at a slightly lower temperature than its melting temperature in a magma chamber at the base of the crust (due to the pressure dependence of saturation temperature).

7. This process is repeated 10^6 times for different values of t_c, F_{Px} and T_{crys}, as defined by their uncertainties, in a Monte Carlo error propagation.

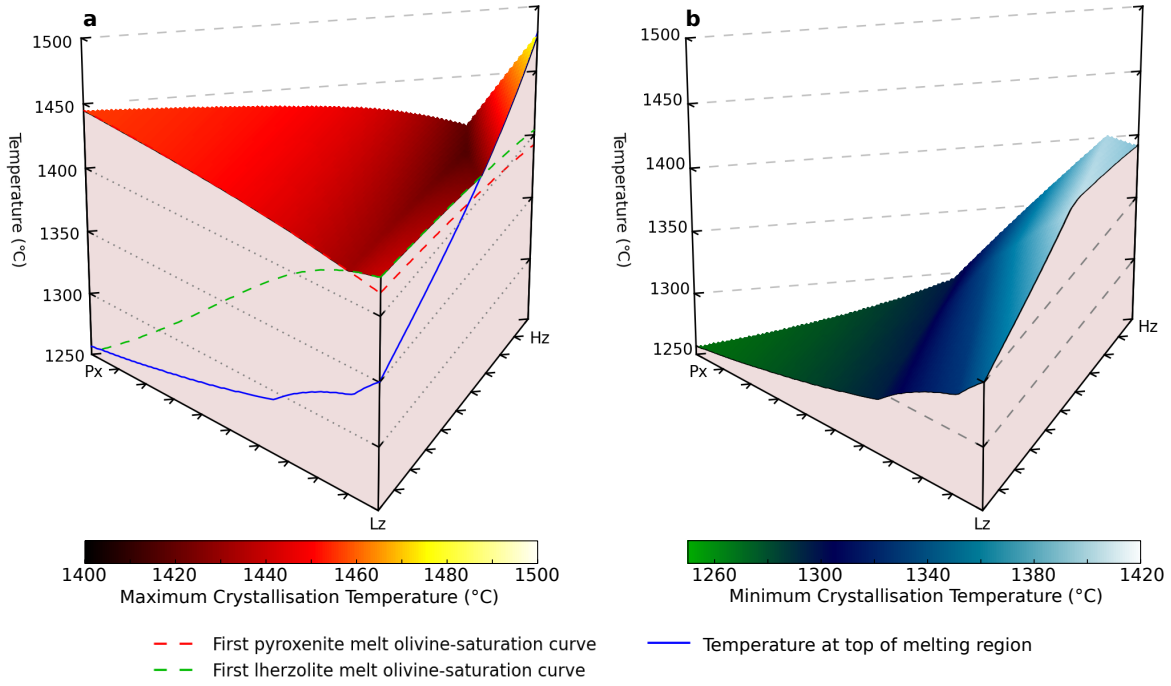

Figure 3.6: Crystallisation temperatures of primary melts derived from a $T_p = 1480°C$ mantle, as a function of lithology. Plot a shows the surface of maximum crystallisation temperature, and the lines show the crystallisation temperatures of end-member melts for the lherzolite-pyroxenite and lherzolite-harzburgite joins. Plot b shows the minimum crystallisation temperature, which is identical to the temperature of the geotherm at the top of the melting region (except at high ϕ_{Hz}), since olivine crystallization is defined at the same depth.

This is analogous to the method used by Putirka (2008a, 2016, 2005); Putirka et al. (2007) in that estimated melt fraction determines the magnitude of the latent heat of fusion correction. I obtain the magnitude of the correction by finding the best-fitting geotherm (as illustrated in Figures 3.7 and 3.8). The steps in this process are discussed in detail below.

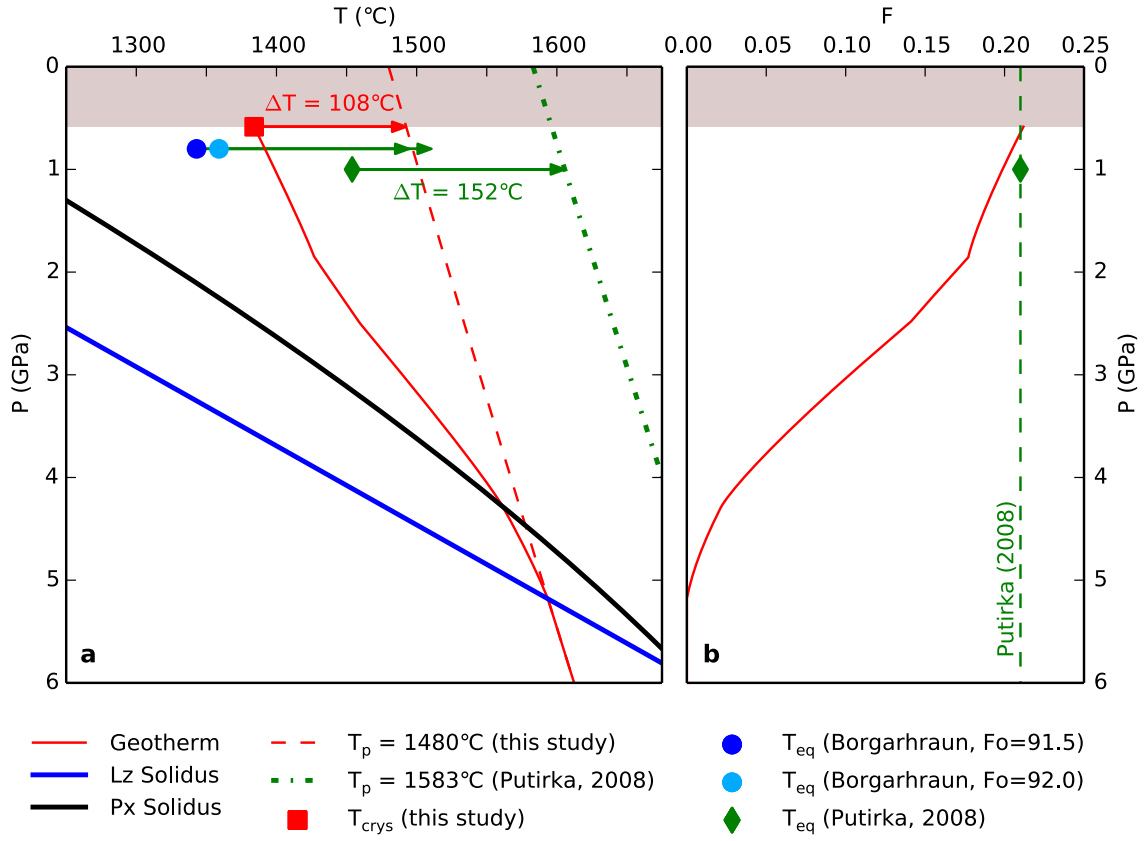

Figure 3.7: Panel a shows the calculated geotherm for the best fit model for Iceland found by the inversion. The red arrow indicates the magnitude of the correction for the heat of fusion calculated. The green diamond shows the pressure and temperature of olivine-liquid equilibration calculated by Putirka (2008a) for Iceland, and the green arrow the magnitude of the heat of fusion correction he applies. The blue circles indicate olivine-liquid Mg-Fe equilibration conditions calculated in this study for Borgarhraun; the green arrows connecting to them show the same heat of fusion correction as Putirka (2008a). Panel b shows the melt fraction calculated along the best fit geotherm, and that calculated by Putirka (2008a) for Iceland. Shading indicates the crustal thickness.

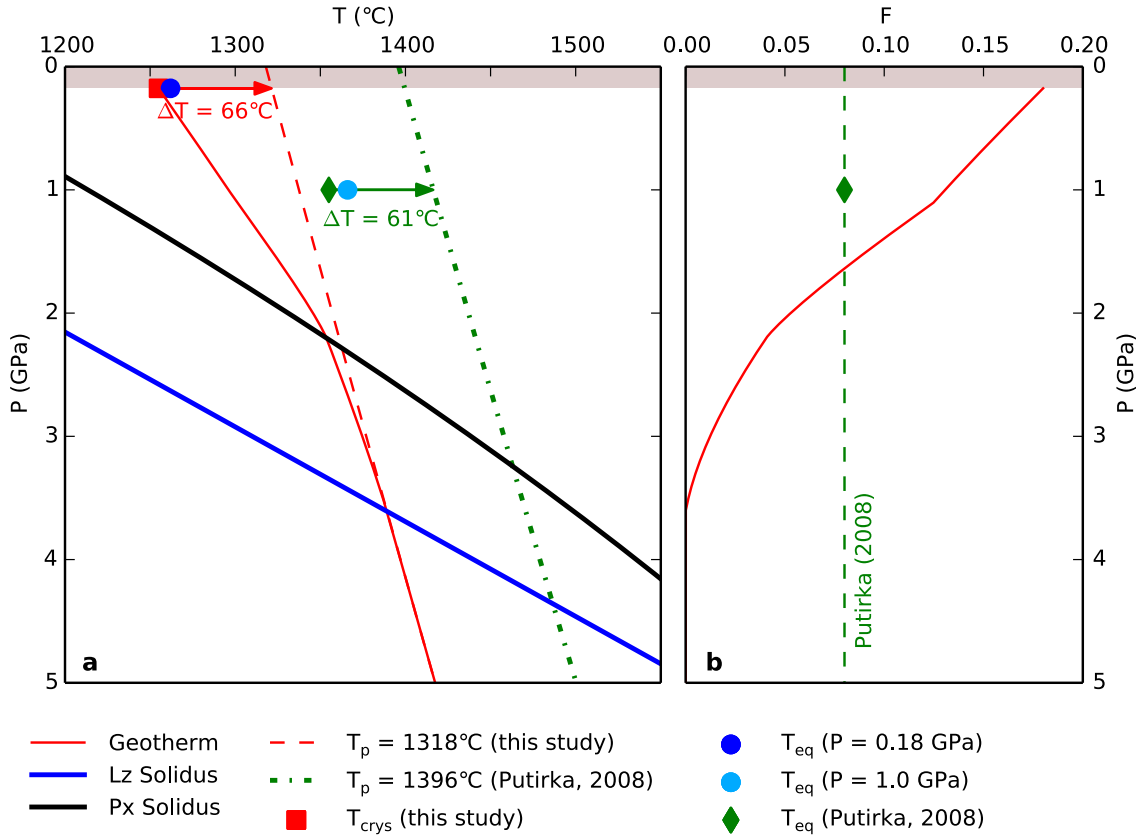

Figure 3.8: Panel a shows the calculated geotherm for the best fit model for Siqueiros found by the inversion. The red arrow indicates the magnitude of the correction for the heat of fusion calculated. The green diamond shows the pressure and temperature of olivine-liquid equilibration calculated by Putirka (2008a) for Siqueiros, and the green arrow the magnitude of the heat of fusion correction he applies. The blue circles indicate olivine-liquid Mg-Fe equilibration conditions calculated in this study for Siqueiros using the primary melt composition inferred by Putirka (2008a), with olivine added until it is in equilibrium with $Fo_{91.5}$ olivine at the pressure of interest. Panel b shows the melt fraction calculated along the best fit geotherm, and that calculated by Putirka (2008a) for Siqueiros. Shading indicates the crustal thickness.

3.2.1 Effects of Melting and Melt Transport on Olivine Saturation Temperature

Mantle of a single T_p will melt over a range of temperature as the mantle is cooled by latent heat of fusion and adiabatic expansion. The highest melting temperatures will occur at the onset of melting, and the lowest at the top of the melting column where the mantle has undergone the most melt extraction, as shown in Figure 3.4a. Without reconstructing the chemistry of the magmas parental to the olivine and spinel crystals, the depth at which they were generated, and therefore the magnitude of the correction required for the latent heat of melting, is uncertain. I therefore consider two end-member cases: melts formed at the base of the melting region, and those formed at the top of the melting region.

Once a melt has been generated it ascends through the mantle by diffuse or channelised flow, at a greater speed than the solid matrix (McKenzie, 1984; Spiegelman and Kelemen, 2003). As soon as the magma leaves its source it will be out of thermal and chemical equilibrium. The magma is in chemical disequilibrium because the equilibrium magma composition depends on temperature, pressure and matrix composition, all of which have changed. Higher up in the melting region, more sensible heat has been converted to the latent heat of fusion, and the matrix will thus be cooler than the melts generated beneath it. The extent to which equilibrium can be re-established depends upon the timescale of heat diffusion (for thermal equilibrium) and mass transfer (for chemical disequilibrium). If, by thermally re-equilibrating, the magma becomes over- or under-saturated in olivine, additional chemical disequilibrium is generated. In order for olivine saturation to be re-established the melt must gain or lose MgO and FeO by precipitating or dissolving olivine. The melt may also be out of chemical equilibrium if its Mg# is not in equilibrium with the Mg# of the matrix. Since the Mg# does not uniquely determine the temperature at which olivine is saturated in the melt (Roeder and Emslie, 1970), this component of chemical equilibrium is not considered further here.

The MgO and FeO contents of magmas derived from an upwelling column of mantle vary with depth, therefore the temperature at which the magma will saturate in olivine in a magma chamber at the base of the crust must also vary. Putirka (2008b), after Helz and Thornber (1987), parametrized the temperature of olivine saturation with pressure and melt composition. The relationship between olivine saturation temperature and pressure can be described by the olivine saturation curve, equivalent to the liquidus of a magma when olivine is the first phase to saturate. Since the temperature of olivine saturation depends on magma composition, different fractional melts will have their own olivine saturation curve. The composition of the magma parental to the olivine crystals is unknown, but since the magma is saturated in olivine when it forms, one point of the olivine saturation curve must be the pressure and temperature of magma formation. By making the curve intersect the pressure and temperature of magma formation, the compositional dependence of the olivine saturation curve is accounted for. The remaining term is the pressure dependence, which can be used to extrapolate the curve to low pressure. This process is shown schematically by the dashed lines in Figure 3.4b. If

melts arrive at a higher temperature than the saturation temperature (and have not re-equilibrated by dissolving olivine from the matrix) they may need to undergo cooling before olivine saturation. If melts arrive at a lower temperature than their predicted saturation temperature, either the MgO and FeO concentrations will have re-equilibrated at this temperature by precipitating olivine, or they will be supercooled and the first olivine to crystallise will do so at the melt's arrival temperature. Since the shallow melt end-member (Figure 3.4b) represents melt derived at the temperature of the matrix at the top of the melting region, melts cannot become supercooled below this temperature during transport. The two end-member bounds therefore define the range of possible olivine saturation temperatures; any re-equilibration during transport will shift the saturation temperature between these bounds.

If some amount of disequilibrium prevails during melt transport it is possible for the same olivine saturation temperature to be produced by mantle regions of different T_p. The partial re-equilibration process therefore introduces uncertainty in relating crystallisation temperature to mantle potential temperature. Although it is likely that the magmas will undergo some amount of re-equilibration during their ascent, this cannot be quantified without making further assumptions. By taking the saturation temperatures of the deepest and shallowest melts (assuming complete disequilibrium) as bounds, the uncertainty introduced by partial re-equilibration during transport can be included in the T_p estimates. The shallowest melt production, and therefore the top of the melting region, is assumed to coincide with the base of the crust, calculated from the melting model using Eq. (6) of White et al. (1992).

When modelling olivine saturation temperatures, an estimate of the crystallisation pressure is required. Pressure estimates for crystallisation derived from clinopyroxene-melt equilibria in Borgarhraun lava flows by Winpenny and Maclennan (2011) indicate crystallisation of primitive melts takes place at a mean pressure of 8.1 kbar, near or below the Moho. In the models presented here, the magma chamber is placed at the base of the crust, as calculated from the melting model. In consequence, the olivine saturation temperature for the shallow-melt end-member is equal to the matrix temperature at the top of the melting region.

3.2.2 Effects of Lithological Heterogeneity on the Thermal Structure of the Melting Region

The diversity in Pb-isotope ratios observed in melt inclusions from single Icelandic eruptions (Maclennan, 2008b) indicates that the Icelandic mantle hosts high-amplitude chemical variability within single melting regions. This isotopic heterogeneity is likely to map onto lithological heterogeneity in the Icelandic mantle (Chauvel and Hémond, 2000; Shorttle and Maclennan, 2011).

The presence of pyroxenitic components in the Icelandic mantle has been inferred using a variety of trace element, isotopic and major element tracers (Chauvel and Hémond, 2000; Kokfelt et al., 2006; Shorttle and Maclennan, 2011; Sobolev et al., 2008; Stracke et al., 2003a). In contrast, Herzberg et al. (2016) argue for a pyroxenite-free mantle below Iceland on the basis of low olivine Ni concentrations from three eruptions in Theistareykir. However, the discrepancy between Shorttle et al. (2014) and Herzberg et al. (2016) can be reconciled by the fact that chemically variable melts are supplied to the crust, representing different contributions from pyroxenitic and lherzolitic lithologies. The three eruptions studied in Herzberg et al. (2016) are all depleted (Nb/Zr $\leq$ 0.06), and are in the population identified by Shorttle and Maclennan (2011); Shorttle et al. (2014) as representing partial melts of lherzolite. These samples therefore do not represent the enriched components present in other Icelandic neovolcanic zone eruptions, such as Gaesafjöll and Stapafell, the major element and olivine minor element chemistry of which Shorttle and Maclennan (2011) showed to be consistent with partial melting of a KG1-like lithology. Although the highest crystallisation temperatures observed are from a geochemically depleted eruption in Theistareykir, and therefore have little contribution from a pyroxenite source, pyroxenite must still be considered as its presence in the melting region will influence the thermal structure of the melting region.

Shorttle et al. (2014) additionally argue the Iceland plume must contain a significant quantity of harzburgite in order to reconcile the volume and the chemistry of Icelandic volcanism with estimates of the plume volume flux (Jones et al., 2014b). Whilst Brown and Lesher (2014) show that crustal thickness and Nd-isotope observations, from both central and coastal Iceland, can be reconciled with a lherzolite-pyroxenite mantle, they do not consider the additional constraint of matching plume volume flux (Jones et al., 2014b) and therefore do not find a requirement for harzburgite components as Shorttle et al. (2014) do. As I discuss in Section 3.2.3, I do not consider plume buoyancy or volume flux here, but do allow the fraction of harzburgite to vary from 0% in the models.

Lithological heterogeneity exerts a control on both magma chemistry and the thermal evolution of the mantle during decompression melting (Phipps Morgan, 2001; Sleep, 1984; Stolper and Asimow, 2007). To incorporate the effect that lithological heterogeneity will have on possible crystallisation temperatures, I model the end-member scenario of a mechanical mixture of fusible and refractory components within lherzolite, using the model described by Shorttle et al. (2014). I use the Katz et al. (2003) parameterization of KLB-1-like lherzolite melting, the Pertermann and Hirschmann (2003) G2 pyroxenite parameterization for pyroxenite melting, and assume harzburgite does not melt, following Shorttle et al. (2014). A comprehensive description of the melting model is given by Phipps Morgan (2001) and Shorttle et al. (2014). In Section 3.2.7 I discuss using a KG1 pyroxenite parametrization (Shorttle et al., 2014) in place of the G2 pyroxenite. Complete thermal equilibrium between the solid components is assumed. Since the thermodynamic properties of each of the sources are poorly constrained, they are all set to the values given by Katz et al. (2003).

3.2.3 Effects of Mantle Flow Field on the Melting Region

In order to account for the thickness (38–40 km, Darbyshire et al. (1998)) and composition of the crust in central Iceland, a mantle flow field with a substantial component of plume-driven upwelling is required. However, the thickness (20–21 km, Darbyshire et al. (2000)) and composition of the crust at Theistareykir, near the northern coast of Iceland, are consistent with passive plate-driven upwelling (Maclennan et al., 2001a). Since the crystallisation temperature dataset presented here shows no significant temperature offset with along-axis distance, and the highest temperature crystals are from the northern part of the Northern Volcanic Zone, I do not consider the effects of plume-driven upwelling further.

3.2.4 Forward Model of Mantle Melting

The behaviour of the model for mantle containing lherzolite and pyroxenite in mass proportions of $\phi_{\mathrm{Lz}} = 70\%$ and $\phi_{\mathrm{Px}} = 30\%$, is illustrated in Figure 3.5. End-member melts generated at the point of initial solidus intersection for each lithology, and at the top of the melting region are considered. Increasing the mantle potential temperature causes the olivine saturation temperature of each end-member melt to rise, since both melts are then generated at higher temperatures. Olivine saturation temperatures at the base of the crust are calculated using the olivine saturation curves described in Section 3.2.1. For each T_p, a range of crystallisation temperatures is calculated, corresponding to the diversity of fractional melts generated. Increasing the mantle potential temperature also increases the range of olivine saturation temperatures of primary melts. The deepest melts are produced deeper and at a higher temperature, and more cooling occurs due to the longer melting interval, thereby reducing the temperature of the shallowest melts. In a $\phi_{\mathrm{Lz}} = 70\%$ and $\phi_{\mathrm{Px}} = 30\%$ mantle, a T_{crys} =1300 °C crystallisation temperature would be consistent with a mantle T_p of 1350–1470 °C. The low T_p bound assumes the melt parental to the crystals is derived from the base of the melting region, and therefore requires zero latent heat of fusion correction. The high T_p bound assumes derivation of the melt from the top of the melting region, requiring the maximum latent heat of fusion correction.

The effect of varying mantle lithology proportions, whilst maintaining a fixed T_p, is shown in Figure 3.6. As ϕ_{Px} rises, the range in T_{crys} increases dramatically. The decrease in temperature of the lower T_{crys} surface (blue-green in Figure 3.6) arises from the greater productivity of pyroxenite relative to lherzolite resulting in a greater total melt fraction and therefore more sensible heat consumption during melting. The increase in T_{crys} of the upper surface (red-yellow in Figure 3.6) originates from melts pooling at the base of a thicker crust; the temperature of melt formation is unchanged since it is controlled by the pyroxenite solidus. Since the olivine saturation curve has a positive gradient

in pressure-temperature space, a melt of a given composition will saturate in olivine at a higher temperature at greater pressure.

As harzburgite fraction ϕ_{Hz} increases, Figure 3.6 shows an initial contraction, followed by expansion, of T_{crys} range. Increasing ϕ_{Hz} causes the proportion of melting lithologies to decrease: less melt is produced and less thermal energy consumed. Melts are therefore produced over a narrower temperature range. Where the temperature at the top of the melting region becomes greater than the temperature of olivine saturation in deeply derived melts at high ϕ_{Hz} in Figure 3.6, the range in T_{crys} begins increasing again. When ϕ_{Hz} is sufficiently high, the geotherm (blue line in Figure 3.6) becomes very close to the solid adiabat (green dashed line in Figure 3.4). Since the olivine saturation curve has a shallower gradient than the solid adiabat in pressure-temperature space (Figure 3.4), shallower melts will now crystallise at higher temperatures than deep melts. The inversion results discussed in Section 3.2.5 do not result in high ϕ_{Hz} solutions, it is therefore valid to equate the two surfaces with shallow and deep melts in the context of these results. A similar effect is seen for small values of ϕ_{Px}. In the pyroxenite-only melting region, the geotherm may remain very close to the solid adiabat until lherzolite melting begins. This is shown by the crossing green and red dashed lines on Figure 3.6a.

3.2.5 Inverting for T_p

The forward model (Section 3.2.4) shows that varying mantle lithology can cause crystallisation of primitive mantle melts over a temperature range of over 200 °C, even at constant mantle T_p. Differences in crystallisation temperatures of primary melts between two locations could therefore be explained by a variable mantle lithology or processes of melt extraction (i.e. how biased towards deep or shallow melt production the crystallisation temperatures are), rather than by T_p variations.

The simplest case is to assume a lherzolitic ($\phi_{\mathrm{Lz}} = 100\%$) mantle. The Fo_{91} crystals from Iceland (outlined in yellow in Figure 3.1) have a mean T_{crys} of 1385 °C, which the inverse model shows is consistent with a T_p of 1430–1520 °C (lower left corner of Figure 3.9). For the Siqueiros Fracture Zone (MORB) the four highest T_{crys} points in the Coogan et al. (2014) dataset have a mean of 1253 °C, which the inverse model shows is consistent with a T_p of 1270–1350 °C. The range in consistent T_p arises from uncertainty in which fractional melt is parental to the high- T_{crys} olivine. Allowing the proportions of each lithology to vary between 0–100% results in the Iceland T_{crys} data being matched by a mantle T_p as low as 1385 °C, if the mantle is harzburgitic, and in excess of 1550 °C if the mantle is dominated by pyroxenite (Figure 3.9). The minimum bound (Figure 3.9b) on inferred mantle T_p shows very little variation with lithology, since as long as fusible pyroxenite is present this bound is controlled by the position of the pyroxenite solidus. The small variation in minimum inferred mantle T_p arises from the varying crustal thickness as the bulk mantle productivity changes, except at high ϕ_{Hz} where it instead corresponds to shallow melts as discussed in Section 3.2.4 and Figure 3.6. The

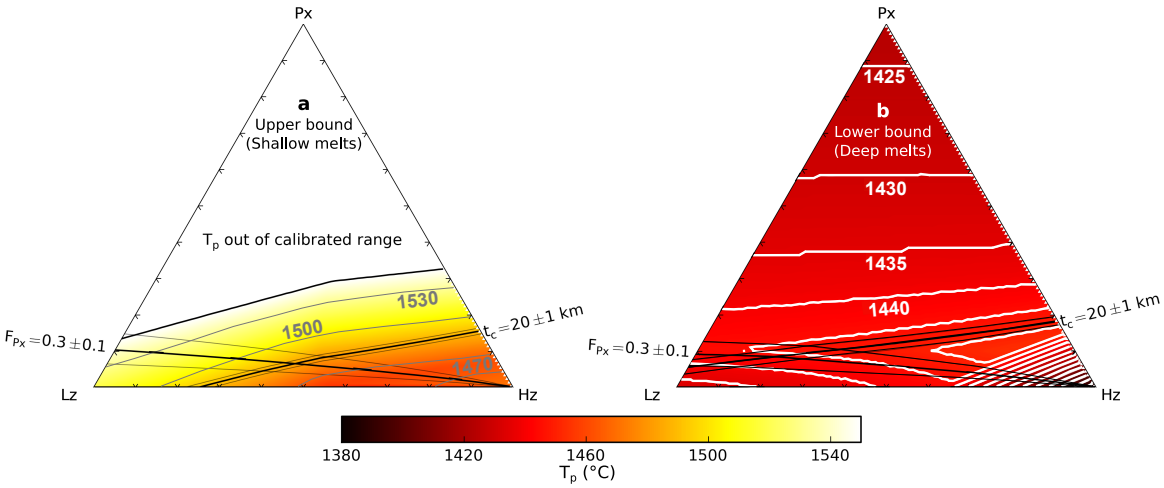

Figure 3.9: Upper (a) and lower (b) bounds on mantle T_p as a function of mantle lithology, inferred from a crystallisation temperature of 1385°C. The upper bound (a) corresponds to shallow melts and the lower bound (b) to deep melts, apart from at high ϕ_{Hz} as shown in Figure 3.6. White contours are T_p in °C. Also shown are lines for $t_c = 20 \pm 1$ km and $F_{\mathrm{Px}} = 0.3 \pm 0.1$. At the highest T_p the melting pressure and temperature are far beyond the conditions at which the melting model is calibrated.

maximum bound on inferred mantle T_p is much more sensitive to lithology; since it corresponds to the shallowest melts (except at high ϕ_{Hz}) it is primarily controlled by the geothermal gradient in the melting region, which itself is strongly controlled by the bulk mantle productivity. Allowing lithology to vary for the inversion of the Siqueiros data shows T_{crys} can be matched by mantle T_p of . By varying mantle lithology it is possible to match the observed variation in primary melt T_{crys} between Siqueiros and Iceland with the same mantle T_p.

The very lowest mantle T_p estimates arise from 100% harzburgitic mantle, i.e. mantle that has undergone no melting and so has followed the solid adiabat to the surface. This solution clearly does not match the 20 km crustal thickness observed at Iceland's coasts (Darbyshire et al., 2000), or the substantial contribution of lherzolitic and pyroxenitic sources to the chemistry of erupted basalt (Shorttle and Maclennan, 2011). Equally, the 100% pyroxenite mantle which results in the highest temperature estimates must produce thick crust to be consistent with the observed T_{crys}, and cannot explain the contribution of lherzolitic melts to basalt chemistry (Shorttle and Maclennan, 2011), nor be reconciled with plume buoyancy (Shorttle et al., 2014). There is in consequence a subset of solutions that are consistent with all observational constraints. The inversion process uses three observations: crystallisation temperature, T_{crys}, crustal thickness, t_c, and the proportion of bulk crust derived from pyroxenitic melts, F_{Px}, to invert for three variables in the model: mantle T_p, ϕ_{Px} and ϕ_{Hz}, where $\phi_{\mathrm{Lz}} = 1 - \phi_{\mathrm{Px}} - \phi_{\mathrm{Hz}}$.

The combination of the t_c and F_{Px} constraints with T_{crys} is illustrated in Figure 3.9; two points in lithology-T_p space, one for each of the low and high T_p bounds, can be identified that satisfy all three

Table 3.4: Input parameters and their source for the Iceland and Siqueiros model inversions. Uncertainties are one standard deviation. [a] Distribution of values from Monte Carlo thermometer error propagation, mean quoted here.

Parameter	Value	Source
Iceland		
t_c	20 ± 1 km	Darbyshire et al. (2000)
F_{Px}	0.3 ± 0.1	Shorttle et al. (2014)
T_{crys}	1385 °C	This study[a]
Siqueiros		
t_c	5.74 ± 0.27 km	Aghaei et al. (2014)
F_{Px}	0.175 ± 0.100	Hirschmann and Stolper (1996)
T_{crys}	1253 ± 25 °C	Coogan et al. (2014)

constraints. The values of the input parameters, and their sources, are given in Table 3.4. Since the highest crystallisation temperatures and most forsteritic olivines in the Coogan et al. (2014) MORB dataset are from the Siqueiros Fracture Zone, inversion parameters were chosen for Siqueiros, and are shown in Table 3.4. A Monte Carlo method (using 10^6 calculations) was used for the inversions, where values for F_{Px}, t_c and, for Siqueiros, T_{crys} were selected with a probability defined by a Gaussian distribution. The mean Siqueiros T_{crys} value was taken as the mean of the four highest T_{crys} points. For Iceland, T_{crys} was selected at random from the distributions of T_{crys} estimates derived from the Monte Carlo error propagation of the thermometer; only the results from the four highest T_{crys} crystals were used. The input distributions are shown in Figures 3.10 (Iceland) and 3.11 (Siqueiros), panels d, e and f, as black lines.

3.2.6 Inversion Results

The results of the inversion for Iceland are shown in Figure 3.10 and for MORB in Figure 3.11. In each case the results of the inversion (T_p, ϕ_{Px} and ϕ_{Hz}) are shown alongside the distributions of input parameters for which solutions were found. Medians and 95% confidence limits are given in Table 3.5. For each setting, two sets of solutions are found, one for the upper T_p bound arising from the cooler shallow melts (Figure 3.9a), and one for the lower T_p bound arising from the deeper hotter melts (Figure 3.9b).

For Iceland, solutions were found for all values of t_c and F_{Px} for both bounds, and for all T_{crys} values for the high T_p (shallow melts) bound. For the low T_p (deep melts) bound no solutions were found for the lowest values of T_{crys}. As T_{crys} decreases the solution T_p must decrease and ϕ_{Px} must increase in order to match observed t_c. The combination of lower T_p and higher ϕ_{Px} is not compatible with the F_{Px} constraint. This effect is seen only for the solutions for the low T_p (deep melts) bound in

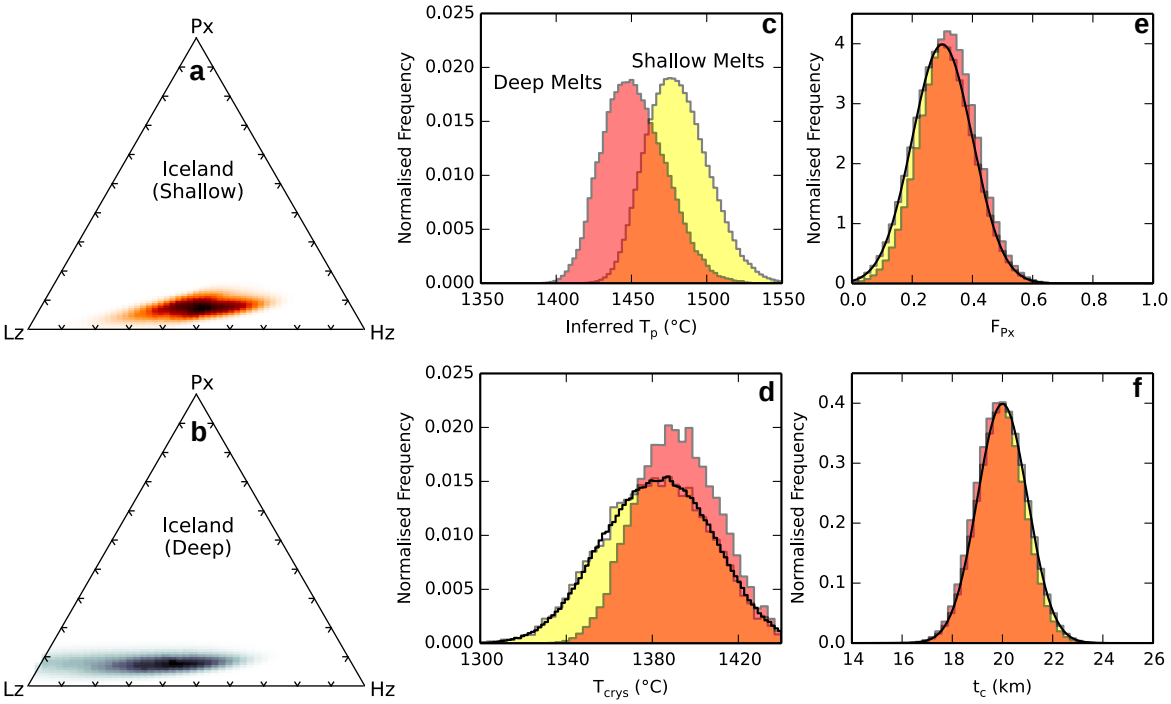

Figure 3.10: Results from inverting the melting model using observations from Iceland. Two solutions are shown, corresponding to the two end-member cases: highest and lowest T_{crys} for a given T_p, assuming a shallow and deep melt origin respectively. Panels a and b show the mantle lithologies (expressed as ϕ_{Px} and ϕ_{Hz}) consistent with the observations. Similarly panel c shows the consistent T_p distributions. The black lines in panels d, e and f show the input distributions of T_{crys}, F_{Px} and t_c. The filled histograms show the values of each parameter for which solutions were found.

Iceland because the solutions for the high T_p (shallow melt) bound have been generated with a higher T_p melting model.

For Siquieros, solutions for the lowest T_{crys} values do not exist for either deep or shallow melts, though this is most pronounced for deep melts. Since the inferred T_p for a given T_{crys} is always lower for the deep melt case, the value of T_p for which 5.7 km of crust can no longer be produced whilst maintaining F_{Px} occurs at a higher T_{crys} for such melts.

The results of the inversion for Iceland and Siqueiros (MORB) are compared in Figure 3.12. When T_{crys}, t_c and F_{Px} constraints are combined, a significantly higher mantle T_p is required to explain the enhanced crustal thickness and higher crystallisation temperatures for Iceland compared to Siqueiros. Since no combination of the solutions from high T_p and low T_p bounds allow the same mantle T_p in both the Siqueiros mantle and Icelandic mantle, variation in the depth from which the melts parental to the high T_{crys} are derived cannot explain the difference in T_{crys} between Siqueiros and Iceland. Though different proportions of lherzolite, pyroxenite and harzburgite are required to fit the observations, variation in lithology alone cannot reproduce the observations. The T_p values inferred from the

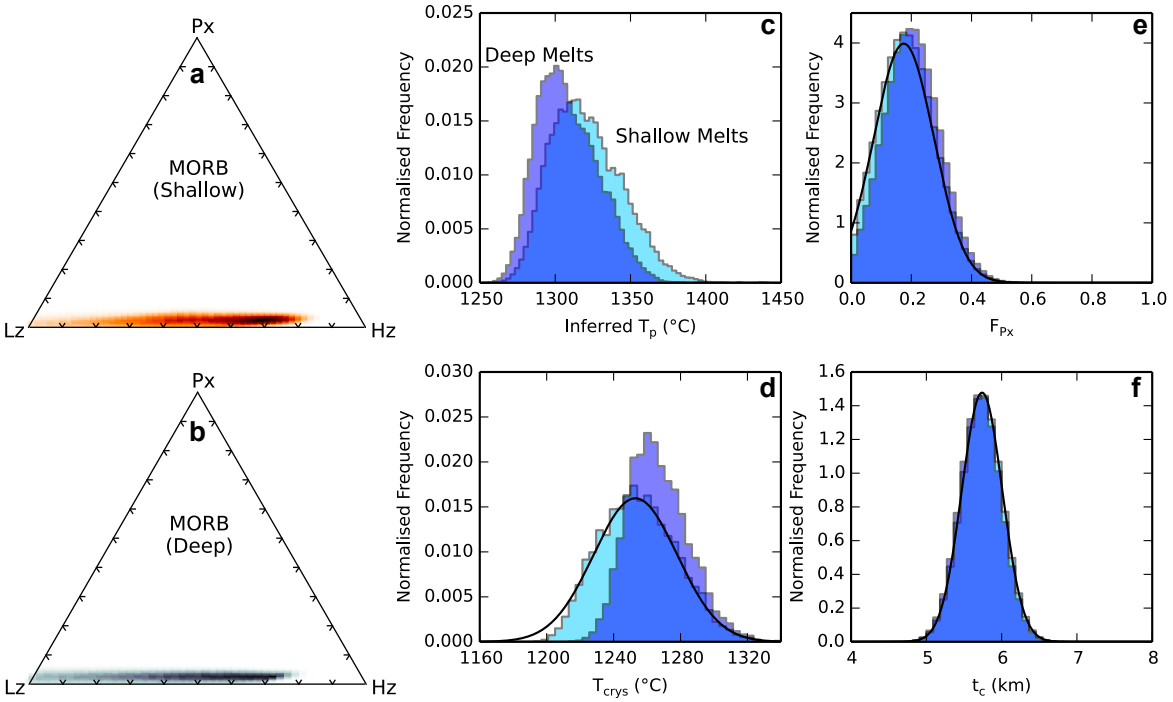

Figure 3.11: Results from inverting the melting model using observations from Siqueiros. Two solutions are shown, corresponding to the two end-member cases: highest and lowest T_{crys} for a given T_p, assuming a shallow and deep melt origin respectively. Panels a and b show the mantle lithologies (expressed as ϕ_{Px} and ϕ_{Hz}) consistent with the observations. Similarly panel c shows the consistent T_p distributions. The black lines in panels d, e and f show the input distributions of T_{crys}, F_{Px} and t_c. The filled histograms show the values of each parameter for which solutions were found.

inversions are consistent with estimates based on REE inversions (Maclennan et al., 2001a; McKenzie and O'Nions, 1991) and major element chemistry (Herzberg and Asimow, 2015). Though the offset in T_p of MORB and Iceland obtained from the inversion is a similar magnitude to the offset in T_p estimated by Putirka (2008a, 2016), the absolute T_p estimates calculate here are $\sim$100 °C lower.

Results of the same inversion routine, but based on a forward model calculated using a KG1 pyroxenite melting parametrization (Kogiso et al., 1998; Shorttle et al., 2014) in place of the G2 pyroxenite parametrization, are reported and discussed in Section 3.2.7. Using a KG1 pyroxenite results in lower estimates of ϕ_{Hz}, but has only a minor effect on estimated T_p.

3.2.7 Results from KG1 inversion

Shorttle and Maclennan (2011) estimated the major element composition of the enriched end-member melt in Iceland, and found it to be very close to the composition of experimental melts of KG1 pyroxenite (Kogiso et al., 1998). A parametrization of the melting behaviour of KG1 was provided by

	T_p (°C)	ϕ_{Px}	ϕ_{Hz}
Iceland (Shallow)	1480^{+37}_{-30}	$0.08^{+0.04}_{-0.04}$	$0.47^{+0.16}_{-0.19}$
Iceland (Deep)	1451^{+37}_{-30}	$0.08^{+0.04}_{-0.04}$	$0.35^{+0.22}_{-0.29}$
Siqueiros (Shallow)	1318^{+44}_{-32}	$0.03^{+0.02}_{-0.02}$	$0.54^{+0.21}_{-0.39}$
Siqueiros (Deep)	1306^{+39}_{-27}	$0.03^{+0.02}_{-0.02}$	$0.45^{+0.26}_{-0.28}$

Table 3.5: Results from the inversion (using G2 pyroxenite) for Iceland and Siqueiros, for both deep and shallow melt end-members. Medians and 95% confidence limits are reported.

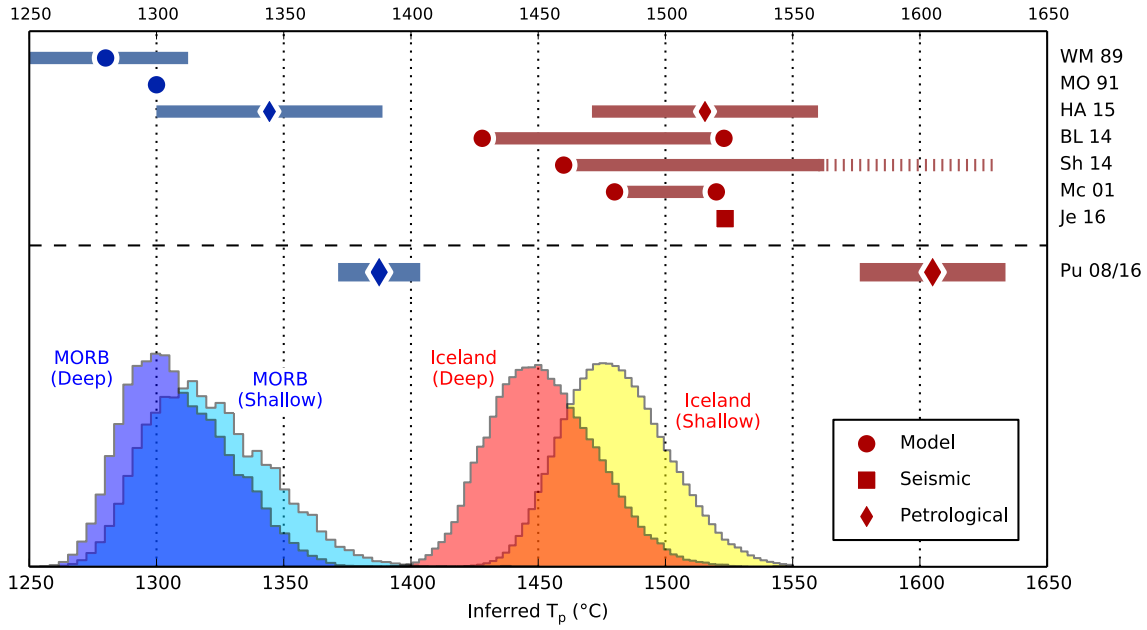

Figure 3.12: Comparison of previous T_p estimates for mid-ocean ridges (blue) and Iceland (orange/yellow), with the results of the T_p inversions presented here as histograms in the lower half of the figure. Estimates of T_p derived from olivine-liquid equilibration temperatures by Putirka (2016, 2008b) (Pu 08/16) are shown below the dashed line. The two inversion results for each setting are from the two end-member cases: maximum and minimum T_{crys} for a given T_p, corresponding to melts sourced from deep and shallow within the melting region respectively. Jenkins et al. (2016) (JE 16) estimate a ΔT_p of 210 °C, shown here relative to the median T_p from the MORB inversion. Shorttle et al. (2014) (Sh 14) report a minimum bound, represented by the point and dashed line. The other literature estimates are BL14: Brown and Lesher (2014), HA 15: Herzberg and Asimow (2015), Mc 01: Maclennan et al. (2001a), MO 91: McKenzie and O'Nions (1991) and WM 89: White and McKenzie (1989). Where there are two symbols a range of estimates is reported; single symbols and bars indicate a single estimate and its reported uncertainty.

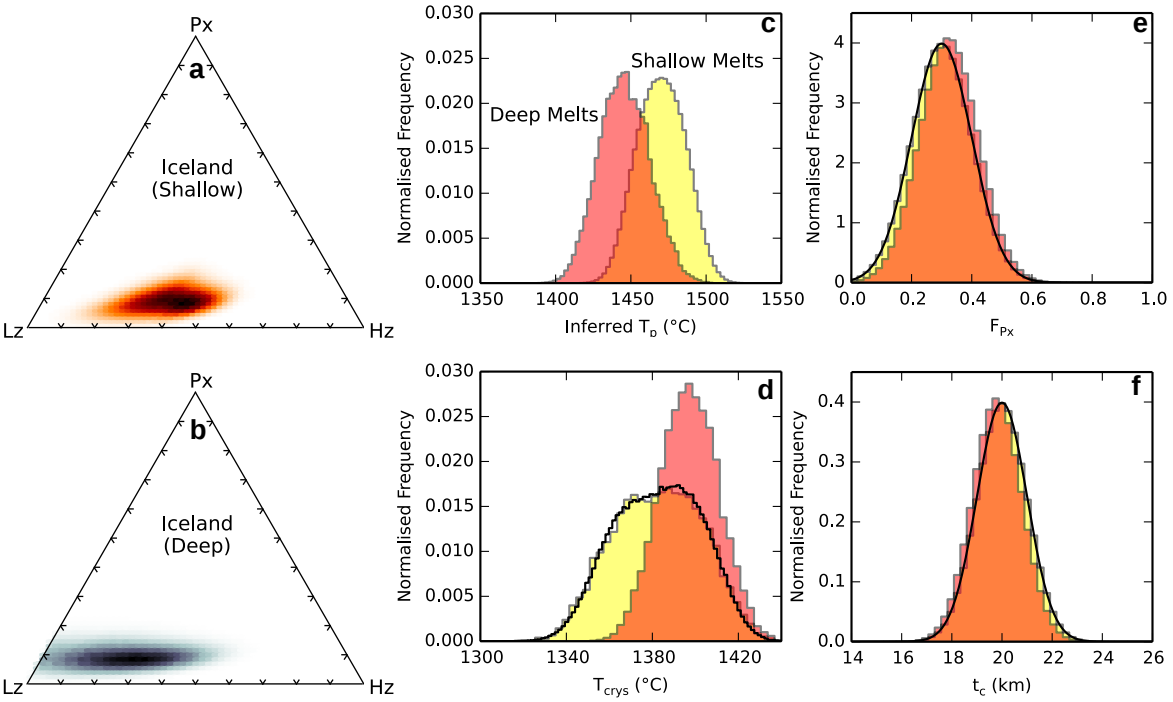

Figure 3.13: Results from inverting the KG1 Pyroxenite melting model using observations from Iceland. Two solutions are shown, corresponding to the two end-member cases: highest and lowest T_{crys} for a given T_p, assuming a shallow and deep melt origin respectively. Panels a and b show the mantle lithologies (expressed as ϕ_{Px} and ϕ_{Hz}) consistent with the observations. Similarly panel c shows the consistent T_p distributions. The black lines in panels d, e and f show the input distributions of T_{crys}, F_{Px} and t_c. The filled histograms show the values of each parameter for which solutions were found.

Shorttle et al. (2014) and can be implemented in place of G2 pyroxenite (Pertermann and Hirschmann, 2003) in the melting model presented here. The two models differ in the position of their solidii (KG1 melts at higher temperature), and their productivity (KG1 is less productive). The G2 pyroxenite therefore represents a good end-member for the behaviour of pyroxenite; it melts at a much lower temperature and is extremely productive compared to KLB-1-like lherzolite.

Results of the inversion for Iceland and Siqueiros are given in Table 3.6 and shown in Figures 3.13 and 3.14, respectively. For the low T_p (deep melts) bound of the Iceland inversion no solutions were found for the lowest values of T_{crys}, similar to the G2 Model inversion. For Siqueiros solutions for the lowest T_{crys} values do not exist for either deep or shallow melts, though this is most pronounced for deep melts. The same effect is seen in the G2 inversion results. The distributions of T_p estimate are very similar to those calculated by inverting the melting model containing G2 pyroxenite (Figures 3.10 and 3.11). A bigger difference is seen in the estimates of ϕ_{Hz} which are considerably lower. A decrease in ϕ_{Hz} results in a less refractory bulk mantle, harzburgite fraction trades off against pyroxenite fusibility.

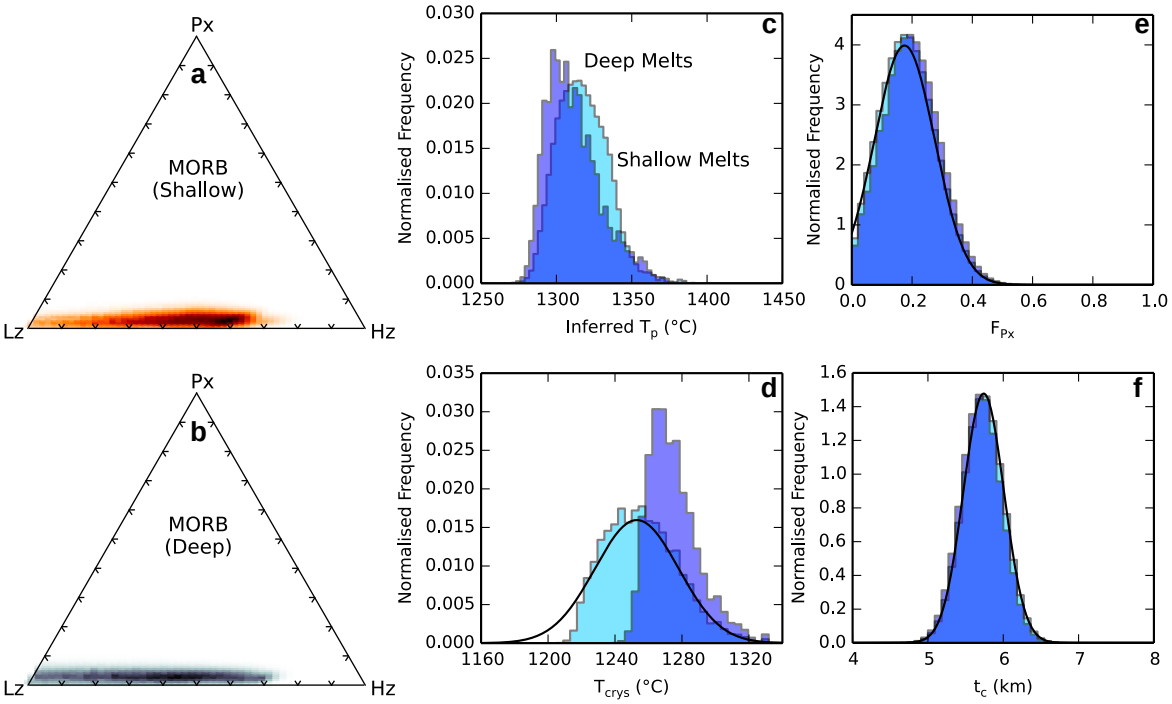

Figure 3.14: Results from inverting the KG1 Pyroxenite melting model using observations from Siqueiros. Two solutions are shown, corresponding to the two end-member cases: highest and lowest T_{crys} for a given T_p, assuming a shallow and deep melt origin respectively. Panels a and b show the mantle lithologies (expressed as ϕ_{Px} and ϕ_{Hz}) consistent with the observations. Similarly panel c shows the consistent T_p distributions. The black lines in panels d, e and f show the input distributions of T_{crys}, F_{Px} and t_c. The filled histograms show the values of each parameter for which solutions were found.

	T_p (°C)	ϕ_{Px}	ϕ_{Hz}
Iceland (Shallow)	1470^{+32}_{-29}	$0.09^{+0.06}_{-0.05}$	$0.38^{+0.15}_{-0.19}$
Iceland (Deep)	1448^{+40}_{-28}	$0.09^{+0.06}_{-0.05}$	$0.26^{+0.24}_{-0.22}$
Siqueiros (Shallow)	1316^{+29}_{-24}	$0.03^{+0.03}_{-0.02}$	$0.44^{+0.20}_{-0.34}$
Siqueiros (Deep)	1309^{+39}_{-21}	$0.03^{+0.02}_{-0.02}$	$0.36^{+0.30}_{-0.31}$

Table 3.6: Results from the inversion (using KG1 pyroxenite) for Iceland and Siqueiros, for both deep and shallow melt end-members. Medians and 95% confidence limits are reported.

Though the results of the inversion are influenced by the choice of pyroxenite lithology, the effect on estimated T_p is comparatively small. I argue, therefore, the mantle temperature estimates calculated here are robust against the uncertainty in choice of pyroxenite melting model. Less robust are the calculated lithology fractions.

3.3 Discussion

3.3.1 Olivine-Spinel Al-Exchange Thermometry

The crystallisation temperatures measured here for the Northern Volcanic Zone of Iceland are similar to the temperatures for zero-age Iceland measured by Spice et al. (2016), though the new dataset extends the observed range in olivine forsterite content and T_{crys} (Figure 3.3). The less forsteritic crystals preserve crystallisation temperatures similar to the Tertiary crystallisation temperatures of Spice et al. (2016) at the same forsterite content. The magnitude of temperature variation for these Icelandic olivines is consistent with the fractional crystallisation models shown in Figure 3.3. The olivines that lie furthest from the KR4003 line are from the same eruptions as olivines that lie directly on the line and therefore do not definitively indicate differences in mantle temperature. Instead, these offsets may arise from the presence of diverse melts in deep magma chambers, each with its own liquid line of descent. It is also possible the Mg and Fe content of the olivine has been diffusively reset during mush residence (Thomson and Maclennan, 2012), which would change the positions of crystals in forsterite-T_{crys} space. Since it is only the fast-diffusing elements Mg and Fe that are likely to have re-equilibrated in the olivine, this process would not affect Al-exchange temperatures.

The highest crystallisation temperatures presented here are from the northernmost part of the Northern Volcanic Zone, whilst those closest to the plume centre, Kistufell and Herðubreiðartögl (Shorttle et al., 2010), show lower crystallisation temperatures. Both Kistufell and Herðubreiðartögl sample a population of olivine macrocrysts with relatively low forsterite (Figure 3.2), the lower T_{crys} estimates are therefore consistent with the olivine macrocrysts being derived from a more evolved parental melt. With the available data, it is therefore not possible to resolve any variation in along-axis mantle T_p within Iceland, highlighting the dangers of interpreting offsets in distributions of crystallisation temperature.

A more reliable indicator of T_p variation is the offset in T_{crys} at fixed olivine forsterite content, as this must represent a difference in the composition of melt leaving the mantle. As discussed in Section 3.2.4, such a difference in melt composition, and therefore T_{crys}, can arise from both a difference in mantle T_p and mantle lithology. Although there is little offset in T_{crys} between the zero-age Iceland data (from this study and Spice et al. (2016)) and the Tertiary Iceland data (from Spice et al. (2016)),

secular change in the temperature of the Icelandic mantle cannot be ruled out since mantle T_p can vary without changing T_{crys} (Section 3.2.4). Instead the style of melt extraction or composition of the mantle may change to offset the change in T_p.

3.3.2 Thermal Equilibration

In calculating the forward model, thermal equilibrium is assumed in the solid matrix. Phipps Morgan (2001) and Katz and Rudge (2011) argue this is a reasonable assumption as long as the heterogeneities have a lengthscale of < 1 km. Though this is likely to be the case, considering combinations of end-member lithologies means the model can still be applied if it is not, but it will no longer be applicable to predicting properties sensitive to the bulk melting region, for example t_c and F_{Px}. Melts are likely to approach thermal equilibrium with the mantle through which they pass, and therefore the bound on T_p given by the deepest melts is likely unrealistically low. However, perturbations from the model geotherm in the melting region arising from channelisation reactions and advection of heat by rising magma could allow melts to equilibrate at higher temperatures than the modelled geotherm. Since the effects of these processes are poorly constrained, maximum possible disequilibrium is assumed, i.e. melts follow the liquid adiabat to the magma chamber. By using such conservative bounds, the uncertainty in the thermal history during melt transport can be fully propagated.

3.3.3 Melting Parameterizations

The melting behaviour of the lithological end-members must be assumed when constructing the model. In addition to G2 pyroxenite, Shorttle et al. (2014) also describe the behaviour of the melting model for a pyroxenite formed from a mixture of MORB and lherzolite, KG1 (Kogiso et al., 1998), after Shorttle and Maclennan (2011) found that melts from such a lithology provided a good fit to the chemistry of enriched basalts. The melting behaviour of these two pyroxenites differ in the position of their solidii (G2 begins melting at higher pressure) and their productivity, $\frac{dF}{dP}$, beyond the solidus (G2 is more productive). Using the G2 parametrisation over the KG1 parametrisation in the model has the effect of increasing the temperature of first melt generation (and therefore the upper crystallisation temperature bound) and increasing the melt fraction, increasing the t_c estimate and reducing the temperature in the melting region. Using the G2 melting parametrization therefore makes the T_{crys} bounds more conservative. As I showed in Section 3.2.7, the choice of pyroxenite parametrization has only a small effect on inferred T_p.

I assume the harzburgite component will not undergo melting, which may not be true; indeed the lherzolite parametrization includes an interval of melting after clinopyroxene exhaustion when the residue is harzburgitic. However, the extent of harzburgite melting will be very small, or zero for

modest ϕ_{Hz}, and will begin significantly after the onset of both lherzolite and pyroxenite melting. This assumption therefore has no effect on the high T_{crys} bound, and only a very minor effect on the position of the low T_{crys} bound and predicted t_c.

Since the melting parameterizations employed here are not necessarily realistic for the Icelandic mantle, the results of the inversion for composition must be interpreted with care. In particular, how the inferred harzburgite component should be interpreted is unclear. The effect of adding harzburgite could be replicated by changing other properties of the mantle. Since including harzburgite decreases the bulk melt productivity, a high ϕ_{Hz} may imply the lherzolite and pyroxenite components are less productive than modelled. This is borne out by the lower ϕ_{Hz} estimate resulting from using a less fusible pyroxenite model (Section 3.2.7). Incorporating the harzburgite component is not only required to satisfy plume buoyancy constraints (Shorttle et al., 2014), but it also allows the model to accommodate variations in mantle fusibility without affecting estimated T_p (though the relative fusibilities of lherzolite and pyroxenite are fixed, and control the effect of the F_{Px} constraint). Though the melting parametrizations are used to model fractional melting they are based on batch melting experiments; the addition of a harzburgite component will compensate for overestimates of melting productivity resulting from this (Stolper and Asimow, 2007).

In application of both the lherzolite and pyroxenite parameterizations, I assume that no hydrous melting takes place. When a small amount of water or carbon is present in the upwelling mantle, melting begins earlier and at higher temperature (Canil and Scarfe, 1990; Dasgupta and Hirschmann, 2006; Wyllie and Huang, 1975), resulting in an increased high T_{crys} bound. However, the effect on bulk melt production (and therefore the low T_{crys} bound and t_c estimate) is very small since only very small melt fractions are produced during this phase of volatile-present melting. These very first, highly volatile and incompatible trace element-enriched, melts have never been seen in melt inclusions and so are unlikely to move far in the mantle before reacting or mixing with other higher-volume melts (Rudge et al., 2013). Whilst the current high T_{crys} bound suffers from the same argument it is unclear where the deepest depth of equilibration should be, and so the high T_{crys} bound is rather conservative.

3.3.4 Crystallisation Depth

A depth of crystallisation must be assumed when calculating the basalt liquidus temperature. In all models presented here it is taken to be the base of the crust, as calculated from the melting model. Barometry on high-Mg# clinopyroxene crystals from wehrlite nodules in Borgarhraun by Winpenny and Maclennan (2011) indicates that erupted clinopyroxenes crystallized near or below the Moho at 20–25 km. Since the olivine crystals used in the inversion are all highly forsteritic and petrographically similar to the olivine fround in the wehrlitic nodules, they are likely to be part of this deep population. Though crystallisation depth is unconstrained for the Siqueiros olivines, the uncertainty arising from

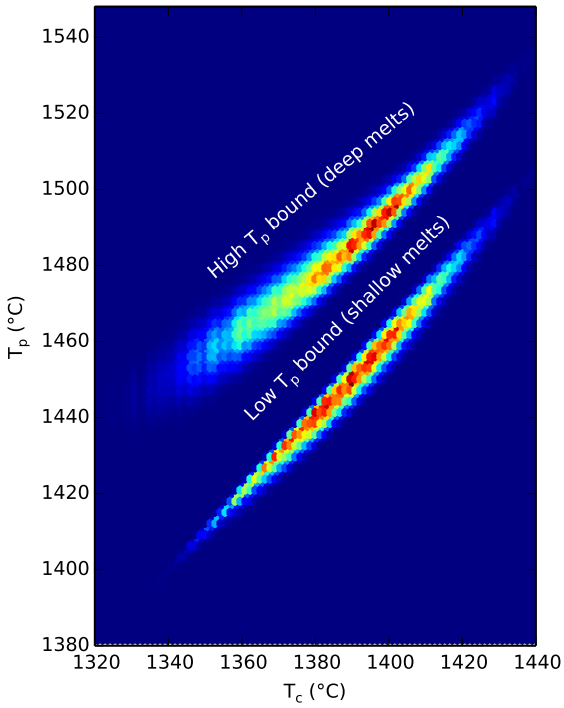

Figure 3.15: Histogram showing the relationship between T_p estimate and T_{crys} for the Iceland inversion. Both the upper and lower T_p bounds are shown. Brightness corresponds to density of results.

crystallisation depth (less than 10°C for Borgarhraun) is much smaller than the uncertainty in the thermometer calibration and the uncertainty in the thermal history of the melt.

3.3.5 Inferring Mantle T_p

For a single value of T_{crys}, the model predicts a large range of consistent T_p, 170 °C for T_{crys} =1385 °C (Figure 3.9), suggesting a very large offset in primitive crystal T_{crys} is required before a difference in T_p can be robustly inferred from thermometry alone. When the range of solutions can be constrained using other parameters, t_c and F_{Px} in this case, a much narrower range in consistent T_p can be identified. Figure 3.15 shows the uncertainty in this inversion propagates mostly from the uncertainty in T_{crys} and melt source depth.

The subset of solutions consistent with the t_c and F_{Px} constraints has T_p distributions (Figure 3.12) that coincide with those estimated using other techniques and observations. Since t_c is an integral part of the inversion it is not surprising that the inversion yields similar answers to studies that have fitted melting models to t_c observations, though in general such models do not allow the source composition to vary.

Brown and Lesher (2014) do allow pyroxenite fraction to vary in their model, but do not consider the effect of harzburgite. Without a harzburgite fraction, the bulk productivity of a mantle containing

only lherzolite and pyroxenite will be greater. The greater mantle productivity, in addition to a small component of active upwelling, allows the same pyroxenite fraction and crustal thickness observations to be matched with a slightly lower T_p than both Shorttle et al. (2014) and the shallow melt solution. Brown and Lesher (2014) infer higher T_p in central Iceland in order to match the thicker crust and basalt Nd-isotope geochemistry. Their model achieves thicker crust by increasing both the melt fraction and the degree of active upwelling, both a consequence of higher mantle T_p. I do not consider crustal thickness observations from central Iceland, or active upwelling here, for the reasons set out in Section 3.2.3.

The analysis presented here shows that T_p inferred from T_{crys} estimates can be reconciled with T_p estimates derived from other observations, whereas those presented by Putirka (2005) are systematically higher. The origin of this discrepancy is discussed in Section 3.3.6.

The positions of the T_p distributions estimated for Iceland (Figure 3.12) show a small offset between the shallow and deep melt solutions; however it is the shallow melt distribution that shows the closest correspondence to other T_p estimates. This similarity suggests that the highest T_{crys} observations come from melts derived from the shallow parts of the melting region. Measurements of olivine-hosted melt inclusions from Borgarhraun (Maclennan et al., 2003b) show that the most highly-forsteritic olivines in Borgarhraun have trapped melts with exceptionally low La/Yb, also suggesting the parental melts originated shallow in the melting region. Within both the MORB and Iceland datasets there is approximately 150 °C variation in crystallisation temperature for primitive olivine crystals. As shown in Figure 3.6 this is a similar magnitude to the predicted range in crystallisation temperature for lithology combinations with moderate amounts of pyroxenite and harzburgite. However, this would imply the crystals preserving the highest T_{crys} are derived from the deepest melts, contrary to that implied by the correspondence of T_{crys} estimates and melt inclusion measurements made in highly forsteritic Borgarhraun macrocrysts.

3.3.6 Discrepancy with olivine-melt thermometry

Iceland

There exists a 100°C discrepancy between the estimated T_p for Iceland in this study and that by Putirka (2008a), despite both being based on observations of the Borgarhraun lava flow. This discrepancy arises due to an elevated estimate of olivine-liquid equilibration temperature and from the magnitude of the latent heat of melting correction used by Putirka (2008a), as illustrated in Figure 3.7.

A key parameter used in calculating the magnitude of the latent heat of melting correction is the melt fraction. The melt fraction estimated by Putirka (2008a) is similar to that estimated here (Figure 3.7b),

therefore the larger latent heat of melting correction applied by Putirka (2008a) originates from using different thermodynamic constants. However, this explains only 44 °C of the total T_p discrepancy.

The olivine-liquid equilibration temperature estimated by Putirka (2008a) relies on using a compilation of whole-rock major element data to infer the composition of melt in equilibrium with Fo_{92} olivine. The temperature dependence of Mg-Fe partitioning between olivine and melt is then used to estimate the equilibration temperature. Keiding et al. (2011) and Herzberg (2011) suggest incomplete mixing of fractional melts leads to overestimation of the FeO concentration in the magma that equilibrated with the highest forsterite olivine. Shorttle and Maclennan (2011) demonstrate such major element diversity is observed in whole-rock geochemistry in Iceland. Figure 3.16 shows chemical data from a compilation of northern Northern Volcanic Zone whole-rock analyses. La/Yb ratios are a measure of geochemical enrichment, and show a clear positive correlation with FeOt (total FeO, assuming all Fe is ferrous), as described by Shorttle and Maclennan (2011). Much of this range is seen in olivine-hosted melt inclusions found in the Borgarhraun lava flow (Maclennan et al., 2003b). The most forsteritic olivine crystals have trapped the most depleted (lowest La/Yb) melts exclusively, and their La/Yb is indicated by the vertical line on Figure 3.16a. I therefore argue that only the most FeO-poor melts are likely to have been in equilibrium with Fo_{92} olivine.

To test the effect of using an FeO-poor melt on the calculated olivine-liquid equilibration temperature I estimate the composition of the melt parental to average Borgarhraun whole rock (Maclennan et al., 2003b) by adding olivine until equilibrium with a chosen olivine composition is reached (Table 3.7). This is analogous to the regression employed by Putirka (2008a, 2016, 2005); Putirka et al. (2007). I use Eq. (4) of Putirka et al. (2007), and equilibrate with Fo_{92} olivine (after Putirka (2008a)) and $Fo_{91.5}$ olivine (the most forsteritic olivine analysed in this study). The equilibration pressure is assumed to be 0.8 GPa (after Winpenny and Maclennan, 2011), the exchange partition coefficient as 0.31 (after Putirka (2008a)), and the $Fe^{3+}/\Sigma Fe$ ratio as 0.16 (after Öskarsson et al., 1994; Shorttle et al., 2015). The resulting estimates are shown as blue circles in Figure 3.16, and are close to the Al-exchange temperature, though slightly lower. When the Putirka (2008a) latent heat of melting correction is applied a similar mantle T_p to that calculated in this study is found (Figure 3.7a).

This effect is tested further by calculating the olivine-melt equilibration temperature for each composition in the northern Northern Volcanic Zone dataset. The same methodology as applied to the Borgarhraun whole-rock composition is employed here, setting the olivine composition as Fo_{92}. The results are shown in Figure 3.16b. The vertical line on the figure shows the Al-exchange temperature for highly forsteritic olivine reported in this study, demonstrating that this method is in agreement with temperatures calculated using Mg-Fe exchange provided a melt with low FeO_t is used. The estimated temperature drop during melting from the latent heat of fusion was estimated using the method of Putirka et al. (2007), where melt fraction was calculated using his Eq. (A1). The colour

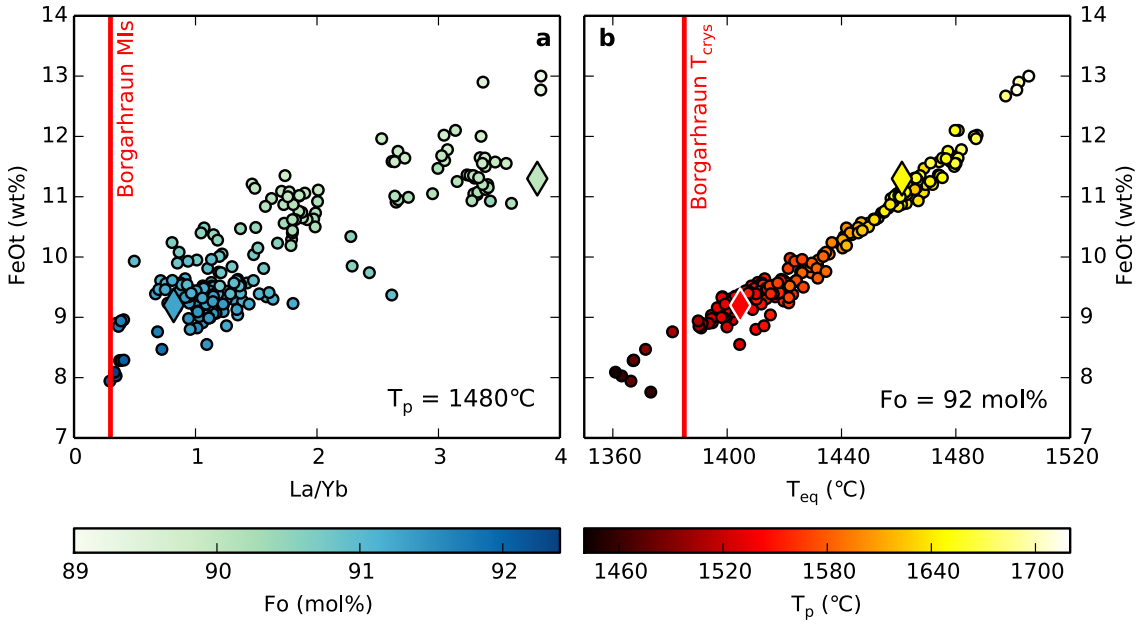

Figure 3.16: Panel a shows whole-rock chemical data for basalts with MgO >8 wt% from the northern part of the Northern Volcanic Zone of Iceland. The La/Yb ratio found in the most forsteritic melt inclusions from Borgarhraun is indicated by the vertical line. The colour indicates the olivine composition calculated to be in equilibrium with the estimated parental melt for a mantle of T_p =1480 °C. Panel b shows the calculated temperature of olivine-liquid equilibration as a function of melt composition, assuming the estimated parental melts are in equilibrium with Fo_{92} olivine at 0.8 GPa. The colors show the mantle T_p calculated using the method of Putirka et al. (2007). The vertical line indicates the crystallisation temperature estimated for Borgarhraun using olivine-spinel aluminium exchange thermometry. In both panels the diamonds indicate the depleted and enriched end-members identified by Shorttle and Maclennan (2011). Data from Hardarson et al. (1997); Hemond et al. (1993); Kokfelt et al. (2006); Maclennan et al. (2001a, 2003b); Nicholson et al. (1991); Peate et al. (2010); Sims et al. (2013); Skovgaard et al. (2001); Slater et al. (2001); Stracke et al. (2003b)

	Fo (mol%)	SiO_2	Al_2O_3	FeO	Fe_2O_3	MgO
Putirka et al. (2007)	92	47.2	12.3	7.8	1.7	18.2
Borgarhraun	91.5	48.9	14.2	7.1	1.4	13.2
Borgarhraun	92	48.7	13.9	7.1	1.4	14.2

	Fo (mol%)	TiO_2	MnO	CaO	Na_2O	K_2O
Putirka et al. (2007)	92	0.7	0.2	10.5	1.4	0.1
Borgarhraun	91.5	0.6	0.2	12.6	1.6	0.05
Borgarhraun	92	0.7	0.2	12.3	0.6	0.05

Table 3.7: Major element composition of melts (wt%) used to calculate olivine-melt Mg-Fe exchange temperatures for Iceland in this study and by Putirka et al. (2007). Compositions calculated by finding equilibrium with the olivine composition indicated, as described in the text. FeO and Fe_2O_3 reported on the basis of a $Fe^{3+}/\Sigma Fe$ of 0.16 (Öskarsson et al., 1994)

in Figure 3.16b indicates the corresponding T_p estimate, with those calculated for the lowest FeO_t compositions in agreement with my estimate.

Much of the range of whole-rock compositions from the northern Northern Volcanic Zone was found by Shorttle and Maclennan (2011) to represent mixed, but not fractionated, mantle melts. They should therefore be consistent with a single mantle T_p, but may reflect variable melt fraction and mantle olivine composition. To test this hypothesis, the required olivine composition to be consistent with a T_p =1480 °C mantle was calculated for each melt in the dataset. Olivine was added to each melt until the calculated T_p was equal to 1480 °C, with a new latent heat of melting correction calculated for the new liquid composition at each step. Fo_{92} olivine was obtained for the lowest FeO_t melts, whilst Fo_{90} was calculated for the more FeO_t rich (and trace element-enriched) melts. This is consistent with the absence of enriched (high La/Yb) melt inclusions in Borgarhraun olivines more forsteritic than Fo_{90}.

Siqueiros

A discrepancy of 80 °C exists between the Siqueiros mantle T_p inferred here and by Putirka (2008a). Figure 3.8 demonstrates how the discrepancy arises from the 100 °C difference in temperature estimate from olivine-spinel Al-exchange thermometry (Coogan et al., 2014) and olivine-melt Mg-Fe exchange thermometry (Putirka, 2008a). Coogan et al. (2014) argue this difference arises via incomplete mixing of mantle melts in much the same way as I suggest for Iceland, and was previously suggested by Keiding et al. (2011) and Herzberg (2011); however coexisting olivine and glass are in Mg#

equilibrium in Siqueiros rocks (Putirka et al., 2007). Instead, I propose the discrepancy arises from the differing assumptions about olivine-liquid and olivine-spinel equilibration pressure. In the inversions presented here the temperature recorded by the Al-exchange thermometer is assumed to represent the temperature of melts crystallising at the base of the crust, at a pressure of 0.18 GPa. In contrast, Putirka (2008a) assume an olivine-melt equilibration pressure of 1 GPa. In my calculation of mantle T_p, pressure is needed only to calculate T_p once a temperature on the solid adiabat has been estimated (except for the deep melts end-member when it is also required to estimate the liquidus temperature at low pressure, as illustrated in Figure 3.4). However, the method employed by Putirka (2008a, 2016, 2005); Putirka et al. (2007) requires an assumption about equilibration pressure to extract a temperature estimate from the olivine-liquid equilibrium, in addition to calculating T_p once a temperature on the solid adiabat has been estimated.

To test the effect of pressure assumptions on olivine-liquid Mg-Fe exchange temperature estimate, I use the method outlined above to estimate this temperature for the pressure at the base of the Siqueiros crust. Following Putirka (2008a)the melt is allowed to equilibrate with $Fo_{91.5}$ olivine by addition of olivine. Though the melt composition is inferred on the basis of $Fo_{91.5}$ equilibrium, this step ensures consistency with my choice of parameters. An olivine-liquid Mg-Fe exchange temperature of 1262°C is calculated, shown by the dark blue circle on Figure 3.8a, which is extremely close to the maximum Coogan et al. (2014) Al-exchange temperature. In order to show my choice of calculation parameters is not responsible for this different Mg-Fe exchange temperature estimate, I repeat the procedure for 1.0 GPa (light blue circle in Figure 3.8a). Though my choice of parameters does result in a small discrepancy, the effect is a bias towards higher equilibration temperature estimates. I argue 0.18 GPa is a more appropriate choice for the pressure of melt-liquid equilibration, assuming either equilibration during crystallisation or during mantle melting/transport. Though one of the bounds of the model assumes melt-mantle equilibration at the base of the melting region, I do not apply a correction for the latent heat of fusion in this case. If the melt was in equilibrium with mantle olivine at 1 GPa prior to extraction, the latent heat of fusion correction should represent the melt fraction at that depth. Whilst it is possible that the melt fraction calculated by Putirka (2008a) reflects the melt fraction at this depth, there is a clear discrepancy with the melt fraction-pressure curve calculated here (Figure 3.8b).

In further contrast to the Iceland discrepancy, the corrections for the temperature lost during melting due to the latent heat of fusion calculated in this study and by Putirka (2008a) differ only by 5°C. The lower melt fraction estimate by Putirka (2008a) counteracts the effect of differing choice of thermodynamic parameters. In summary, if the melt-olivine equilibration pressure is set to 0.18 GPa, Al-exchange and Mg-Fe exchange thermometry are consistent for Siqueiros.

3.4 Summary

I have obtained new crystallisation temperature estimates for four eruptions in the Northern Volcanic Zone of Iceland using the Coogan et al. (2014) Al-exchange thermometer. The maximum crystallisation temperature calculated is 1399 °C, substantially higher than the maximum crystallisation temperature in the Coogan et al. (2014) MORB dataset of 1270 °C. To explore the mantle controls on crystallisation temperature, I developed a thermal model of mantle melting, and used this to quantify the uncertainties in converting crystallisation temperature to mantle potential temperature. The uncertainties considered in the model arise from uncertainties in mantle lithology and the thermal history of melts after they have been generated. When crystallisation temperature is the only observation used to constrain mantle potential temperature, the maximum crystallisation temperature for Iceland can be satisfied by a mantle potential temperature as low as 1385 °C and in excess of 1550 °C, depending on the parental melt's depth of origin. I used crustal thickness and the fraction of bulk crust derived from pyroxenitic melts to constrain the mantle potential temperature further, yielding an estimate for T_p of 1480^{+37}_{-30}°C for Iceland and 1318^{+44}_{-32}°C for Siqueiros. These mantle potential temperature estimates are consistent with estimates derived using other techniques.

Chapter 4

Controls on CO_2-trace element systematics

When estimating mantle carbon budgets, the CO_2 concentrations in basaltic lavas are often ratio-ed to trace element concentrations to remove signals from mantle melting and crystallisation (Section 1.1). Previous studies have assumed that positive correlations between CO_2 and Ba or Nb demonstrates that no CO_2 has been lost be degassing (e.g. Saal et al., 2002). In this Chapter I consider the role of magma mixing and degassing on CO_2-trace element systematics more robustly, and demonstrate that most basaltic melts, even those whose CO_2 and Ba or Nb concentrations correlate, are likely to have lost significant proportions of their primary CO_2 budget. It is therefore essential to consider the role degassing plays in generating the CO_2 concentrations in datasets used to infer mantle carbon budgets.

4.0.1 Comparing CO_2 to lithophile trace elements

The presence of correlations between CO_2 and highly incompatible trace elements in suites of co-genetic CO_2-undersaturated glasses (Figure 4.1), has become an important empirical basis for inferring the behaviour of CO_2 during mantle melting and degassing. The strong correlation between CO_2 and Nb in such glass datasets underlies the inference of a close correspondence between the behaviour of CO_2 and Nb during mantle melting (Saal et al., 2002). This interpretation has been nuanced by recent experimental results, that show that CO_2 behaves more incompatibly than Nb, having a bulk mantle-melt partition coefficient closer to that of Ba (Rosenthal et al., 2015).

During differentiation and crustal processing, the persistence of correlated enrichments and depletions of incompatible trace elements and CO_2 is thought to imply that CO_2 has remained soluble in the melt.

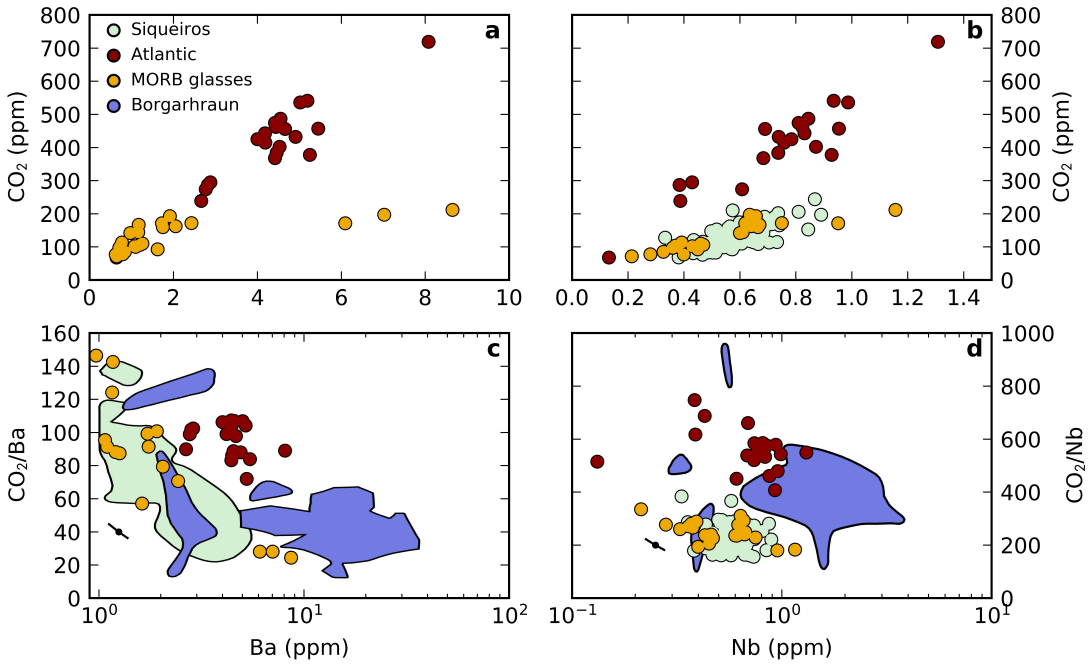

Figure 4.1: Compilation of Ba, Nb and CO_2 data for mid-ocean ridge melt inclusion and glass datasets reported as being undegassed. Modified from Rosenthal et al. (2015). Data sources: Siqueiros Nb: Saal et al. (2002); Siqueiros Ba: Saal et al. unpublished data reported by Rosenthal et al. (2015); Atlantic: Le Voyer et al. (2017); MORB glasses: Michael and Graham (2015) and Shimizu et al. (2016); Borgarhraun (Northern Iceland): Hauri et al. unpublished data reported by Rosenthal et al. (2015). The black lines and circles in panels c and d show how a 10% uncertainty in Ba or Nb concentration could cause a spurious negative correlation to develop, this effect is much smaller than the signal shown by the datasets. Error in CO2 measurements will cause vertical displacement of the data points only.

Le Voyer et al. (2017) and Saal et al. (2002) identify their melt inclusion suites as being undegassed on this basis. Rosenthal et al. (2015) instead suggest that many of the samples in such co-genetic suites have lost CO_2, based on their scatter to low CO_2/Nb ratios (Figure 4.1). Understanding the controls on CO_2-trace element systematics is therefore vital for assessing if mantle CO_2/trace element ratios are reflected in basalts.

4.0.2 The role of mixing in generating trace element systematics

Near-fractional melting of the mantle is expected to generate melts with diverse trace element chemistry. Although considerable variation in trace element concentrations is found in some melt inclusions suites (e.g. Sobolev et al., 1994), it is still significantly less than the diversity predicted

from models of fractional melt generation (Kelemen et al., 1997a; Maclennan et al., 2003b). In more evolved basaltic matrix glasses, very little variation is preserved (Maclennan, 2008a). This decrease in variability with melt evolution has been understood in terms of concurrent mixing and crystallisation (Maclennan, 2008a; Shorttle et al., 2016; Sobolev, 1996). The mixing process can efficiently dilute the most incompatible trace-element enriched, and therefore CO_2 enriched, fractional melts prior to melt inclusion entrapment even in primitive olivine macrocrysts.

Simple statistical models of melt mixing have been able to reproduce many of the observed chemical systematics of melt inclusion and glass suites (Rudge et al., 2013; Shimizu et al., 2016; Shorttle et al., 2016). These models utilise the properties of the Dirichlet distribution to model the geochemical consequences of progressive mixing of mantle melts. I build upon such models here, applying them to the creation of volatile element variability in mantle-derived melts and the destruction of this variability by mixing and degassing in the crust.

4.1 Modelling concurrent mixing and degassing

The model comprises three sequential processes, summarised in Figure 4.2. Firstly, a melting model for passively upwelling mantle is used to generate the masses and chemistry of fractional melts for a typical mid-ocean ridge (Section 4.1.1, Figure 4.2a). These melts are then placed at a pressure corresponding to magma storage in the crust, and melts that are oversaturated in CO_2 degas until they are in equilibrium (Section 4.1.2, Figure 4.2b). Finally, the melts are partially mixed (Section 4.1.3, Figure 4.2c). I do not attempt to model fractional crystallisation since the melt inclusions preserving primary CO_2/Nb and CO_2/Ba ratios represent the most primitive melts.

4.1.1 Melting Model

To generate the fractional melts used by the mixing and degassing model, I first calculate the melt extracted, X, as a function of pressure for passively upwelling mantle using the parameterization of lherzolite melting by Katz et al. (2003). The mantle potential temperature is set to 1318 °C, a temperature appropriate for normal mid-ocean ridges (Chapter 3), and cease melting once the base of the crust is reached. A pressure, P, decrement of 0.006 GPa is used during numerical integration of the melting equations. For computational convenience the results of these calculations are remapped from $X(P)$ to $P(X)$, in steps of equal melt fraction increment (0.01%) using linear interpolation.

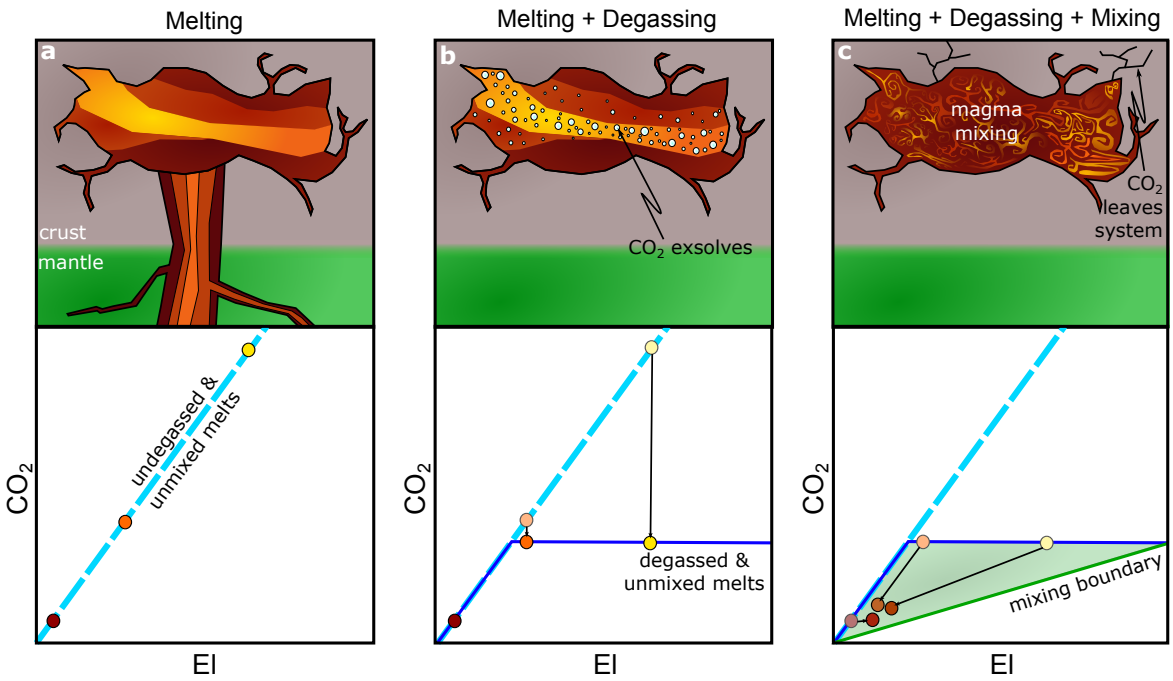

Figure 4.2: Cartoons showing how the mixing and degassing calculations proceed. 'El' represents a trace element which behaves identically to CO_2 during mantle melting. In the lower panels, the circles show schematically the behaviour of individual melts throughout the process, whilst the lines show the behaviour of a continuous distribution of melt compositions. The blue dashed line shows the undegassed and unmixed melts (panel a), the solid blue line shows the degassed and unmixed melts (panel b), and the shaded green region (panel c) shows the region between mixing bounds (the solid blue lines and green line). The positions of the solid blue and green lines are determined by the magma storage pressure.

The trace element chemistry of the generated melts is calculated assuming near fractional melting, modelled with the equation:

$$C_l = \frac{C_0}{(1-\phi)D+\phi}(1-X)^{\frac{(1-\phi)(1-D)}{(1-\phi)D+\phi}} \tag{4.1}$$

(Zou, 2007), where C_l and C_0 are the concentrations of the trace element in the liquid and original solid, D is the partition coefficient (for simplicity assumed independent of pressure), ϕ is the residual melt fraction, and X is fraction of extracted melt. The concentrations of trace elements initially in the solid are set to those in 'Average DMM' of Workman and Hart (2005). The liquid compositions are calculated assuming $\phi = 0.5\%$ by mass and Ds appropriate for typical melting conditions of lherzolite (Workman and Hart, 2005). Initial CO_2 concentrations in the melts are calculated in the same manner, assuming a bulk partition coefficient of 5.5×10^{-4} (Rosenthal et al., 2015) and a CO_2/Ba ratio in the solid of 140, except where noted otherwise.

In these calculations I consider melt generation from a single chemically homogeneous lithology. Though there is evidence for heterogeneity in the depleted mantle, the contribution of melts from heterogeneous domains is likely small (Hirschmann and Stolper, 1996, and Chapter 3). Furthermore, I find melting of a single homogeneous source reproduces the observed CO_2-trace element systematics adequately. In Section 4.2.8 I demonstrate how varying some of the constants used in the melting model affects the statistics described in Section 4.2.

4.1.2 Degassing Model

Once mantle melts have been generated, they may be transported upwards through the mantle in high porosity channels, allowing much of the geochemical variability arising from the melting process to be retained (Spiegelman and Kelemen, 2003). At depths where the melt fraction is not sufficient for high porosity melt channels to form, the melts may become homogenised (Rudge et al., 2013), though this process has only a minor effect on the conclusions drawn here (Section 4.2.5).

Melts can only be preserved in melt inclusions once they have begun to crystallise. Structural and geochemical observations from the Oman ophiolite (Boudier et al., 1996; Kelemen et al., 1997b), and magma storage pressures derived from OPAM and clinopyroxene-melt barometry performed on samples from the Icelandic rift zones and mid-ocean ridges (Herzberg, 2004; Maclennan et al., 2001b; Neave and Putirka, 2017; Winpenny and Maclennan, 2011), indicate that crystallisation in oceanic rift settings begins beneath the Moho and proceeds to low pressure. This process is shown schematically in Figure 4.2a.

The pressure of MORB crystallisation will have a major control on how much of mantle-derived CO_2 variability is preserved in melt inclusions, as pressure is the primary control on CO_2 solubility in basaltic melts (Dixon and Stolper, 1995; Moore, 1979). At the pressures associated with magma storage and crystallisation, even at the Moho, the melts most enriched in CO_2 are likely to be CO_2-oversaturated. An oversaturated melt will tend to return to saturation by degassing CO_2 (Figure 4.2b). To quantify the solubility of CO_2 in the melts, and therefore their variable extents of degassing, I use the solubility model of Shishkina et al. (2014). In addition to modelling the pressure dependence of CO_2 solubility, Shishkina et al. (2014) also quantify the effect of the major element composition of the melt, through a parameter they call π^*. To retain simplicity in the models π^* is set to a constant value of 0.34, typical of mid-ocean ridge tholeiites. In detail, π^* will correlate with trace element concentration, even in melts from a single-lithology mantle, as melt major element chemistry correlates with depth and degree of melting (Klein and Langmuir, 1987). A variable π^* is, however, a secondary effect to the melting and mixing processes incorporated in to the model. The melts are assumed not to retain supersaturation, which means that the results are conservative estimates for

the effect of degassing on preserved CO_2-trace element ratios as some degree of supersaturation is required to drive bubble nucleation (e.g. Bottinga and Javoy, 1990).

A single pressure is chosen for each run of the model, corresponding to the magma storage depth. Melts that have a saturation pressure lower than this retain their initial CO_2 concentration. The most enriched melts may reach CO_2 saturation at greater pressures than the crustal depths used in the models, and therefore may begin degassing before the single degassing stage used in the model. Since CO_2 solubility monotonically decreases with decreasing pressure, even if these melts lose CO_2 during transport they will in all likelihood still arrive oversaturated in CO_2 at the pressure of magma storage. Degassing during transport will never cause the melts to lose more CO_2 than they would during a single (efficient) degassing interval at the pressure of magma storage. The melts are likely to continue mixing and crystallising as they travel upwards through the crust, and therefore may experience many episodes of degassing followed by mixing. Since the melt inclusions that are most likely to preserve mantle CO_2/Ba or CO_2/Nb values are entrapped at the first stage of crystallisation and then remain isolated from the melt, subsequent mixing or degassing is not considered.

4.1.3 Mixing Model

The final step in the model is the mixing of the partially degassed melts generated in the previous two steps (Sections 4.1.1 and 4.1.2), shown schematically in Figure 4.2c. In making this the last stage of the model, I am implicitly assuming the timescale of degassing, controlled by bubble nucleation, is faster than the timescale of mixing. I use the statistical mixing methodology used by Rudge et al. (2013) to model the partial mixing process. Rudge et al. (2013) utilise the properties of the Dirichlet distribution, in particular it has very strong independence properties, meaning that all melts are treated equally according to their relative proportions, denoted as ω_i. A comprehensive description of the model is given by Rudge et al. (2013), and so I provide only a summary here.

A mixed melt of composition $\hat{C}$ is generated by randomly mixing m melt compositions entering the crust, $C^{(i)}$, according to their proportions $\hat{r}_i$:

$$\hat{C} = \sum_{i=1}^{m} \hat{r}_i C^{(i)} \tag{4.2}$$

where the hats on $\hat{C}$ and $\hat{r}_i$ indicate that they are random variables. The mean composition of the melts entering the crust is fixed by the mass proportion of each melt present, ω_i:

$$\bar{C} = \sum_{i=1}^{m} \omega_i C^{(i)} \tag{4.3}$$

therefore, to conform with mass balance the expectation value for the proportions of melts going into a mixture, $\hat{r}_i$, is given by:

$$\mathbb{E}(\hat{r}_i) = \omega_i \tag{4.4}$$

Formally, the proportions that the melts are mixed with are distributed according to a Dirichlet distribution with parameters:

$$\{\hat{r}_1, \hat{r}_2, \ldots, \hat{r}_m\} \sim \mathrm{Dir}(\alpha_1, \alpha_2, \ldots, \alpha_m) \tag{4.5}$$

where α_i is related to the mixing parameter, N, by:

$$\alpha_i = (N-1)\omega_i \tag{4.6}$$

N can range from unity, representing no mixing, to ∞, representing complete mixing. Melts are weighted by ω_i values corresponding to a triangular melting region, i.e. the deepest melts have a greater weighting than more shallow melts. Maclennan (2008a) showed that melts in Iceland become increasingly mixed as crystallisation proceeds and the melts become more evolved; Rudge et al. (2013) successfully modelled this by varying the mixing parameter from 12, for the most primitive melts, to 108 for the most evolved. In the models presented here a constant mixing parameter of 16 is used, typical of the earliest stages of crystallisation. The effect of the mixing parameter on the results is discussed in Section 4.2.6.

Correlations between CO_2 and trace elements are a primary consideration of this contribution. The properties of the Dirichlet distribution allow calculation of the variance of individual elements, the covariance of two elements, and from these the Pearson correlation coefficient (Rudge et al., 2013). For melts from a single lithology, as modelled here, the variance of a single element, $\hat{C}^{(1)}$, is given by:

$$\mathrm{var}\left(\hat{C}^{(1)}\right) = \frac{1}{N}\sum_{i=1}^{n} \omega_i \left(c_i^{(1)} - \bar{C}^{(1)}\right)^2 \tag{4.7}$$

and the covariance of two elements, $\hat{C}^{(1)}$ and $\hat{C}^{(2)}$, by:

$$\mathrm{cov}\left(\hat{C}^{(1)}, \hat{C}^{(2)}\right) = \frac{1}{N}\sum_{i=1}^{n} \omega_i \left(c_i^{(1)} - \bar{C}^{(1)}\right)\left(c_i^{(2)} - \bar{C}^{(2)}\right) \tag{4.8}$$

The Pearson correlation coefficient between two elements can be expressed as:

$$\mathrm{cor}\left(\hat{C}^{(1)}, \hat{C}^{(2)}\right) = \frac{\mathrm{cov}\left(\hat{C}^{(1)}, \hat{C}^{(2)}\right)}{\sqrt{\mathrm{var}\left(\hat{C}^{(1)}\right)\mathrm{var}\left(\hat{C}^{(1)}\right)}} \tag{4.9}$$

since the mixing parameter, N, cancels, the correlation coefficient between two elements is independent of degree of mixing, assuming the remaining range in the element concentrations is significantly above the level of analytical uncertainty.

Whilst it is the correlation between CO_2 and trace elements that has been used to assess the behaviour of CO_2 during melting (and whether it has subsequently degassed), the calculation of the mantle CO_2 concentration assumes direct proportionality between the CO_2 concentration and CO_2/trace element (El) ratios. The behaviour of CO_2/trace element ratios are therefore also of interest. Unfortunately, simple analytical expressions for the variance, covariance and correlation of element ratios at low degrees of mixing do not exist, but can be calculated by drawing a large number of samples from the Dirichlet distribution. Since the variance of a single element ratio and the covariance of two ratios do not depend on the mixing parameter, N, in a simple way, the correlation coefficient between element ratios is also a function of mixing parameter (as shown in Section 4.2.6).

4.2 Mixing systematics

Before applying the mixing model, qualitative inferences may be drawn about the covariance and correlation between CO_2 and trace elements by considering mixing arrays between end member fractional melts. Firstly, the simplest case is characterised: the correlation between CO_2 and a trace element that behaves identically to CO_2 prior to CO_2 vapour saturation (Section 4.2.1). This approach is then generalised to the correlation between CO_2 and trace elements with differing compatibility during melting (Section 4.2.2). Finally, to quantify the correlations between CO_2 and trace elements, the Dirichlet mixing scheme is introduced in Section 4.2.2. The implications of mixing for apparent similarities in behaviour of CO_2 and trace elements are discussed in Section 4.2.3. In Section 4.2.4 the control degassing pressure exerts on the resulting CO_2-trace element correlations is explored.

4.2.1 Identical CO_2-trace element partitioning

If a trace element behaves identically to CO_2 during mantle melting and crustal differentiation (prior to CO_2 saturation), concentrations in fractional and variably differentiated melts will describe a straight line passing through the origin when plotted against CO_2 concentration (Figure 4.2a). The most enriched of these fractional melts will be oversaturated in CO_2 vapour at crustal pressures, and therefore will degas CO_2 until they reach CO_2 saturation (Figure 4.2b). This degassing process causes the CO_2 concentrations of the most enriched melts to be decoupled from the trace element concentrations, whilst the depleted melts are unaffected.

Mixing of fractional melts may only produce melt compositions lying within the extremes of the unmixed fractional melts. These bounds may coincide with the arrays of primary fractional melts, otherwise they correspond to mixing lines between extreme compositions (Figure 4.2c). Melts generated by mixing of these fractional melts must therefore lie within the green-shaded area on Figure 4.2c. When melts originally at CO_2 vapour saturation mix with undersaturated melts, the mixed melts will become undersaturated, since π^* is not allowed to vary. Mixed melts lying within this triangle will define a positive correlation, with an average CO_2/El ratio that will be considerably lower than the mantle CO_2/El ratio. In the next Section, I explore how differing trace element behaviour affects this observation, and in Section 4.2.4 I show that the average CO_2/El ratio, even for correlated CO_2-El datasets is controlled primarily by the pressure of degassing.

Though the compositional limits of near-fractional melt mixing can be determined very simply using the process described above, the space enclosed by these limits is not inhabited with uniform likelihood. For extents of melting expected at mid-ocean ridges ($\leq$15%), most melts are produced at high melt fractions once the residual mantle has already been almost entirely stripped of incompatible trace elements. Due to the overwhelming proportion of depleted fractional melts, mixed melt compositions are biased towards the depleted region. In the Section 4.2.2 I quantify this phenomenon with the Dirichlet mixing model.

4.2.2 Generalised CO_2- trace element partitioning

The methodology developed in the preceding section can be generalised to elements with differing compatibilities to CO_2. The primary melts, rather than falling on a straight array, now define a curve (Figure 4.3a). Little change from the identical partitioning case is seen for trace elements behaving more incompatibility than CO_2, this is due to the residual porosity retained throughout melting, which damps variability in extracted melts when $D_{\mathrm{El}} < \phi$. In addition to the systematics in trace element (El)-CO_2 space, I also show the behaviour in CO_2/El – El space (Figure 4.3b), and CO_2/El – 1/El space (Figure 4.3c). Figure 4.3b may be compared with the data compilation in Figure 4.1; plotting CO_2/El ratios against 1/El concentrations offers the advantages of linear mixing bounds and an expansion of the region containing maximum CO_2/El observations (the depleted melts; Figure 4.3c).

The green shading in Figure 4.3 shows the logarithmic probability distribution of mixed melts, demonstrating that they are biased towards the depleted region of the space, as discussed in Section 4.2.1. It is immediately apparent from Figure 4.3a that positive correlations between CO_2 and trace elements are generated from partially degassed melts. Importantly, the greatest population density of these melts is seen in a narrow array, similar in appearance (but not gradient) to the expectation from a suite of undegassed melts. This feature persists in spite of the broad mixing bounds (green and blue lines) defined by mixing of endmember melt compositions. The gradient of this array is lower than the

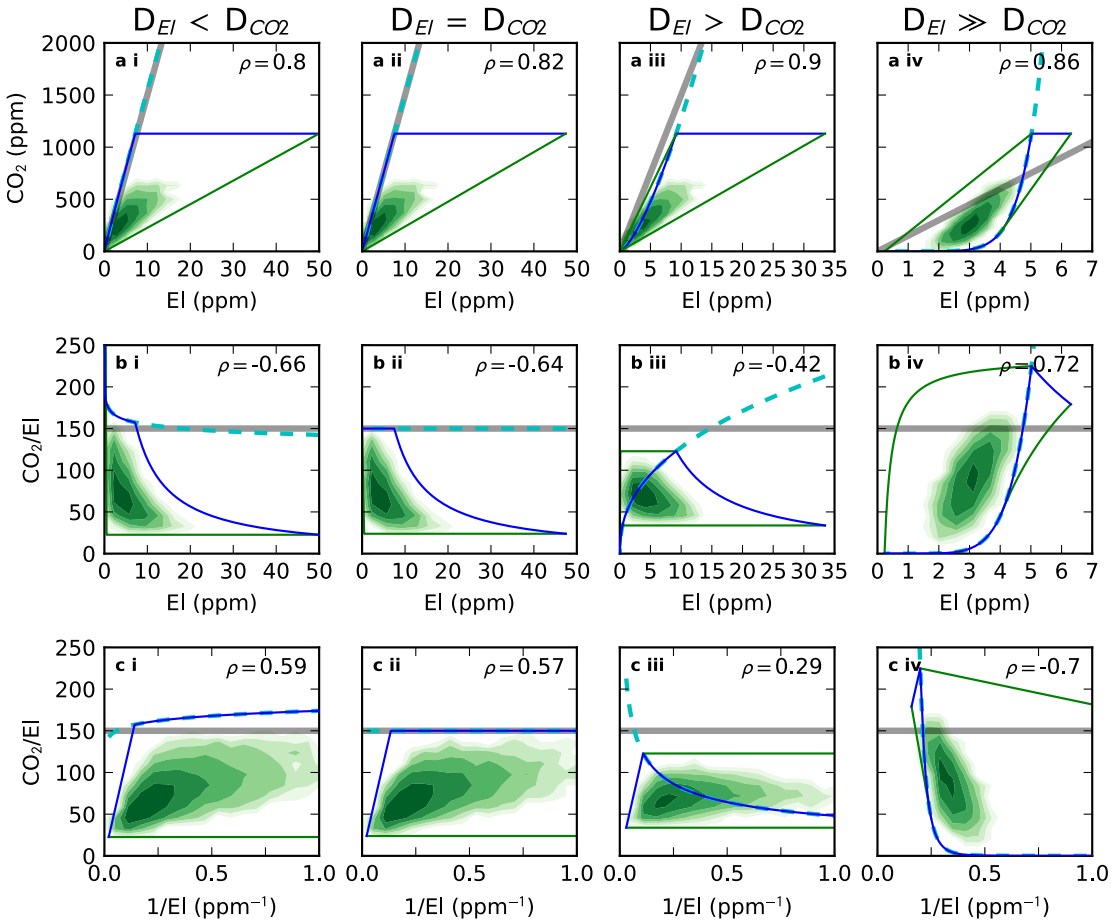

Figure 4.3: Systematics for trace elements with varying compatibility relative to CO_2 (column headings) according to the mixing and degassing model. Trace element concentrations in the solid mantle are set to 0.5 ppm. Each row represents a different way of plotting the systematics, as indicated by the axes labels. See Figure 4.2 for descriptions of each line. Undegassed and unmixed melts are represented by the cyan dashed line. Degassed and unmixed melts are represented by the solid blue line. The boundaries of the space that can be inhabited by mixed melts are shown by solid green lines, in addition to the solid blue lines. The grey band represents the CO_2/El ratio of the mantle source. The shading represents the logarithmic density of mixed melts generated by the model. The Pearson correlation coefficient (ρ) for the mixed distribution is shown in the upper right hand corner of each panel. Calculation parameters are described in the text, the degassing pressure is set to 2 kbar.

CO_2/El ratio of the source (Figure 4.3b and c) and the average CO_2/El ratio is much lower than the source CO_2/El ratio (horizontal grey line), although the maximum of the probability distribution does tend towards the source value. In fact, the maximum of the distribution can exceed the source CO_2/El it if the trace element is more incompatible (Figure 4.3bi), or much more compatible (Figure 4.3biv) than CO_2. These two scenarios are distinguished from one another by the relation of maximum CO_2/El to El concentration: in the $D_{El} \ll D_{CO_2}$ case, CO_2/El of the melts exceeds the source in the most incompatible trace element depleted melts, whereas for $D_{El} \gg D_{CO_2}$ case, the most incompatible trace element enriched melts have CO_2/El greater than the source. I discuss the implications of this for identifying mantle CO_2/El values in Section 4.3.

CO_2/El ratios in melts will only reflect the trace element ratio of the source if CO_2 has not been fractionated from the trace element. Degassing very strongly fractionates CO_2 from all trace elements in melts that are oversaturated at the pressure of magma storage, and significantly reduces the CO_2/El ratio of the most enriched melts. Subsequent mixing between the high, primary, CO_2/El ratio of the trace element depleted endmember with the low, degassed, CO_2/El ratio of the trace element enriched endmember, tends to generate negative correlations in CO_2/El-El space (Figure 4.3bi-iii) and positive correlations in CO_2/El-1/El space (Figure 4.3ci-iii). Only for the most compatible elements is the original pre-degassing positive correlation of the CO_2/El-El array, or negative correlation for the CO_2/El-1/El array, retained (Figure 4.3biv and Figure 4.3civ). Sufficient concentrations of more compatible elements persist in the residue during melting such that many of the higher degree primary melts continue to have significant compatible trace element concentrations, whilst having a primary depletion in CO_2. These moderately enriched melts do not saturate in CO_2 vapour and so retain their primary CO_2/El ratio and therefore continue to provide an enriched high CO_2/El mixing endmember.

Since degassing exerts a control on the systematics of data plotted in CO_2/El-1/El space, this behaviour can be used to check for and track any degassing processes that a dataset has experienced. To quantify this behaviour the Pearson correlation coefficient may be used. A coefficient value of 0 indicates no correlation and values of -1 and +1 indicate perfect negative and positive correlations, respectively. The value of the coefficient for the mixed distributions shown in Figure 4.3 is displayed in the top right-hand corner of each panel. Figure 4.4 shows how correlations in CO_2-El – 1/El space vary with degassing pressure and trace element partitioning coefficient. When there is no degassing (black line), the transition between positive and negative correlations is rapid, and occurs when the trace element switches from being infinitesimally more incompatible, to infinitesimally more compatible than carbon. When partial degassing has taken place a much smoother transition is seen, and correlations cross from negative to positive at progressively greater trace element partition coefficients as the pressure of degassing decreases. Positive correlations are generated by having many low CO_2/El melts at low 1/El (Figure 4.3c), these are the most degassed and incompatible trace element enriched melts. As degassing pressure decreases a greater number of melts degas, and the CO_2 they retain decreases; the positive correlation will tend to be enhanced. Negative correlations are generated by decoupling

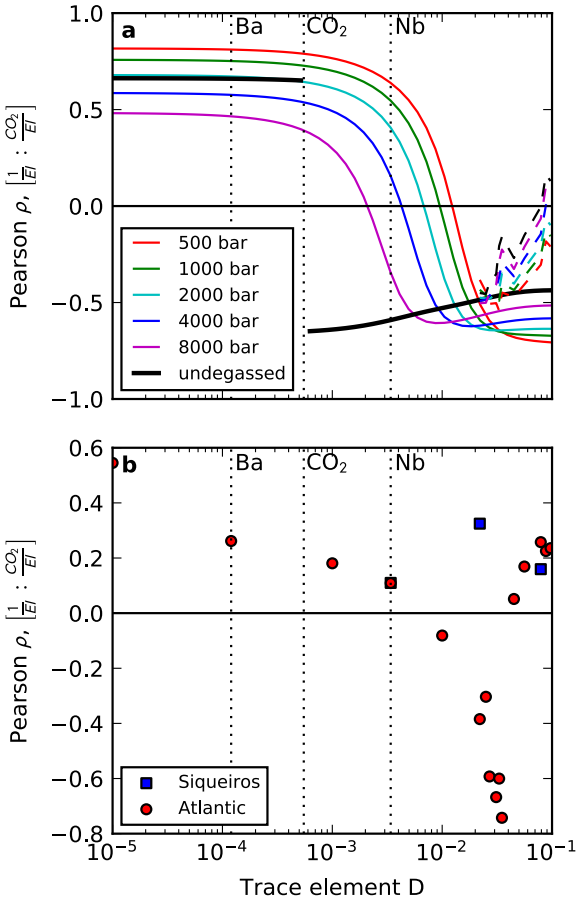

Figure 4.4: Panel a shows the variation of the Pearson correlation coefficient between 1/El and CO_2/El calculated for melts mixed following degassing at different pressures. A switch from positive to negative correlation is seen at increasing D as degassing pressure decreases. Since there is zero variance in CO_2/El for undegassed melts when the trace element partitions identically to CO_2, the correlation coefficient is undefined. The trace element *D* values are partition coefficients during mantle melting. The vertical dotted lines show the partition coefficients for Ba, CO_2 and Nb, as reported by Workman and Hart (2005) and Rosenthal et al. (2015). The dashed lines indicate the effect of garnet in the source: trace element concentrations are calculated using the alphaMELTS frontend (Smith and Asimow, 2005) for the pMELTS thermodynamic model (Ghiorso et al., 2002) using variable bulk partition coefficients calculated from constant mineral-melt partition coefficients (McKenzie and O'Nions, 1991, 1995). CO_2 concentrations were calculated by assuming identical behaviour to Ba. The calculation was run in the CFMAS-Ti system with the depleted mantle composition of Workman and Hart (2005), starting at a temperature of 1500 °C at pressure of 30 kbar (sufficient for garnet to be the stable aluminous phase at the start of melting), and stopped at 2.5 kbar. The trace elements are plotted at the partition coefficients given by Workman and Hart (2005). Panel b shows the Pearson correlation coefficient between CO_2/El and 1/El for the Equatorial Atlantic dataset (Le Voyer et al., 2017) and the Siqueiros dataset (Saal et al., 2002).

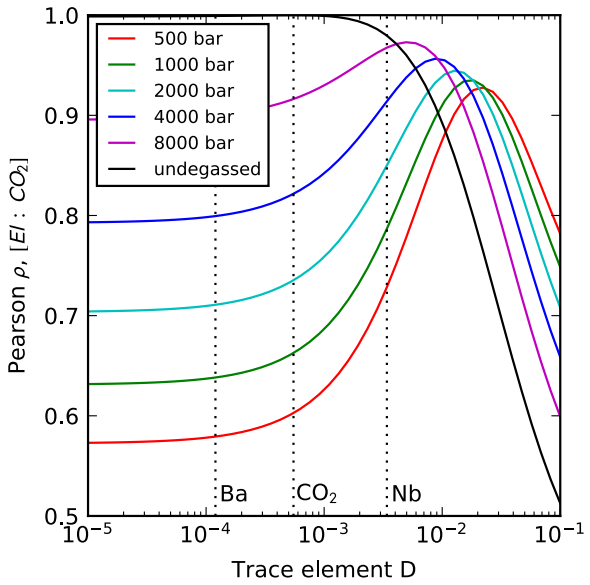

Figure 4.5: Variation of the Pearson correlation coefficient between concentrations of trace elements of varying partition coefficient during mantle melting (D) and CO_2 concentrations, for different pressures of degassing. When melts have partially degassed the best correlation is seen between CO_2 and more compatible trace elements. See the caption to Figure 4.4 for description of additional lines and data sources.

between CO_2 and El during melting and so are most prevalent for the most compatible elements. The partition coefficient at which the transition from positive to negative correlation occurs is determined by the competition between these two effects, the tendency to observe a positive correlation in CO_2/El vs. 1/El space increases with decreasing degassing pressure. The model also makes predictions about the variance in CO_2/El with El concentration, however existing datasets do not contain sufficient analyses to accurately estimate these parameters and allow us to test the model.

4.2.3 Apparent mantle partitioning behaviour from CO_2-trace element correlations

Empirical constraints have been placed on the partitioning behaviour of CO2 during mantle melting by the degree of correlation between CO_2 and trace elements (Le Voyer et al., 2017; Michael and Graham, 2015; Saal et al., 2002). Saal et al. (2002) and Michael and Graham (2015) find the strongest correlation between CO_2 and Nb, whilst Le Voyer et al. (2017) find CO_2 correlates equally well with Rb, Ba and Nb. Such relationships between carbon and trace elements only directly reflect mantle partitioning behaviour if no degassing has occurred, with the results above showing that positive correlations are readily generated in partially degassed melts (Figure 4.3).

The behaviour of the correlation coefficient between CO_2 and trace elements as a function of partition coefficient is displayed in Figure 4.5. When there is no degassing, CO_2 correlates extremely well with the most incompatible elements; the lack of variation in correlation coefficient for the most incompatible elements arises from the residual porosity during melting (i.e., using a continuous

melting model as opposed to pure fractional). The correlation coefficient between CO_2 and trace elements then decreases with increasing trace element compatibility (Figure 4.5, black line).

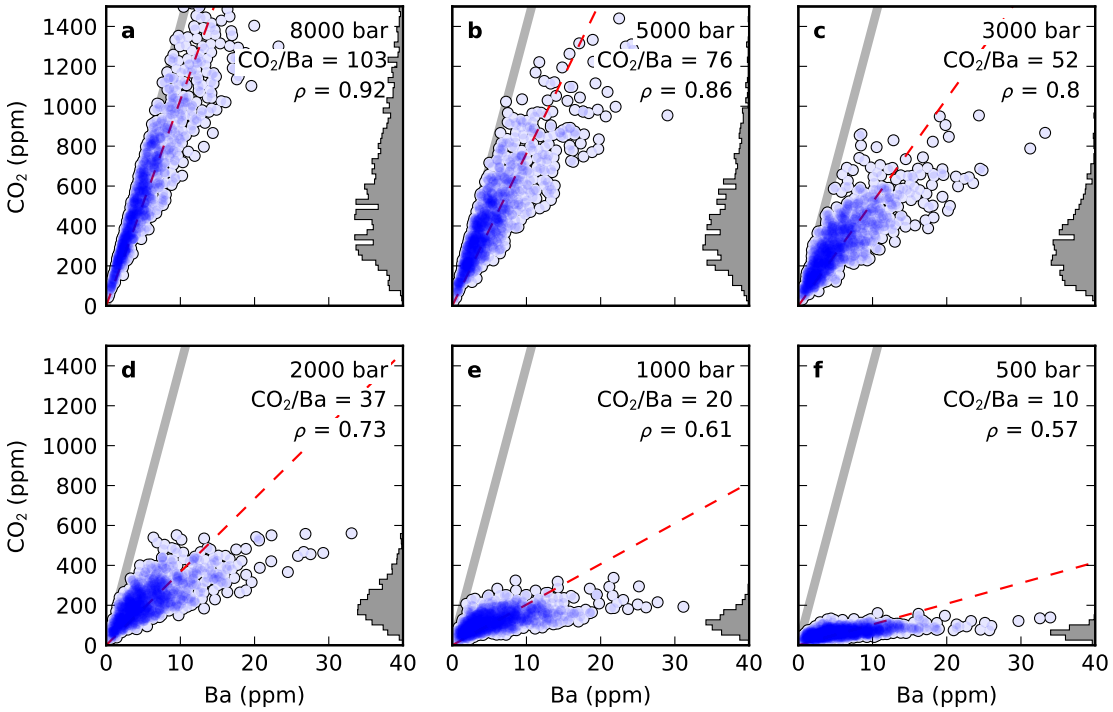

Figure 4.6: Each panel displays the CO_2-Ba systematics generated by mixing melts degassed at different pressures (shown in bar, in the upper right corner). As the degassing pressure decreases, the array of melt compositions rotates to lower CO_2/Ba. Histograms of mixed melt density shown on the right hand side. The shading indicates density of data. The thick grey line shows the CO_2/Ba ratio of the source mantle (140), and the red-dashed line the CO_2/Ba ratio obtained by orthogonal distance regression on the mixed melts (also shown in the top right hand corner of each panel).

In contrast, when partially degassed melts are mixed, the correlation coefficient does not decrease monotonically as the reference trace element becomes increasingly compatible. Instead, mixing of degassed melts creates a maximum in correlation coefficient centred on a higher (i.e. more compatible) partition coefficient than CO_2 (Figure 4.5). This pattern is also present in the synthetic data presented in Figure 4.3aiii, which shows data lying within a tight wedge. This result owes to a smaller range in trace element concentrations being generated when the trace element D is high. Model runs shown in Figure 4.6, where CO_2 is plotted against Ba, and Figure 4.7, where CO_2 is plotted against Nb, show how better correlations may be developed between CO_2 and Nb, rather than CO_2 and Ba, despite the carbon partition coefficient used in the models being closer in value to Ba (Rosenthal et al., 2015).

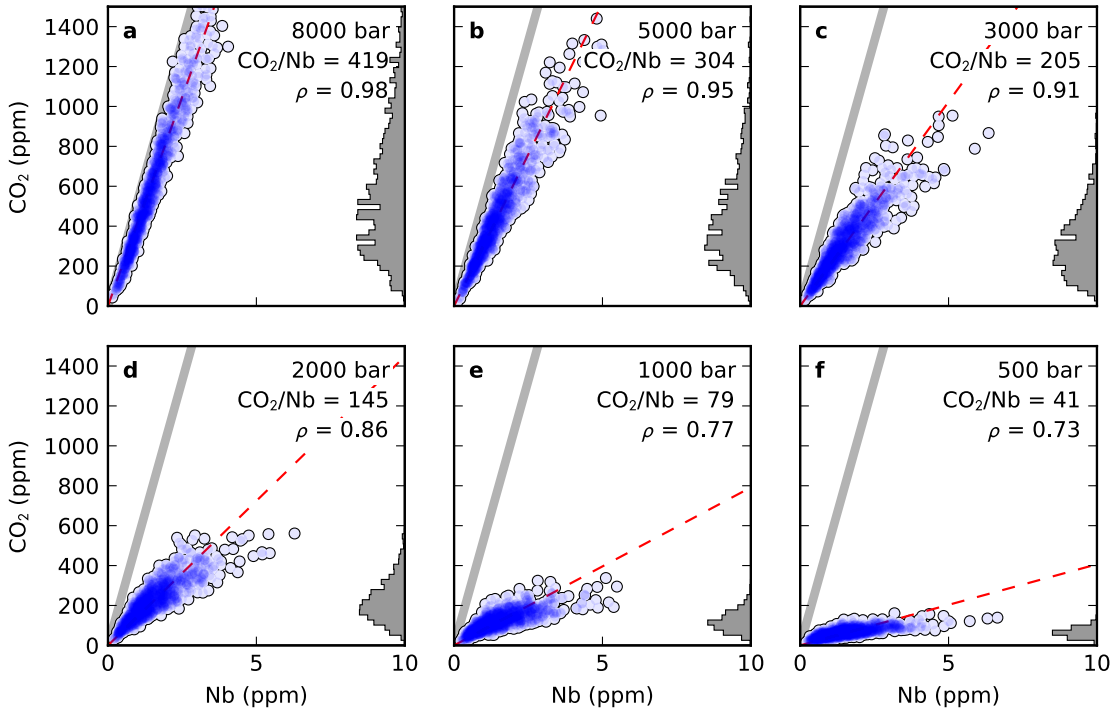

Figure 4.7: Each panel displays the CO_2-Nb systematics generated by mixing melts degassed at different pressures (shown in bar, in the upper right corner). As the degassing pressure decreases, the array of melt compositions rotates to lower CO_2/Nb, but with better correlations than seen for CO_2 and Ba (Figure 4.6). Histograms of mixed melt density shown on the right-hand side. The shading indicates density of data. The thick grey line shows the CO_2/Nb ratio of the source mantle (531), and the red-dashed line the CO_2/Nb ratio obtained by orthogonal distance regression on the mixed melts (also shown in the top right hand corner of each panel). The CO_2 concentration in the mantle source is identical to that used in the calculations shown in Figure 4.6.

4.2.4 Effect of degassing pressure

The CO_2/El ratios of the melts generated by the model are controlled by mixing between a trace element depleted, but high, primary, CO_2/El endmember, and a trace element enriched, but low, degassed, CO_2/El endmember. The value of the low CO_2/El endmember is determined by the CO_2 content of the melts at saturation, which is controlled by pressure. Reducing the pressure of degassing has the effect of rotating the array in CO_2-trace element space to shallower slopes (Figure 4.6 and Figure 4.7).

The mantle CO_2/Nb ratio has often been constrained by fitting a line through the data in CO_2-trace element space. This process should be carried out using orthogonal distance regression, since neither

variable is strictly dependent. I fit an equation of the form:

$$f(\mathrm{El}) = m \cdot \mathrm{El} \tag{4.10}$$

where El is the concentration of the trace element, and m is varied so that the misfit between CO_2 and $f(\mathrm{El})$ is minimised. The parameter m corresponds to the best fit CO_2/El ratio. Calculations were performed using the ODRPACK library (Brown and Fuller, 1990) with the SciPy interface (Jones et al., 2014a). The results of these calculations are shown by the red dashed lines in Figure 4.6 and Figure 4.7, and the values of the best fit CO_2/El ratio are shown in the top right corner of each panel. Any amount of degassing reduces the CO_2/El ratio inferred by this method, despite an apparently good fit to the data in CO_2-trace element space. As the number of draws from the distribution increases, the best fit ratio will tend towards the mean ratio of the starting melts.

4.2.5 Effect of homogenisation during transport

Soon after mantle crosses the peridotite solidus, the melt fraction will be low and the high porosity melt channels, thought to be critical in preserving primary melt variability, may be yet to form. Melts may therefore homogenise at these depths, (Rudge et al., 2013) find such a process is required for subsequent melt mixing to produce the binary isotope arrays observed in Iceland.

The effect of this process, with varying homogenisation depth, is shown in Figure 4.8. As the homogenisation depth increases more melts are mixed together, and the variability of the melts entering the crust is reduced. At the greatest extents of homogenisation (Figure 4.8e and f), the extremely high concentrations of CO_2 in the deepest melts is sufficiently diluted by the addition of shallower melts that CO_2 saturation is no longer reached; the melts preserve the mantle CO_2/Ba ratio. At more modest extents of homogenisation (Figure 4.8c and d), the variability in CO_2 concentration has been removed, but the deepest melts are not sufficiently diluted that they do not saturate in CO_2 in the crust; binary mixing now takes place between a trace element enriched degassed melt, and an extremely depleted undegassed melt, and the mantle CO_2/Ba ratio is not preserved. When only limited homogenisation takes place (Figure 4.8b), the variability of melts is reduced but not sufficiently for a binary mixing array to be produced; the scatter about the average ratio is considerably less than the unhomogenised case (Figure 4.8a), however.

Since binary mixing arrays in CO_2-trace element space are not observed in the published datasets, it is likely that only limited homogenisation has taken place. Small amounts of homogenisation do not change the results or conclusions of this paper.

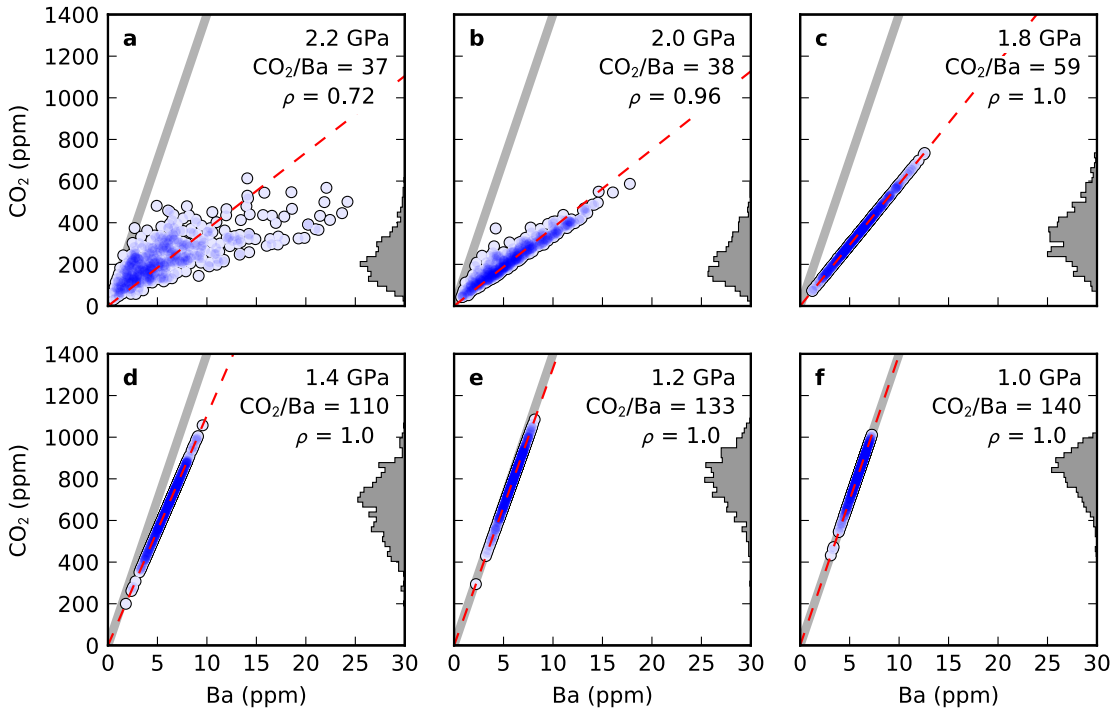

Figure 4.8: Each panel shows the results of the mixing-degassing calculation for melts that have been variably homogenised during transport. As the extent of homogenisation increases, the variability in the CO_2/Ba ratio decreases, and the array rotates towards the mantle CO_2/Ba ratio. The pressure in the upper-right corner of each panel shows the pressure below which all melts produced are completely mixed. Degassing occurred at 2000 bar. See Figure 4.6 for more information.

4.2.6 Effect of Mixing parameter

The effect of the mixing parameter on the distribution of data in CO_2-trace element space in shown in Figure 4.9. As the mixing parameter increases, the array condenses towards the most depleted melts. A small change in the best fit ratio is seen in Figure 4.9, however this is due to having insufficient draws from the distribution to characterise the mean ratio accurately. As the number of analyses increases the best fit ratio will tend towards the mean ratio, regardless of mixing parameter. The smaller the degree of mixing, the more likely it is for the mantle CO_2/Ba ratio to be preserved, shown by the number of points lying on the grey line in Figure 4.9. The general systematics described in the main text are not affected by small changes in the mixing parameter. Estimates of the minimum number of analyses required to observe mantle CO_2/Ba ratios (Section 4.4.3) will be sensitive to this however, and so these results should be used with care.

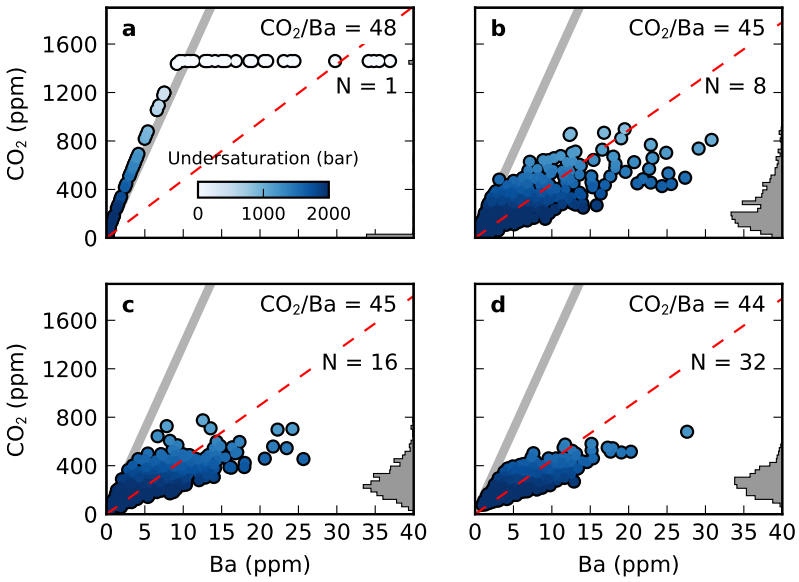

Figure 4.9: CO_2-Ba systematics resulting from varying mixing parameter, and degassing at 2000 bar. As mixing parameter increases, the array condenses towards the depleted melt endmember. Colour indicates CO_2 undersaturation at 2000 bar. See the caption to Figure 4.6 for further description.

4.2.7 Effect of analytical uncertainty

Using plots where one variable appears in the expressions plotted on both x and y axes can lead to the appearance of spurious correlations (Jackson and Somers, 1991). Analytical error in El concentration will not only affect the concentration of El (or 1/El) plotted on the x axis, but also the value of CO_2/El plotted on the y axis. Measurements of trace element and CO_2 concentrations in melt inclusions generally have uncertainties $\sim$10% (Le Voyer et al., 2017; Saal et al., 2002), the vector that describes the effect of this uncertainty is shown by the black lines and circles in Figure 4.1c and 4.1d. In the datasets considered here the signal is much greater than the analytical uncertainty.

4.2.8 Sensitivity of Pearson correlation coefficient to melting parameters

As described in the main text, degassing has a dramatic effect on the behaviour of the Pearson correlation coefficient between CO_2/El and 1/El, moving the change from positive to negative coefficient towards higher trace element partition coefficient. The pressure at which degassing takes place is a major control on where this transition happens, and the magnitude of the correlation coefficients either side. These properties of the correlation coefficient are not controlled uniquely by degassing pressure however, Figure 4.10 demonstrates how the mixing parameter, source CO_2 concentration, the residual porosity during melting and homogenisation during transport (Section 4.2.5), affects the behaviour of the correlation coefficient. Plots of this type are therefore useful for qualitatively identifying the presence of degassing, but cannot be used to extract degassing pressure quantitatively.

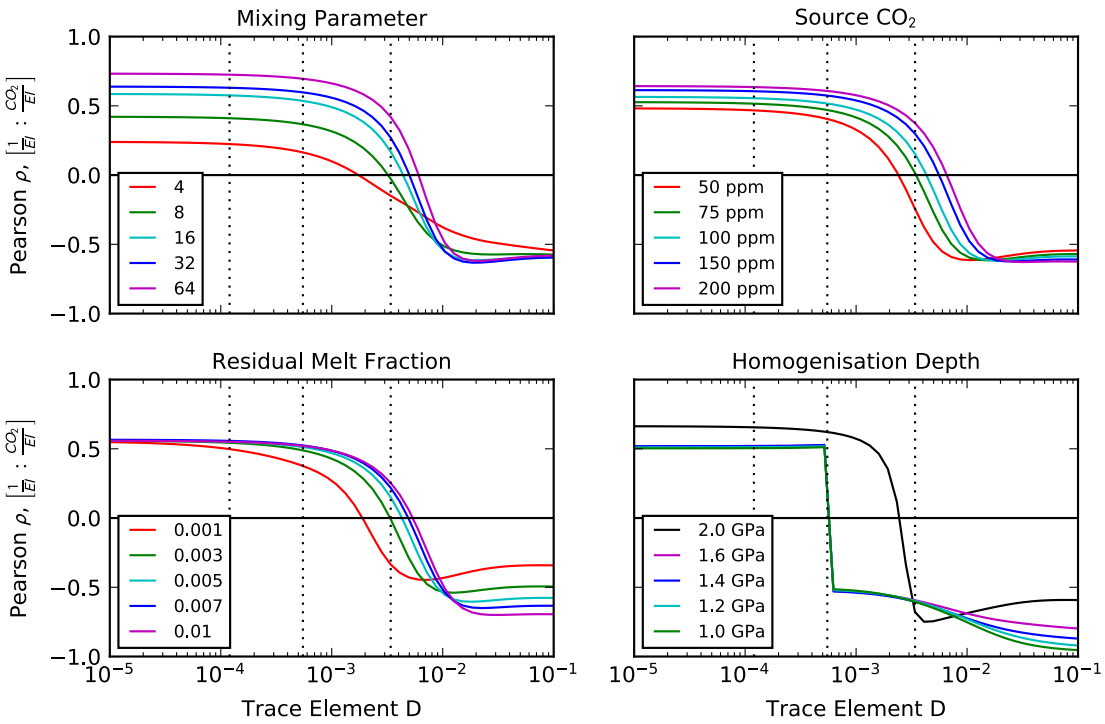

Figure 4.10: The effect of variables other than degassing pressure on the Pearson correlation coefficient between 1/El and CO_2/El. Calculations performed at 2000 bar, with other parameters as described in main text, unless noted in the panel key.

4.3 Graphite Saturated Melting

The calculations of melt CO_2 concentrations in the main text are valid only if carbon is present as carbonate in the mantle. The stability of carbonate over graphite is controlled by the oxygen fugacity of the mantle. Though the mantle beneath mid-ocean ridges is likely sufficiently oxidised for carbon to be present as carbonate, I explore the effects graphite saturated melting would have on CO_2-trace element systematics.

The CO_2 content of the melt at graphite saturation was calculated as a function of melt composition and oxygen fugacity using the formulation of Duncan et al. (2017). Once graphite is exhausted, I assume C is entirely depleted from the solid residue. To maintain consistency with other trace elements, which are modelled as melting continuously, C is allowed to remain within the residual porosity with a growing degree of dilution. I assume C behaves perfectly incompatibly.

For a single melting increment of dF_n with a residual porosity of ϕ:

$$C_n = \frac{\phi - dF_n}{\phi} C_{n-1} \tag{4.11}$$

where C_n and $C_(n-1)$ are the CO_2 concentrations in the residual porosity after, and before the nth melting increment, respectively. This can be applied recursively to yield:

$$C_n = \left[\frac{\phi - dF_n}{\phi}\right]\left[\frac{\phi - dF_{n-1}}{\phi}\right]\cdots\left[\frac{\phi - dF_1}{\phi}\right] C_0 \tag{4.12}$$

$$C_n = \frac{C_0}{\phi^n} \prod_{i=0}^{n-1} \phi - dF_{n-i} \tag{4.13}$$

where C_0 is the CO_2 concentration in the melt at the point of graphite exhaustion. Setting $dF_{n+1} = dF_n = dF$,

$$C_n = C_0 \left(1 - \frac{dF}{\phi}\right)^n \tag{4.14}$$

and since:

$$dF = \frac{\Delta F}{n} \tag{4.15}$$

where $\Delta F = F - F_{\text{graphite-exhaustion}}$, the concentration at a given ΔF may be written:

$$C(\Delta F) = C_0 \left(1 - \frac{\Delta F}{\phi n}\right)^n \tag{4.16}$$

in the limit $dF \to 0$ and $n \to \infty$:

$$C(\Delta F) = C_0 e^{-\frac{\Delta F}{\phi}} \tag{4.17}$$

Examples of these calculations for variable oxygen fugacity, are shown in Figure 4.11. Graphite saturation during melting decreases the CO_2 content of the most enriched melts, and increases the CO_2 concentration in the more depleted melts. Since the degassing step substantially reduces the CO_2 concentration of the most enriched melts in most runs of the model, the most pronounced effect of graphite saturation is on the depleted melts. Depleted melts generated from a very reduced melting region have extremely high CO_2/Ba ratios (Figure 4.12). Dissolution of CO_2 exsolved from enriched melts, into undersaturated depleted melts has the same effect on the CO_2-trace element systematics.

4.4 Implications for existing datasets

In Section 4.2.2 I demonstrated that positive correlations between CO_2 and trace elements are not a unique property of undegassed melts. Published datasets that have utilised the presence of CO_2-

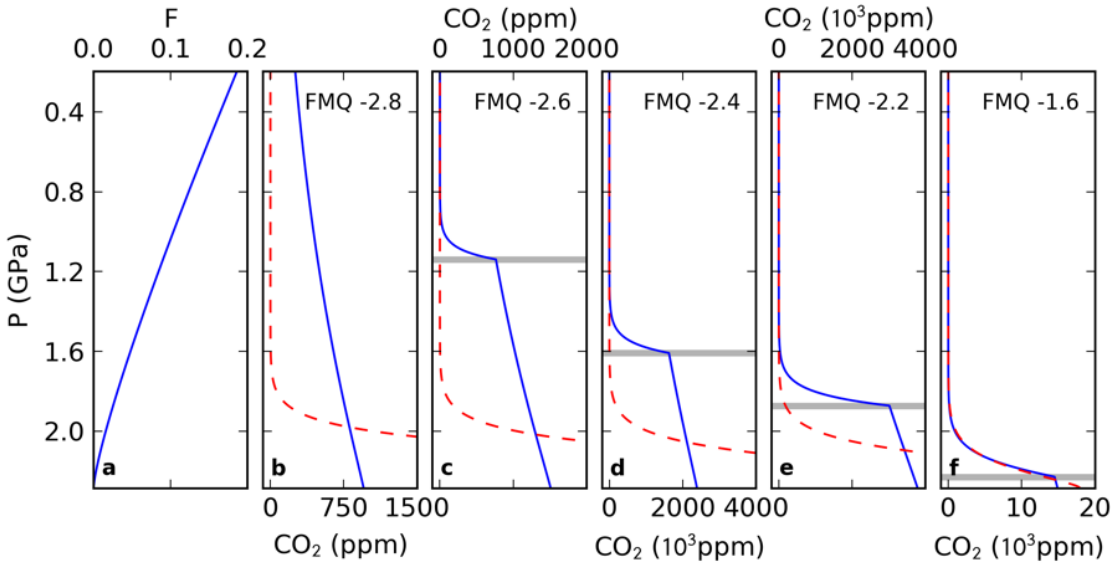

Figure 4.11: Panel a shows the melt fraction as a function of pressure, calculated as described in the main text. The solid blue lines in panels b-f show the calculated CO_2 concentration of melts generated at variable oxygen fugacity, buffered relative to the FMQ buffer. Below the grey line the mantle is graphite saturated. The red dashed line shows the concentration of CO2 in the melts in a mantle sufficiently oxidised that graphite is never saturated during melting, i.e. the result used previously in this chapter.

trace element correlations as a criterion for identifying the absence of degassing must, therefore, be reassessed.

4.4.1 Signatures of partial degassing in nominally undegassed sample suites

Since degassing only affects the melts that have the highest concentrations of CO_2, additional structure is introduced into the data: rather than almost horizontal arrays in CO_2/Ba-Ba space, partially degassed melts will exhibit negative correlations. Figure 4.1c demonstrates that the data from Siqueiros, Northern Iceland, Equatorial Atlantic and the undersaturated D-MORB glasses all exhibit these negative correlations between CO_2/Ba and Ba. Furthermore, if CO_2 has not degassed prior to inclusion entrapment, the correlation coefficient between CO_2/El and 1/El should reverse sign as trace elements go from being more incompatible to more compatible than CO_2 during melting (Figure 4.4). The data from both Siqueiros and Equatorial Atlantic retain a positive correlation far beyond the experimental CO_2 partition coefficient (Rosenthal et al., 2015), and beyond Nb which CO_2 has been likened to empirically (Saal et al., 2002). This decoupling between the apparent partition coefficients of C and trace elements in all these datasets also suggests that they have experienced partial degassing.

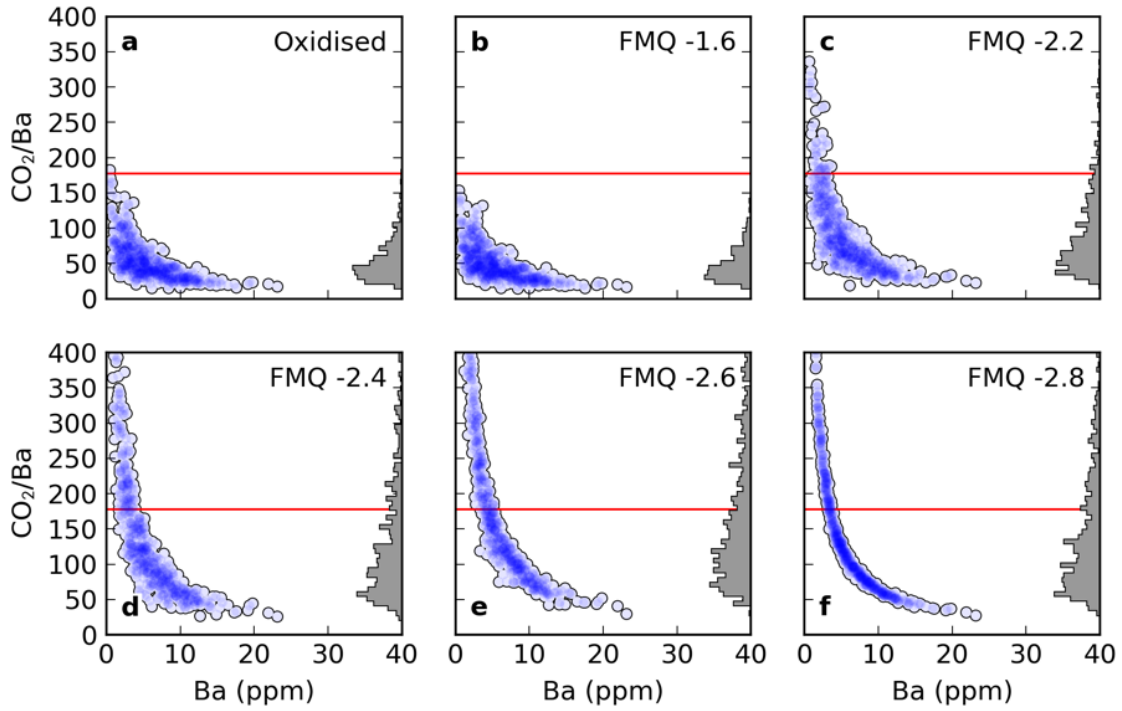

Figure 4.12: Results of the mixing and degassing model for melts produced during graphite saturated melting (Duncan and Dasgupta, 2017) and degassing at 2000 bar. The horizontal red lines show the source CO2/Ba ratio. The shading shows the distribution density.

At higher values of trace element *D*, the correlation coefficients between CO_2/El and 1/El calculated from the published data departs from the predicted behaviour (Figure 4.4b). This departure is likely to arise from the behaviour of these elements during garnet-field melting or fractional crystallisation. When garnet is in the residue, the bulk partition coefficients during mantle melting increase significantly. This variation can be modelled with the alphaMELTS frontend (Smith and Asimow, 2005) to the pMELTS thermodynamic model (Ghiorso et al., 2002), and the resulting correlations are shown in Figure 4.4 (dashed lines, calculation details given in figure caption). Garnet-field melting can account for this discrepancy, though I do not rule out the role of fractional crystallisation.

The undersaturated glass dataset, shown in Figure 1.3 and 4.1, displays CO_2 co-variation with both Ba and Nb; additionally, and a negative correlation between CO_2/Ba and Ba. These properties are consistent with the partial degassing and mixing model despite the dataset not representing co-genetic melts. The partial degassing and mixing process may still be controlling the systematics of this dataset if the glasses are derived from melts sampling sources with the same CO_2/Ba, but with different proportions of low and high degree melts, and mixing occurring at similar pressures. Whilst this uniformity is not ubiquitous in the global mid-ocean ridge system, it may well be present when only undersaturated glasses are considered. Alternatively, varying mantle Ba concentration, at near-constant

CO_2 concentration, could generate the observed covariation between CO_2/Ba and Ba concentrations in the glasses.

Previous studies have interpreted melt inclusions from the Siqueiros fracture zone to be near primary melts, having undergone negligible mixing and fractionation within the crust (Perfit et al., 1996). However, the CO_2- trace element systematics are difficult to explain without the partial degassing and mixing processes. The Siqueiros melts are very depleted in trace elements. Furthermore, whilst the trace element data might be matched by batch melting models, it does not preclude their origin from mixing of more variable fractional melts. U-Series disequilibria provide support for fractional melting, indicating that Siqueiros fracture zone melts segregated from their residue at small porosities in a process that must therefore have been near-fractional (Lundstrom et al., 1999). Recent seismic evidence suggests axial magma chambers are present beneath ultra-slow spreading ridges (Jian et al., 2017). Therefore, despite the lower rates of magma supply, these slow spreading systems nonetheless retain melt that new primitive magmas may interact with during their transport and storage in the crust.

4.4.2 Global mantle CO_2 heterogeneity

Substantial heterogeneity in the CO_2/Nb and CO_2/Ba ratios of the depleted mantle has been inferred from the variation in averages of these ratios, obtained by fitting lines though data in CO_2-Ba and CO_2-Nb space from Siqueiros, Northern Iceland and the Equatorial Atlantic. For the reasons outlined above, the inclusions measured in these studies are all likely to be preserving partially degassed melts. When partial degassing and mixing has taken place the apparent ratio in CO_2-Ba and CO_2-Nb space is determined not by the primary mantle ratios, but by the degassing pressure (Section 4.2.4). Instead, the best estimate of mantle CO_2 concentration comes from the maximum ratio CO_2/Ba ratio recorded by the most trace element depleted melts in the dataset; these melts are the most likely to have remained CO_2 undersaturated (Section 4.2.2). The maximum CO_2/Ba ratios observed in melt inclusions from Siqueiros and Northern Iceland, and the undersaturated D-MORB glasses, are all $\sim$140 (with a maximum value of 146). If this observed maximum ratio is close to the real maximum of the distributions of mixed melts, then it suggests all three datasets are consistent with a single depleted mantle CO_2/Ba ratio. Furthermore, apart from one extreme outlier, the maximum CO_2/Ba ratios in melt inclusions from Axial Seamount (Helo et al., 2011) and Gakkel Ridge (Shaw et al., 2010; Wanless et al., 2014) are consistent with this (Figure 1.3). In contrast, the maximum CO_2/Ba ratio observed in the Equatorial Atlantic melt inclusions is 107. This could be reconciled either by the Equatorial Atlantic dataset not adequately characterising the maximum CO_2/Ba ratio in the distribution, or by localised mantle CO_2/Ba heterogeneity as might be expected given the presence of Ba/Nb heterogeneity in the MORB source (Michael and Graham, 2015). Though small-scale mantle heterogeneity has been observed in both the MORB and Iceland mantle sources, linking this to volatile

elements such as carbon is intrinsically difficult owing to a bias in preserving the CO_2/Ba ratios of only the most depleted melts.

An alternative possibility to the model I have developed here is that diversity in melt CO_2/Ba and CO_2/Nb arises from mantle CO_2/Ba and CO_2/Nb heterogeneity. Melting of such a heterogeneous mantle must produce both a high CO_2/Ba, low Ba component, and a low CO_2/Ba, high Ba component. For the observed negative correlations between CO_2/Ba and Ba to be generated, a low CO_2/Ba, low Ba component cannot be involved in mixing. However, generating such melts is a natural consequence of melting mantle heterogeneities beyond the smallest of melt fractions, at which point even enriched lithologies are depleted in highly incompatible elements such as Ba. Therefore, mantle heterogeneity alone is highly unlikely to account for the observed correlations.

4.4.3 Constraining mantle CO_2/Ba

In a partially degassed dataset, the CO_2/Ba measurement most likely to represent the mantle CO_2/Ba ratio is the maximum ratio observed. A disadvantage of utilising maxima in geochemical datasets is that they are strongly dependent on sample size. For melts to preserve high CO_2/Ba they must have minimal interaction with degassed melts. Depending on the diversity of melts entering magma storage regions, only a small proportion of melts may retain their primary CO_2/Ba. It is therefore most pragmatic to consider the likelihood of melts retaining a CO_2/Ba ratio within 10% of the mantle value. Figure 4.13 shows the minimum number of melt inclusion analyses (or here, Dirichlet distributed draws from a population of synthetic melts) required for the maximum CO_2/Ba ratio measured to be within 10% of the mantle value (with $>$99.8% certainty), for a melting column typical of normal mid-ocean ridges. Since Siqueiros has been identified as sampling ultra-depleted mantle, Figure4.13b demonstrates how the minimum number of analyses changes if trace element concentrations are more depleted in the mantle source (Workman and Hart, 2005). At constant source CO_2/Ba ratio, a source more depleted in trace elements will produce melts that are, on average, less CO_2 rich, and therefore more likely to retain their primary CO_2/Ba ratio. The number of analyses required increases as degassing pressure decreases and mantle CO_2/Ba increases; both these changes cause the proportion of melts degassing CO_2 to increase, therefore increasing the likelihood of an undegassed melt mixing with degassed melt and thus erasing the signal of primary CO_2/Ba from the population of melts. In addition, the value of the mixing parameter will affect the position of the contours in Figure4.13, with greater degrees of mixing making observing mantle CO_2/Ba less likely. Making large numbers of analyses on melt inclusions trapped at high pressure offers the greatest prospect of observing the mantle CO_2/Ba ratio.

Both the Borgarhraun and Siqueiros datasets consist of around 100 melt inclusion analyses each (Figure 4.13a). Provided these inclusions were trapped at sufficient pressure, the maximum CO_2/Ba

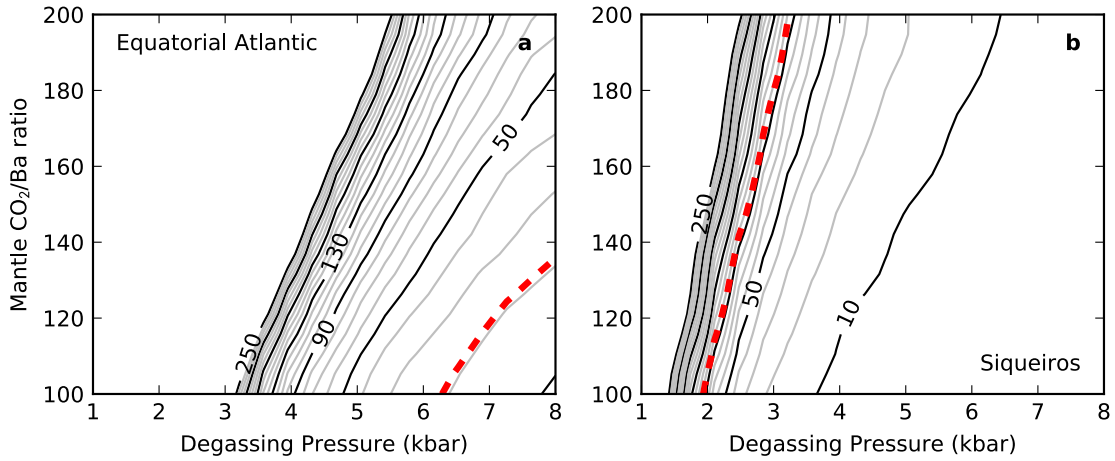

Figure 4.13: Contours of the minimum number of analyses required to get at least one analysis (in all of 500 model runs) recording a CO_2/Ba ratio within 10% of the mantle value, as a function of degassing pressure and mantle CO_2/Ba ratio. Contours are spaced at intervals of 10 analyses. In panel a the melting model described in Section 4.1.1 is used and is appropriate for the comparison to the Equatorial Atlantic dataset (Le Voyer et al., 2017), which contains 21 melt inclusion analyses, indicated by the thick red dashed line. Panel b uses a similar melting model, but with a mantle Ba concentration typical of the D-MORB source (Workman and Hart, 2005), and is appropriate for comparison with the Siqueiros dataset (Saal et al., 2002), which contains 97 analyses. In both panels the mixing parameter is set to $N = 16$.

they record is likely to be very close to the mantle value. However, the Mid-Atlantic dataset consists of 21 melt inclusion analyses only (Figure 4.13a). Barometry indicates crystallisation takes place at pressures as high as 10 kbar beneath the Mid-Atlantic ridge, though erupted liquids predominantly equilibrate at lower pressures (Herzberg, 2004). If the Mid-Atlantic dataset is also sampling a mantle of CO_2/Ba = 140, Figure 4.13 suggests the maximum observed CO_2/Ba ratio will only preserve the mantle value if inclusions were entrapped at the deepest extents of crystallisation (>8 kbar). Therefore, the Mid-Atlantic dataset may also be consistent with a mantle CO_2/Ba ratio of 140.

Assuming a Ba concentration in the depleted mantle of 0.563 ppmw (Workman and Hart, 2005), a CO_2/Ba ratio of 140 ppmw implies a mantle CO_2 content of 79 ppmw, more than double that inferred by (Workman and Hart, 2005) from the canonical CO_2/Nb ratio (Saal et al., 2002). (Rosenthal et al., 2015) reach a similar conclusion, and also discuss the likely CO_2 content of mantle melting beneath intra-plate volcanoes.

4.4.4 Origin of CO_2 undersaturation

Both the Siqueiros melt inclusions and undersaturated mid-ocean ridge glass datasets record CO_2 concentrations that are undersaturated at the pressure of eruption, and the CO_2 concentrations present in the Equatorial Atlantic dataset would be undersaturated at during crystallisation within the oceanic crust. This CO_2 undersaturation has been used as further evidence for the absence of degassing (Michael and Graham, 2015; Saal et al., 2002). Though the mixing-degassing model requires some of the fractional melts to become CO_2 saturated, they subsequently mix with highly CO_2 undersaturated melts, resulting in all melts becoming undersaturated at the pressure of degassing (Figure 4.6). If a sufficient mass of depleted melts are present, this undersaturation may be retained at the pressure of eruption, as in the Siqueiros and undersaturated mid-ocean ridge glass datasets, even with mixing in of enriched low CO_2/El melts having occurred.

4.5 Summary

CO_2 concentrations in melt inclusions provide an important constraint on global CO_2 flux from the mantle at mid-ocean ridges and ocean islands and are vital for assessing CO_2 heterogeneity in the mantle. Melt inclusion datasets are a key petrological tool for addressing these problems, and in this study I have formalised the robustness of the melt inclusion archive to the common magmatic processes of mixing and degassing.

I have identified how trace elements co-vary with CO_2 in melts, following mixing of trace element depleted CO_2 undersaturated melts with trace element enriched CO_2 saturated melts. I show that when degassing occurs, CO_2 may have a stronger correlation with Nb, even if its partitioning behaviour during melting is more similar to Ba (Rosenthal et al., 2015). I find that the average CO_2/Ba ratio in a melt inclusion dataset is dominated by the pressure of degassing, rather than the mantle CO_2/Ba ratio. The best estimate of mantle CO_2/Ba ratio is, instead, the maximum CO_2/Ba ratio observed.

Comparison of the model results with CO_2-undersaturated D-MORB glasses (Michael and Graham, 2015), and melt inclusion datasets from Northern Iceland (Hauri et al., 2018), Siqueiros (Saal et al., 2002) and the Equatorial Atlantic (Le Voyer et al., 2017), suggests these datasets all record CO_2 concentrations generated by mixing of partially degassed melts (Section 4.4). I argue that the available datasets are all consistent with a depleted mantle CO_2/Ba of 140, and do not require heterogeneity in mantle CO_2/Ba.

The role of mixing in the generation of melts trapped in melt inclusions has been neglected in the interpretation of CO_2 concentrations, leading to underestimation of the CO_2 content of the mantle and

inferences of CO_2 heterogeneity. Despite the likely presence of partial degassing in all melt inclusion datasets, fully characterising the maxima of CO_2/Ba values by making many melt inclusion analyses may allow the mantle CO_2/Ba ratio to be extracted from the data. Subject to the assumptions of the simple melting and mixing models, the likelihood of recovering mantle CO_2/Ba in melt inclusion datasets can be estimated, a result which is useful in preparing analytical studies.

Chapter 5

Controls on H_2O-trace element systematics

In the previous chapter the comparison of magmatic CO_2 concentrations to trace elements was justified on the basis of needing to identify datasets that have lost CO_2 due to degassing. Whilst the solubility of H_2O in magmas is much greater than CO_2 (Dixon and Stolper, 1995), H^+ can diffuse extremely quickly through olivine (Mackwell and Kohlstedt, 1990). Melt inclusions, therefore, may not record their primary H_2O concentrations (Bucholz et al., 2013; Danyushevsky et al., 2002; Gaetani et al., 2012; Hartley et al., 2015).

In this Chapter I consider how H^+ diffusion may affect H_2O-trace element systematics in melt inclusion suites, and demonstrate that primary magmatic H_2O/Ce ratios may be inferred from melt inclusion datasets in some cases. Making the comparison between H_2O and trace element concentrations is advantageous as corrections for mantle melting and crystal fractionation are not required for calculating mantle H_2O concentrations. I begin by assessing the evidence for the similarity in partitioning behaviour between H_2O and the incompatible trace elements during mantle melting (Section 5.1), and then consider the effect of H^+ diffusion on melt inclusion H_2O concentrations (Section 5.3).

5.1 H_2O partitioning behaviour

In Section 1.2 I discuss previous studies of mantle H_2O, many of which utilised H_2O-trace element ratios in an attempt to remove the signals of mantle melting and crystallisation (e.g Dixon et al., 2017; Hirschmann, 2018; Michael, 1995). Ce has been the trace element most widely employed for this

approach, after Michael (1995) argued Ce and H_2O behave identically during mantle melting and crystallisation. Michael (1995) made this inference based on the observation that the H_2O/Ce ratios of MORB glasses show little co-variation with indices of melting and source enrichment, such as La/Sm and Nb/Zr ratios, on a regional scale. In contrast, Dixon et al. (1988) argued H_2O behaves most similarly to La during melting, based on the relative homogeneity of H_2O/La in basaltic glasses from the Juan de Fuca Ridge. Danyushevsky et al. (2000) used similar observations to suggest H_2O may behave most similarly to La in depleted-MORB and Ce in enriched-MORB.

In all the cases above, it is the empirical H_2O-trace element systematics of natural basalt suites that have been used to evaluate water partitioning behaviour and find its lithophile element twin (El). A potential shortcoming of this approach, however, is if the source is heterogeneous in its H_2O/El ratio because of a process that affects H_2O but not its lithophile element twin (e.g. degassing). In this case, the denominator element minimising variance is not necessarily the element with the most similar partitioning behaviour to H_2O during mantle melting and crystallisation. Empirical approaches would then risk aliasing in heterogeneity and melting/differentiation processes into their selection of water's lithophile element twin.

This aliasing of source and process is important to consider as the MORB-source mantle is evidently heterogeneous: studies employing dense sampling of small sections of mid-ocean ridges have demonstrated that trace-element enrichment generally correlates with radiogenic isotope ratios, and the enrichment is therefore a long-live feature of the MORB source (e.g. Bergmanis et al., 2007; Gale et al., 2013b; Gill et al., 2016). Moreover, this heterogeneity has been interpreted as resulting from subduction recycling (e.g Eiler et al., 2000; Hemond et al., 2006; Ulrich et al., 2012) and so could readily have included sources that have gained or lost water independently of lithophile trace elements (Hirschmann, 2018). These observations require that MORB magmas are assembled from varying mixtures of melts from a heterogeneous mantle, which may not have a uniform H_2O/El.

Significant covariation in H_2O/Ce with trace-element and radiogenic isotope enrichment has been observed in plume influenced MORB (e.g. Dixon et al., 2017). If the enriched material in the MORB-source mantle (distant from plumes) has a similar history to the enriched material in plumes, then we might expect the H_2O/Ce ratio of MORB to also co-vary with enrichment. The lack of co-variation between H_2O/Ce and enrichment seen by Michael (1995) could, therefore, instead imply an inappropriate choice of lithophile twin, and that H_2O and Ce are not equally compatible during melting.

Determining the partitioning of H_2O between silicate melts and minerals has also been approached experimentally (Aubaud et al., 2004; Hauri et al., 2004, 2006; Koga et al., 2003; Tenner et al., 2009). Hauri et al. (2006) and Tenner et al. (2009) found a strong dependence of the H_2O partition coefficient between melt and the mantle mineral assemblage, $D(H_2O)$, on the Al_2O_3 content of the pyroxene.

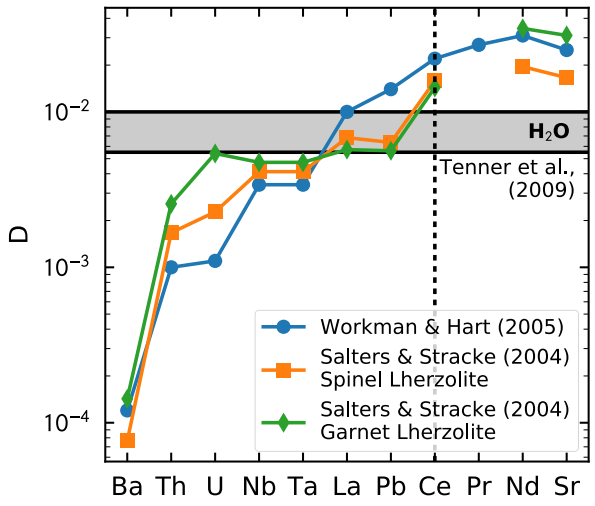

Figure 5.1: Comparison of the experimental bounds on H_2O partitioning during mantle melting determined by Tenner et al. (2009), shaded grey, with the partition coefficients of the most incompatible trace elements compiled by Salters and Stracke (2004) and Workman and Hart (2005). The vertical dotted line highlights Ce.

Pyroxene Al_2O_3 changes significantly with pressure, causing $D(H_2O)$ to vary simultaneously. The range of $D(H_2O)$ for typical mantle melting as calculated by Tenner et al. (2009) is shown in Figure 5.1. The values of $D(H_2O)$ overlap with the values for D(La) reported by Salters and Stracke (2004) and Workman and Hart (2005), but fall below estimates D(Ce). The experimental constraints therefore suggest La may be the best lithophile twin for H_2O, rather than Ce.

5.2 Modelling MORB H_2O-trace element systematics

Since it is likely that the mantle heterogeneities variably sampled by depleted- and enriched-MORB have different H_2O/Ce (and H_2O/La) ratios, fractionation between H_2O and Ce during near-fractional melting, followed by partial mixing, may contrive to generate lavas with apparently invarient H_2O/Ce with enrichment. I test this by applying the Rudge et al. (2013) Dirichlet mixing model, described in Section 4.1.3, to fractional melts from a comparatively enriched mantle source and a depleted mantle source. Melt compositions are generated using pMELTS (Ghiorso et al., 2002) with alphaMELTS interface (Smith and Asimow, 2005). Variable trace element partition coefficients are used for garnet and clinopyroxene (Van Westrenen et al., 1999; Wood and Blundy, 1997) and constant partition coefficients are used for olivine, orthopyroxene and spinel (McKenzie and O'Nions, 1991, 1995). The partition coefficient of H_2O is calculated using the parameterised equations of Tenner et al. (2009). The calculations are performed with Si, Al, Fe^{2+}, Fe^{3+}, Mg, Ca, Ti and Na, using the composition of the depleted mantle estimated by Workman and Hart (2005). Trace element concentrations are set to the 'DDM' and 'EDM' endmembers calculated by Workman and Hart (2005). To generate the depleted melts, melting starts in the spinel-stability field, following adiabatic decompression from

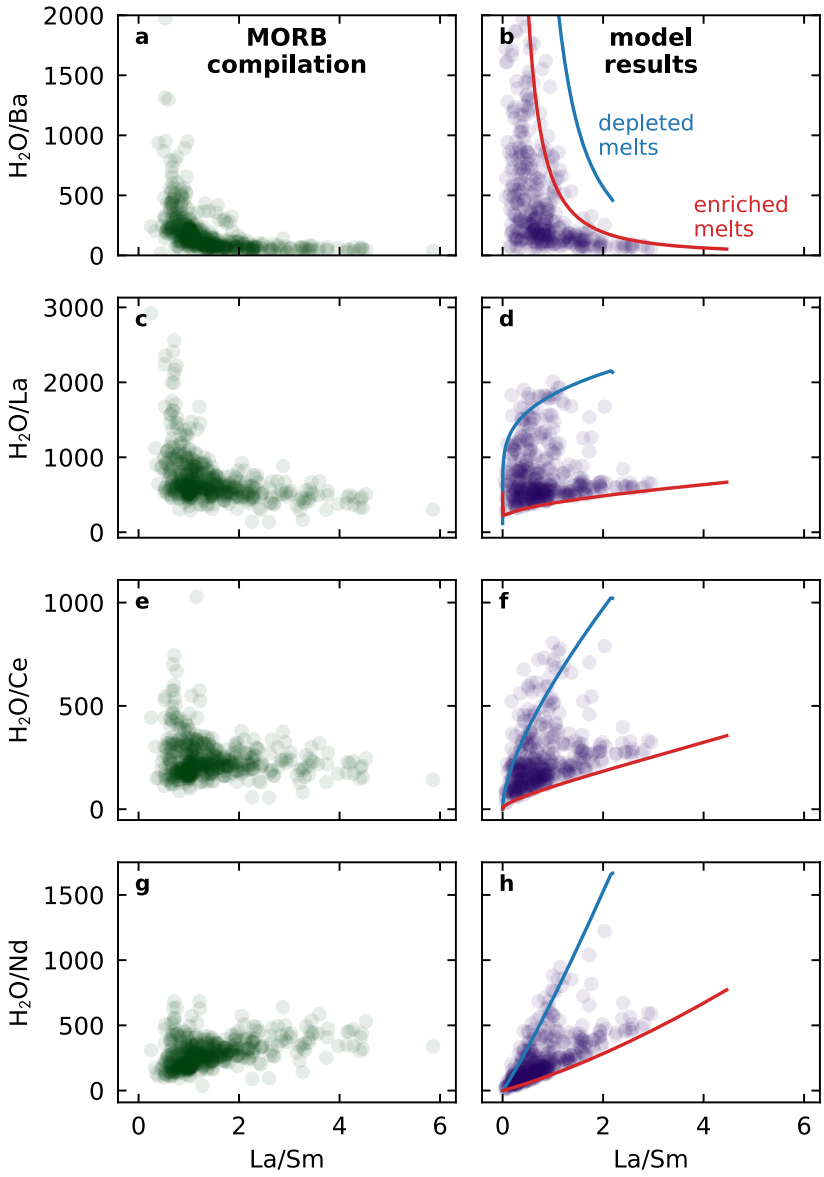

Figure 5.2: Panels a, c, e and g show data from a compilation of global MORB (sources in Appendix B). Panels b, d, f, and h show the results from the melting and mixing model described in the text. The scatter points show 400 draws from the distribution of mixed melts. The lines show the loci of 'depleted' spinel-field melts and 'enriched' garnet-field melts. In all panels the shading indicates the data density.

4.5 GPa and 1430 °C. In order for the enriched melts to have high LREE/HREE ratios melting is started in the garnet-stability field by increasing the starting temperature to 1580 °C.

The results of the melting and mixing model are shown alongside a compilation of MORB glasses in Figure 5.2. The model matches the general shapes of the H_2O/Ba, H_2O/La, H_2O/Ce and H_2O/Nd distributions, suggesting that locally variable H_2O/Ce and $D(H_2O)\sim D(La)$ are consistent with the main features of global MORB. Locally invarient H_2O/Ce and $D(H_2O)\sim D(Ce)$ during melting and crystallisation, as suggested by Michael (1995), are not required by the data. The smaller range in La/Sm seen in the samples from the studies by Dixon et al. (1988) and Danyushevsky et al. (2000), than in the compilation by Michael (1995) lend support to this hypothesis.

5.3 Overcoming diffusive H_2O re-equilibration in melt inclusions

Though melt inclusions can retain higher pressures than their surroundings, allowing them to retain higher volatile concentrations during eruption, the melt may diffusively re-equilibrate with the host crystal and surrounding melt. The diffusion of H^+ through olivine is particularly rapid in comparison to other elements (Mackwell and Kohlstedt, 1990), and there is abundant experimental and empirical evidence for both H^+ loss and gain from melt inclusions by diffusive exchange with the external melt (Bucholz et al., 2013; Danyushevsky et al., 2002; Gaetani et al., 2012; Hartley et al., 2015). Melt inclusions are therefore unlikely to preserve their primary H_2O concentration. However, if eruption is sufficiently rapid, the inclusions may preserve the H_2O concentration they obtained during storage despite syn-eruption degassing of their carrier melt. In this scenario, though H_2O has been decoupled from the lithophile trace elements by diffusive re-equilibration, the melt inclusion still preserves the pre-eruptive H_2O budget of the carrier magma.

To assess the fidelity of melt inclusions for preserving their pre-eruptive H_2O concentrations, I examine the H_2O budget of melt inclusions where their carrying melt is unlikely to have lost H_2O upon eruption. Submarine eruptions along the mid-ocean ridge system are erupted at sufficient pressure that H_2O may be expected to remain soluble during eruption. Figure 5.3 shows melt inclusion data from two such eruptions: the first from the Siqueiros fracture zone (Saal et al., 2002) and the second from the Equatorial Atlantic (Le Voyer et al., 2017). Both datasets preserve excellent correlations between Ce and Nb concentrations, elements whose partition coefficients bracket the partitioning behaviour of H_2O (Figure 5.1). In the absence of diffusive re-equilibration, H_2O concentrations in magmas might be expected to mimic Nb and Ce, and therefore similarly strong correlations between Ce, Nb and H_2O would be expected. No such correlation exists in Figure 5.3a and b, suggesting diffusive re-equilibration of H_2O in melt inclusions has occurred in both of these eruptions. However, the mean

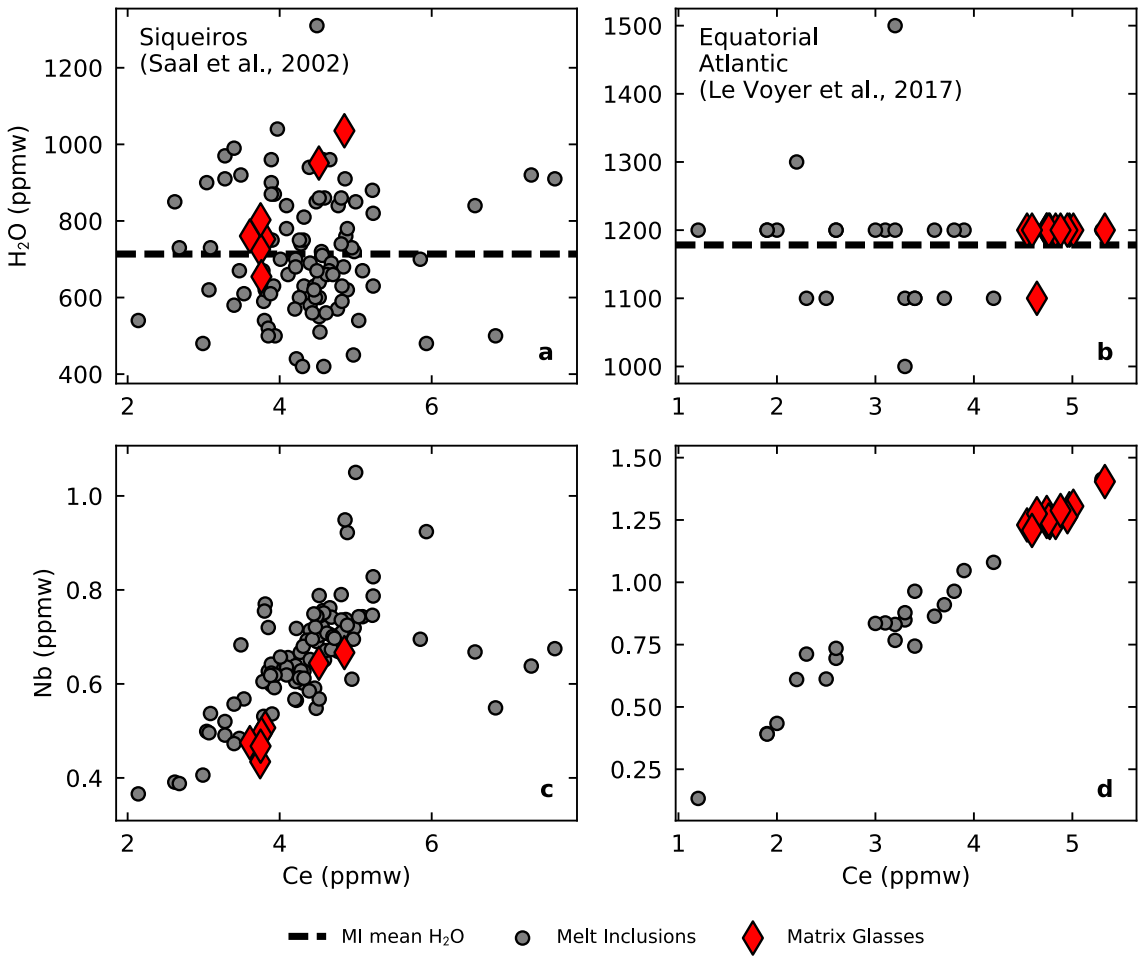

Figure 5.3: Panels a and b show the H_2O and Ce concentrations in melt inclusions and glasses from Siqueiros (Saal et al., 2002) and the Equatorial Atlantic (Le Voyer et al., 2017). The mean water content of the melt inclusions is shown by the horizontal dashed line. Panels c and d show the correlations present between the similarly incompatible elements Nb and Ce.

H_2O concentration of the melt inclusions (indicated by the horizontal dashed line in Figure 5.3) is close to matrix glass H_2O concentration.

The coincidence of the melt inclusion mean H_2O concentration with the H_2O concentration in matrix glasses for the Siqueiros and Equatorial Atlantic eruptions shown in Figure 5.3, suggests melt inclusions may offer a view of the pre-eruptive H_2O concentrations of their carrier melt. Whilst this offers little advantage for eruptions where the matrix glass has remained undersaturated in H_2O vapour, it might enable assessment of pre-eruptive H_2O concentrations in sub-aerially erupted lavas where the matrix has undergone H_2O loss.

For melt inclusions to retain a record of the pre-eruptive H_2O concentrations, the timescale between H_2O vapour loss and quenching must be sufficiently short that significant H_2O has not been lost from the inclusions by re-equilibration with the degassing carrier melt. The melt inclusion mean H_2O is therefore a minimum bound on the pre-eruptive H_2O concentration, and the likelihood that they underestimate pre-eruptive H_2O must be assessed on an eruption by eruption basis. If H_2O has remained undersaturated during crustal storage, then the mean melt inclusion H_2O may be combined with the La concentration in the matrix glass to estimate the H_2O/La ratio of the primary melt (and in turn of the mantle). The La concentration in the matrix should be used in preference to the melt inclusion mean La concentration because any changes in H_2O and La concentration due to crystallisation may not be preserved by early trapped melt inclusions. In Section 7.2 I evaluate and apply the mean H_2O method to the Iceland melt inclusion dataset, in order to place new constraints on the H_2O heterogeneity in the Iceland plume.

5.4 Summary

The experimental data for H_2O partitioning between silicate minerals and melt suggests that La is the best lithophile twin element for H_2O, being the least likely element to be fractionated from H_2O during melting and crystallisation (Section 5.1). In spite of the experimental evidence, H_2O concentrations are most frequently compared to Ce, rather than La, when filtering out the signal of melting and crystallisation within a dataset. In Section 5.2 I demonstrated that aliasing of H_2O/Ce fractionation during melting with H_2O/Ce heterogeneity in the MORB source mantle may have lead empirical studies to conclude that the behaviour of Ce most closely matches H_2O during melting and crystallisation. In Section 5.3 I argued that though melt inclusions are unlikely to retain their primary H_2O concentrations, they are likely to be a good record of the H_2O concentration in the matrix glass pre-eruption. Melt inclusion H_2O concentrations may therefore be a valuable tool in assessing the H_2O/Ce ratios in the mantle sampled by sub-aerial eruptions.

Chapter 6

Carbon Heterogeneity in the Icelandic Mantle

In this chapter I seek to assess the presence of carbon rich mantle reservoirs in the Earth. In order to deconvolve the signals of CO_2 degassing and mantle heterogeneity, large numbers of melt inclusions from eruptions sampling a diversity of mantle sources are required to be analysed for both their trace element and CO_2 concentrations. I approach this by considering mantle carbon heterogeneity on the scale of both a single well sampled mantle plume (Iceland), and a global scale with more sparsely sampled mid-ocean ridges and ocean islands. Iceland offers an excellent opportunity for studying carbon heterogeneity within a single mantle plume due to the number of previous melt inclusion studies (Bali et al., 2018; Hartley et al., 2014; Hauri et al., 2018; Neave et al., 2014; Schipper et al., 2016), to which I supplement with four additional datasets (Sections 2.1.2 and Section 6.1).

Comparisons between the CO_2-trace element systematics present within the Iceland melt inclusion compilation and the global compilation enable us to make a new assessment of the effects of crustal storage and melt inclusion decrepitation (Section 6.5). Though this secondary crustal processing signal dominates the global CO_2/Ba and CO_2/Nb arrays, in Section 6.6 I demonstrate that a signal of mantle source CO_2 heterogeneity still remains in the Iceland compilation. By inversion of binary mixing models (Section 6.6.2) I estimate CO_2 concentrations, and their uncertainties, in endmember mantle components within the Iceland plume. I find evidence that CO_2 concentrations higher than in the depleted are present within both recycled and primordial mantle.

6.1 New melt inclusion observations from Iceland

Melt inclusion CO_2 and Ba concentrations, with and without bubble corrections, are shown for each eruption in Figure 6.1. All four eruptions show considerable variation in their CO_2/Ba ratios, but only Háleyjabunga and Stapafell display positive correlations between CO_2 and Ba. Only three Háleyjabunga melt inclusions analysed by SIMS contained bubbles in which CO_2 vapour was detected (a further three were measured by Raman only, as shown in Figure 6.2d). Though five Stapafell melt inclusion hosted bubbles contained CO_2 vapour (Figure 6.2e), only one was contained in an inclusion analysed by SIMS. No CO_2 vapour was detected in any of the bubbles hosted in Heilagsdalsfjall inclusions. A substantial fraction of Berserkjahraun inclusions contained bubbles in which CO_2 vapour was detected. In Háleyjabunga, Stapafell and Berserkjahraun, the highest CO_2 concentrations are in inclusions where corrections have been applied. For Háleyjabunga and Stapafell, the corrected inclusions do not have higher CO_2/Ba than uncorrected inclusions. However, the corrections applied to the Berserkjahraun inclusions are extremely large and consequently significantly increase the CO_2/Ba ratios recorded by the melt inclusion population. The large magnitude of the corrections arises from high CO_2 vapour densities up to 0.75 g cm^{-3}. Though this density is above the maximum density of vapour in coexistence with liquid CO_2 at room temperature ($\sim$0.2 g cm^{-3}), any heating by the Raman instrument's laser could move the bubble beyond the CO_2 triple point. The bubble volume fraction exerts some control on the corrected CO_2 concentration, but little dependence on CO_2 vapour density is observed (Figure 6.3). A sub-population of three Háleyjabunga melt inclusions have much higher (bubble-uncorrected) CO_2 concentrations than the general population (distinguished on Figures 6.1 and 6.4), the origin of this feature is discussed further in Section 6.4.

Trace element concentrations in the four melt inclusion suites are shown in Figure 6.4. Melt inclusions from Háleyjabunga (Figure 6.4a) show extreme variability in relative trace element enrichment, Maclennan (2008b) and Neave et al. (2018) argued this variability is most likely mantle derived. The Háleyjabunga matrix has a depleted trace element pattern (Skovgaard et al., 2001). Four Háleyjabunga inclusions have anomalously high Ba and Nb concentrations relative to the light rare earth elements; since their CO_2 concentrations are similar to the main population of inclusions they have not retained high CO_2/Ba or CO_2/Nb ratios. The Háleyjabunga inclusion with highest CO_2/Ba ratio is part of the high-CO_2 population, but as I discuss in Section 6.4 this may not reflect a mantle value, and so I treat this inclusion as an anomaly here. Ignoring this anomalous inclusion, the highest CO_2/Ba ratios ($>$200) are observed in inclusions with depleted trace element patterns, but are not anomalously depleted among the larger population of Háleyjabunga inclusions. However, the Stapafell inclusions with highest CO_2/Ba (Figure 6.4b) show trace element patterns with anomalously low Ba and Nb concentrations relative to the light and middle rare earth elements. Despite the anomalous trace element patterns of a small number of Stapafell inclusions, Ba, Nb and CO_2 appear to be unfractionated from each other, as discussed in Section 6.3. The Stapafell melts show enriched

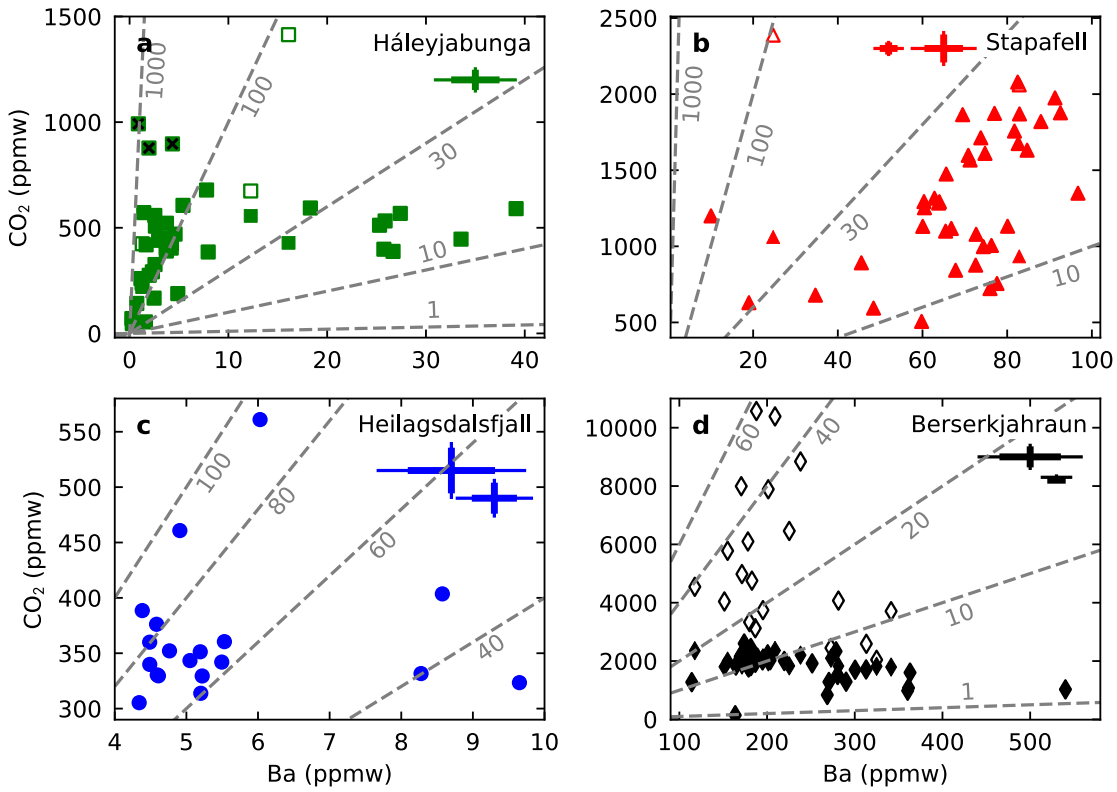

Figure 6.1: Melt inclusion glass (filled symbols) and reconstructed (open symbols) CO_2 concentrations plotted against Ba concentration for each of the four eruptions studied here. The dashed grey lines indicate constant CO_2/Ba ratio. In panel a (Háleyjabunga), the three inclusions thought to represent a different population, as discussed in the main text, are highlighted with black crosses. Error bars show typical uncertainties for enriched (large error bars), and depleted (small error bars) melt inclusion analyses in each eruption. The bold lines show the estimated 1 s.d. precision, and thin lines show 1 s.d. combined precision and accuracy. The uncertainties for the depleted Háleyjabunga inclusions are smaller than the markers.

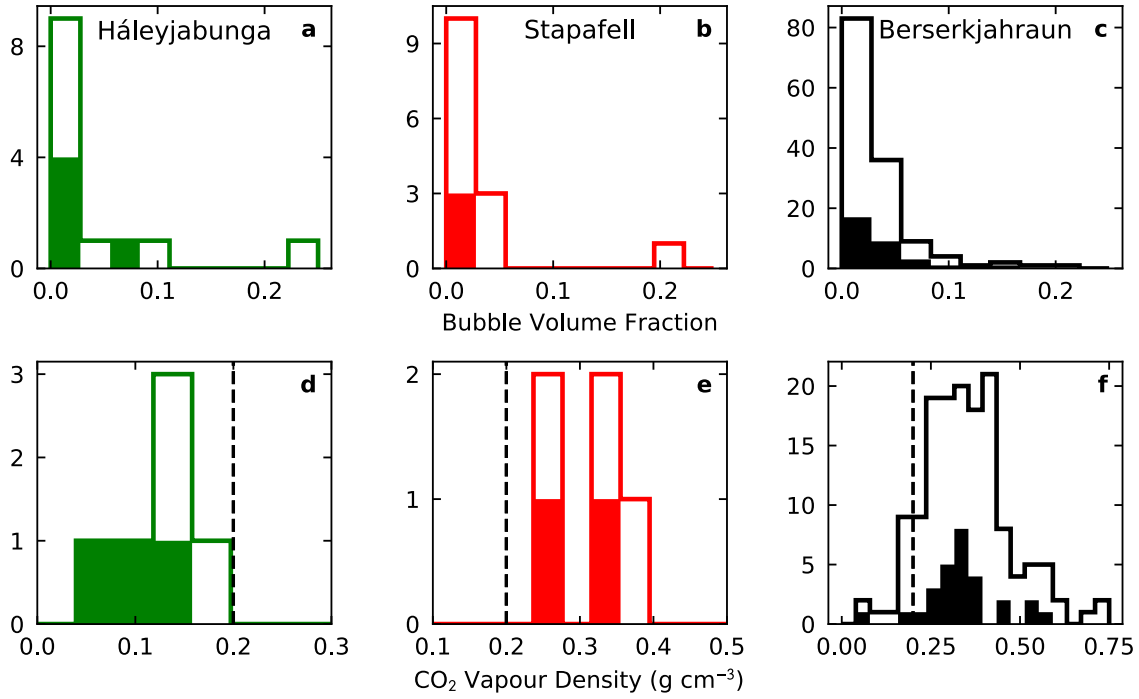

Figure 6.2: Distributions of the bubble volume fractions of the melt inclusions that host them for Háleyjabunga, Stapafell and Berserkjahraun (panels a. b and c), and the CO_2 vapour density calculated from Raman spectra for each eruptions (panels d, e and f). The vertical dashed line in panels d, e and f shows the maximum CO_2 vapour density when the temperature is below the triple point of CO_2. Filled bars show inclusions for which SIMS data were collected.

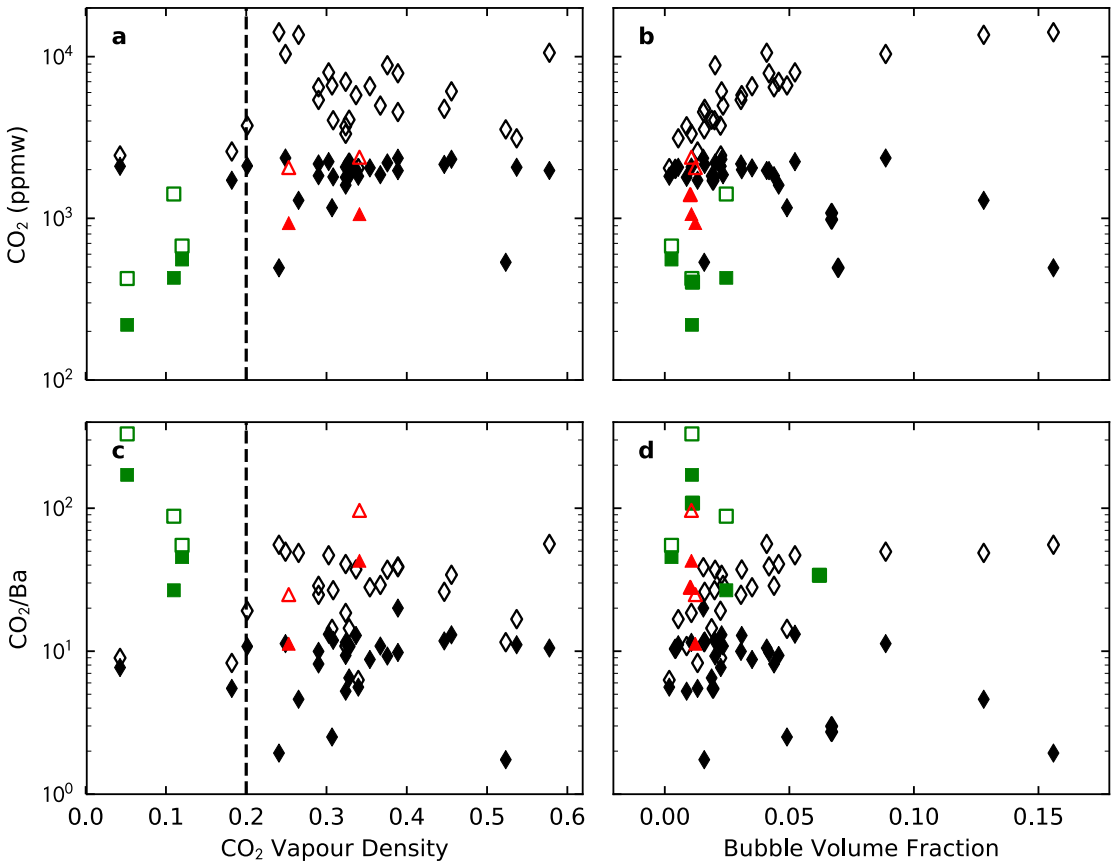

Figure 6.3: The CO_2 concentrations and CO_2/Ba ratios of bubble-corrected (unfilled symbols) and uncorrected (filled symbols) melt inclusions, as a function of CO_2 vapour density and bubble volume fraction. The vertical dashed line in panels a and c shows the maximum CO_2 vapour density when the temperature is below the triple point of CO_2. Symbols as used in the main text (Berserkjahraun: black diamonds; Stapafell: red triangles; Háleyjabunga: green squares).

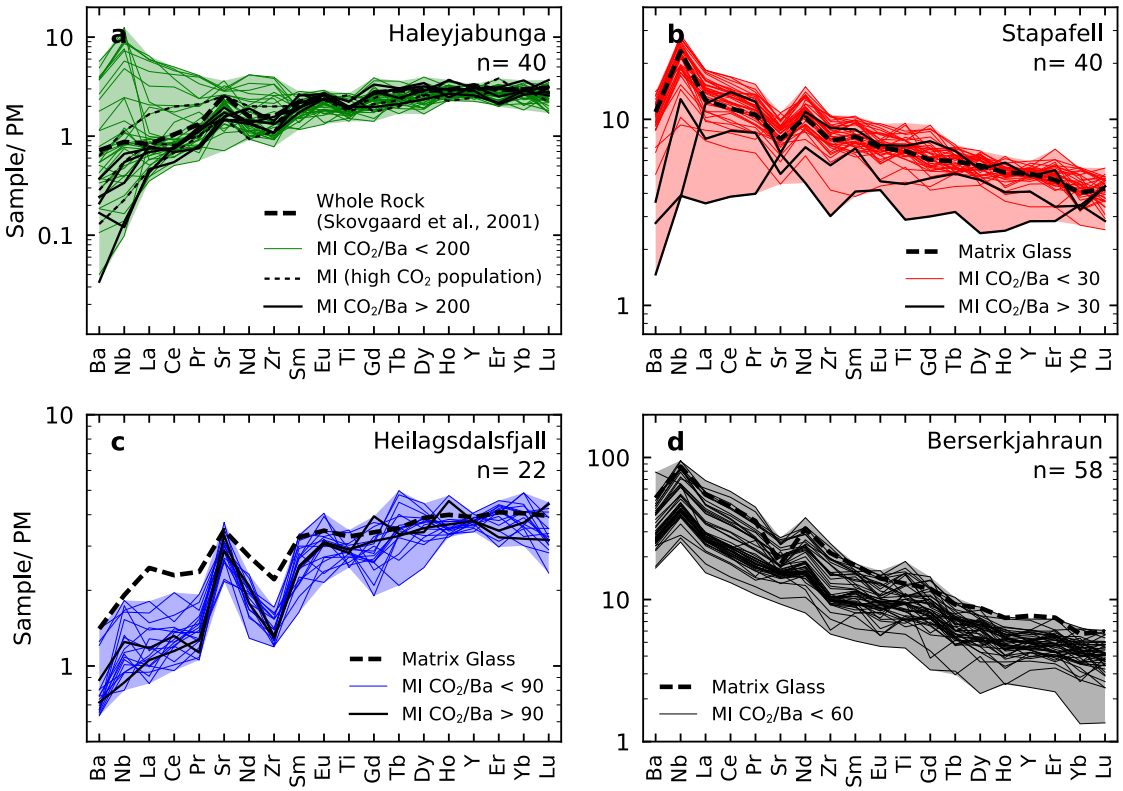

Figure 6.4: Normalised melt inclusion trace element concentrations. The region between the most extreme melt inclusions of each eruption is shown by shading. Also shown (as thick dashed lines) are the means of matrix glasses analyses for Stapafell, Heilagsdalsfjall and Berserkjahraun, and the whole rock analysis of Háleyjabunga reported by Skovgaard et al. (2001). The melt inclusions preserving the highest CO_2/Ba ratios are highlighted in black, with the threshold CO_2/Ba used reported in the legend for each panel. All analyses are normalised to the primitive mantle of Palme and O'Neill (2003).

trace element patterns, and the new observations are consistent with the conclusions of Neave et al. (2018) that the variability is not mantle derived, but largely reflects variable crystal fractionation. The Heilagsdalsfjall melt inclusions (Figure 6.4c) show little trace element variability, and have a strong depleted mantle signature. Berserkjahraun melt inclusions (Figure 6.4d) show the most extreme enriched signatures of the four eruptions, and show little mantle-derived variability among the inclusions. The small Sr- and Zr-anomalies seen in many of the inclusions from all four eruptions are likely the result of interaction with plagioclase in the crust (e.g. Aigner-Torres et al., 2007).

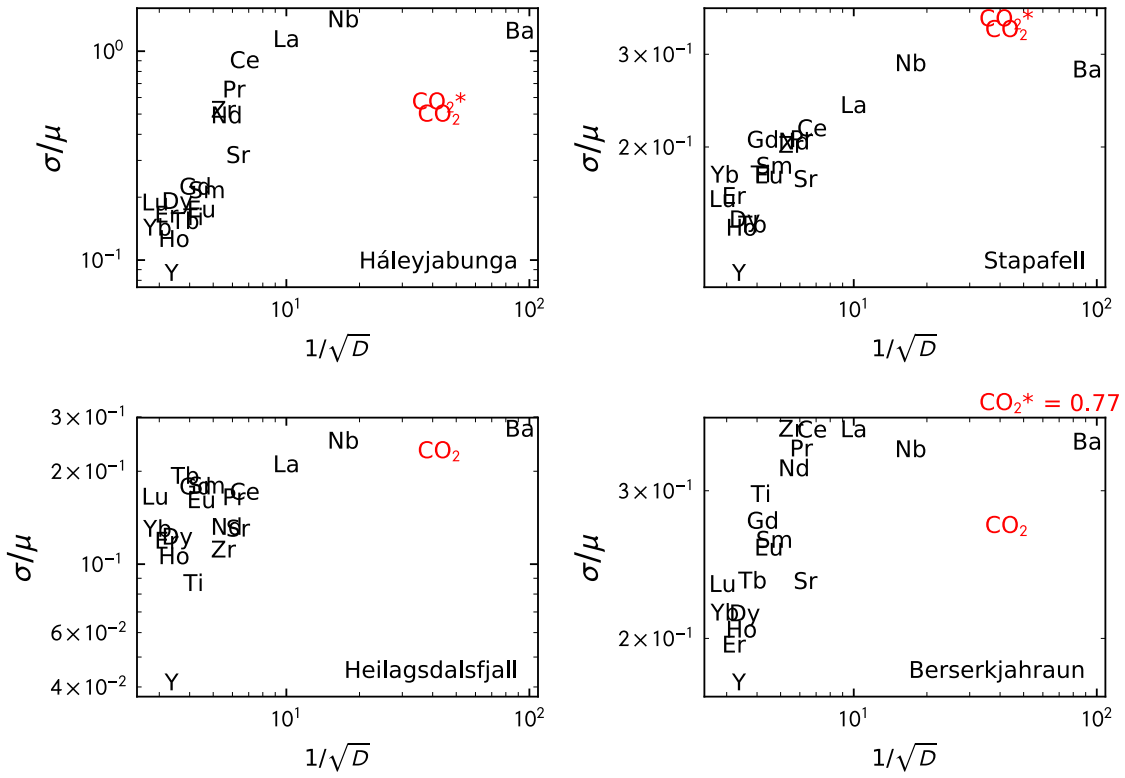

Figure 6.5: Each panel shows the variance structure of the melt inclusion population for the eruption shown in the bottom right-hand corner. The standard deviation (σ), normalised to the mean (μ), of each element is shown as a function of partition coefficient (D). The trace element partition coefficients reported by Workman and Hart (2005) are used. When elements are fractionated by fractional melting they will lie on a linear line of positive gradient in this space (Rudge et al., 2013). When elements have not been fractionated by any process they lie on a horizontal line. CO_2 is shown in red at the experimental partition coefficient determined by Rosenthal et al. (2015), CO_2* shows the same statistic when the bubble-correct CO_2 concentration is used. In panel d, the bubble corrected CO_2 variance plots off the top of the plot, and so its y-coordinate is shown.

6.2 Bubble corrections without CO_2 vapour density measurements

The bubble corrections applied to the melt inclusions in this study are all derived from observations of the CO_2 vapour density in the bubble. An alternative approach that has been used, for example in the Borgarhraun dataset by Hauri et al. (2018), is to calculate the CO_2 vapour density that would have been in equilibrium with the melt at the glass transition temperature. However, this assumes that diffusion of CO_2 through the inclusion was not kinetically limited. Neave et al. (2014) made comprehensive observations to show that any CO_2 present in the bubbles within melt inclusions from the Skuggafjöll eruption must be below detection limit, despite significant CO_2 concentrations within the glass. I therefore believe that such corrections must be regarded with great caution.

The variance structure of the Borgarhraun melt inclusions analysed by Hauri et al. (2018) is shown in Figure 6.6a. The positive trend between $1/\sqrt{D}$ and the normalised standard deviation (σ/μ) for elements more incompatible than Nb is consistent with them being fractionated from each other by fractional melting. The plateau defined by Nb, Th, U, Ba and Rb, suggests these elements were not fractionated from each other during fractional melting. Uncorrected CO_2 sits below this plateau, indicating the variance in CO_2 concentration has been reduced, most likely be partial degassing. When the bubble-corrected CO_2 concentrations are used instead (shown by the red CO_2*) the variance is higher than expected, given the variance of similarly compatible elements. For comparison, Figure 6.5 shows similar plots for the data presented here. Berserkjahraun and Stapafell also have CO_2* with a greater variance than expected. However, Berserkjahraun is most likely to have significant under-corrections for the CO_2 it has lost (see main text for discussion) and so this enhanced variance most likely represents scatter from variably incomplete correction. The uncorrected CO_2 concentrations from Stapafell also have a higher than expected variance, this is most likely to be generated by the melt inclusions preserving two stages of partial degassing and mixing. Borgarhraun has much simpler CO_2-trace element systematics, suggesting a single stage degassing and mixing process. This is supported by the correlation coefficients between 1/El and CO_2/El (where El is the concentration of a trace element) shown in Figure 6.6b. If CO_2 were behaving identically to a trace element, and had not undergone partial degassing and mixing, the correlation coefficient should rapidly decrease at the partition coefficient for CO_2, shown by the vertical dashed line (Chapter 4). The calculated correction should not give an incomplete correction, and so it is most likely that the elevated variance arises from over-correcting the CO_2 concentrations. I therefore omit these corrected values from the analysis presented here.

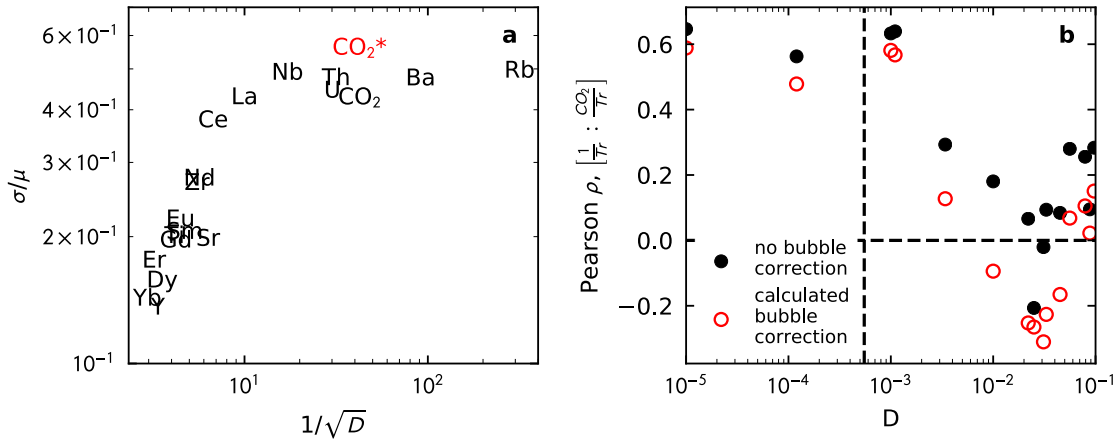

Figure 6.6: Panel a shows the variance structure of the Borgarhraun dataset. The standard deviation normalised to the mean for each trace element is shown as a function of its partition coefficient (D) as reported by Workman and Hart (2005). CO_2* indicates bubble-corrected CO_2 concentrations. Panel b shows the Pearson correlation coefficient for 1/El vs CO_2/El (where El is a trace element), as used in Chapter 4. The vertical dashed line shows the partition coefficient of CO_2 during melting as determined by Rosenthal et al. (2015).

6.3 Fractionation of Ba, Nb and CO_2 during melting

Primary magmas will only preserve mantle CO_2/Ba and CO_2/Nb ratios if Ba, Nb and CO_2 are not fractionated from each other during mantle melting. Crustal processes are not expected to fractionate Ba from Nb, but magma degassing will cause CO_2 to be fractionated from both. The melt inclusions least affected by degassing can be identified by taking the highest CO_2/Ba ratios (Chapter 4).

However, neither this filtering process, nor observations of the distribution of CO_2-trace element ratios, can conclusively rule out small degrees of fractionation of CO_2 from Ba and Nb during melting. Experimental work by Rosenthal et al. (2015) suggests that during mantle melting CO_2 should behave marginally more compatibly than Ba, and less compatibly than Nb. Therefore, if Nb and Ba have not been fractionated from each other during melting, then it is unlikely that CO_2 was fractionated from either. Fractionation of Ba and Nb will generate variations in the Ba/Nb ratio of melts systematically with Ba and Nb concentration. Figure 6.7a shows this is not seen in any of the eruptions in this study, or the other Icelandic eruptions in the compilation. The scatter in Ba/Nb ratio arises largely from analytical imprecision, but could also reflect small scale source heterogeneity.

Another approach to assessing fractionation is to compare the variability of trace element concentrations. The more incompatible an element behaves during melting, the greater its variability amongst instantaneous fractional melts of the mantle. If two elements in a dataset have the same mean-

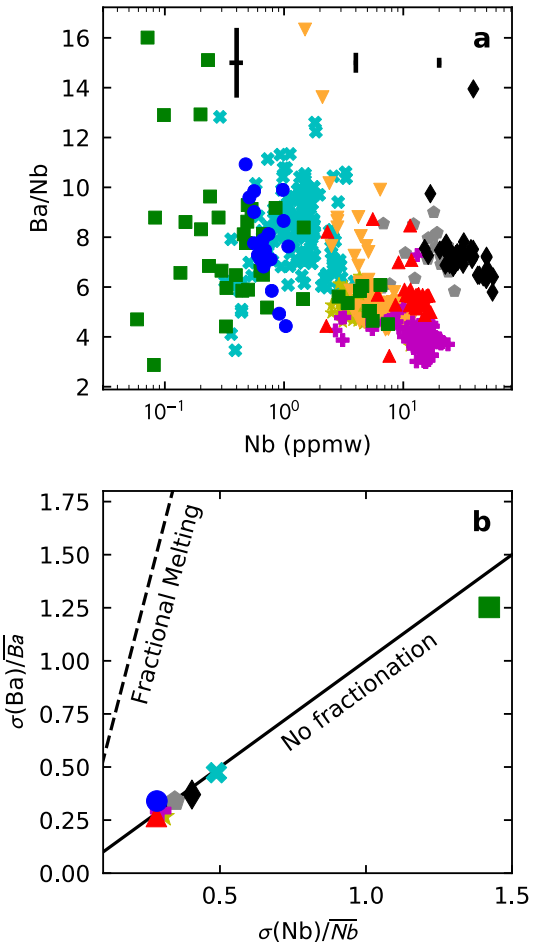

Figure 6.7: Panel a shows the Ba/Nb ratio of the melt inclusions from the eruptions in Figure 2.2. Three representative error bars are shown, illustrating the 1 s.d. precision on the Ba/Nb ratio and Nb concentrations with varying enrichment, calculated from variably enriched secondary standard analyses. Panel b compares the standard deviation of Ba and Nb in melt inclusions from each eruption, normalised to their mean. The solid line shows the expected relationship if the two elements are not fractionated from each other during melting, the dashed line shows the expected relationship if they are fractionated by perfect fractional melting (Rudge et al., 2013), using the partition coefficients from Workman and Hart (2005).

normalised variance, the melting process has not fractionated the elements from each other (Rudge et al., 2013). The relative variance of Ba and Nb for each Icelandic melt inclusion suite are shown together in Figure 6.7b, providing further evidence that Ba and Nb have not been fractionated from each other. Elements more compatible than Nb have been fractionated from each other, as demonstrated by their relative variances (Figure 6.5). Assuming that the behaviour of CO_2 during mantle melting can be modelled as an incompatible element, and that it has partition coefficient between Ba and Nb (Rosenthal et al., 2015), the apparent lack of fractionation between Ba and Nb would suggest that primary magmatic CO_2/Ba and CO_2/Nb ratios will record mantle source ratios.

6.4 Processes controlling CO_2-trace element systematics

Háleyjabunga and Stapafell both display correlations between CO_2 and Ba concentrations (Figure 6.1). Additionally, Háleyjabunga shows the increased variance of CO_2 concentration with Ba concentration

typical of datasets generated by partial degassing and mixing (Chapter 4). Stapafell exhibits somewhat more complexity, possibly due to a prolonged history of mixing and fractional crystallisation. Heilagsdalsfjall and Berserkjahraun do not exhibit correlations between CO_2 and Ba concentrations, likely a result of more extensive degassing and mixing.

Three (uncorrected) Háleyjabunga melt inclusions form a sub-population with higher CO_2 concentrations than the other Háleyjabunga melt inclusions (Figure 6.1). The higher CO_2 concentrations may reflect inclusion entrapment at an earlier stage of magma evolution, where the melts had higher CO_2 concentrations due to a greater storage pressure or by less mixing having taken place. The highest CO_2/Ba ratio in the Háleyjabunga melt inclusions also comes from within this sub-population; if the population is derived simply from being trapped earlier, then this is the value of CO_2/Ba most likely to reflect the Háleyjabunga mantle source. However, to fully assess this hypothesis by consideration of the sub-population's CO_2-trace element systematics requires a much larger sample size. Alternatively, these inclusions may reflect CO_2 being added to depleted melts, possibly by dissolution of CO_2 vapour or by melting in the presence of graphite. Both processes can elevate CO_2 concentrations and CO_2/Ba ratios of depleted melts, and are discussed further in Section 4.3. Since I cannot be certain these inclusions represent mantle CO_2/Ba ratios, I choose to discount them from the following discussion.

6.5 Global Melt Inclusion Array Systematics

In Figure 6.8 I compare the new CO_2 and Ba data from Háleyjabunga, Stapafell, Heilagsdalsfjall and Berserkjahraun, with other Icelandic melt inclusion suites and those from ocean-island and mid-ocean ridge settings. I exclude inclusions from arc volcanoes since their enrichment in H_2O complicates our understanding of CO_2 solubility. In both the Iceland compilation (Figure 6.8a) and the global compilation (Figure 6.8b), there is a striking negative correlation between CO_2/Ba and Ba concentration. This correlation is bounded above and below by lines of constant CO_2 concentration, though bubble-corrected inclusions break through this upper bound. For the most depleted inclusions the low bound corresponds to approximately 100 ppmw CO_2, and the high bound to 1000-1400 ppmw CO_2. The same systematic is observed in CO_2/Nb–Nb space (Figure 6.9). Whilst the negative correlation could be caused by enriched mantle components having lower CO_2/Ba than depleted mantle components, the same CO_2/Ba ratios must characterise all the depleted and enriched mantle components sampled globally, in order to explain the correspondence between the Icelandic and global compilations. The presence of CO_2-rich shrinkage bubbles in many of these inclusions demonstrates that many of the melts must have contained more CO_2 in the past; furthermore, in Chapter 4 I argued that most melts are likely to have lost substantial quantities of CO_2 before being entrapped as melt inclusions.

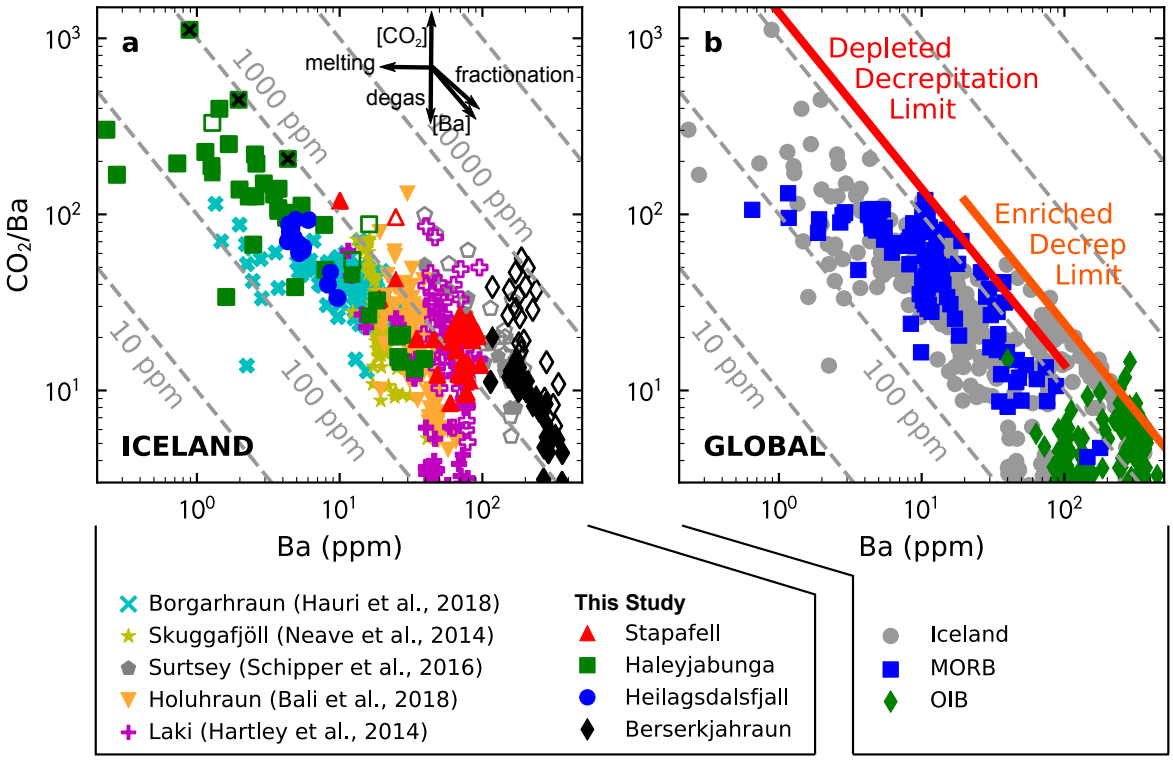

Figure 6.8: CO_2/Ba ratios in the melt inclusion glass for the four eruptions studied here, and compiled data from other eruptions in Iceland (panels a and b), from along the mid-ocean ridge system (MORB), and from ocean-islands (OIB) (panel b). Filled symbols show values for CO_2/Ba derived from CO_2 hosted in the glass only, open symbols show the values of CO_2/Ba where bubbles have been added back to the glass. The vectors in panel a show the effects of mantle melting, fractionation during melting, CO_2 degassing, CO_2 addition, and Ba addition. Diagonal dashed-grey lines show constant CO_2 concentration (10 ppm, 100 ppm, 1000 ppm, 1 wt%, and 10 wt%). Solid red and orange lines in panel b show the inferred decrepitation limits at 1400 ppmw and 2400 ppmw respectively. The 1 s.d. uncertainty is the size of the markers. Data from Bali et al. (2018); Cabral et al. (2014); Hartley et al. (2014); Hauri et al. (2018); Le Voyer et al. (2017); Métrich et al. (2014); Neave et al. (2014); Saal et al. (2002); Schipper et al. (2016); Sides et al. (2014); Wanless et al. (2014); Wanless and Shaw (2012); Wanless et al. (2015).

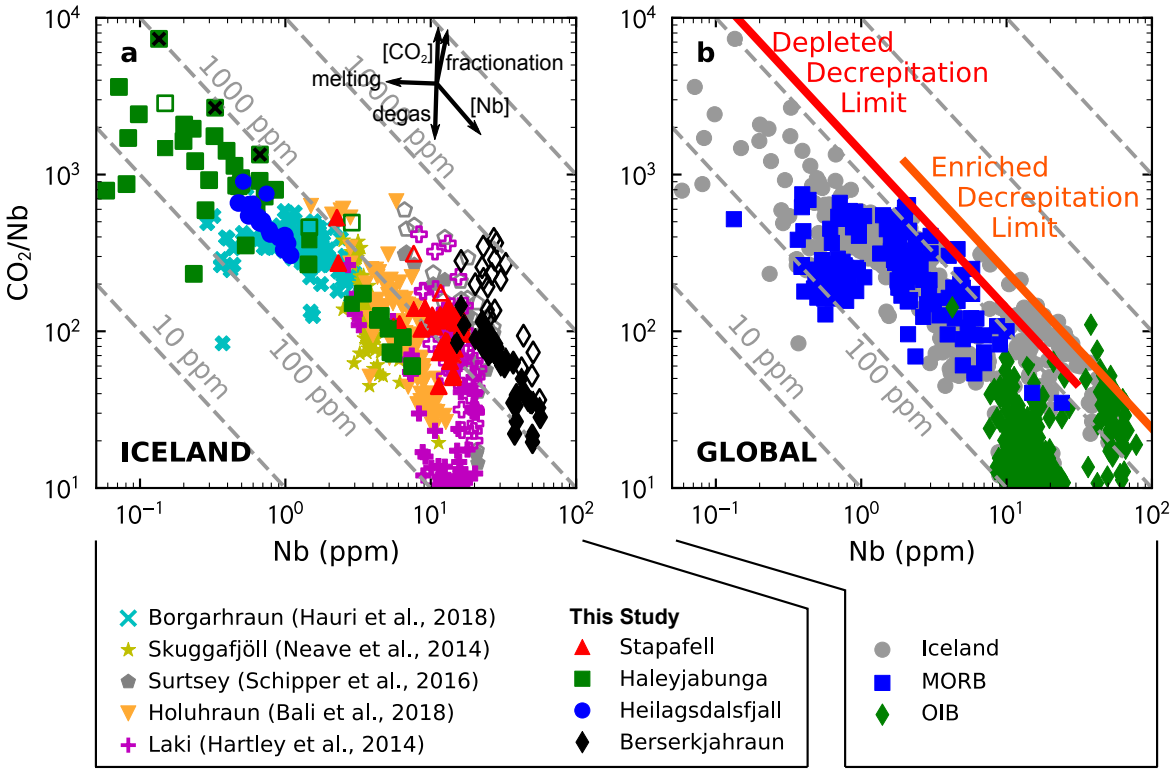

Figure 6.9: Panel a shows the compiled melt inclusion CO_2/Nb data for Iceland, and panel b shows the global compilation split into Iceland, OIB (green) and MORB (blue). See the caption to Figure 6.8 for more information.

A simpler explanation requires a process that limits the CO_2 concentration within the melt inclusion. The lower limit corresponds to CO_2 solubility for magma storage in shallow crustal magma chambers, the handful of inclusions with lower CO_2 concentrations than this probably owe their undersaturation to mixing with extremely CO_2-depleted partial mantle melts (Chapter 4). The upper bounds on CO_2 concentration in depleted melt inclusions of 1000–1400 ppmw correspond to saturation pressures in the range of 1–3 kbar, depending on the solubility model chosen (Figures 6.10 and 6.11). This pressure range coincides with that expected for olivine decrepitation (Maclennan, 2017; Wanamaker et al., 1990), where the crystal undergoes brittle failure when it can no longer support the pressure difference between the inclusion and its surroundings. Experiments by Wanamaker et al. (1990) predict that overpressures of up to 2.2 kbar may be supported. This is very close to the maximum entrapment pressure of the moderately-depleted inclusions when calculated with the CO_2 solubility model of Iacono-Marziano et al. (2012).

The dependence of CO_2 solubility on melt composition allows significantly different CO_2 concentrations to equilibrate at the same pressure. Melt polymerisation tends to reduce CO_2 solubility, whilst the presence of cations with an affinity for forming carbonate increases CO_2 solubility (Shishkina et al., 2014). The enriched inclusions are significantly richer in total-alkalis ($Na_2O + K_2O$) for similar SiO_2

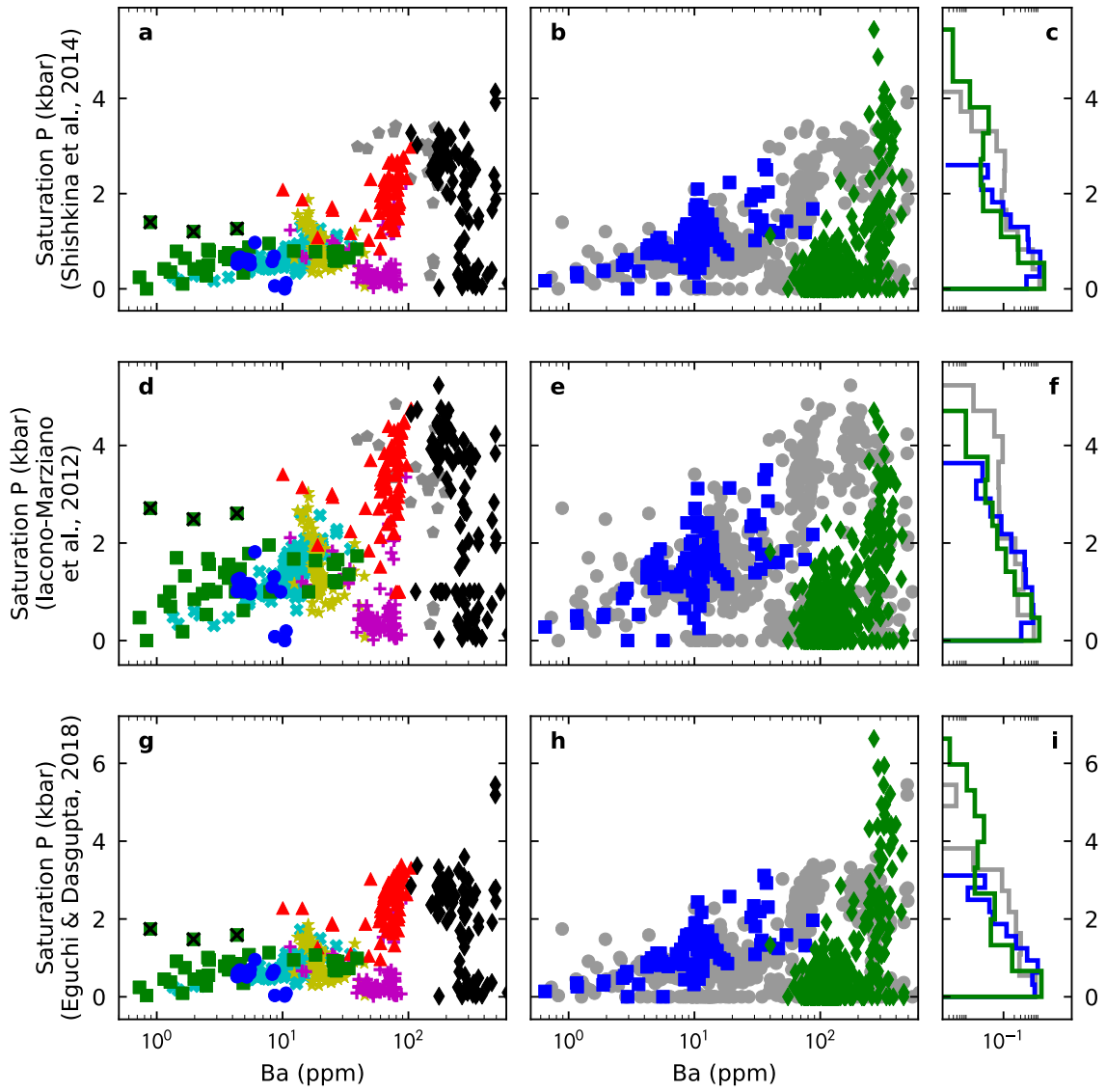

Figure 6.10: Panels a, d and g show the saturation pressures of each melt inclusion in the Iceland compilation, b, e and h show saturation pressure for each melt inclusion in the global compilation, and panels c, f and i show histograms of the saturation pressures for Iceland (grey), MORB (blue) and OIB (green). The saturation pressures are calculated using three different models: Shishkina et al. (2014) (a,b,c), Iacono-Marziano et al. (2012) (d,e,f) and Eguchi and Dasgupta (2018) (g,h,i). The effect of H_2O is neglected in all calculations, as the melts contain sufficiently low H2O concentrations that CO_2 solubility will be little affected. The calculations do not include bubble-corrections. Symbols as used in Figure 6.8.

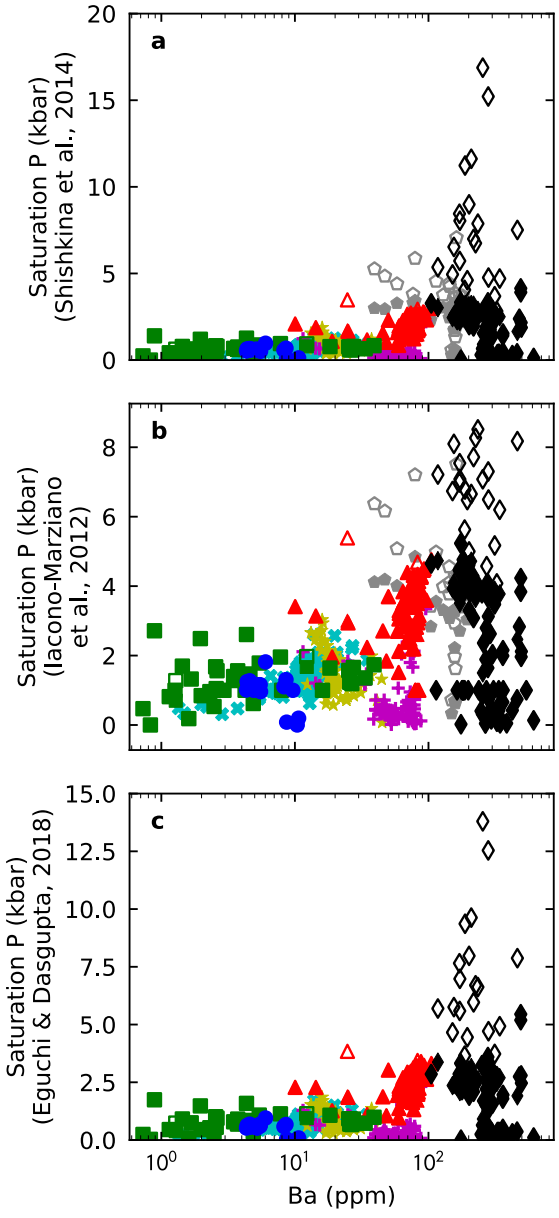

Figure 6.11: Saturation pressures of the bubble-uncorrected inclusions (reproduced form Figure 6.10), and saturation pressures calculated after bubble corrections have been applied (unfilled symbols). See the caption to Figure 6.10 for further information. Symbols as used in Figure 6.8.

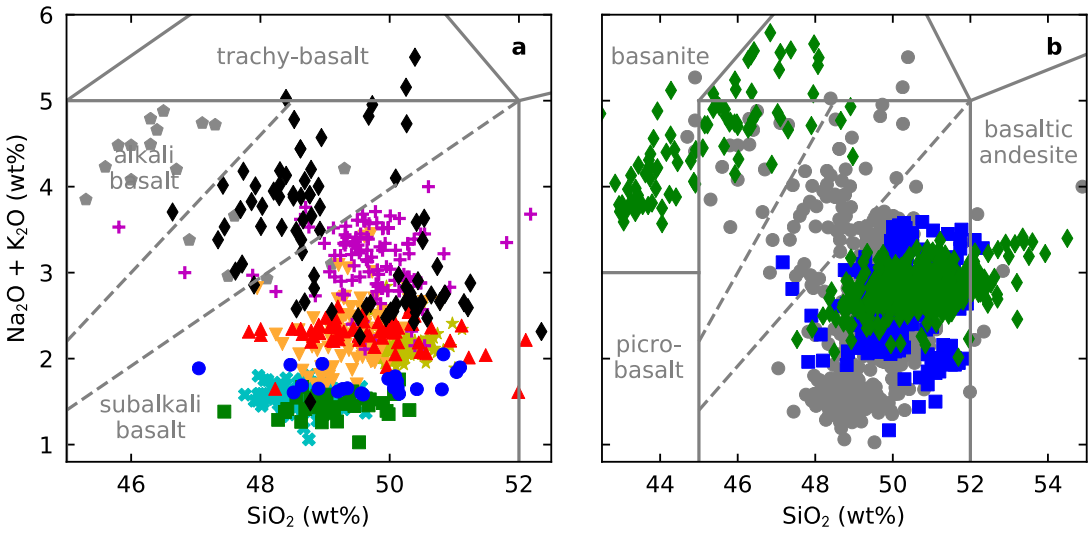

Figure 6.12: Total alkalis vs silica plot for all melt inclusions in the Iceland compilation (panel a, and grey points in panel b), and in the MORB compilation (blue symbols in panel b), and in the OIB compilation (green symbols in panel b). The fields shown are defined by Le Maitre et al. (2005). Symbols as used in Figure 6.8.

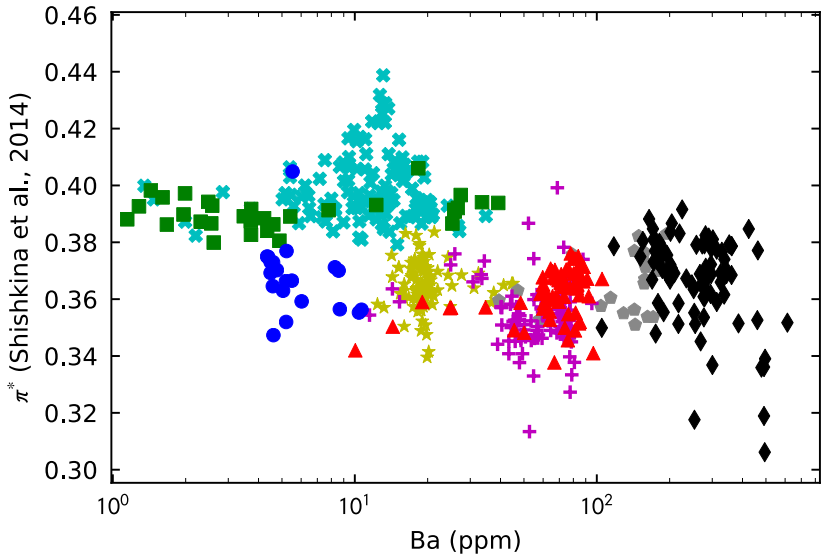

Figure 6.13: The value of the compositional parameter π^* for each melt inclusion in the Iceland compilation, used in the calculation of saturation pressure with the model by Shishkina et al. (2014). Symbols as used in Figure 6.8.

contents (Figure 6.12), but this does not translate into significant differences in the π^* compositional parameter used by Shishkina et al. (2014) in their CO_2 solubility model (Figure 6.13). Though the concentration of alkali elements in the enriched inclusions acts to increase the CO_2 solubility, they have lower MgO and CaO concentrations which stabilise carbonate in the magma. It is therefore unclear why the decrepitation limit should vary with eruption enrichment, though it could reflect inadequate characterisation of the compositional dependence of CO_2 solubility. The persistence of the same CO_2/Ba–Ba trend at the global scale further supports the decrepitation hypothesis over control by mantle variability.

The formation of bubbles, and the diffusion of CO_2 into them, increases the maximum CO_2 capacity of the inclusion system at constant pressure (Maclennan, 2017). Bubble-corrected inclusions can therefore exceed the decrepitation limit, as shown by the most enriched eruptions in Figure 6.8a. Whether or not decrepitation is modulating the CO_2/Ba systematics of a dataset is therefore of great importance. Where an eruption's melt inclusion population sits below the decrepitation threshold, as do Háleyjabunga, Borgarhraun and Heilagsdalsfjall, they may never have reached a sufficient over-pressure for decrepitation to occur. Alternatively, the CO_2 concentration in the melt was sufficiently low that there was no CO_2 vapour exsolution prior to, or in response to decrepitation. Where significant bubble-corrections have been applied to melt inclusions, as has been done for Berserkjahraun and Surtsey, the corrected CO_2/Ba ratios may not have been affected by decrepitation, though prior decrepitation cannot be ruled out. Even when decrepitation can be ruled out as the process determining the maximum CO_2/Ba ratio, the observed CO_2/Ba value may still be substantially lower than the mantle source value, if the melts lost substantial CO_2 to magmatic degassing prior to inclusion entrapment. I consider the implications of this process further in the following section.

6.6 Identifying mantle CO_2 heterogeneity

The gross structure of both the Icelandic and Global melt inclusion arrays shown in Figure 6.8 is primarily controlled by low-pressure processes: storage in shallow magma chambers and olivine decrepitation (Section 6.5). However, many eruptions sit almost entirely within the bounds imposed by shallow storage and decrepitation, or have partitioned a significant fraction of their CO_2 budget into bubbles thereby overcoming the decrepitation threshold. Many of these datasets may still preserve the CO_2/Ba ratios of their melts at the time of entrapment. In Chapter 4 I argued that the diversity of CO_2/Ba ratios in individual eruptions indicates that they have experienced partial CO_2 loss by degassing, but have regained a positive (albeit scattered) correlation between CO_2 and Ba by magma mixing.

A consequence of this process is the average value of CO_2/Ba for an eruption is more sensitive to the degassing pressure than to the CO_2/Ba ratio inherited by the primary melts from their mantle source. Since the degassing, mixing and decrepitation processes all act to lower the CO_2/Ba ratio recorded by melt inclusions, it follows that the maximum CO_2/Ba value observed in melt inclusions from a single eruption is the value least affected by CO_2 loss and therefore most likely to preserve the mantle CO_2/Ba ratio.

An eruption's CO_2/Ba distribution may have a long tail towards the mantle value, depending on the extent of degassing prior to mixing and the efficiency of mixing. The probability of sampling this tail could be very low. Without knowledge of the distribution of melts entering the crust, and the history of degassing and mixing they subsequently undergo, it is impossible to constrain the shape of this distribution and therefore assess the likelihood of a given melt inclusion suite preserving the mantle CO_2/Ba ratio in one or more of the inclusions.

Though we cannot tell whether an individual dataset preserves the mantle CO_2/Ba ratio when taken in isolation, comparison with a large number of melt inclusions from a diversity of eruptions can provide a context in which to consider the maximum CO_2/Ba values preserved by an individual eruption. If the maximum CO_2/Ba ratios of eruptions vary systematically with their mantle sources, and systematic biases from crustal processing can be ruled out, greater confidence may be placed in the recorded CO_2/Ba ratios reflecting their mantle source.

In Section 6.6.1 I critically assess the limits of this methodology when applied to melt inclusion datasets. I then apply this approach first to the melt inclusion compilation from Iceland, supplemented with my new data, in order to identify and place quantitative estimates on mantle CO_2 heterogeneity (Section 6.6.2). I then explore in Section 6.6.4 whether this approach yields information on the global variability in the upper mantle, as sampled by mid-ocean ridge basalts (MORBs).

To avoid interpreting analytical artefacts, Rosenthal et al. (2015) and Hirschmann (2018) avoid using the highest CO_2/Ba values, suggesting these analyses may have incorporated carbon derived from cracks in the sample. Standard practice when collecting melt inclusion datasets is to avoid analyses in the vicinity of cracks, and the ^{12}C count rates would vary erratically in such a situation. In carefully collected datasets such analytical artefacts will be eliminated, and it is more likely that the highest CO_2/Ba ratios instead reflect sampling of low probability-density tail to the CO_2/Ba distribution. In Figures 6.15 and 6.16 I demonstrate the difference between taking the dataset maximum CO_2/Ba and CO_2/Nb ratios, as opposed to the upper limit of the main CO_2/Ba and CO_2/Nb data density. The dataset maximum CO_2/Ba ratios do not coincide with extreme values of Ba/Nb (Figure 6.17), providing further evidence the highest CO_2/Ba ratios do not arise from fractionation between Ba, Nb and CO_2 during melting.

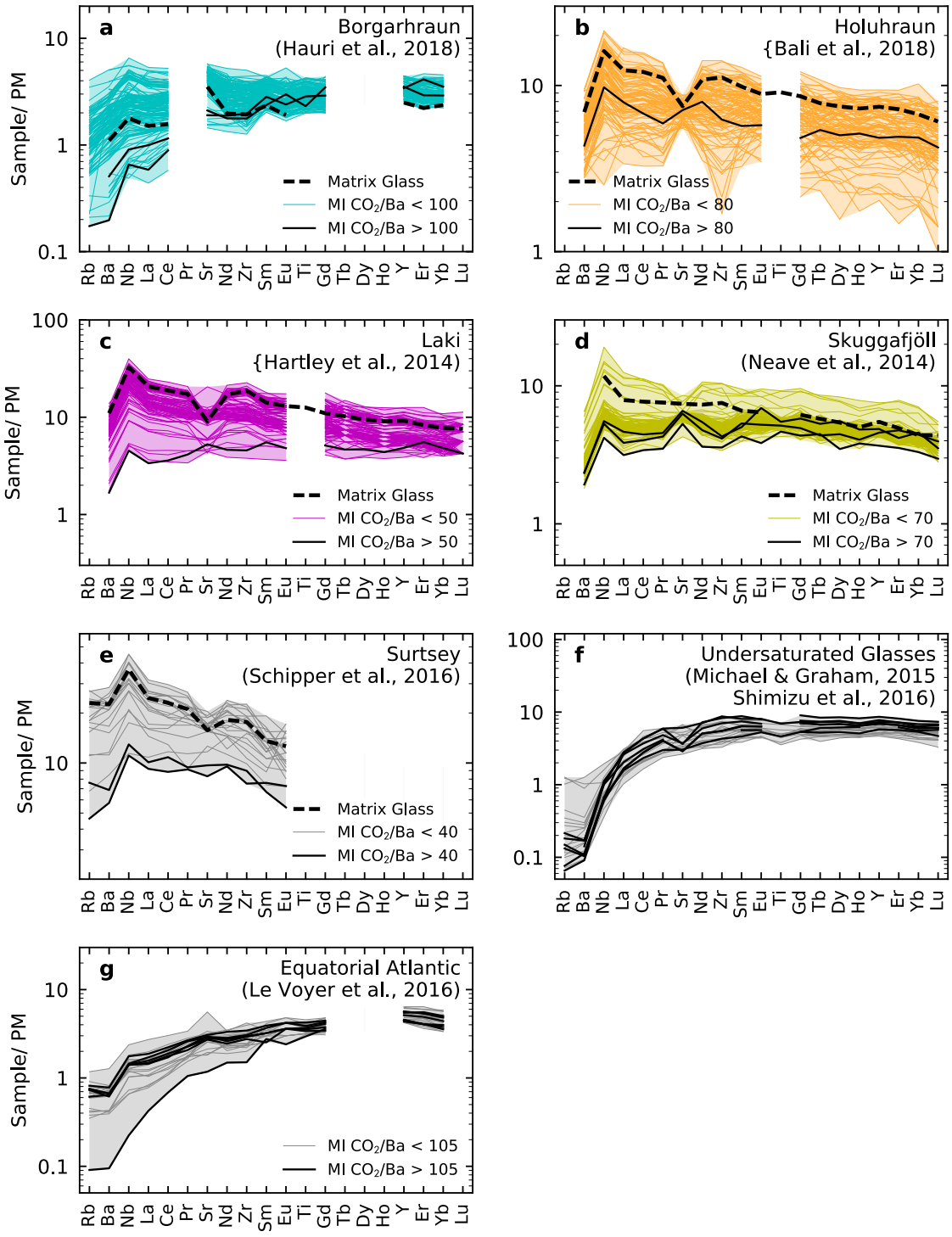

Figure 6.14: Trace element diagrams for the eruptions from previous studies discussed in the main text. Panel h shows the trace element concentrations in the combined undersaturated glass datasets of Michael and Graham (2015); Shimizu et al. (2016), the other panels show the melt inclusion data from Bali et al. (2018); Hartley et al. (2014); Hauri et al. (2018); Le Voyer et al. (2017); Neave et al. (2014); Schipper et al. (2016). See the caption to Figure 6.4 for more information.

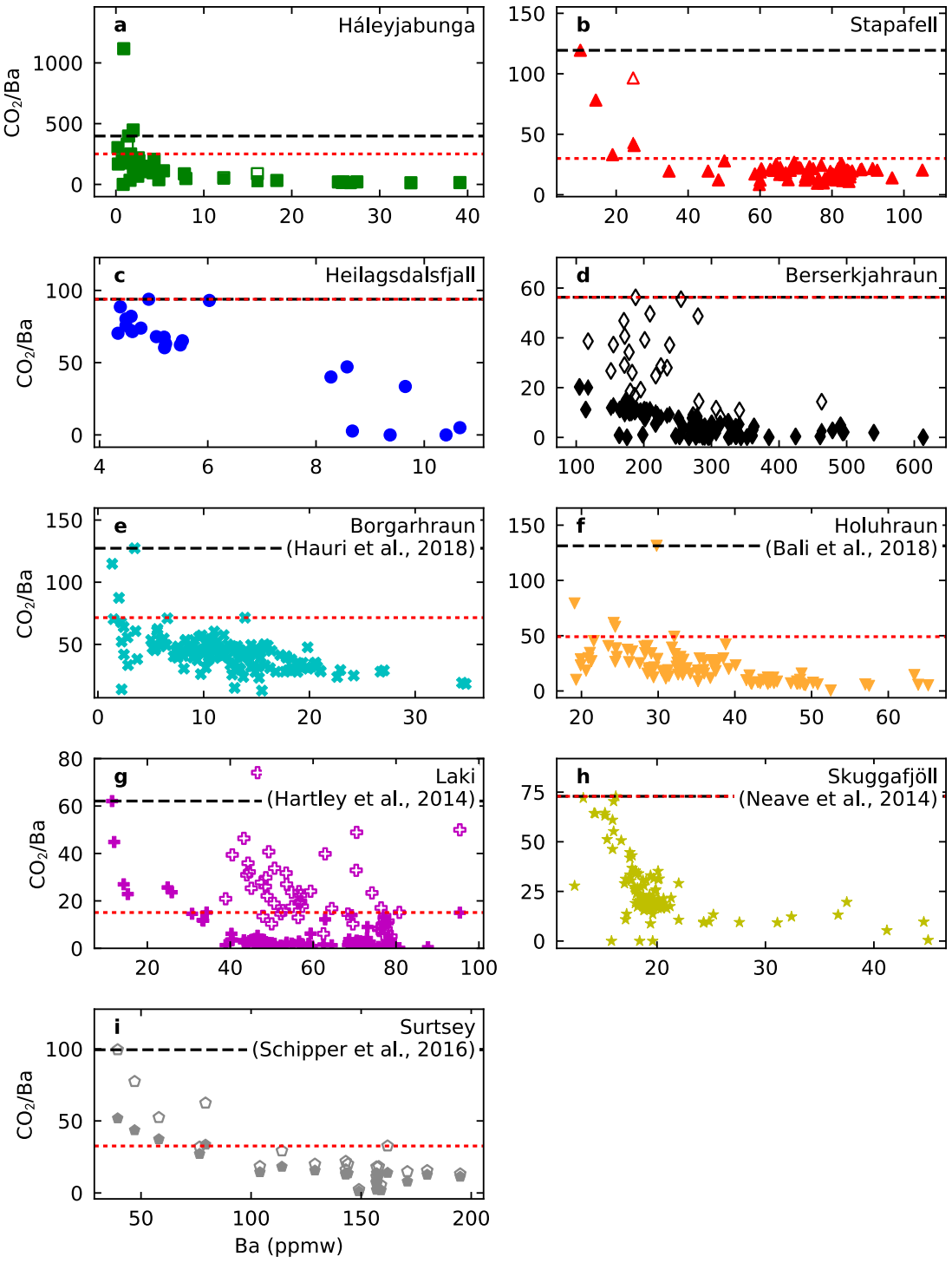

Figure 6.15: CO_2/Ba ratios shown against Ba concentration for each eruption in the Iceland compilation, shown in linear-linear space. The horizontal dashed black lines show the maximum CO_2/Ba values taken from each dataset, used in Figure 6.18 and the inversion calculations in Section 6.6.2. The horizontal dashed red lines show the maximum values of the main data population, shown in Figure 6.20 and used in the inversion calculations shown in Figures 6.26, 6.27 and 6.28.

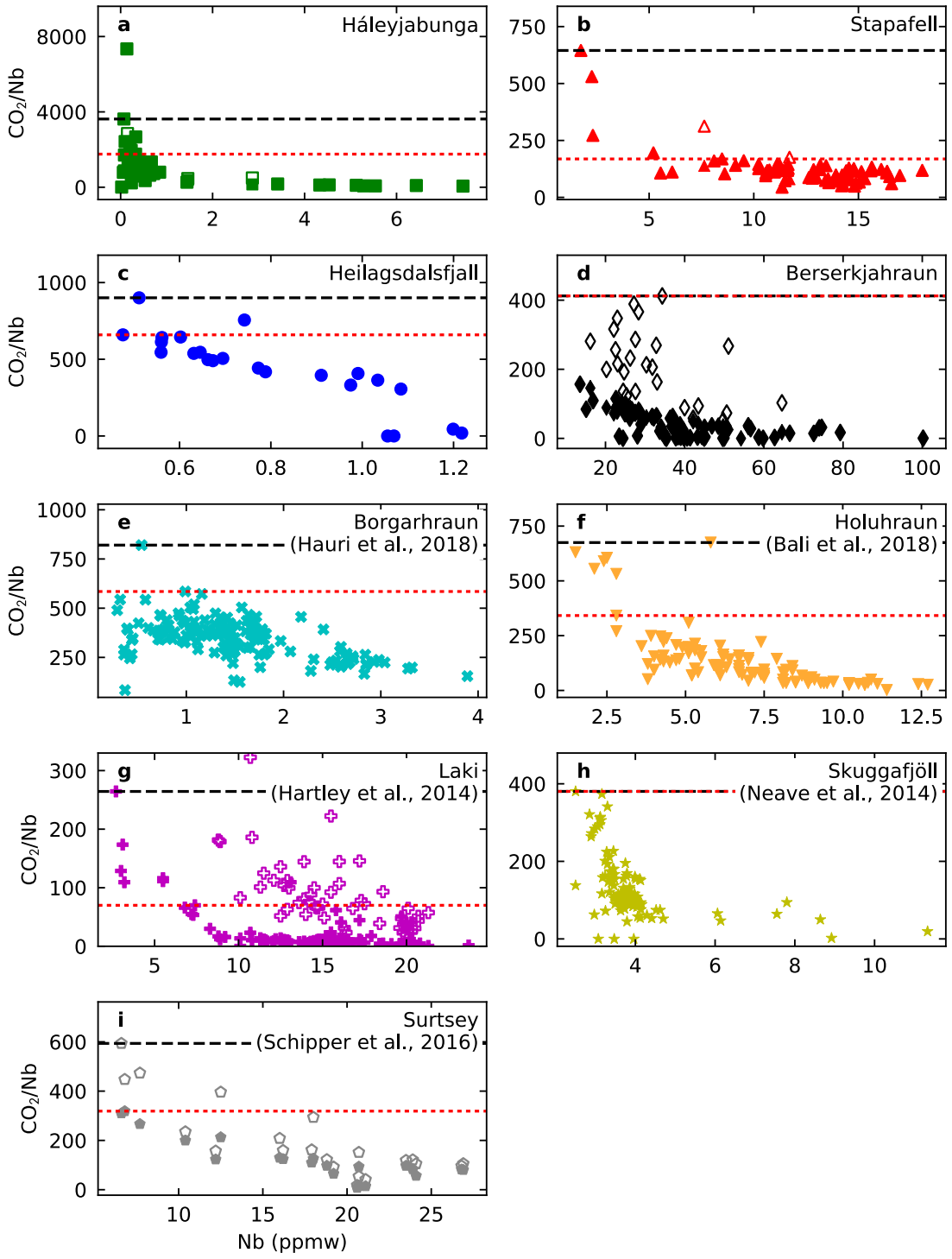

Figure 6.16: CO_2/Nb ratios shown against Nb concentration for each eruption in the Iceland compilation, shown in linear-linear space. The horizontal dashed black lines show the maximum CO_2/Nb values taken from each dataset, used in Figure 6.19 and the inversion calculations in Section 6.6.2. The horizontal dashed red lines show the maximum values of the main data population, shown in Figure 6.21 and used in the inversion calculations shown in Figures 6.26, 6.27 and 6.28.

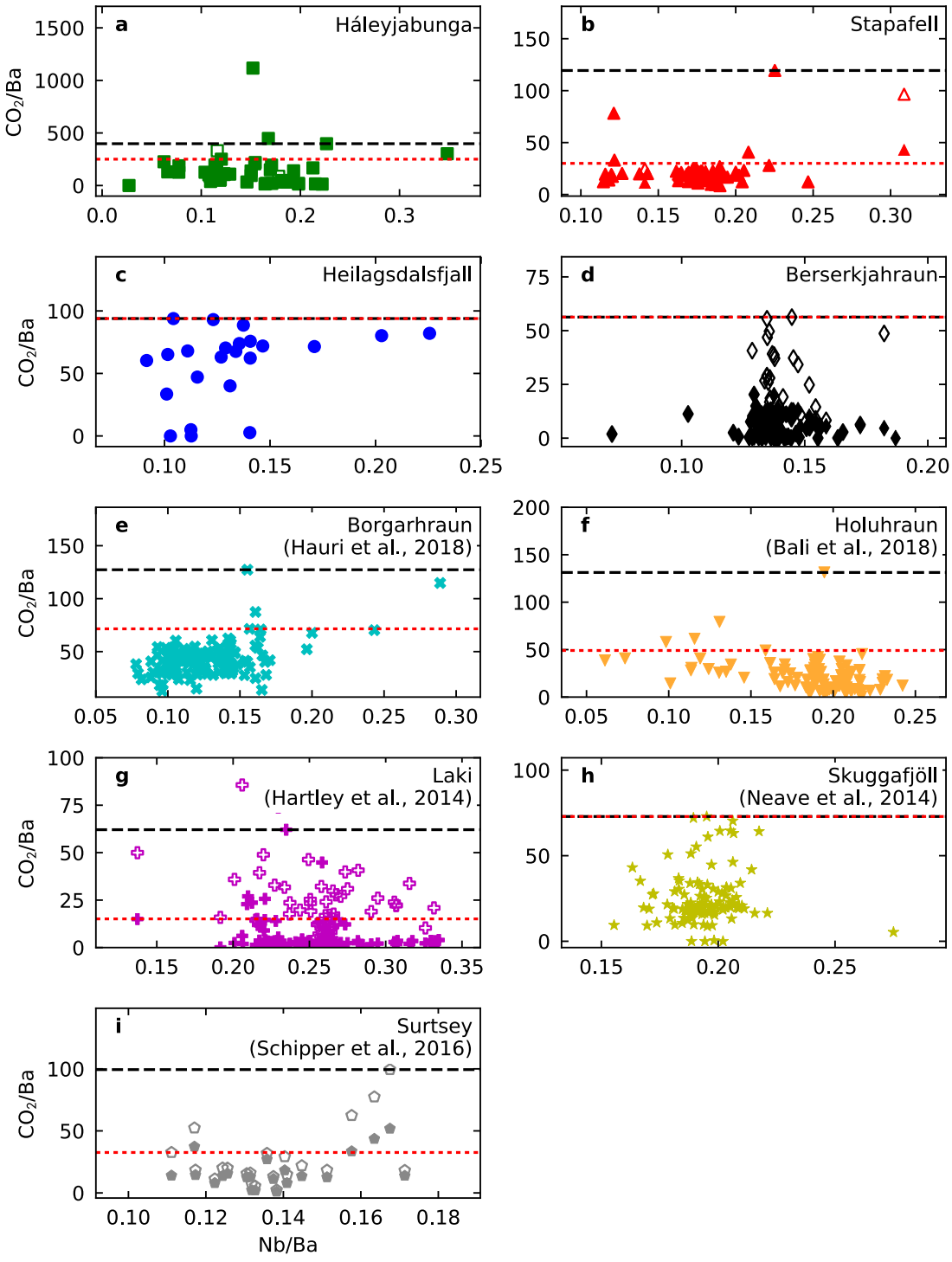

Figure 6.17: CO_2/Ba ratios shown against Nb/Ba ratio for each eruption in the Iceland compilation, shown in linear-linear space. The horizontal dashed black lines show the maximum CO_2/Ba values taken from each dataset, used in Figure 6.18 and the inversion calculations in Section 6.6.2. The horizontal dashed red lines show the maximum values of the main data population, shown in Figure 6.20 and used in the inversion calculations shown in Figures 6.26, 6.27 and 6.28.

Eruption	Max CO_2/Ba	Max CO_2/Ba (main pop.)	Max CO_2/Nb	Max CO_2/Nb (main pop.)
Berserkjahraun	56.3±12.4	56.3	412 ± 91	412.3
Háleyjabunga	398 ± 88	250.6	3620 ± 800	1758
Stapafell	119 ± 26	30	645 ± 141	168.8
Heilagsdalsfjall	94 ± 21	93.9	901 ± 198	659.2
Borgarhraun	127 ± 15	71.5	820 ± 98	584.8
Laki	62.1	15.1	264.4	70
Skuggafjöll	72.9	72.9	380.4	380.4
Holuhraun	131.3	49.1	674.8	341.8
Surtsey	99.4	32.6	593.6	318.8
Miðfell	566	396	4573.28	3199.68

Table 6.1: Maximum CO_2/Ba and CO_2/Nb ratios extracted from each dataset in the compilation.

6.6.1 Preservation of small-scale mantle CO_2 heterogeneity in melts

In applying the method laid out above, it is implicitly assumed that the CO_2/Ba ratio of a single melt inclusion is representative of the heterogeneous mantle that contributes melt to the whole eruption. However, mantle-derived Pb-isotope heterogeneity is present within melt inclusions from single Icelandic eruptions, including single hand-specimens from Háleyjabunga and Stapafell (Maclennan, 2008b). This observation clearly demonstrates that heterogeneity in Pb-isotope ratios survives the melting and melt transport processes operating beneath Iceland.

However, CO_2, Ba and Nb are much more incompatible than Pb and are likely to be almost entirely removed from the solid residue in the first increments of melting. Though channelised mantle flow can transport significant mantle derived chemical heterogeneity in melts, the deepest melts are likely to be well mixed (Kelemen et al., 1997a; Spiegelman and Kelemen, 2003), and may subsequently be diluted in varying amounts by higher degree melts. I therefore consider it likely that any fine scale mantle heterogeneity in CO_2/Ba and CO_2/Nb ratios will be averaged in any melts extracted from it.

In comparing melt inclusion CO_2/Ba and CO_2/Nb to bulk-rock radiogenic isotopes ratios, it is implicitly assumed that these isotope ratios are also indicative of the bulk mantle source. Unlike for CO_2, Ba and Nb, the radiogenic isotope ratios of individual melt inclusions do not represent the bulk melt source, however whole-rock samples are the end-product of extensive crustal mixing of the initially diverse mantle melts. Rudge et al. (2013) demonstrate the radiogenic isotope systematics of a compilation of whole-rock data from Iceland can be matched by variable mixing of melts from a uniformly heterogeneous mantle, suggesting that we might expect the CO_2/Ba and CO_2/Nb ratios preserved in melt inclusions to be decoupled from the whole-rock radiogenic isotope ratios. A more suitable isotope system would utilise elements that are at least as incompatible as Nb. One such

system is $^{3}He/^{4}He$, typically shown normalised to the atmospheric value (denoted as R/R_a), which I use in complement to Pb-, Nd- and Sr-isotopes in the following analysis.

6.6.2 Heterogeneity within the Icelandic plume

Radiogenic isotope observations require multiple enriched and depleted source components within the Icelandic mantle (Peate et al., 2010; Thirlwall et al., 2004). These mantle components may also be heterogeneous in their CO_2 content. The Pb-, Nd-, and Sr-isotope systems are sensitive to ancient melt extraction and recycling events, whilst the $^{3}He/^{4}He$ system is diagnostic of primordial (or undegassed) mantle reservoirs. Though there is a large quantity of melt inclusion data from Iceland, from a number of spatially and temporally restricted eruptions with diverse geochemistry, it is not yet sufficient to fully resolve the CO_2 concentrations in the diversity of mantle components beneath Iceland.

We therefore proceed on the basis of finding the minimum number of distinct components required to explain the coupled CO_2/Ba and radiogenic isotope observations, whilst acknowledging the end-members I invert for are some average of the full diversity of heterogeneities present in the Icelandic mantle. Figures 6.18a and 6.18b demonstrate there is no systematic covariation of CO_2/Ba within $^{206}Pb/^{204}Pb$–$^{208}Pb/^{204}Pb$ space, or $^{87}Sr/^{86}Sr$–$^{143}Nd/^{144}Nd$ space. Though not shown here, this is also true of any combination of Pb-isotopes with Sr- and Nd-isotopes.

Whilst the lithophile isotope systems excel at separating contributions from enriched and depleted mantle reservoirs, the primordial mantle lies of the middle of lithophile isotope space (Hart et al., 1992). Helium isotopes, in contrast, reveal contributions from primordial mantle components clearly, as undegassed mantle has extremely high $^{3}He/^{4}He$ ratios (e.g. Class and Goldstein, 2005). When $^{3}He/^{4}He$ ratios are plotted with $^{143}Nd/^{144}Nd$ ratios (Figure 6.18c) a weak covariation of CO_2/Ba with position across the space does emerge. The sense of the covariation suggests mantle material with high (primordial) $^{3}He/^{4}He$ is associated with high magmatic values of CO_2/Ba, whilst melts derived from depleted mantle (with $R/R_a \sim 8$) have moderate CO_2/Ba and those from enriched mantle (with $R/R_a \leq 8$) have low CO_2/Ba. The same trends are observed if CO_2/Nb is used in place of CO_2/Ba (Figure 6.19), and a similar co-variation is observed if the upper-limits of the CO_2/Ba and CO_2/Nb ratios in the main data population are used in place of the dataset maxima (Figures 6.20 and 6.21).

The association of high CO_2/Ba with primordial undegassed mantle material was first made by (Miller et al., in review), based on the elevated CO_2/Ba ratios seen in the Miðfell eruption in Iceland. Utilising a comparison to melt inclusions from Borgarhraun (Hauri et al., 2018), Miller et al. (in review) argue that the elevation in CO_2/Ba in Miðfell is not caused by crustal processing, since both eruptions have similar trace element concentrations. Though it could be argued that Borgarhraun has seen more extensive CO_2 loss by magmatic degassing prior to inclusion entrapment, this seems unlikely given

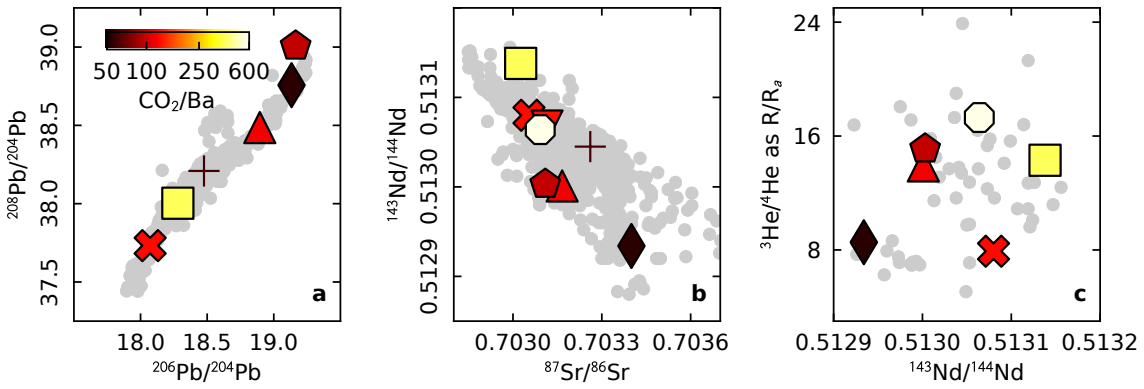

Figure 6.18: Radiogenic isotope compositions of the whole rocks from eruptions discussed in this text (large symbols), data sources are given in Table 2.2. The symbols used are the same as in Figure 6.8, but each symbol is coloured for the maximum CO_2/Ba ratio observed in melt inclusions from that eruption, as described in the text. Grey circles show the compilation of Iceland whole-rock isotope analyses, data sources are given in Appendix B. In panel c, schematic mixing arrays as used in the inversions discussed in Section 6.6.2 are shown by arrows between three endmembers: 'DM' (depleted mantle), 'EM' (enriched, or recycled, mantle), and 'PM' (primordial mantle).

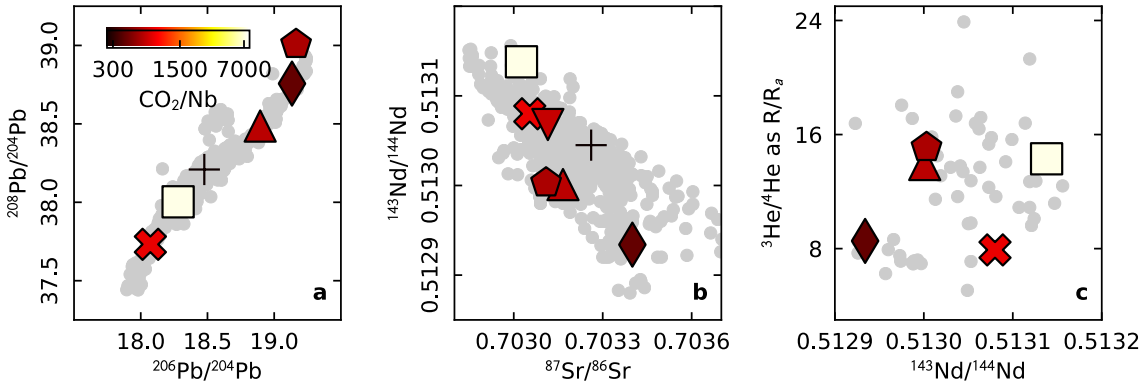

Figure 6.19: The covariation of maximum CO_2/Nb recorded by melt inclusions with radiogenic isotope ratios of associated whole rocks. See the caption to Figure 6.18 for further information.

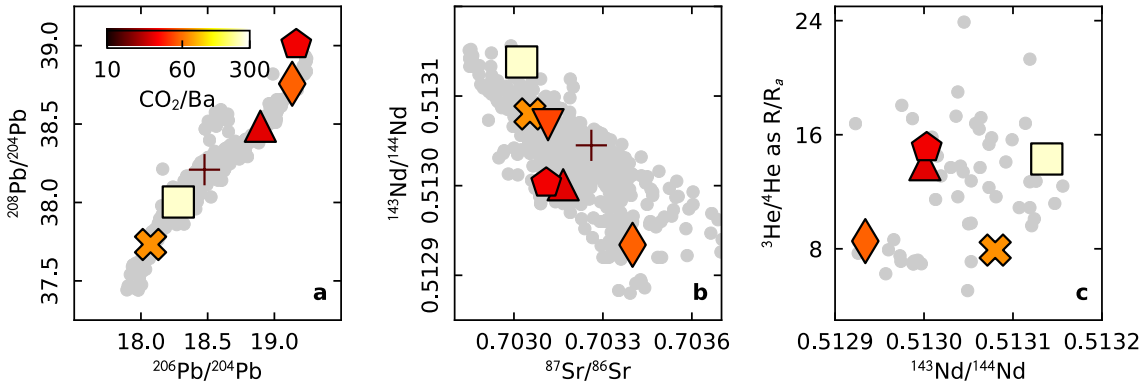

Figure 6.20: The covariation of the upper limit of the CO_2/Ba ratios preserved in the main melt inclusion population, with radiogenic isotope ratios of associated whole rocks. See the caption to Figure 6.18 for further information.

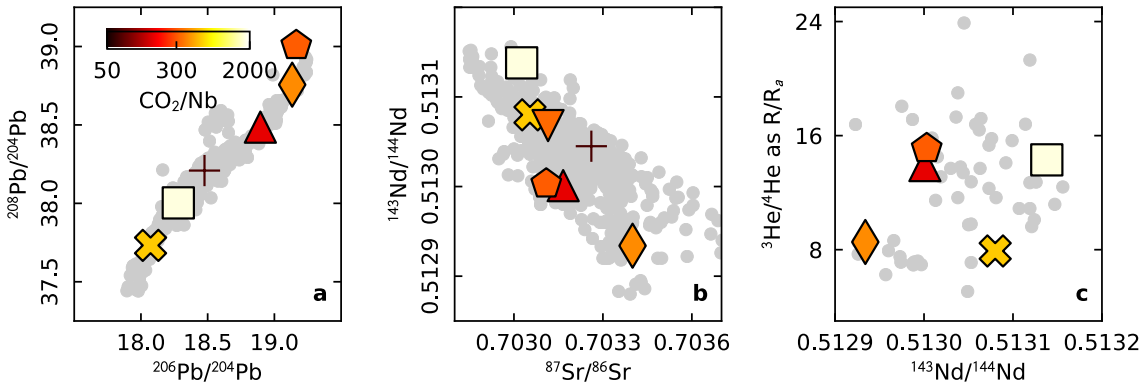

Figure 6.21: The covariation of the upper limit of the CO_2/Nb ratios preserved in the main melt inclusion population, with radiogenic isotope ratios of associated whole rocks. See the caption to Figure 6.18 for further information.

the high (6–8 kbar) pressures of crystallisation (Neave and Putirka, 2017; Winpenny and Maclennan, 2011) and the Borgarhraun melt inclusions' distance from the decrepitation threshold (Figure 6.8a). The new data from Háleyjabunga lends further support to their hypothesis.

However, the same argument cannot be used when making a comparison to the more enriched eruptions, such as Berserkjahraun and Stapafell, as they have significantly higher trace element concentrations in their melt inclusions. If these melts started off with the same or higher CO_2/Ba ratio than Borgarhraun, the Stapafell and Berserkjahraun melts must retain considerably higher CO_2 concentrations. Such high CO_2 concentrations make these melts more susceptible to degassing and the inclusions more susceptible to CO_2 gas loss during decrepitation; crustal processing will therefore tend to introduce a systematic bias towards low CO_2/Ba ratios in enriched magmas. Regardless of whether the low CO_2/Ba in the enriched Berserkjahraun magmas is a result of low CO_2/Ba in the enriched source or not, three end-members are required to deconvolve the primordial mantle signal.

Here I consider mixing between three mantle end-members:

1. *Depleted mantle (DM)*- containing low trace element concentrations with radiogenic Nd- and He-isotope ratios ($R/R_a \sim 8$), typical of the upper mantle (Workman and Hart, 2005)
2. *Enriched mantle (EM)*- containing higher trace element concentrations with unradiogenic Nd-isotopes and radiogenic He-isotope ratios ($R/R_a \leq 8$), representing recycled material (Peate et al., 2010; Stracke et al., 2003a)
3. *Primordial mantle (PM)*- containing trace element concentrations and isotope ratios typical of bulk silicate Earth, though I also consider whether the results change if this component instead has a depletion in trace elements (and concomitant ingrowth of radiogenic Nd), much like a 'FOZO' (Hart et al., 1992) mantle component (Table 6.3, and Figures 6.25 and 6.27).

In principle, a mixing surface which closely matches the covariation of CO_2/Ba across $^{143}Nd/^{144}Nd$–$^{3}He/^{4}He$ space can be found. The position and shape of this surface is a complicated function of the CO_2, Ba, Nd and He concentrations in each endmember, and each endmembers' $^{3}He/^{4}He$ and $^{143}Nd/^{144}Nd$ isotope ratios, a total of 18 chemical parameters. The mixing surface is described by only 7 parameters, leaving the problem significantly under-constrained (Sohn, 2013). Whilst prior constraints may be placed on many of the parameters, such as the trace element concentrations in the mantle sources, the concentrations of He in the mantle end-members is extremely poorly determined (Ozima and Podosek, 2002).

To make the ternary-mixing problem more tractable I utilise the distinct isotopic character of the eruptions to reduce it to two binary-mixing problems: the first between DM and EM (constrained by Borgarhraun and Berserkjahraun), and the second between DM and PM (constrained by Hàleyjabunga

Parameter	DM	EM	PM
$^{143}Nd/^{144}Nd$	0.51316–0.51326	0.51220–0.51290	0.512638 ± 10
	Su (2003)	See caption[a]	Hamilton et al. (1983)
Nd (ppmw)	0.483–0.703	0.284 ± 0.28	0.595 ± 0.12
Ba (ppmw)	0.227–1.219	2.55 ± 0.25	6.6 ± 0.66
Nb (ppmw)	0.0864–0.2462	0.742 ± 0.074	0.60 ± 0.12
	Workman and Hart (2005)	Stracke et al. (2003a)[b]	McDonough and Sun (1995)

Table 6.2: The priors set on the parameters in the inversions reported in the main text. For CO_2 content a uniform prior between 1 ppm to 2 wt% CO_2 was used. The sources from which the priors are based are shown in the table. Where ranges are quoted for isotope ratios a uniform distribution between those bounds is used, for trace element concentrations it is a log-uniform distribution. Otherwise a normal distribution with the quoted mean and standard deviation are used. [a] The low Nd-isotope ratio bound for enriched mantle end-member is taken to be lower than the least radiogenic ocean island basalt (Stracke et al., 2005), and the high bound is taken to be lower than the least radiogenic observation from Iceland (Figure 2.2). [b] The trace element concentrations are taken as a third recycled crust (Stracke et al., 2003a), and two thirds depleted mantle (Workman and Hart, 2005).

and Miðfell), as shown schematically on Figure 6.18c. Though the DM-PM mixing array is described by a vector with both $^3He/^4He$ and $^{143}Nd/^{144}Nd$ components, I consider only the component parallel to $^{143}Nd/^{144}Nd$. The importance of the $^3He/^4He$ component in the ternary-mixing space is represented by separately considering unradiogenic- and radiogenic-He binary mixing arrays.

There are two principle disadvantages to this approach, we lose constraints on the problem by eliminating Stapafell and Surtsey as they sit on neither binary array, and we are required to assume there is no contribution from recycled components in the Háleyjabunga and Miðfell magmas. If recycled material was in the mantle source of these two eruptions, its effect would be most likely to decrease the observed CO_2/Ba ratio, biasing us towards inferring a low PM CO_2 concentration.

Binary mixing of Nd-isotopes is modelled using the equation from Faure and Mensing (2005):

$$\left(\frac{^{143}Nd}{^{144}Nd}\right)_M = \left(\frac{^{143}Nd}{^{144}Nd}\right)_A f_A \frac{[Nd]_A}{[Nd]_M} + \left(\frac{^{143}Nd}{^{144}Nd}\right)_B (1-f_A)\frac{[Nd]_B}{[Nd]_M} \tag{6.1}$$

where subscript M refers to the mixed melt, and A and B refer to the end-member melts. $[Nd]_A$ and $[Nd]_M$ are the Nd concentrations in the A endmember and mixed melts, respectively, and f_A is the mass fraction of component A in the mixture. Binary mixing of the CO_2/Ba and CO_2/Nb ratios is calculated by finding the concentration of each species in the mixed melt using the simple mass balance statement:

$$C_M = C_A f_A + C_B(1-f_A) \tag{6.2}$$

where C is the concentration of the species of interest.

In order for the prior assumptions about mantle source chemistry to be applied consistently, I take a Bayesian approach to estimating the CO_2/Ba ratio and CO_2 concentration of the mantle sources. To provide further constraint I simultaneously invert for the CO_2/Nb ratio. The prior distributions are described in Table 6.2 and its caption, and are shown schematically in Figure 6.22. I implement the Bayesian calculation using the importance nested sampling Monte-Carlo inversion routine 'Multinest' (Feroz and Hobson, 2008; Feroz et al., 2009, 2013) with the pymultinest python wrapper (Buchner et al., 2014). The DM-PM and DM-EM binaries are inverted for simultaneously, to ensure the calculations return an internally-consistent CO_2 concentration in the depleted mantle. For simplicity I ignore the uncertainty in the $^{143}Nd/^{144}Nd$ ratio of the samples, calculating the log-likelihood of each mixing model based only on the misfit between CO_2/Ba or CO_2/Nb of the observation and modelled mixing line. The log-likelihood ($ln(L)$) for a given model with n constraints is:

$$\begin{aligned} ln(L) = & -\frac{1}{2}\sum_{1}^{n} ln\left(2\pi^{C/Ba}\sigma_n^2\right) - \sum_{1}^{n}\frac{(^{C/Ba}x_n - ^{C/Ba}\mu_n)^2}{2^{C/Ba}\sigma_n^2} \\ & -\frac{1}{2}\sum_{1}^{n} ln\left(2\pi^{C/Nb}\sigma_n^2\right) - \sum_{1}^{n}\frac{(^{C/Nb}x_n - ^{C/Nb}\mu_n)^2}{2^{C/Nb}\sigma_n^2} \end{aligned} \tag{6.3}$$

assuming the constraints follow a normal distribution (Lee, 2012), where $^{C/Ba}\mu_n$ and $^{C/Nb}\mu_n$ are the observed CO_2/Ba and CO_2/Nb ratios, and $^{C/Ba}\sigma_n$ and $^{C/Nb}\sigma_n$ are their one standard deviation uncertainties. Using Equation 6.1 the mixing proportions required by the $^{143}Nd/^{144}Nd$ ratio of the nth observation are calculated. The CO_2/Ba and CO_2/Nb ratios, $^{C/Ba}x_n$ and $^{C/Nb}x_n$ are then calculated for these mixing proportions using the model endmembers.

Inversion results

The results of the inversion are shown in Figure 6.22. In the calculations shown and discussed in the main text the constraint from Berserkjahraun (Figures 6.22l and 6.22o) is excluded, as the model fit is extremely poor when included. The poor fit most likely arises from the maximum CO_2/Ba and CO_2/Nb ratios observed being much lower than the mantle value, suggesting that even bubble-corrected Berserkjahraun inclusions lost additional CO_2 due to previous decrepitation events or by magmatic CO_2 degassing before inclusion entrapment. Results of the inversion when the Berserkjahraun observations are imposed as constraints are shown in Table 6.3 and Figure 6.24.

A consequence of excluding Berserkjahraun from the calculation is the EM endmember becomes poorly constrained, and may have CO_2/Ba and CO_2/Nb ratios either lower or far in excess of the depleted mantle. However, the enrichment of Ba and Nb in the EM source relative to depleted mantle results in the greatest posterior probability density of CO_2 concentration being higher than the depleted mantle, even when the CO_2/Ba and CO_2/Nb ratios are lower. The calculated CO_2/Ba and CO_2/Nb

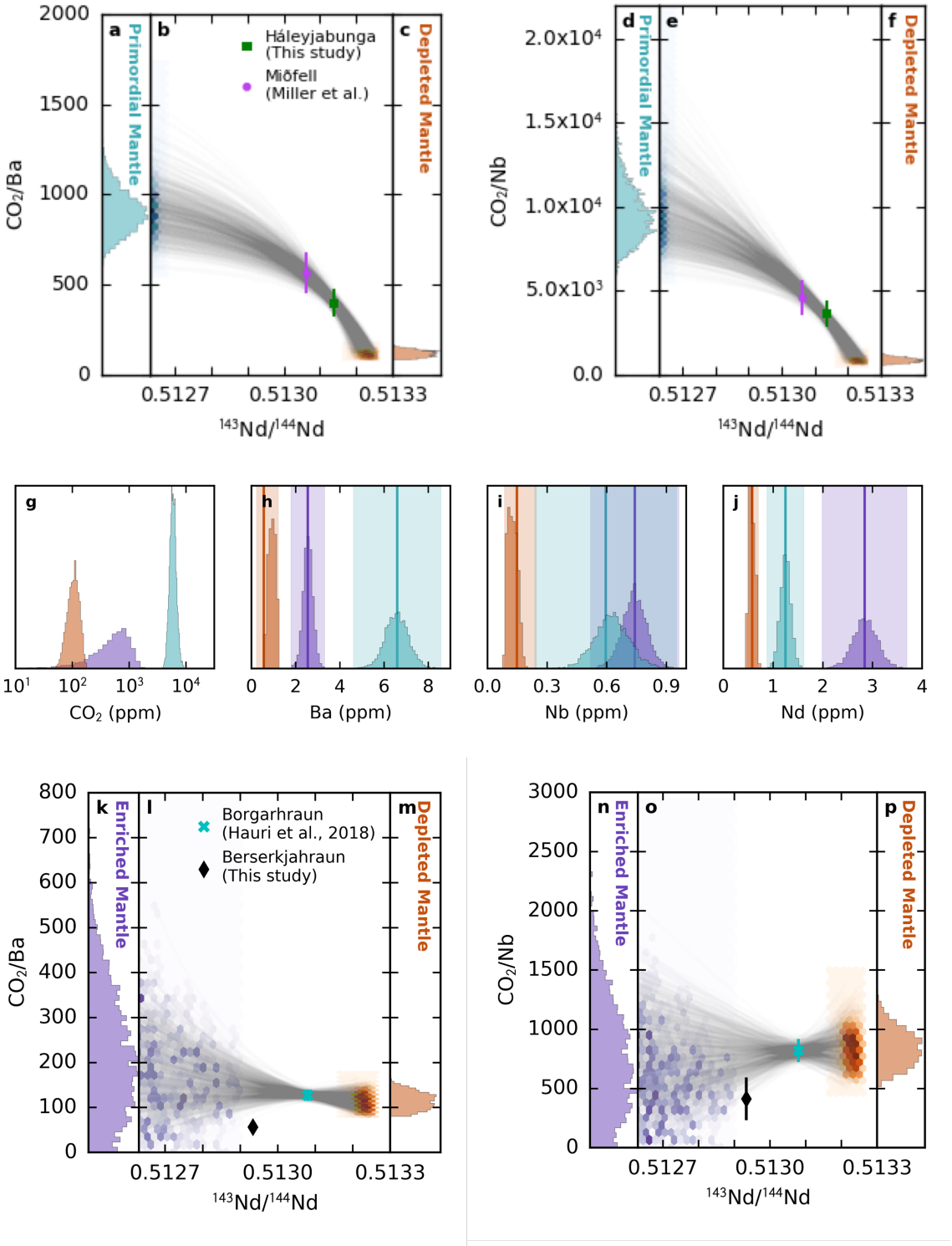

Figure 6.22: Results of the Bayesian inversion for mantle endmember CO_2 concentrations. Panels b, e, l and o show the binary mixing spaces for Nd-isotopes and both CO_2/Ba and CO_2/Nb. *Continued on the following page.*

Figure 6.22: The posterior distributions on the endmember $^{143}Nd/^{144}Nd$ ratios and CO_2/Ba or CO_2/Nb ratios are shown as 2D histograms (with colour density indicating frequency), mixing lines between the endmembers are shown in light-grey, and the observations used to constrain the calculation are shown as scatter points with 2σ errorbars. Panels a, c, d, f, k, m, n, and p show the posterior distributions of the mantle endmember CO_2/Ba and CO_2/Nb ratios as histograms. Panels g, h, i, and j show the posterior distributions on mantle endmember CO_2, Ba, Nb and Nd concentrations. The vertical bars indicates the prior median concentrations for EM and PM endmembers, and the average depleted mantle concentrations reported by Workman and Hart (2005) for the DM endmember. The shaded bars indicate three standard deviations of the prior distribution for the EM and PM endmembers, and the range on the uniform prior for the DM endmember.

ratios of the DM end-member are comparable to previous estimates for the upper mantle (Hirschmann, 2018; Rosenthal et al., 2015).

The inferred CO_2/Ba and CO_2/Nb ratios of the PM endmember are extremely high. This result remains even if the PM end-member is assumed to have a FOZO-like composition, though the posterior distribution extends to lower values of CO_2/Ba and CO_2/Nb (Figure 6.25 and Table 6.3).

My new mantle CO_2 concentration estimates are the first to be made for different mantle components in one location. Figure 6.23 shows that the estimate for the depleted mantle CO_2 concentration (106^{+18}_{-18} ppmw) compares favourably with the concentrations inferred from MORB melt inclusion suites (Le Voyer et al., 2017; Rosenthal et al., 2015), undersaturated glasses (Michael and Graham, 2015) and with estimates derived from CO_2–He systematics (Marty, 2012; Tucker et al., 2018). The new estimate for primordial mantle (5900^{+560}_{-520} ppmw) is much higher than most previous estimates of the CO_2 content of plume mantle, or bulk mantle as estimated by Marty (2012), whilst the estimate of CO_2 concentration in the recycled mantle (540^{+270}_{-240} ppmw) is significantly lower than the plume and bulk mantle estimates. This difference most likely arises from previous estimates averaging high- and low-CO_2 mantle reservoirs.

The inversion was repeated using the upper limits of CO_2/Ba and CO_2/Nb values in the main melt inclusion populations, as opposed to the maximum values in the dataset. Using these lower values allows a better fit to the Berserkjahraun CO_2/Ba and CO_2/Nb constraints, but does not change the qualitative conclusions of the above analysis (Table 6.3, and Figures 6.26, 6.27 and 6.28). However, since the maximum CO_2/Ba and CO_2/Nb ratios observed in Berserkjahraun are likely to represent degassed melts, the better fit is most likely a consequence of using degassed CO_2/Ba and CO_2/Nb constraints from the other eruptions.

Model		CO_2/Ba	CO_2/Nb	CO_2 (ppmw)
Maximum Values	DM	115^{+14}_{-15}	840^{+112}_{-112}	106^{+18}_{-18}
(main text)	EM	212^{+108}_{-93}	733^{+371}_{-322}	540^{+270}_{-240}
	PM	901^{+84}_{-82}	9450^{+1270}_{-1030}	5900^{+560}_{-520}
Maximum Values	DM	$171.8^{+8.5}_{-7.9}$	1426^{+104}_{-98}	161^{+17}_{-15}
(including Berserkjahraun)	EM	$14.0^{+7.1}_{-6.4}$	55^{+30}_{-25}	38^{+21}_{-17}
	PM	837^{+87}_{-74}	8400^{+1000}_{-830}	5430^{+550}_{-460}
Maximum Values	DM	117^{+14}_{-13}	870^{+120}_{-110}	107^{+19}_{-16}
(PM as FOZO)	EM	191^{+98}_{-83}	660^{+330}_{-280}	480^{+250}_{210}
	PM	875^{+197}_{-132}	8360^{+2210}_{-1400}	2930^{+600}_{-550}
Plateau Values	DM	$77.2^{+2.7}_{-2.8}$	680^{+33}_{-26}	$76.7^{+7.5}_{-7.3}$
	EM	$19.7^{+12.6}_{-9.8}$	72^{+46}_{-36}	52^{+33}_{-26}
	PM	714^{+72}_{-64}	6670^{+830}_{-750}	4530^{+420}_{-400}
Plateau Values	DM	$76.7^{+3.0}_{-3.0}$	713^{+38}_{-38}	$77.5^{+7.1}_{-6.7}$
(PM as FOZO)	EM	$20.7^{13.2}_{-9.9}$	75^{+45}_{-36}	54^{+34}_{-26}
	PM	1110^{+430}_{-290}	5880^{+1430}_{-1060}	1800^{+430}_{-370}
Plateau Values	DM	49^{+13}_{-15}	420^{+110}_{-130}	50^{+14}_{-14}
(without Berserkjahraun)	EM	353^{+165}_{-151}	1270^{+590}_{-550}	910^{+430}_{-390}
	PM	751^{+79}_{-71}	7050^{+930}_{-770}	4800^{+450}_{-460}

Table 6.3: Summary of the inversion results for each set of assumptions used. Median values and the 25% confidence intervals are given for the CO_2/Ba, CO_2/Nb and CO_2 concentration of each of the three mantle endmembers (DM, EM and PM).

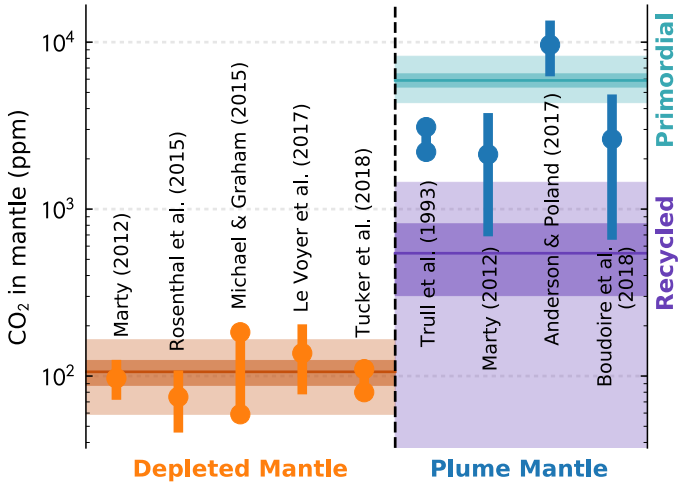

Figure 6.23: Comparison of the inversion results with previous estimates of the CO_2 concentration in depleted mantle and plume mantle. The horizontal bar shows the median value from the posterior distributions of CO_2 concentration, the dark shaded region shows the 25th and 75th percentiles, and the light shaded region shows the 1st and 99th percentiles. The 1st percentile on the Recycled (EM) result plots below the lower limit of the y-axis. Published estimates from Anderson and Poland (2017); Boudoire et al. (2018); Le Voyer et al. (2017); Marty (2012); Michael and Graham (2015); Rosenthal et al. (2015); Trull et al. (1993); Tucker et al. (2018).

6.6.3 Difficulties in inferring the recycled mantle CO_2 budget

I have demonstrated that reasonable constraints can be placed on the CO_2 budget of depleted and primordial mantle reservoirs. Difficulties remain, however, for identifying the CO_2 content of recycled mantle material. The first of these difficulties is made clear by the quantitative analysis above: eruptions which sample predominantly recycled mantle components are also extremely trace element enriched. The trace element enrichment of enriched basalts results in a greater likelihood of CO_2 loss due to degassing and decrepitation if the CO_2/Ba of the recycled mantle material is similar or greater than the depleted mantle. A further difficulty is the possibility for decoupling between the extremely incompatible elements CO_2, Ba and Nb, and the moderately incompatible elements Pb, Nd and Sr. Much higher degrees of melting are required for a refractory depleted component to contribute to the Nd, Sr and Pb budget of a magma, than for the CO_2, Ba and Nb budget to be strongly influenced. Therefore, where the extent of melting is controlling the relative contribution of depleted and enriched mantle to the Pb-, Nd- and Sr-isotope ratios, rather than source composition, the observed CO_2/Ba and CO_2/Nb ratios may reflect an average of the enriched and depleted components in the source. As discussed in Section 6.6.1, this is not an issue for the signal of high CO_2/Ba with high $^3He/^4He$, as He also behaves extremely incompatibly during mantle melting.

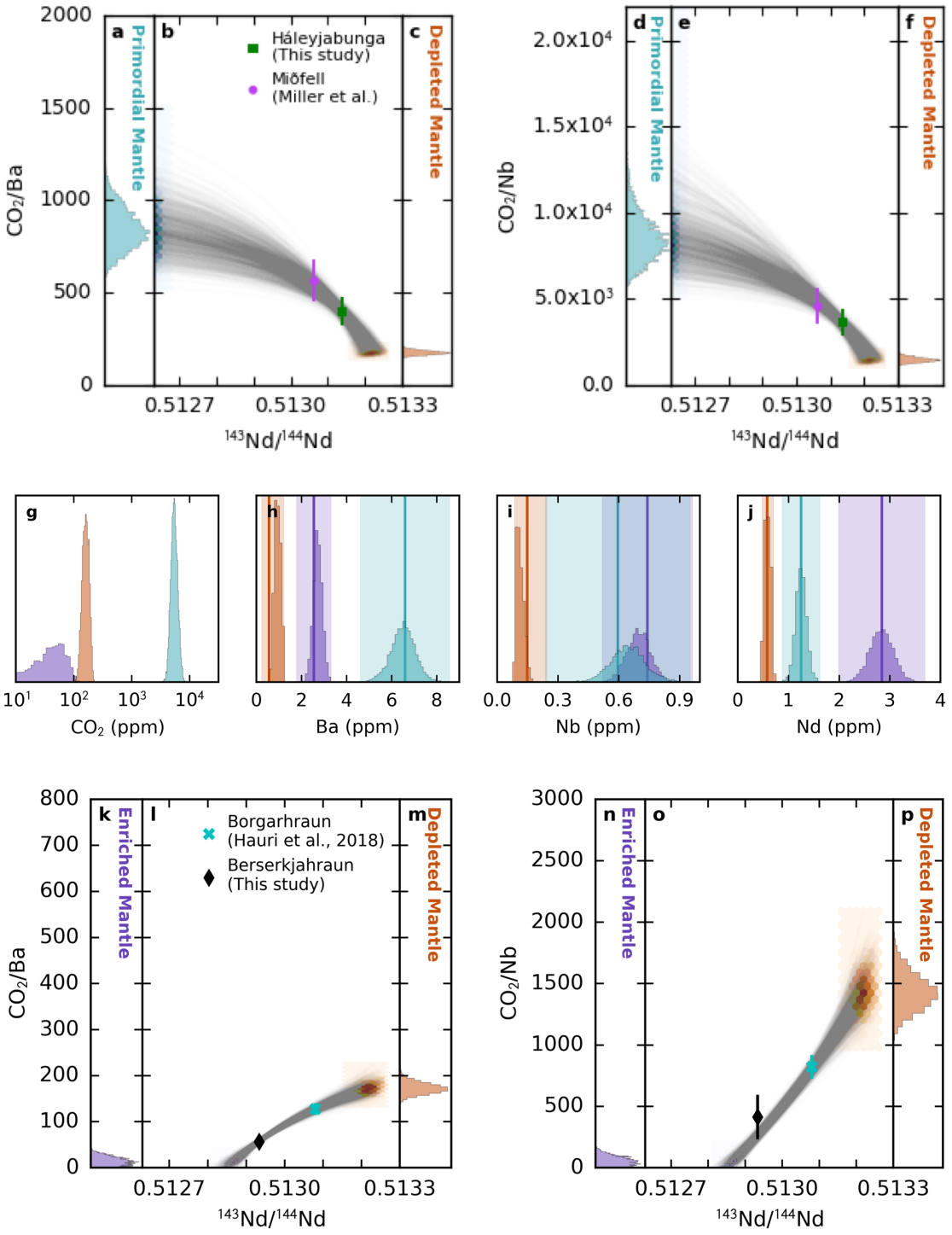

Figure 6.24: Inversion results for the calculation described in the main text when the maximum CO_2/Ba and CO_2/Nb ratios observed in Berserkjahraun are imposed as a constraint. 'Maximum Values (including Berserkjahraun)' in Table 6.3. See the caption to Figure 6.22 for more information.

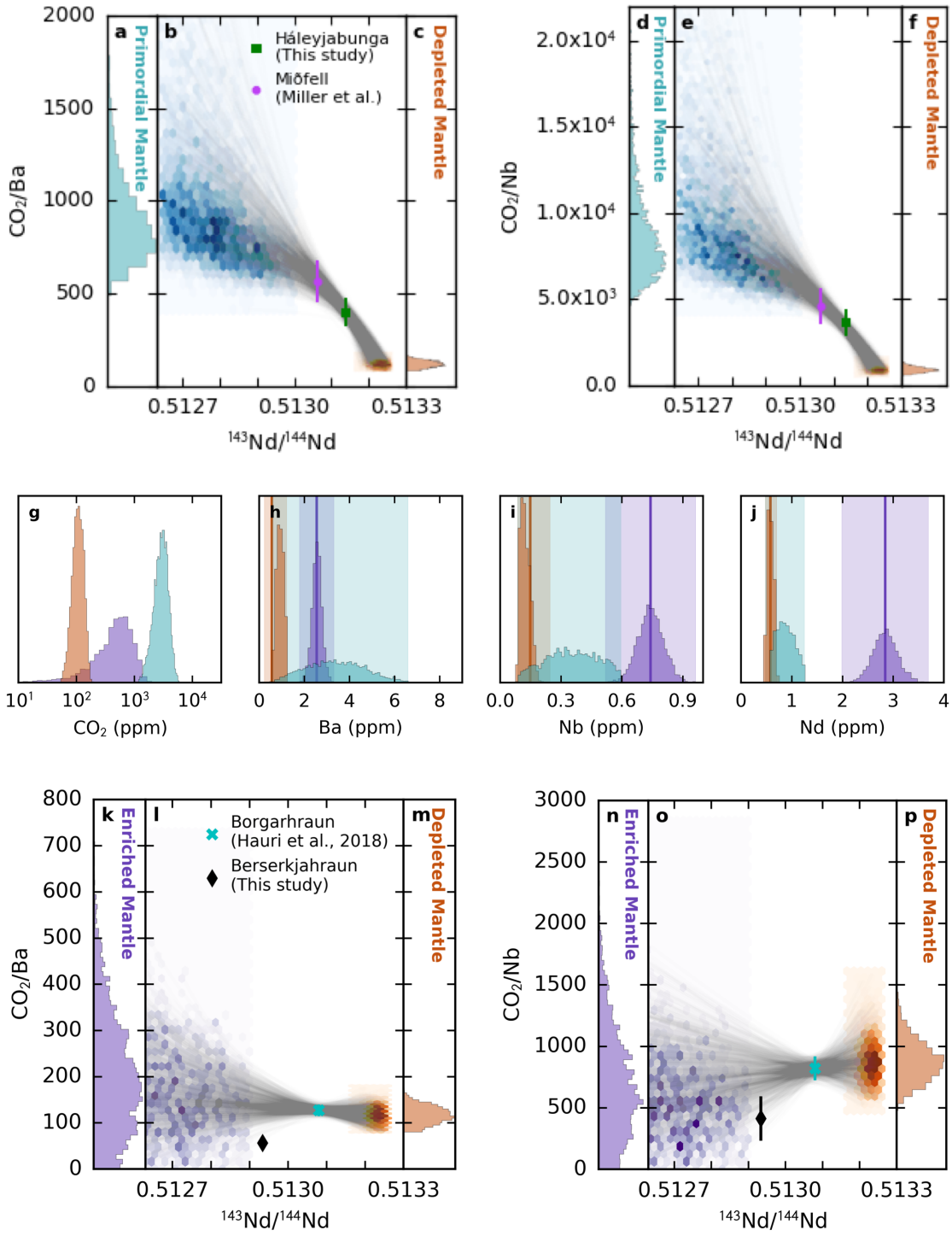

Figure 6.25: Inversion results for the calculation described in the main text when the PM member is assumed to be 'FOZO'-like. 'Maximum Values (PM as FOZO)' in Table 6.3. See the caption to Figure 6.22 for more information.

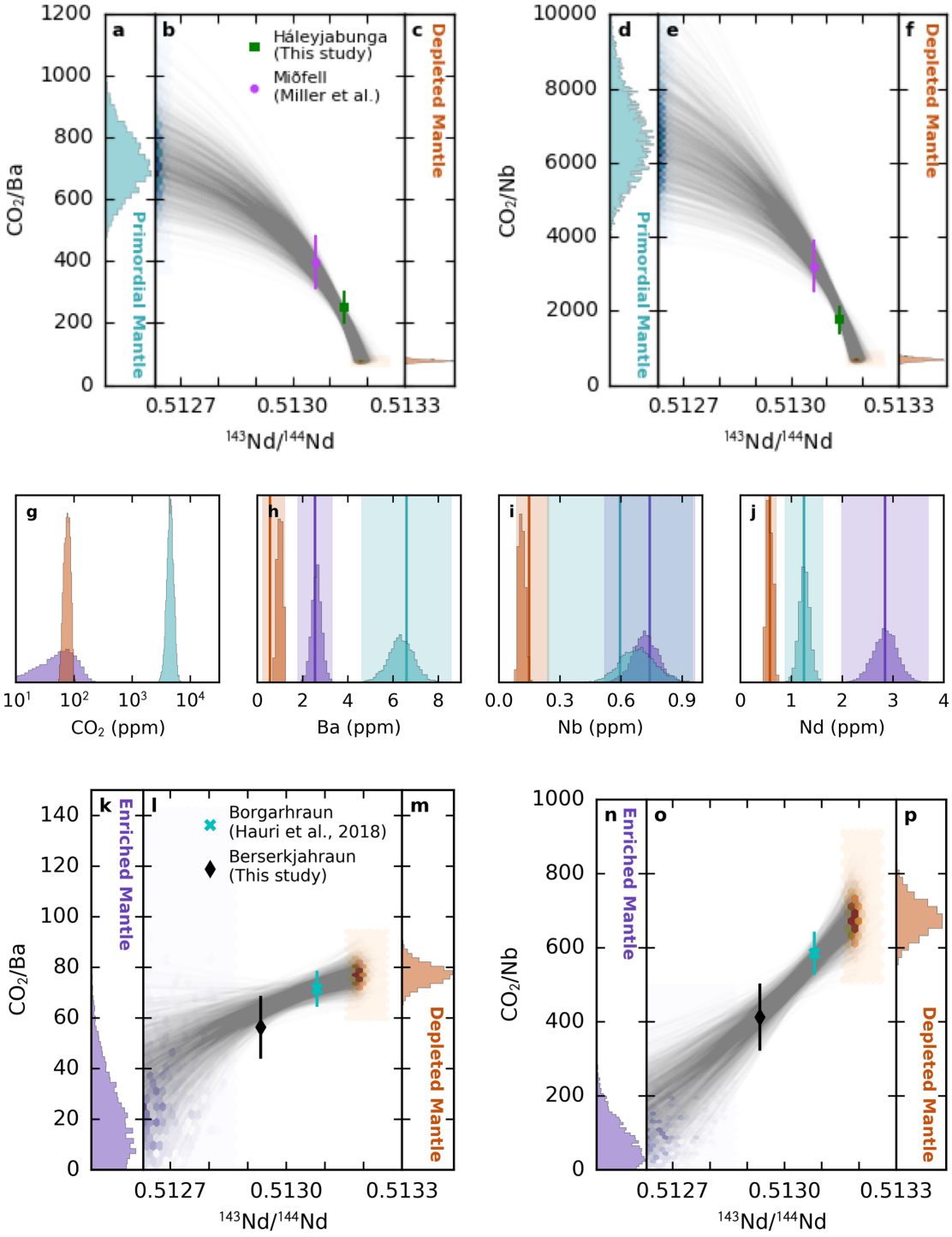

Figure 6.26: Inversion results when the CO_2/Ba and CO_2/Nb constraints are taken to be the upper limits of the main melt inclusion populations. Berserkjahraun is included as a constraint. 'Plateau Values' in Table 6.3. See the caption to Figure 6.22 for more information.

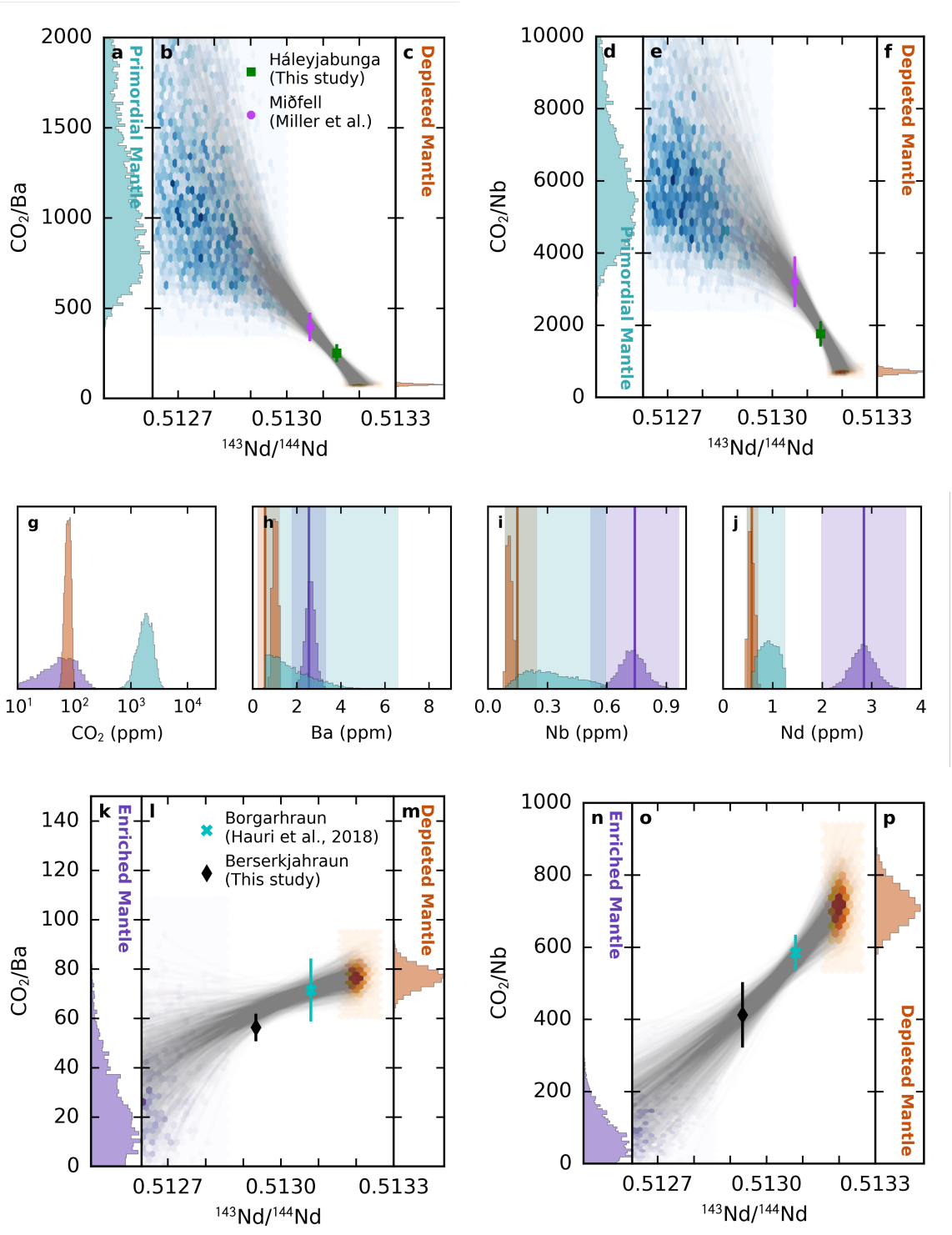

Figure 6.27: Inversion results when the CO_2/Ba and CO_2/Nb constraints are taken to be the upper limits of the main melt inclusion populations, and the PM endmember is assumed to be FOZO like. Berserkjahraun is included as a constraint. 'Plateau Values (PM as FOZO)' in Table 6.3. See the caption to Figure 6.22 for more information.

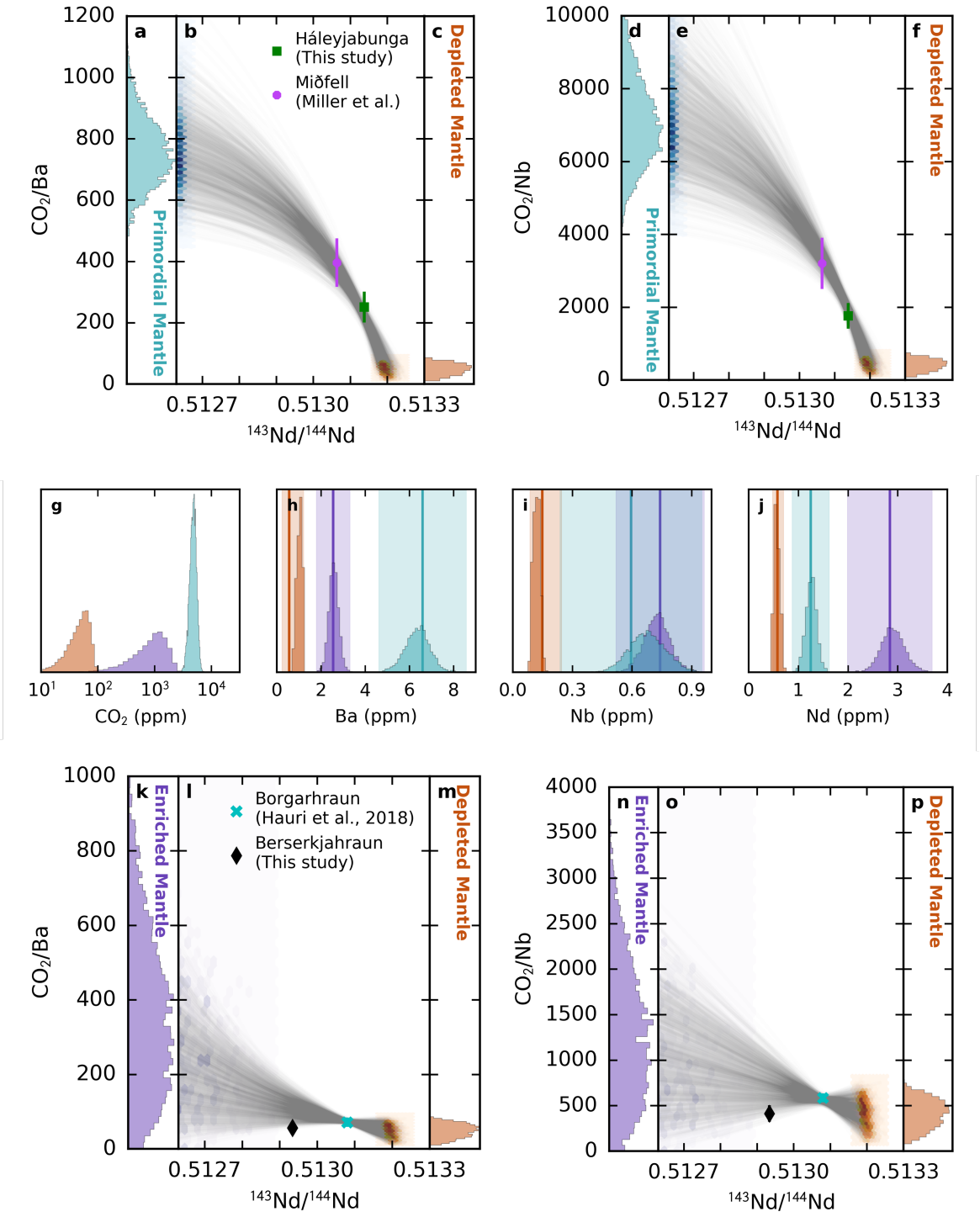

Figure 6.28: Inversion results when the CO_2/Ba and CO_2/Nb constraints are taken to be the upper limits of the main melt inclusion populations. Berserkjahraun is excluded. 'Plateau Values' in Table 6.3. See the caption to Figure 6.22 for more information.

6.6.4 Implications of carbon rich mantle reservoirs

The extremely high CO_2/Ba and CO_2/Nb inferred for the primordial mantle in the inversion (Section 6.6.2) stems from the observations of high CO_2/Ba and CO_2/Nb in melt inclusions from two eruptions. One way of rationalising this observation is if the primordial material is extremely depleted in lithophile trace elements such as Ba and Nb. Whilst it has been suggested that the high $^3He/^4He$ mantle may be more depleted than bulk silicate Earth (Hart et al., 1992), if the high $^3He/^4He$ contained similar CO_2 concentrations as the depleted mantle it would have to be at least an order of magnitude more depleted to explain the high observed CO_2/Ba and CO_2/Nb. The conclusion that the primordial mantle is CO_2 rich is then unavoidable.

This extremely high CO_2 budget is considerably greater than can be stored in the peridotite mineral assemblage (Rosenthal et al., 2015), though storage in silicate minerals is implicitly assumed when CO_2 is treated as a trace element during melting. For typical mantle oxygen fugacities (fO_2) carbon is stabilised in a reduced phase (either graphite or diamond) below the melting region (Dasgupta and Hirschmann, 2010). As mantle decompresses, mineral equilibria shift and cause the reduced carbon to be oxidised to carbonate (CO_3^{2-}).

At typical mantle potential temperatures this carbonate-bearing assemblage is above the carbonated peridotite solidus, meaning the transition is accompanied by 'redox' melting (Dasgupta and Hirschmann, 2010). Dilution of this melt by higher degree silicate melts is unavoidable; the carbon liberated from the residue by redox melting will apparently behave as an extremely incompatible element and therefore remain coupled to Ba and Nb. However, when the mantle contains a considerable concentration of carbon, the carbon itself may influence redox equilibria. If graphitic carbon is able to coexist with silicate magma, the magmatic CO_2 concentration will be much lower, but will persist long after Ba and Nb are exhausted from the residue (Duncan and Dasgupta, 2017). Graphite-present melting provides a mechanism for CO_2 to be fractionated from Ba and Nb, and consequently partial melts with both extremely high and extremely low CO_2/Ba and CO_2/Nb ratios will be produced (Section 4.3)

In Section 4.3 I assessed the CO_2–trace element systematics arising from graphite-saturated melting. Whilst the CO_2–trace element systematics of Háleyjabunga and Miðfell rule out equilibrium with graphite for most of the melting region, it is not implausible that the most extreme values of CO_2/Ba and CO_2/Nb could be generated in this way. I emphasise, however, that this process may only be important when mantle carbon concentrations are extremely large or the mantle is significantly more reduced than indicated by $Fe^{3+}/\Sigma Fe$ ratios of Icelandic basalts (Shorttle et al., 2015), or MORB (Berry et al., 2018; Cottrell and Kelley, 2011), and so this does not change the conclusions of this study.

Despite the unparalleled quantity of melt inclusion data available for Iceland, it is not possible to place robust constraints on the carbon content of recycled mantle components. This limitation is due, in part, to having only two eruptions constraining the DM–EM mixing binary, one of which is unlikely to preserve a mantle CO_2/Ba and CO_2/Nb signal. An alternative approach for assessing the effect of recycled material on the mantle CO_2 budget is to assess global variations in CO_2/Ba and CO_2/Nb ratios along the mid-ocean ridge system. The fairly uniform $R/R_a \sim 8$ for MORBs means the influence of primordial (high ^{3}He/^{4}He mantle) is excluded from the dataset. I also include eruptions from Iceland that have $R/R_a \sim 8$ (Borgarhraun and Berserkjahraun), in addition to Heilagsdalsfjall as nearby eruptions all have $R/R_a \sim 8$ (Harðardóttir et al., 2018), though He-isotope measurements have not been made on Heilagsdalsfjall material. Using the global dataset allows us to populate the DM–EM array with more depleted eruptions, i.e. those which are less susceptible to CO_2 loss by magmatic degassing.

Figure 6.29 shows the compilation of CO_2/Ba and CO_2/Nb ratios plotted against ratios used as indices of enrichment: ^{143}Nd/^{144}Nd (as used in Section 6.6.2), ^{206}Pb/^{204}Pb and Ba/Nb. Though not shown here, similar observations can be made with ^{207}Pb/^{204}Pb, ^{208}Pb/^{204}Pb and ^{87}Sr/^{86}Sr. Though the radiogenic isotope ratios are not fractionated by the melting process, their value depends not only on source enrichment, but also age; however, they are potentially still a useful tracer of mantle heterogeneity.

As discussed in Chapter 4, I advocate taking the highest values of CO_2/Ba and CO_2/Nb from melt inclusion datasets as the best proxy for the mantle, in preference to the dataset averages used by previous studies (Hauri et al., 2018; Le Voyer et al., 2017; Saal et al., 2002). In Figure 6.29 I highlight the difference between the two approaches for the datasets which preserve correlations between CO_2 and the trace elements (filled and unfilled blue circles). I distinguish melt inclusion datasets which do not retain a CO_2-trace element correlation (orange circles) since they likely experienced greater extents and a more complex history of CO_2 degassing and magma mixing. CO_2-undersaturated (ultra-depleted) MORB glasses are shown as grey circles.

Figures 6.29a, 6.29b and 6.29c show there is no systematic variation in CO_2/Ba with eruption enrichment. Likewise, Figures 6.29d and 6.29e show there is no covariation of CO_2/Nb with radiogenic isotope tracers of eruption enrichment, however a correlation is observed with Ba/Nb (Figure 6.29f). Hirschmann (2018) also described this feature in his compilation of global CO_2/Ba and CO_2/Nb ratios, though he found a stronger correlation between CO_2/Nb and Ba/Nb than shown here. This small discrepancy arises since Hirschmann (2018) includes datasets associated with plumes (which I do not include as they may have contributions from high ^{3}He/^{4}He mantle) and presents the undersaturated glass measurements as averages.

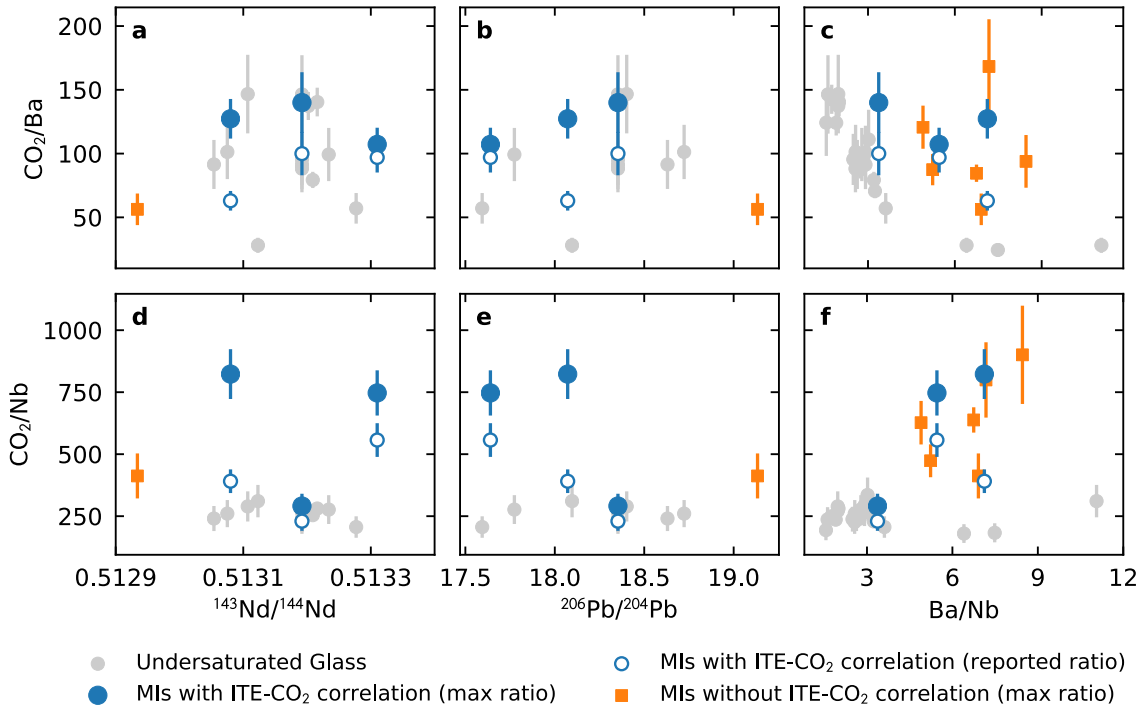

Figure 6.29: Compilation of data from the global mid-ocean ridge system. Melt inclusion datasets are separated into those exhibiting correlations between CO_2 and trace elements (blue circles), and those without a correlation (orange squares). For comparison the CO_2/Ba and CO_2/Nb ratios that were reported for the datasets exhibiting correlations are also shown; these values were derived by taking dataset averages rather than by taking the maximum values as advocated here. Glasses that are undersaturated in CO_2 vapour at the pressure of eruption are shown as grey circles. The $^{143}Nd/^{144}Nd$, $^{206}Pb/^{204}Pb$ and Ba/Nb ratios for the melt inclusion datasets are taken from published analyses of whole-rock or matrix glass from the same eruptions, for the which the sources are listed in Table 2.2. The melt inclusion CO_2/Ba and CO_2/Nb ratios are reported by this study, Hauri et al. (2018); Helo et al. (2011); Le Voyer et al. (2017); Saal et al. (2002); Wanless et al. (2014); Wanless and Shaw (2012). The undersaturated glass CO_2/Ba and CO_2/Nb ratios were reported by Michael and Graham (2015); Shimizu et al. (2016).

The highest CO_2/Ba ratios observed in datasets with CO_2-trace element correlations coincide with the highest CO_2/Ba ratios seen in the undersaturated glasses, lending confidence to the legitimacy of using maximum CO_2/Ba values. Further support comes from the coincidence of CO_2/Ba ratios measured in undersaturated glasses from the Siqueiros fracture zone (Michael and Graham, 2015) with the highest values observed in the Siqueiros melt inclusions (Rosenthal et al., 2015; Saal et al., 2002).

Most of the datasets without a CO_2-trace element correlation have CO_2/Ba ratios lower than datasets with a correlation, this could reflect a greater extent of CO_2 degassing and mixing seen by the datasets that lack a correlation. The undersaturated glasses have CO_2/Ba ratios that overlap with the range displayed by the melt inclusion datasets. If the tendency of the melt inclusion datasets without CO_2-trace element correlations to exhibit lower CO_2/Ba ratios is due to greater CO_2 loss by degassing, then this may suggest the undersaturated glasses with lower CO_2/Ba ratios have also lost CO_2 by degassing. In Chapter 4 I demonstrated that undersaturation at eruption cannot be taken as evidence that CO_2 has not been lost; the undersaturated nature of the glasses may come from mixing of melts undersaturated in CO_2 vapour with mmelts that saturated in CO_2 vapour during magma storage. The lowest CO_2/Ba ratios ($<$50) seen in the undersaturated glasses are significantly lower than the CO_2/Ba ratios seen in melt inclusion datasets at similar Ba/Nb, suggesting they most likely have lost substantial CO_2 vapour during magma storage.

The strength of the correlation between CO_2/Nb and Ba/Nb shown in Figure 6.29f arises from the low CO_2/Nb ratios associated with the samples with low Ba/Nb. The low Ba/Nb samples are from eruptions in fracture zones, including the melt inclusion dataset from the Siqueiros fracture zone (Saal et al., 2002). Hirschmann (2018) suggests that the correlation may arise from Nb being fractionated from Ba and CO_2 during mantle melting. I have shown that Nb and Ba are not fractionated from each other during the melting processes that generated the Iceland melt inclusion suites (Section 6.3). Michael and Graham (2015) suggested that utradepleted glasses are generated where melt aggregation is incomplete, with a particularly low contribution from the deepest melts. This partial aggregation provides a mechanism for fractionating Nb from Ba and CO_2 that is likely to only occur in fracture zones, and therefore may explain the origin of the low CO_2/Nb and Ba/Nb population in Figure 6.29. If fracture-zone eruptions are discounted from Figure 6.29, there still remains a correlation between Ba/Nb and CO_2/Nb, though it is weaker. Given that Ba and Nb have not been fractionated from each other during melting in the petrogenesis of these eruptions, this correlation is most likely a source feature and may reflect a decoupling of Nb and Ba concentrations during recycling (Hirschmann, 2018).

As discussed in Section 6.6.1, it is possible that the variation in $^{143}Nd/^{144}Nd$ observed between Icelandic eruptions is decoupled from CO_2/Ba and CO_2/Nb by melt transport, and so my proxy for source components could be invalid. A more reliable record of the local mantle average Nd-, Sr- and

Pb-isotope ratios is ridge-segment average values (Shorttle, 2015). Figure 6.30 demonstrates that CO_2/Ba and CO_2/Nb do not co-vary with ridge-segment average Nd- and Pb-isotope ratios.

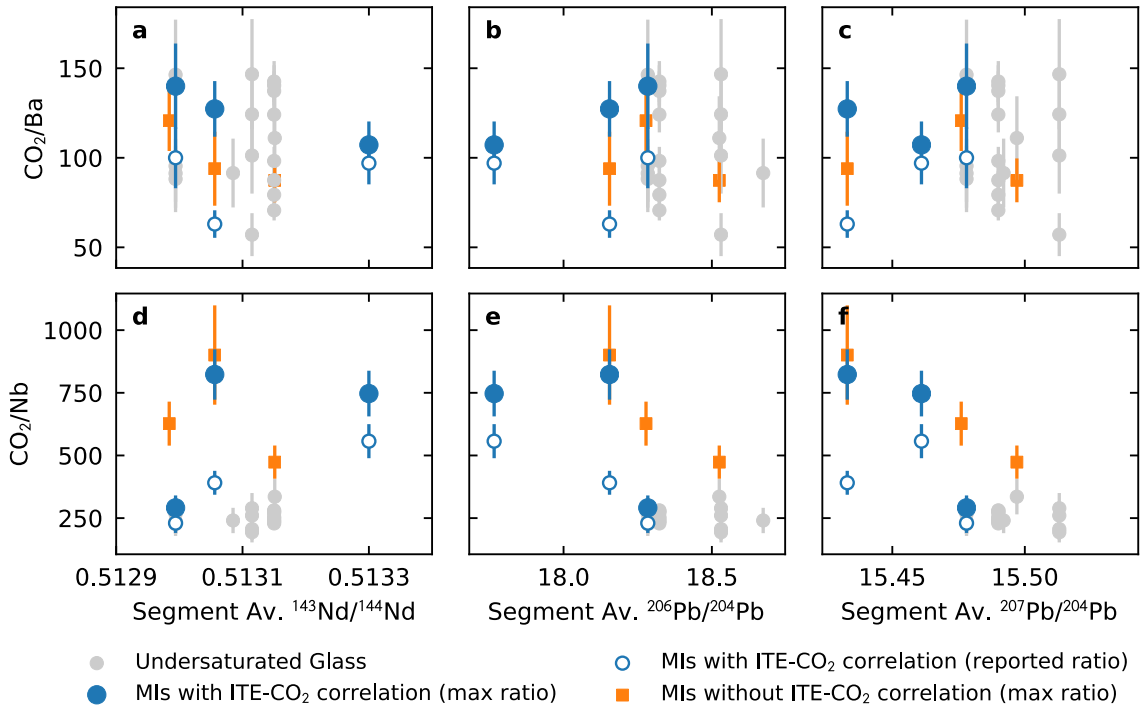

Figure 6.30: Compilation of data from the global mid-ocean ridge system. The $^{143}Nd/^{144}Nd$, $^{206}Pb/^{204}Pb$ and $^{207}Pb/^{204}Pb$ ratios for each sample are calculated by averaging all whole-rock and glass analyses from the same mid-ocean ridge. Where samples are taken from fracture-zones, the segments either side are combined in the average. Data sources are reported in Table 5.4. See the caption to Figure 6.29 for more information

6.6.5 Whole mantle CO_2 mass balance

In Section 6.6.2 I demonstrated that reasonable constraints may be placed on the CO_2 concentration in a depleted mantle component (DM) and a primordial component (PM) in Iceland, but there is little constraint on the CO_2 content in the recycled mantle component (EM). In Section 6.6.4 I showed that there is little variation in the CO_2/Ba ratio with degree of enrichment in the upper mantle. If the variable enrichment of the upper mantle is primarily controlled by varying amounts of recycled material this might be taken to suggest there is little difference in the CO_2/Ba ratio of the depleted mantle and recycled mantle. Figure 6.31 shows the results of a mass-balance calculation to assess how realistic this is on a global scale. In the calculation the CO_2 content of the DM and PM components is taken as the median value of their respective posterior distributions from Section 6.6.2. For varying mass fractions of the DM, PM and EM mantle components, I calculate the CO_2 concentration the

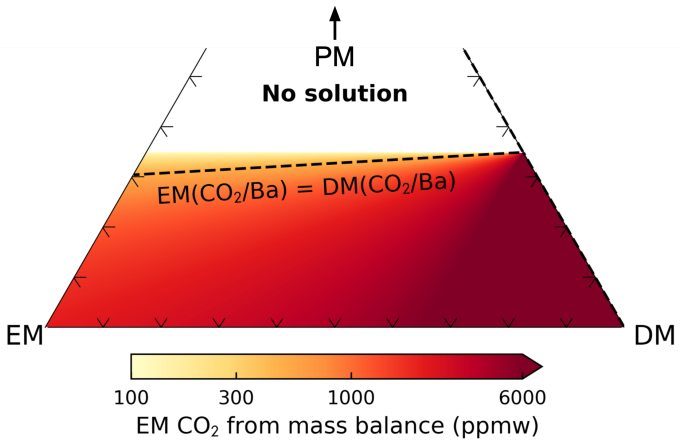

Figure 6.31: The concentration of CO_2 required in the EM component to satisfy mass balance assuming a bulk mantle CO_2 concentration of 2130 ppmw (Marty, 2012), plotted here in a ternary diagram of mass fraction. The calculation assumes the DM mantle component has 106 ppmw CO_2, and the PM component has 5898 ppmw. The dashed line indicates the locus of solutions where the EM and DM components have the same CO_2/Ba ratio, assuming a Ba concentration of 0.563 ppmw in the DM component, and 2.55 ppmw in the EM component (Table 6.2).

EM component must have in order for the total mantle to have the bulk mantle CO_2 concentration of 2130$\pm$1390 ppmw estimated by Marty (2012). If the depleted mantle and enriched mantle have the same CO_2/Ba ratio, approximately 30% of the mantle must be primordial to satisfy this mass balance. This is a significant fraction of the mantle that must have remained undegassed, however it is substantially less than the mass fraction of undepleted mantle ($\sim$70%) calculated from box-modelling of continental crust extraction (Jacobsen and Wasserburg, 1979). However, it is unlikely that this volume of mantle can have remained isolated from vigorous mantle convection through the lifetime of the Earth, as required by noble gas constraints (van Keken et al., 2002). Using 2D mantle convection models Ballmer et al. (2017) demonstrated that 10–15% of the mantle could remain isolated from convection if those domains are anomalously rich in bridgmanite. This smaller mass fraction may be consistent with the enriched mantle having a higher CO_2/Ba ratio than the depleted mantle.

6.7 Summary

I have leveraged a large new melt inclusion dataset of trace element and CO_2 concentrations in geochemically diverse Icelandic eruptions, alongside existing suites of melt inclusions, to place new constraints on the interplay of source and process on CO_2/Ba and CO_2/Nb ratios. I showed that though there is a global covariation of CO_2/Ba with enrichment in melt inclusions, this is a result of olivine decrepitation limiting the CO_2 concentration in melt inclusions. Decrepitation may be avoided if a

significant fraction of a melt inclusions CO_2 budget is partitioned into a vapour bubble. When the CO_2 contained in vapour bubbles is added back into their coexisting glass, substantial heterogeneity in CO_2/Ba between Icelandic eruptions remains.

I demonstrate CO_2/Ba and CO_2/Nb co-varies with radiogenic isotope proxies for the contributions of depleted, primordial and enriched mantle components to the melts, with the highest CO_2/Ba and CO_2/Nb being associated with primordial mantle derived melts, and the lowest with enriched mantle derived melts. Whilst it is likely the low CO_2/Ba and CO_2/Nb associated with the enriched mantle is due to the greater tendancy for enriched melts to be affected by degassing, I argue the elevated CO_2/Ba and CO_2/Nb ratios for primordial mantle derived melts relative to depleted mantle is a consequence of elevated CO_2 in the solid primordial mantle. Using the observed covariation of CO_2/Ba and CO_2/Nb with mantle source I invert for the CO_2 concentration in the Icelandic mantle sources, and find concentrations of 106^{+18}_{-18} ppmw for the depleted mantle, 5900^{+560}_{-520} ppmw for the primordial mantle, and 540^{+270}_{-240} ppmw for the enriched/recycled mantle. Though the CO_2 concentration is likely to be greater in the enriched mantle than the depleted mantle, this could correspond to similar CO_2/Ba and CO_2/Nb ratios in both sources.

The global mid-ocean ridge CO_2/Ba and CO_2/Nb observations show no systematic variation of CO_2/Ba with enrichment, but do show a variation in CO_2/Nb with Ba/Nb ratio; these observations may suggest similar behaviour of Ba and CO_2 during recycling, but different behaviour of Nb. Finally I demonstrated that my estimates of source CO_2 concentrations are consistent with estimates of the total quantity of CO_2 in the mantle.

Chapter 7

H_2O heterogeneity in the Icelandic mantle

As summarised in Section 1.2, significant global heterogeneity in mantle H_2O has been inferred from oceanic basalts, with enriched components being more H_2O rich than depleted components. The same observation was made for the Icelandic mantle by Nichols et al. (2002), who demonstrated that in a suite of submarine glasses collected along the Reykjanes Ridge, the H_2O concentrations increased towards Iceland. Rather than using H_2O-trace element systematics to avoid consideration of the melting and crustal magmatic differentiation processes, Nichols et al. (2002) estimated mantle H_2O concentrations by directly applying a correction for fractional crystallisation and mantle melting, and inferred mantle H_2O concentrations of 165 ppmw at the Southern end of the Reykjanes ridge and beneath Iceland.

In this Chapter I use the Icelandic melt inclusion compilation and new analyses of Reykjanes Ridge glasses to assess whether small scale H_2O heterogeneity is present within the Icelandic mantle. I apply the methodology employing H_2O-trace element systematics developed in Chapter 5, using H_2O/La ratios to filter out the signal of mantle melting and crystallisation. By considering the likely range of trace element concentrations in the Icelandic mantle I show that the inferred heterogeneity in mantle H_2O/La ratios could be consistent with either higher or lower H_2O concentrations in the enriched mantle component relative to the depleted mantle component.

7.1 Primary H_2O/La from melt inclusion datasets

In Section 5.3 I argued that though melt inclusions may not preserve their primary H_2O concentrations due to diffusive re-equilibration, the mean H_2O concentration of a melt inclusion population likely reflects the pre-eruptive H_2O concentration of their carrier melt. Since the La concentration of the matrix is unlikely to change significantly during eruption, an estimate of the mantle H_2O/La ratio may be obtained from the mean H_2O concentration of the melt inclusions and the La concentration in the matrix. The matrix La concentration is used in preference to the melt inclusion mean La concentration because the melt inclusions are likely to preserve less evolved, generally more dilute, melts than the matrix glass.

The distribution of H_2O concentrations in melt inclusions from each Icelandic eruption in the compilation are shown in Figure 7.1. For most of the eruptions the H_2O concentrations closely approximate a normal-distribution. The Berserkjahraun, Holuhraun and Laki distributions (Figure 7.1d, h and i) show sub-populations with lower H_2O concentrations (indicated by the grey histogram bars), plausibly reflecting more extensive diffusive re-equilibration with a partially degassed melt. To remove the effects of degassing, the low H_2O sub-populations are not included in calculation of the mean. The mean H_2O concentrations for each melt inclusion suite are shown by the vertical lines in Figure 7.1, and are divided by the La concentrations in the matrix glass (Table 7.1) to estimate a value for the primary H_2O/La ratio of each eruption. The Háleyjabunga lavas did not quench to form a glassy groundmass, instead whole rock La measurements, $[\mathrm{La}]_{\mathrm{w.r.}}$ are used. Since the measured trace element concentrations are diluted by the phenocryst assemblage presence, a correction is applied to obtain the magmatic La concentration, $[\mathrm{La}]_{\mathrm{magma}}$:

$$[\mathrm{La}]_{\mathrm{magma}} = \frac{[\mathrm{La}]_{\mathrm{w.r.}}}{(1 - f_{\mathrm{crystals}})} \tag{7.1}$$

where f_{crystals} is the mass fraction of crystals in the rock estimated from their volume fraction and assuming densities after Deer et al. (1997).

7.2 H_2O in melts derived from the Iceland plume

As a comparison to the mean melt inclusion H_2O concentrations for eruptions from on-land Iceland, I consider a series of submarine glasses from the Reykjanes Ridge sampled between 57.5°N and 63°N (Murton, 1995; Murton et al., 2002). Volatile (H_2O, CO_2, F and Cl) analyses were performed by Oliver Shorttle at the Edinburgh ion microprobe facility using the same methods described in Chapter 2. Basalts from the Reykjanes ridge are well known to show the increasing influence of the Iceland plume towards Iceland (Schilling et al., 1999). The H_2O and La concentrations of both

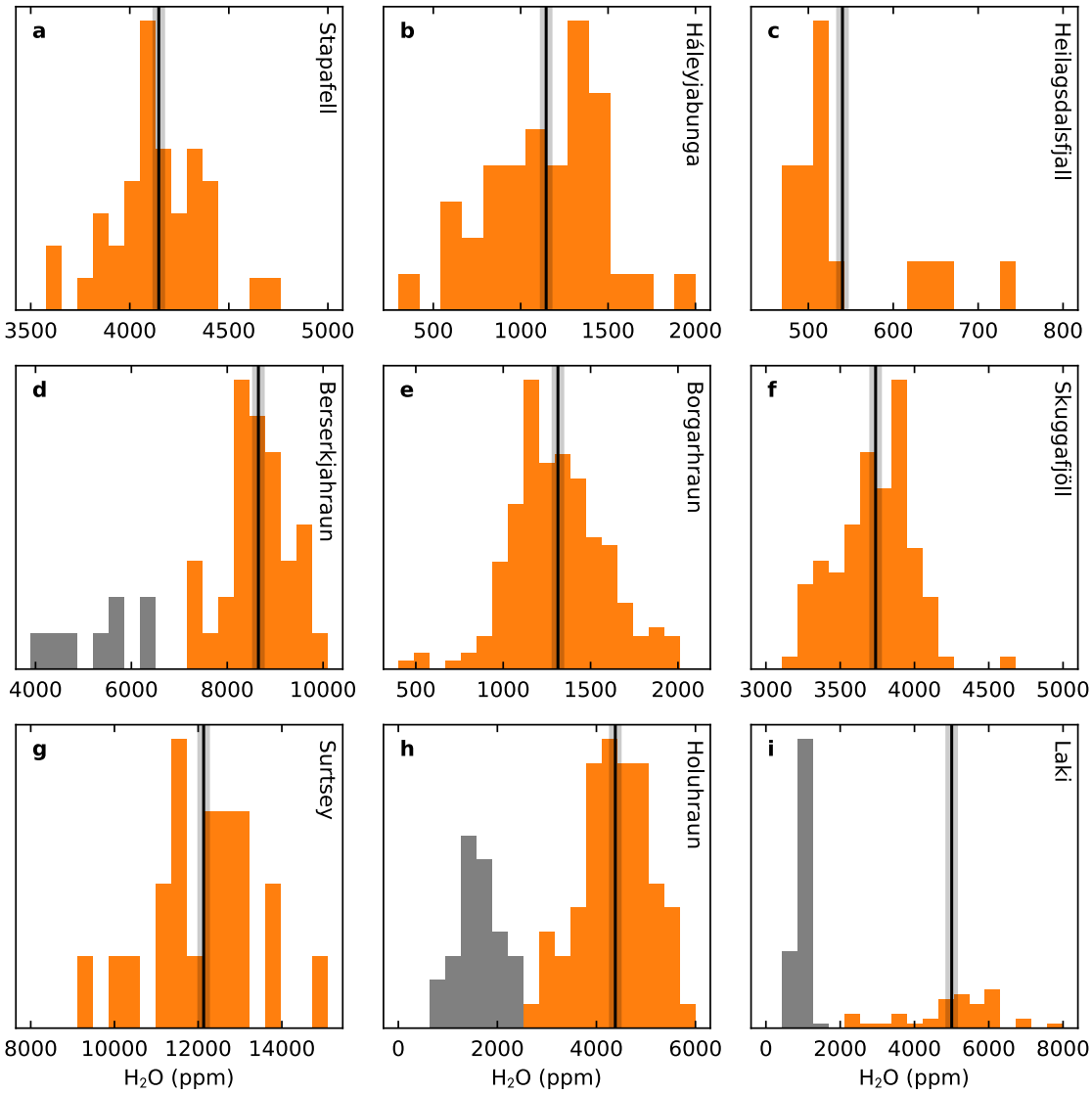

Figure 7.1: Each panel shows the distribution of H_2O concentrations in melt inclusions from the named eruption. The vertical grey bar shows the mean H_2O concentration of the population, excluding the inclusions coloured grey. The sources and locations of the melt inclusion data are shown in Table 2.1 and Figure 2.2.

Eruption	Mean H_2O (ppmw)	σ H_2O (ppmw)	La (ppmw)	Ce (ppmw)	H_2O/La	H_2O/Ce	Matrix Ref.
Berserkjahraun	8650	660	37.5	78.9	231	110	This study
Háleyjabunga[a]	1150	330	1.13	3.62	1018	319	Skovgaard et al. (2001)
Stapafell	4150	230	8.67	20.0	479	208	This study
Heilagsdalsfjall	540	70	1.68	4.03	321	134	This study
Borgarhraun	1310	270	1.03	2.75	1270	476	Hauri et al. (2018)
Laki	5000	1270	14.1	33.0	355	152	Hartley et al. (2014)
Skuggafjöll	3740	240	5.38	13.46	695	278	Neave et al. (2014)
Holuhraun	4380	700	8.44	21.15	519	207	Hartley et al. (2018)
Surtsey	12130	1280	16.8	40.3	722	301	Schipper et al. (2016)

Table 7.1: Mean melt inclusion H_2O concentrations for each eruption and their standard deviation (σ), the matrix glass La and Ce concentrations, and the inferred primary magmatic H_2O/La and H_2O/Ce ratios. References for the matrix glass trace element concentrations are given. [a] Háleyjabunga matrix trace element concentrations are corrected from whole rock using Equation 7.1.

datasets are shown together in Figure 7.2. The Reykjanes Ridge glasses show a gradual increase in both H_2O and La concentrations towards Iceland, starting at 61°N, consistent with similar data from Nichols et al. (2002). Though H_2O and La concentrations increase together towards Iceland, Figure 7.3 demonstrates how the greater relative increase in La causes the H_2O/La ratio of the glasses to fall towards Iceland. The on-land Iceland lavas show much greater variability in both H_2O and La concentrations, and have H_2O/La ratios both greater and less than the Reykjanes Ridge glasses (Table 7.1 and Figure 7.3).

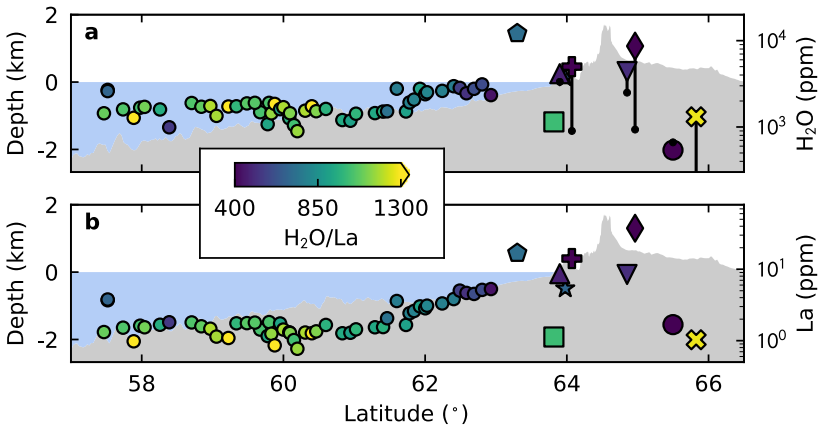

Figure 7.2: Panel a shows the H_2O concentrations in submarine glasses along the Reykjanes ridge (circles) and the mean H_2O concentrations in melt inclusions suites from on-land Iceland. The H_2O content of the matrix glasses from the same eruptions are shown as black dots, connected by vertical lines to the mean melt inclusion H_2O value. Panel b shows the La concentration in the submarine glasses, and the matrix glasses (or whole rock) for the on-land eruptions. The combined 1 s.d. accuracy and precision is smaller than the size of the symbols. All symbols are coloured for their H_2O/La ratio. Bathymetry is shown by the grey background shading, and the water-depth by blue shading. Reykjanes Ridge La concentrations are from Murton et al. (2002). See Figure 6.8 for a key to symbols.

Though varying degrees of mantle melting and fractional crystallisation affect the H_2O and La concentrations, the H_2O/La ratio will be little affected by these processes (Chapter 5). Nichols et al. (2002) applied a crystallisation correction to their H_2O concentration data and showed that the systematic increase in H_2O concentration towards Iceland is not a result of more extensive fractional crystallisation. Additionally, the observed H_2O concentrations are not sufficient for the magmas to have lost significant H_2O by degassing (Dixon and Stolper, 1995; Moore, 1965). Dixon et al. (2017) demonstrated the large variations in H_2O/Ce in variably plume-influenced basalt are controlled by varying contributions from enriched mantle components.

In Iceland, contributions to basalt chemistry from numerous mantle sources have been mapped out using Sr-, Nd- and Pb-isotope ratios (Section 1.4.1). Figure 7.4 demonstrates strong covariation of the

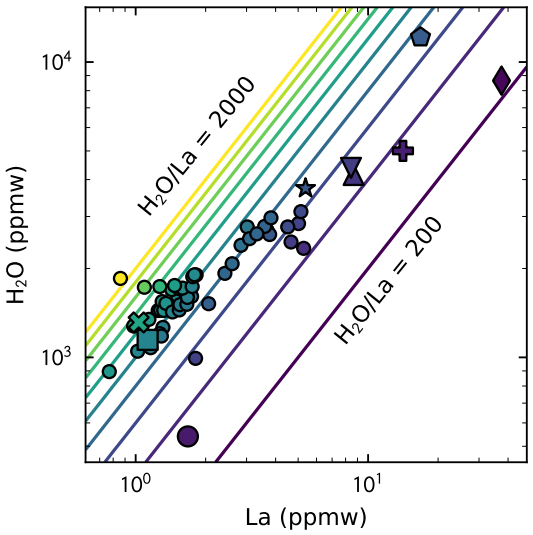

Figure 7.3: H_2O and La concentrations in the Reykjanes Ridge glasses (circles) and mean melt inclusion H_2O and matrix La concentrations for on-land Iceland. Solid lines show contours for constant H_2O/La, in increments of 200. The combined 1 s.d. accuracy and precision is on the order of the symbol size. Symbol colour indicates H_2O/La ratio. See Figure 6.8 for a key to symbols.

H_2O/La ratio with the radiogenic isotopes and Nb/Zr ratios, in both the Reykjanes Ridge glasses and the on-land Iceland eruptions. High Nb/Zr ratios are generated by garnet-field melting (Gurenko and Chaussidon, 1995) and correlate well with the radiogenic isotopes in Icelandic basalts (Shorttle et al., 2013). The covariation of H_2O/La suggests that the H_2O/La variability in both the Reykjanes Ridge glasses and the on-land eruptions is primarily controlled by variable contributions from enriched low H_2O/La melts and depleted high H_2O/La melts.

Figure 7.5 shows that all the Reykjanes Ridge samples, and most of the on-land eruptions, describe a linear trend between $^{206}Pb/^{204}Pb$ and both H_2O/Ce and H_2O/La. The eruptions that fall off this trend are displaced to higher $^{208}Pb/^{204}Pb$ than the array formed by the Reykjanes Ridge glasses in $^{206}Pb/^{204}Pb$–$^{208}Pb/^{204}Pb$ space (Figure 7.6). The deviation in $^{208}Pb/^{204}Pb$ relative to $^{206}Pb/^{204}Pb$ is conveniently expressed as the parameter $\Delta^{208}Pb$ Hart (1984), calculated using the equation:

$$\Delta^{208}\mathrm{Pb} = 100 \times \left(\left[\frac{^{208}\mathrm{Pb}}{^{204}\mathrm{Pb}} \right] - 0.1209 \times \left[\frac{^{206}\mathrm{Pb}}{^{204}\mathrm{Pb}} \right] + 15.627 \right) \tag{7.2}$$

and is a proxy for time-integrated Th/Pb, most likely representing the contribution of another mantle source to the on-land lavas. The points in Figure 7.5 are coloured according to their $\Delta^{208}Pb$ to aid comparison. H_2O/La covariations between $^{87}Sr/^{86}Sr$ and $^{143}Nd/^{144}Nd$ are also observed, though the arrays they describe are less tight than H_2O/La–$^{206}Pb/^{204}Pb$. This might reflect the compatibility of H_2O being closer to the compatibility of Sr or Nd during melting (Section 5.1). Since the H_2O/La–$^{206}Pb/^{204}Pb$ array might reflect mantle heterogeneity most closely, I use this array in preference in the following calculations.

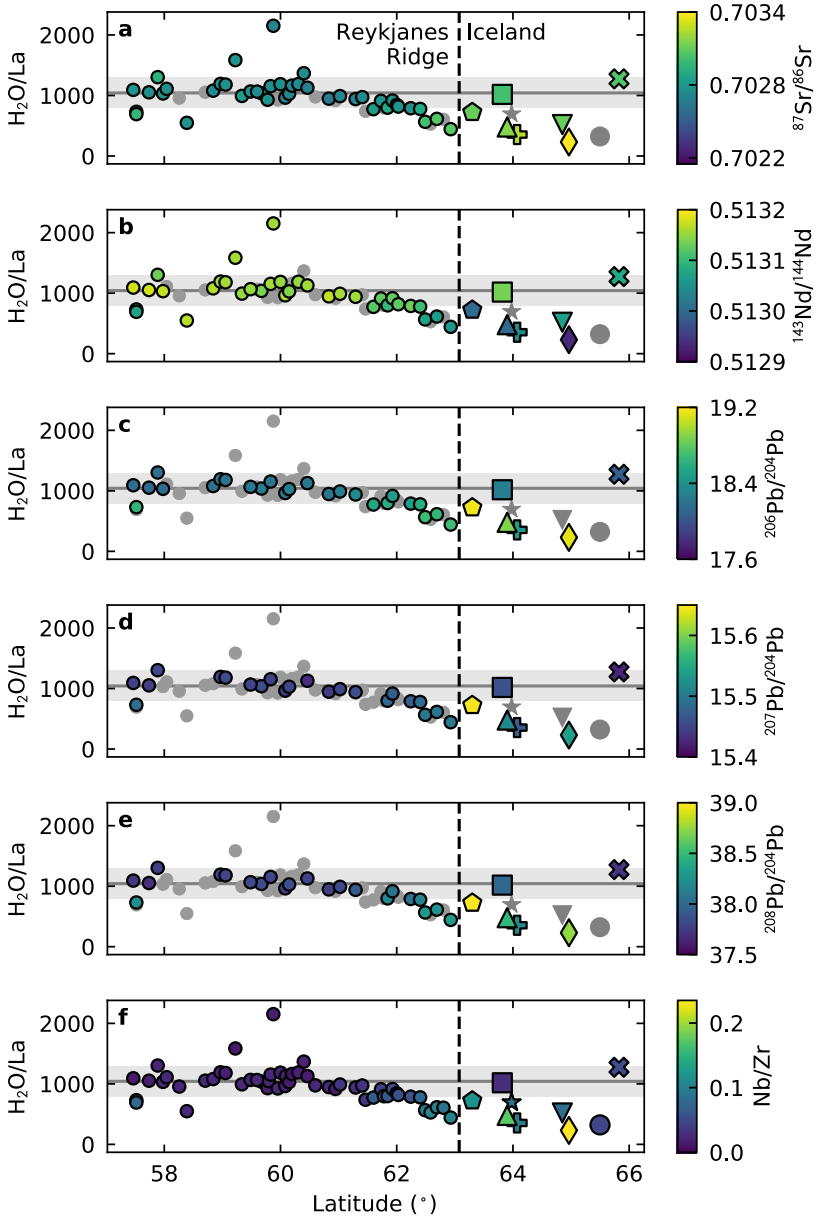

Figure 7.4: Each panel shows the variation of H_2O/La along the Reykjanes ridge, in comparison to the on-land eruptions. Symbols are coloured for the radiogenic isotope ratios (or Nb/Zr ratio) of the same glass for the ridge samples, or whole-rock and matrix glass for the on-land eruptions. The horizontal line and shading shows the average and standard deviation of H_2O/La of the Reykjanes Ridge glasses south of 62°N. The combined 1 s.d. accuracy and precision is smaller than the symbol size. Data sources given in Appendix B and Table 2.2. See Figure 6.8 for a key to symbols.

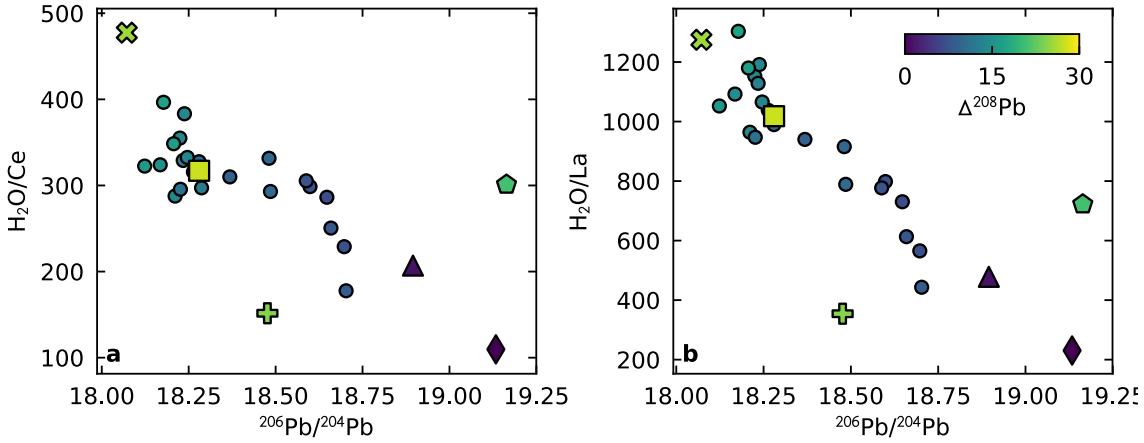

Figure 7.5: Panels a and b demonstrate the covariation of H_2O/Ce and H_2O/La with $^{206}Pb/^{204}Pb$. The submarine Reykjanes Ridge glasses are shown as circles, and on-land Iceland by larger symbols (key in Figure 6.8). The combined 1 s.d. accuracy and precision are on the order of the symbol size. The symbols are coloured by $\Delta^{208}Pb$, calculated using Equation 7.2. Sources for the Pb-isotope data are shown in Table 2.2 and Appendix B.

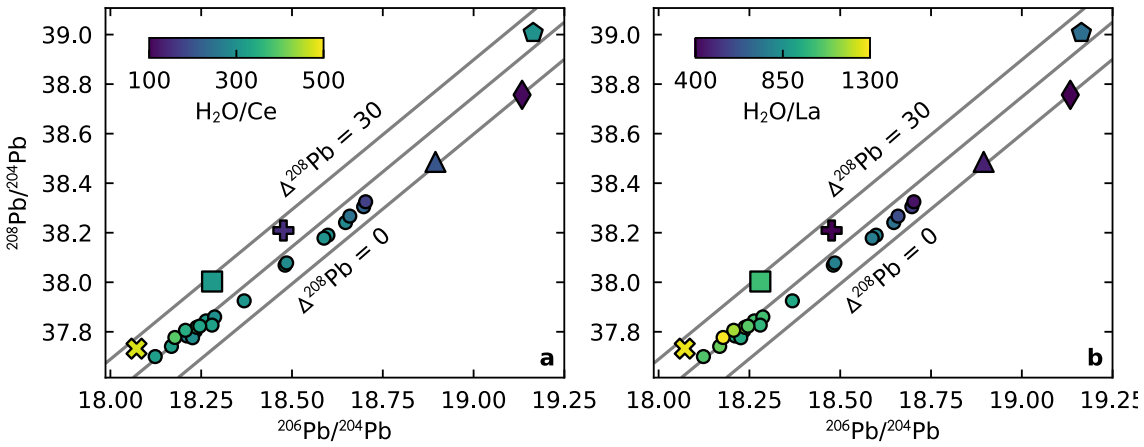

Figure 7.6: Both panels show the $^{206}Pb/^{204}Pb$ and $^{208}Pb/^{204}Pb$ ratios for the Reykjanes ridge glasses, and the matrix glass or whole-rock for the on-land Iceland eruptions. In panel a the points are coloured by H_2O/Ce, and in b by H_2O/La. Grey lines show contours of constant $\Delta^{208}Pb$, calculated using Equation 7.2. Sources for the Pb-isotope data are shown in Table 2.2 and Appendix B. See Figure 6.8 for key to symbols.

The tightest of the two data arrays in Figure 7.5 is seen for H_2O/La. The strength of the correlation between H_2O/La and $^{206}Pb/^{204}Pb$ lends further support to, 1) the behaviour of H_2O being more comparable to La than Ce during melting and crystallisation, and 2) the fidelity of melt inclusions for recording pre-eruptive H_2O concentrations. Laki and Surtsey have H_2O/La and H_2O/Ce ratios that fall off the main array. This might reflect contributions of other mantle components, as suggested by the Pb-isotope systematics, alternatively the melt inclusions may have re-equilibrated with a different melt to the melt that carried the crystals to the surface.

7.3 Mantle H_2O/La ratios and H_2O concentrations

The $^{206}Pb/^{204}Pb$–H_2O/La array defined by the Reykjanes Ridge glass and on-land melt inclusion suites can be approximated by binary mixing between a melt with low $^{206}Pb/^{204}Pb$ and high H_2O/La, and a melt with high $^{206}Pb/^{204}Pb$ and low H_2O/Ce. The simplest way of interpreting these endmembers is by mixing of a depleted-mantle derived melt and an enriched-mantle derived melt. In order to assess the range of mantle H_2O/La and H_2O concentrations this simple model is consistent with, I take a Bayesian approach similar to that used in Chapter 6.

7.3.1 Inversion setup

For each model run a mixing line is calculated in $^{206}Pb/^{204}Pb$–H_2O/La space using equations 6.1 and A.2. Pb, La and H_2O are assumed to remain unfractionated during melting to avoid incorporating melt fraction and partition coefficients into the expressions. The log likelihood, $\ln(L)$, is calculated by summing over the y-misfit of n Reykjanes Ridge glass and on-land eruption observations, ${}^{\mathrm{H/La}}\mu_i$, included in the inversion:

$$ln(L) = -\frac{1}{2}\sum_{i=1}^{n} ln\left(2\pi {}^{\mathrm{H/La}}\sigma_i^2\right) - \frac{1}{2}\sum_{1=1}^{n} \frac{({}^{\mathrm{H/La}}x_i - {}^{\mathrm{H/La}}\mu_i)^2}{{}^{\mathrm{H/La}}\sigma_i^2} \tag{7.3}$$

where ${}^{\mathrm{H/La}}\sigma_i$ is the 1 s.d. uncertainty on the measurement. Laki and Surtsey were not included as constraints. The inversion was performed using the importance nested sampling Monte-Carlo inversion routine 'Multinest' (Feroz and Hobson, 2008; Feroz et al., 2009, 2013) with the pymultinest python wrapper (Buchner et al., 2014).

The binary mixing line in $^{206}Pb/^{204}Pb$–H_2O/La space depends on the $^{206}Pb/^{204}Pb$ ratio, the H_2O/La ratio, and the Pb and La concentrations of both the depleted and enriched mantle end-members. The $^{206}Pb/^{204}Pb$ isotope ratios of the endmembers is assumed to lie in the range of the depleted and enriched Iceland and Reykjanes Ridge mantle endmembers inferred by Thirlwall et al. (2004). The

trace element concentrations of the depleted mantle endmember are assumed to lie within the extreme depleted and enriched bounds calculated by Workman and Hart (2005) for global MORB-source mantle. The trace element composition of the enriched mantle end-member is more uncertain. To propagate the uncertainty in the composition of the enriched mantle end-member on the inversion results, I consider four sets of priors on the enriched-mantle La and Pb concentrations (Table 7.2).

The first enriched mantle trace element composition I consider is the subduction-altered MORB composition calculated by Stracke et al. (2003a), this is the most depleted of the four enriched compositions considered. The second considers the scenario where the enriched source beneath Iceland reflects recycled MORB that escaped fluid alteration during subduction, using the unaltered version of the same MORB composition used by Stracke et al. (2003a). The choice of these end-members reflects a supposition about the process creating enriched mantle components, but this lacks direct observational support from the chemistry of Icelandic basalts.

McKenzie et al. (2004) address this by modelling the enriched source contributing to lavas in the Theistareykir volcanic system in Northern Iceland. They argue a source substantially more enriched than MORB is required, and suggest an OIB lava from Suiko, one of the Emperior Seamounts in the NW Pacific (Regelous et al., 2003), can fit the observations. As the third compositional scenario for the priors, I take this lava composition and modify it for subduction alteration following the method of Stracke et al. (2003a). For the fourth set of priors I leave it unmodified.

In each of the four cases the recycled basalt composition is mixed with average depleted mantle (Workman and Hart, 2005) in a 1:2 ratio as suggested by major element systematics of Icelandic basalts (Shorttle and Maclennan, 2011). For the H_2O/Ce ratio of each endmember a uniform prior $[10^0,10^4]$ is used. The parameters used to define the prior distributions are summarised in Table 7.2, and shown in Figures 7.7–7.10.

7.3.2 Inversion results

The results of the four inversions are shown in Figures 7.7–7.10, and are summarised in Table 7.3. In all four inversions the best fit binary mixing line fits the data well, indicating that assumptions about the composition of the enriched mantle endmember do not affect the ability of the model to match the data. Since the endmember H_2O/La ratios are tightly constrained by the data array (unlike the mantle CO_2 inversions in Section 6.6.2) the posterior H_2O/La distributions vary little between the inversions. The endmember H_2O/La ratios are therefore a robust result of the analysis, and suggest the depleted and enriched mantle components record processes that have fractionated their H_2O and La concentrations. Since the trace element composition of the depleted endmember is very similar in all the inversions, the depleted mantle H_2O concentration also varies little: from 220^{+32}_{-19} to 303^{+28}_{-36} ppmw.

Parameter	Altered MORB	Unaltered MORB	Altered OIB	Unaltered OIB
$[La]_{DM}$ (ppmw)	0.134–0.253	0.134–0.253	0.134–0.253	0.134–0.253
$[La]_{EM}$ (ppmw)	0.681–1.39	1.39±14	1.90±19	4.15±42
$[Pb]_{DM}$ (ppmw)	0.0140–0.0299	0.0140–0.0299	0.0140–0.0299	0.0140–0.0299
$[Pb]_{EM}$ (ppmw)	0.042–0.170	0.170±017	0.102±10	0.484±48
$^{206}Pb/^{204}Pb_{DM}$	17.87–18.15	17.87–18.15	17.87–18.15	17.87–18.15
$^{206}Pb/^{204}Pb_{EM}$	18.15–19.35	18.15–19.35	18.15–19.35	18.15–19.35

Table 7.2: Parameters for the prior distributions used for the Bayesian inversion for the H_2O/La ratio and H_2O concentration of the depleted and enriched mantle endmembers. A uniform prior was used for the $^{206}Pb/^{204}Pb$ isotope ratio of each endmember, between the bounds quoted. The prior distribution for La and Ce concentrations were either log-uniform (where a range is specified), or normal distributions with the median and standard deviation quoted.

Recycled Source	Mantle Component	H_2O/La	Mantle H_2O (ppmw)
MORB-like (altered)	Depleted	1385^{+74}_{-68}	254^{+43}_{-35}
	Enriched	148^{+41}_{-42}	145^{+43}_{-45}
OIB-like (altered)	Depleted	1429^{+84}_{-79}	303^{+28}_{-36}
	Enriched	158^{+38}_{-38}	290^{+72}_{-73}
MORB-like (unaltered)	Depleted	1354^{+68}_{-63}	220^{+32}_{-19}
	Enriched	138^{+45}_{-43}	197^{+65}_{-64}
OIB-like (unaltered)	Depleted	1359^{+73}_{-66}	223^{+33}_{-19}
	Enriched	140^{+43}_{-43}	591^{+181}_{-186}

Table 7.3: Results from inverting for the H_2O/La ratios and H_2O concentrations of the 'enriched' and 'depleted' Icelandic mantle endmembers. The uncertainties quoted are the 25th and 75th percentiles of the posterior distributions.

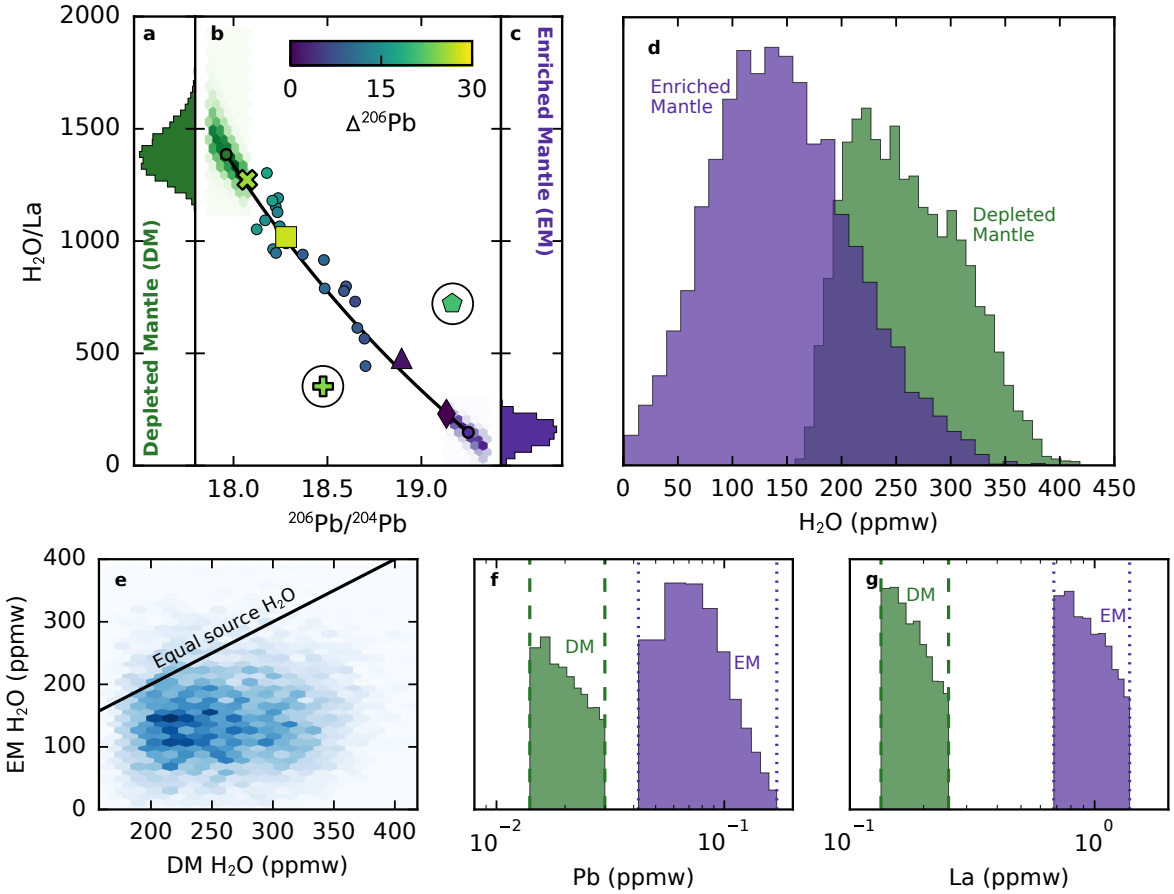

Figure 7.7: Results of the inversion assuming the enriched component has trace element concentrations like the altered MORB of Stracke et al. (2003a). Panels a and c show the H_2O/La ratios of the depleted and enriched mantle endmembers. Panel b shows the distribution of data the inversion fits (see the caption to Figure 7.5 for further information), the mixing line for the median values of the posterior distribution for each parameter, and representations of the distribution of end-member solutions in this space (shading is proportional to posterior density). The circled points are removed from the inversion. Panel d shows the posterior distributions for H_2O concentrations in the depleted and enriched mantle endmembers. Panel e demonstrates there is no trade-off between the H_2O concentrations of the enriched and depleted endmembers (colour density is proportional to posterior distribution density). Panels f and g show the posterior distributions for Pb and La concentrations in each endmember, the vertical lines show the maximum and minimum values of the prior distributions (Table 7.2).

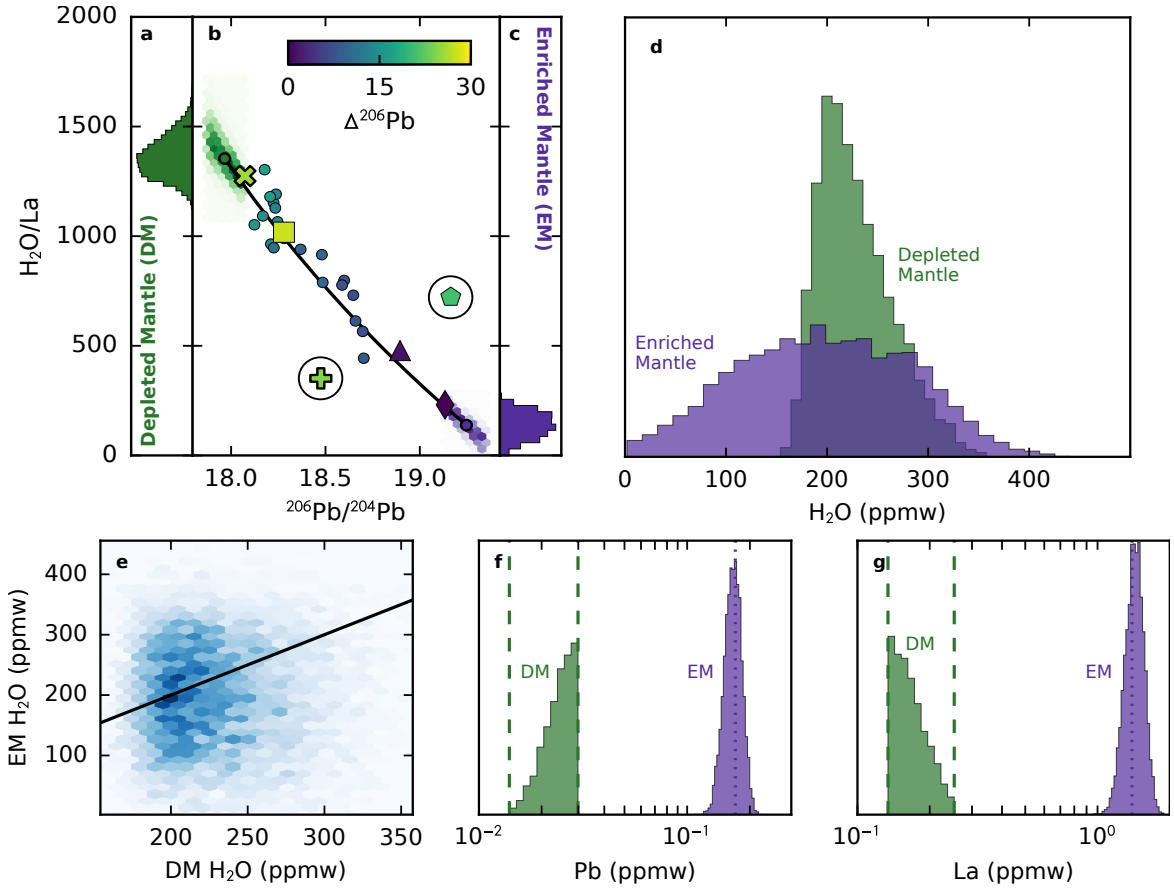

Figure 7.8: Results of the inversion assuming the enriched component has trace element concentrations like the unaltered MORB of Stracke et al. (2003a). See the caption to Figure 7.7 for further information.

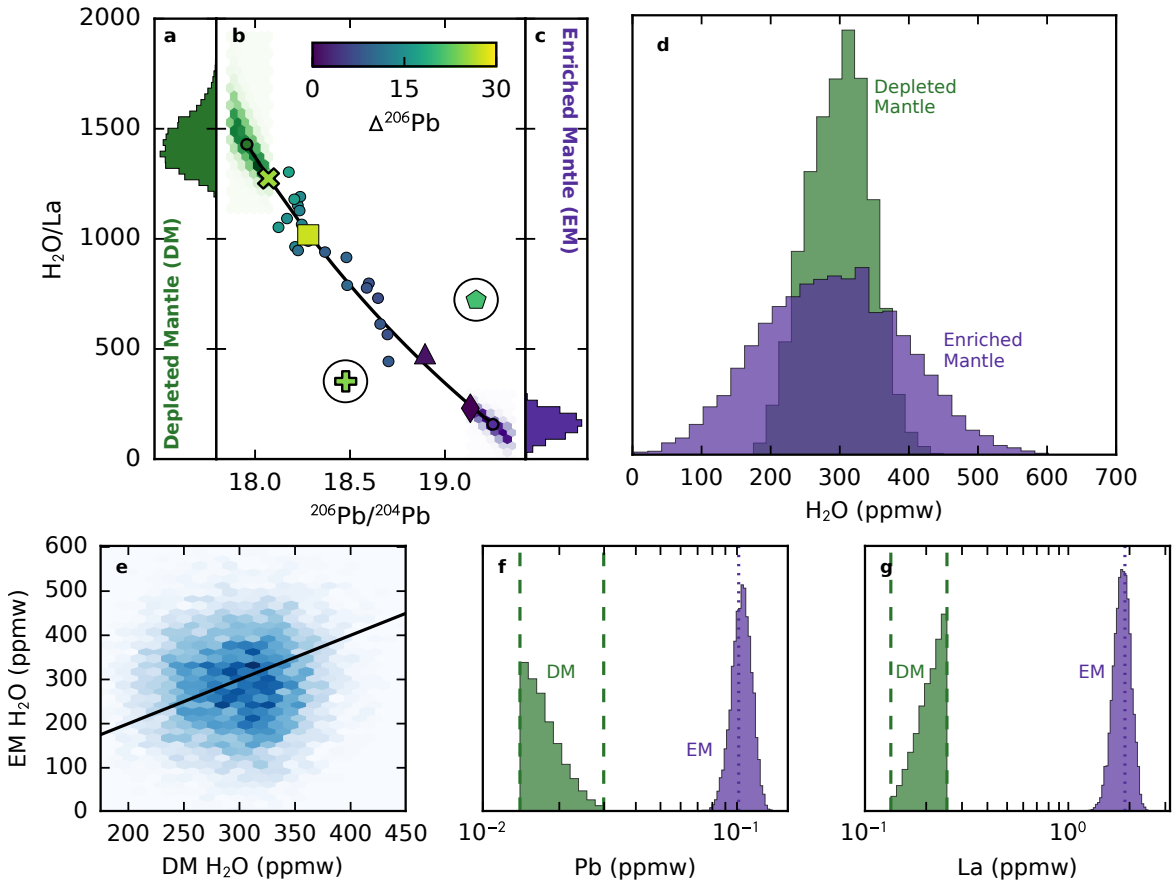

Figure 7.9: Results of the inversion assuming the enriched component has trace element concentrations like the Suiko OIB composition (Regelous et al., 2003) inferred to reside in the mantle beneath Iceland (McKenzie et al., 2004), assuming it has incurred alteration in a subduction zone, following the method of Stracke et al. (2003a). See the caption to Figure 7.7 for further information.

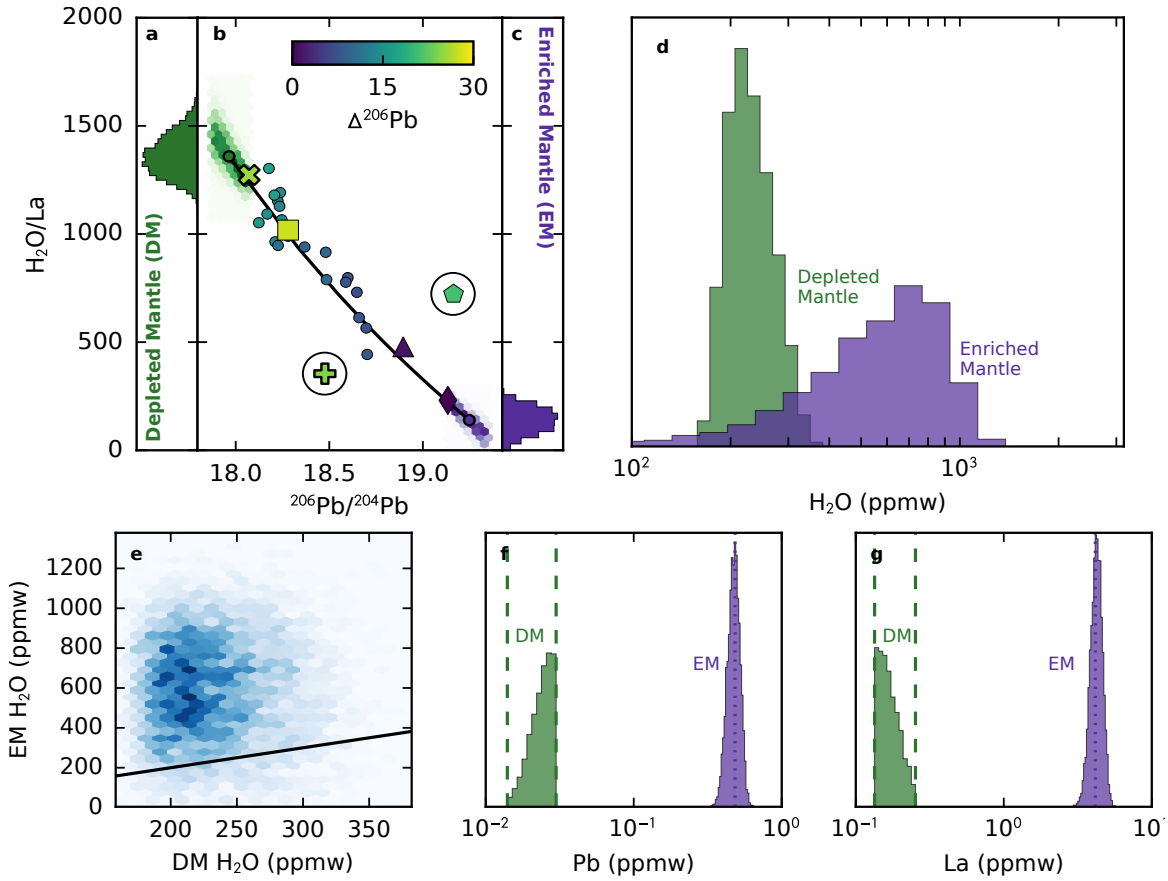

Figure 7.10: Results of the inversion assuming the enriched component has trace element concentrations like the Suiko OIB composition (Regelous et al., 2003) inferred to reside in the mantle beneath Iceland (McKenzie et al., 2004), unaltered by subduction zone processing. See the caption to Figure 7.7 for further information.

However, substantial variation does exist between the H_2O concentrations calculated for the enriched mantle endmembers. This variation in H_2O concentrations results from the extremely different La concentration prior distributions used in each inversion, coupled with little variation in the calculated H_2O/La ratio. The lowest estimated H_2O concentration is for the altered MORB source: 145^{+43}_{-45} ppmw, lower than the H_2O concentration inferred for the depleted mantle in the same model. No trade-off between the H_2O concentrations in the two components exists, and the distribution sits entirely below the 1:1 source H_2O concentration line (Figure 7.7e). Enriched mantle H_2O concentrations are calculated to be very similar to the depleted endmember in the unaltered-MORB and altered-OIB inversions. The only inversion that suggests the enriched mantle is richer in H_2O than the depleted mantle is the unaltered-OIB model, owing to the extreme trace element enrichment in the enriched-mantle prior. When unaltered-OIB is assumed to be the enriched mantle source, the H_2O concentration is calculated as 591^{+181}_{-186} ppmw.

7.4 A discrepancy in the H_2O mass balance of the Iceland Plume?

The primary observations, summarised in Figure 7.2, from Section 7.2 are:

1. The H_2O concentration in Reykjanes Ridge glasses increases towards Iceland
2. The H_2O/La ratio in Reykjanes Ridge glasses decreases towards Iceland
3. On-land lavas record much greater variability in both H_2O concentrations and H_2O/La than the Reykjanes Ridge glasses.

In Section 7.3 I demonstrated the co-variation of H_2O/La with radiogenic isotopes suggests the enriched mantle has significantly lower H_2O/La than the depleted mantle, and depending on the assumed composition of the enriched mantle, this propagates to either lower or higher H_2O concentrations in the enriched mantle than the depleted mantle. Though uncertainties in the melting process make using absolute magma H_2O concentrations to estimate mantle H_2O concentrations problematic, consideration of the melting process may allow assessment of the likelihood of the enriched mantle having lower or higher CO_2 concentrations than the depleted mantle. In particular, sensible melting parameters must be able to recreate the trend of increasing glass H_2O concentrations towards Iceland. Batch melting of a uniformly heterogeneous mantle will generate the opposite trend. To achieve this, I develop two simple models for melting along the Reykjanes Ridge. The mathematical formulation for both models is described in Appendix A.

Parameter	Low Px H_2O	High Px H_2O	Notes
C^s_{Lz}	1	1	
C^s_{Px}	8.75	21.6	Ratio of EM and DM La concentrations used in the mixing calculations (Table XX)
$H_2O^s_{Lz}$	1	1	
$H_2O^s_{Px}$	0.57	6.1	Ratio of EM and DM H_2O concentrations calculated (Table 7.3)
ϕ^0_{Px}	0.1	0.1	
λ	1	1	
F_{Lz}	0.2	0.2	
F_{Px}	0.3	0.3	

Table 7.4: Summary of the parameters used in the Reykjanes Ridge active-upwelling models presented in Figure 7.11. Most parameters were chosen for illustrative purposes, notes are made where prior knowledge has guided parameter choice.

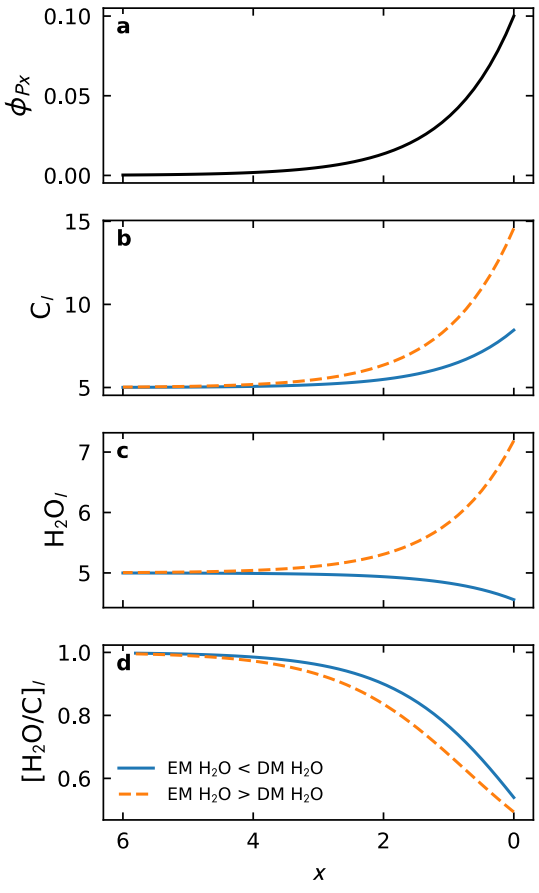

Figure 7.11: Illustrative results from modelling pyroxenite depletion along the Reykjanes ridge. The parameters used for both model results are given in Table 7.4. Panel a shows the changing mass fraction of pyroxenite along the ridge. Panel b shows the trace element concentration in the mixed lavas, and Panel c shows their H_2O concentration. Panel d shows the ratio of H_2O and trace element concentrations.

7.4.1 Plume outflow model

Shorttle et al. (2010) propose that the geophysical and geochemical trends observed along the Reykjanes and Kolbeinsey Ridges can be explained by radial outflow of plume material contaminating the ambient mantle beneath the ridges. Decay of the plume's geochemical signal along the Reykjanes ridge occurs by the increasing spread of plume material. In the models, I consider the depleted geochemical component to be associated with a lherzolite lithology (Lz), and the enriched component with a pyroxenite lithology (Px), after Shorttle and Maclennan (2011) and Shorttle et al. (2014). The parameters used in the models are listed in Table 7.4.

Figure 7.11 shows the predicted lava compositions when the pyroxenite fraction, ϕ_{Px}, in the mantle source decays exponentially along the Reykjanes Ridge (Figure 7.11a). Two results are shown using constraints provided by the inversions in Section 7.3. The first (solid blue line) assumes the pyroxenite component has a composition like altered-MORB with lower H_2O concentrations than the lherzolite component. The second (dashed orange line) has a pyroxenite composition like unaltered-OIB, with higher H_2O concentrations with the lherzolite component. In both cases the trace element concentration, C_l increases along the ridge towards Iceland (Figure 7.11b).

When the pyroxenite is enriched in H_2O over the lherzolite, H_2O concentrations also increase towards Iceland, consistent with the observations in Section 7.2. However, when the pyroxenite H_2O concentrations are lower than in the lherzolite, the H_2O concentrations in the lavas decrease towards Iceland, since the average plume material is less H_2O rich. There is, therefore, a mass balance issue if the pyroxenite H_2O concentrations are lower than in the lherzolite. If the pyroxenite H_2O concentrations are required to be higher than in the lherzolite, this might support the argument made by McKenzie et al. (2004) that the enriched component is derived from recycling of OIB. However, this result is arguably implausible: 1) given the low proportion of the ocean floor with OIB chemistry relative to ocean floor with MORB chemistry, 2) the OIB component must have largely escaped subduction zone alteration. Alternatively, a more complex melting process might be required to reconcile the enriched mantle component having a lower H_2O concentration than the depleted mantle component.

7.4.2 Active upwelling model

Magma production from mantle plumes is driven predominantly by increased mantle T_p and by active, or plume-driven, upwelling. Maclennan et al. (2001a) showed that geochemical and geophysical observations in central Iceland require a significant contribution from active upwelling. By inverting geochemical and geophysical observations from Iceland and the Reykjanes Ridge Brown and Lesher (2014) calculated a small amount of active upwelling is also required at the Northernmost extent of

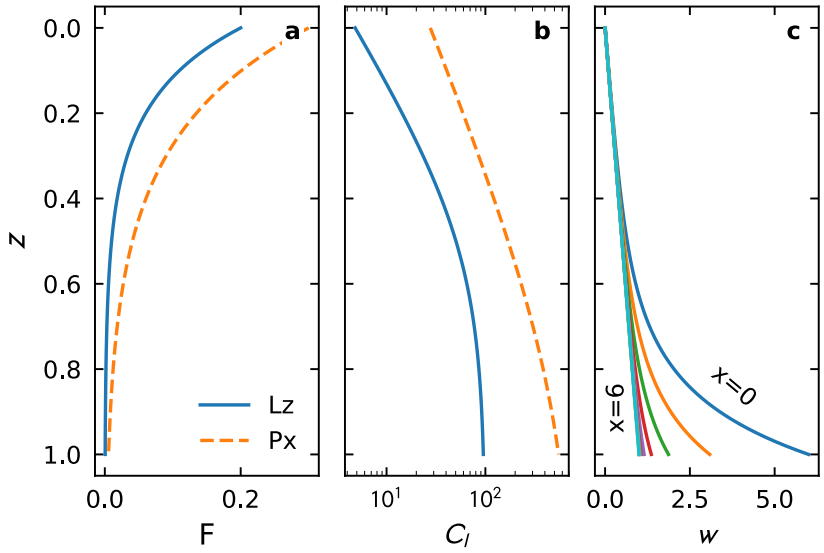

Figure 7.12: Melting region parameters for the Reykjanes Ridge active-upwelling models. Panels a and b show the pyroxenite and lherzolite melt fractions, F and melt trace element concentrations, C_l as a function of normalised melting region pressure, z. Panel c shows the weighting function, as both a function of z and position along the ridge, x. The parameters for the models are shown in Table 7.5.

the ridge, though Maclennan et al. (2001a) argued passive upwelling of high T_p mantle can adequately explain the crustal thickness and geochemistry of lavas at Iceland's coasts.

Active upwelling increases magma production by fluxing more mantle material through the melting region than would occur by the passive upwelling normally occurring under mid-ocean ridges. Since the magnitude of the additional flux of mantle material is likely to be greatest near the base of the melting region, greater masses of the incompatible trace elements are extracted from the mantle. If active upwelling provides a sufficient additional flux of H_2O, the H_2O concentration of lavas may be enriched beyond that expected from passive melting of the source, even whilst the source H_2O/La is retained.

To assess whether a component of active upwelling can resolve the mass-balance discrepancy if the H_2O concentrations in pyroxenite are lower than the lherzolite, I have developed a simple model to replicate the chemical effects of active upwelling. The trace element composition, C_l, of melts as a function of melt fraction, F and depth, z, are calculated for lherzolite and pyroxenite melting (Figure 7.12). An additional weighting, w, is given to melts from the base of the melting region to simulate the additional mass of trace elements derived from active upwelling. The magnitude of this weighting decays as a function of depth in the melting region, and with decreasing magnitude of active upwelling, μ. Both the magnitude of active upwelling and the fraction of pyroxenite are set to decrease exponentially with distance from Iceland (Figure 7.13a and b). The complete list of

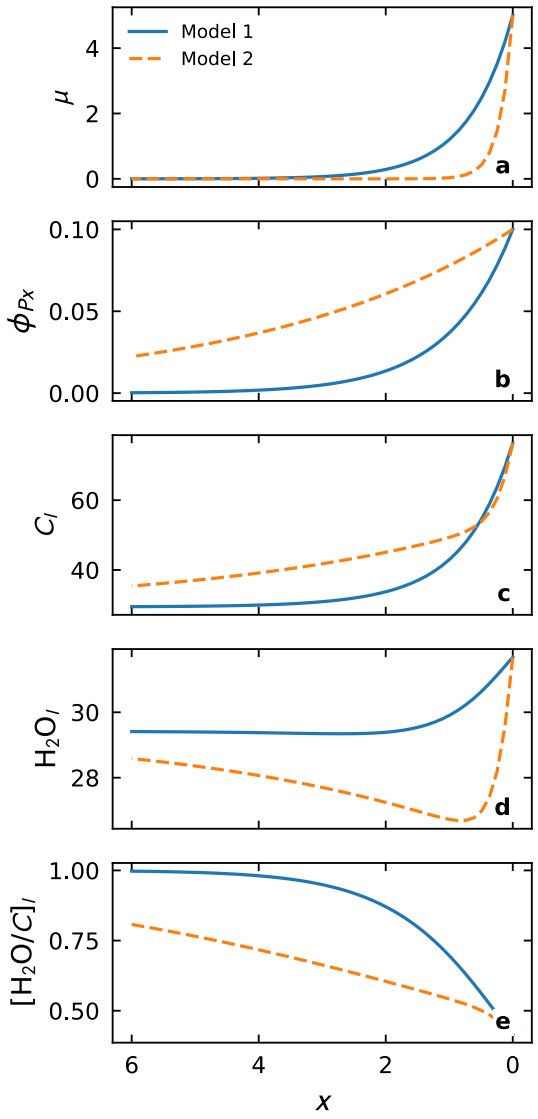

Figure 7.13: Results from two models for active-upwelling along the Reykjanes Ridge. Model 1 demonstrates the ability of active upwelling to enrich lavas in both H_2O and trace elements towards Iceland, whilst the ratio of the H_2O and trace element concentrations decreases. Model 2 demonstrates how the combination of both variable pyroxenite and variably active-upwelling along the ridge can cause a minima in the H_2O concentration. Panel a shows the variation in the amplitude of active upwelling, μ, along the ridge, and panel b shows the decrease in pyroxenite mass fraction, ϕ_{Px}, away from Iceland. Panel c and d show the concentrations of a trace element and H_2O, and Panel e shows their ratio. The parameters used for both models are given in Table 7.5.

parameters used in the two models presented here are given in Table 7.5. To avoid additional variables, I do not allow the melt fraction of each lithology to vary along the ridge. Incorporating this effect would cause H_2O concentrations to decrease towards Iceland, the opposite of the observed trend.

Model 1 in Figure 7.13 (blue solid line) has a wavelength of mantle pyroxenite fraction decay, λ, similar to that of active upwelling decay, λ_μ. Model 1 recreates the increase in both H_2O and La concentrations towards Iceland, whilst the H_2O/La simultaneously decreases, despite lower H_2O concentrations in the plume mantle. Therefore, if there is a component of active upwelling at the Northernmost extent of the Reykjanes ridge, no mass balance issues exist for any of the inversion results from Section 7.3; the increasing lava H_2O concentrations towards Iceland can be consistent with lower H_2O concentrations in the enriched mantle component than the depleted component. The

Parameter	Description	Model 1	Model 2	Notes
C^s_{Lz}	Solid Lz T.E. conc.	1	1	
C^s_{Px}	Solid Px T.E. conc.	8.75	21.6	Ratio of EM and DM La concentrations used in the mixing calculations (Table 7.2)
$H_2O^s_{\mathrm{Lz}}$	Solid Lz H_2O conc.	1	1	
$H_2O^s_{\mathrm{Px}}$	Solid Px H_2O conc.	0.57	0.57	Ratio of EM and DM H_2O concentrations calculated (Table 7.3)
D	Partition coefficient	0.01	0.01	D for La from Workman and Hart (2005)
ϕ^0_{Px}	Solid Px frac. at Iceland	0.1	0.1	
λ	Length scale of Px frac. decay along ridge	1.0	4.0	
$F^{\max}_{\mathrm{Lz}}$	Lz max melt frac.	0.2	0.2	
$F^{\max}_{\mathrm{Px}}$	Px max melt frac.	0.3	0.3	
λ^{Lz}_F	Controls Lz melt productivity	6.0	6.0	
λ^{Px}_F	Controls Px melt productivity	4.0	4.0	
μ_0	Magnitude of active upwelling at Iceland	5.0	5.0	
λ_μ	Length scale of active upwelling decay along ridge	0.7	0.2	
λ_w	Length scale of deep melt weighting decay	7.0	7.0	

Table 7.5: Summary of the parameters used in the Reykjanes Ridge active-upwelling models presented in Figures 7.12 and 7.13. Most parameters were chosen for illustrative purposes, notes are made where prior knowledge has guided parameter choice.

possibility of the Iceland plume having a lower bulk H_2O concentration than the mantle beneath the Reykjanes Ridge differs from the conclusions of Nichols et al. (2002) since they do not consider the effect of active upwelling on lava composition, and apply corrections based solely upon mantle melt fraction.

When pyroxenite is supplied to a ridge dominantly by plume outflow, rather than by active upwelling of plume material, it might be expected that $\lambda \gg \lambda_\mu$. This situation is modelled in Model 2 in Figure 7.13. A minimum in lava H_2O concentrations is generated (Figure 7.13d) where the effect of H_2O depletion in pyroxenite becomes overwhelmed by the excess deep melt production associated with active upwelling. This minima should only be expected in chemical species that are depleted in the pyroxenite relative to the lherzolite, and is therefore not present in the incompatible trace elements (Figure 7.13c).

Though a weak minimum in H_2O concentrations is seen in the Reykjanes Ridge glasses, and becomes larger when a fractional crystallisation correction is applied (Nichols et al., 2002), a weak minima is also seen in the La concentrations (Figure 7.2). The presence of minima in both H_2O and La suggests another process is controlling this, and so it does not lend support to the presence of active upwelling along the Reykjanes Ridge.

7.4.3 Efficiency of deep melt extraction

As shown in the previous section, the concentration of H_2O and the incompatible trace elements in lavas is controlled by the deepest parts of the melting region, whilst the melt fraction is a property of the uppermost part of the melting region. One way of affecting the deep melting behaviour is an increased flux of mantle material through the deepest part of the melting region by active upwelling, described previously.

Another important process might be the scavenging of incompatible elements from a large volume of mantle undergoing low-degree volatile-present melting deep below the main melting region (e.g Asimow et al., 2003; Dasgupta and Hirschmann, 2006; Keller et al., 2017). Low degree hydrous or carbonatitic melts could efficiently extract incompatible elements and concentrate them in the overlying melting region. Therefore the flux of incompatible elements from the melting region might represent a far larger volume of mantle than assumed from simple melting models.

If the efficiency of this process increases towards Iceland, this offers another explanation for the observed increase in lava H_2O concentrations towards Iceland. The efficiency could plausibly be increased by a number of mechanisms. Greater CO_2 concentrations in the Icelandic plume (Chapter 6) causing carbonated melting to start deeper and reach higher melt fractions (e.g. Dasgupta and

Hirschmann, 2010; Dasgupta et al., 2013). Increasing melt fraction towards Iceland (throughout the whole melting region) owing to the increasing mantle temperature towards the plume, could allow melts to be more efficiently extracted (Keller et al., 2017). Since pyroxenite melting is likely to start deeper than lherzolite melting (e.g. Shorttle et al., 2014), the increasing pyroxenite component towards Iceland may increase the volume of mantle contribution to magma production.

The complexity of the effect these processes have on the melting process underscores the advantage using volatile-trace element systematics, in preference to lava volatile concentrations alone, to estimate mantle volatile abundances.

7.5 Implications for the mantle H_2O cycle

Regardless of the H_2O concentration in the enriched mantle component, the data clearly shows the H_2O/La ratio in melts derived from the enriched component is lower than in melts from the depleted component. This observation is consistent with the relative difference in H_2O/Ce ratios between depleted and enriched mantle components often seen elsewhere (Figure 7.14). Lower H_2O concentrations, relative to lithophile trace element concentrations, in enriched components has previously been interpreted to reflect dehydration during subduction (e.g Dixon et al., 2017; Le Voyer et al., 2015). Some authors have also suggested recycled material may continue to lose H_2O after subduction by diffusion of H^+ into neighbouring depleted mantle whilst it is resident in the mantle (Cabral et al., 2014; Workman et al., 2006). I examine the possibility of diffusive modification of the Icelandic mantle H_2O distribution in Section 7.6.

Though the sense of the difference in mantle H_2O concentrations, relative to the lithophile trace elements, of the depleted and enriched Icelandic mantle components is consistent with previous studies (Figure 7.14), the magnitude of the offset is much greater. This may, in part, arise from the use of H_2O/La ratios to infer mantle H_2O concentrations, in place of the H_2O/Ce ratios more frequently used. In Section 5.2 I suggested the melting process might be aliased with mantle H_2O/Ce heterogeneity, decreasing the apparent H_2O/Ce variability. Alternatively the high H_2O/La ratio in the depleted mantle component, and the low H_2O/La in the enriched component, may be real features of the Icelandic mantle and reflect unusually high depleted mantle, and low enriched mantle, H_2O concentrations.

Figure 7.15 compares the estimated H_2O concentrations of the depleted and enriched mantle components, with the H_2O concentrations previously inferred for global depleted and enriched mantle components. Though my estimate of the depleted mantle H_2O concentration is reasonably high, it falls within the range of previous estimates, being most similar to the H_2O concentrations inferred

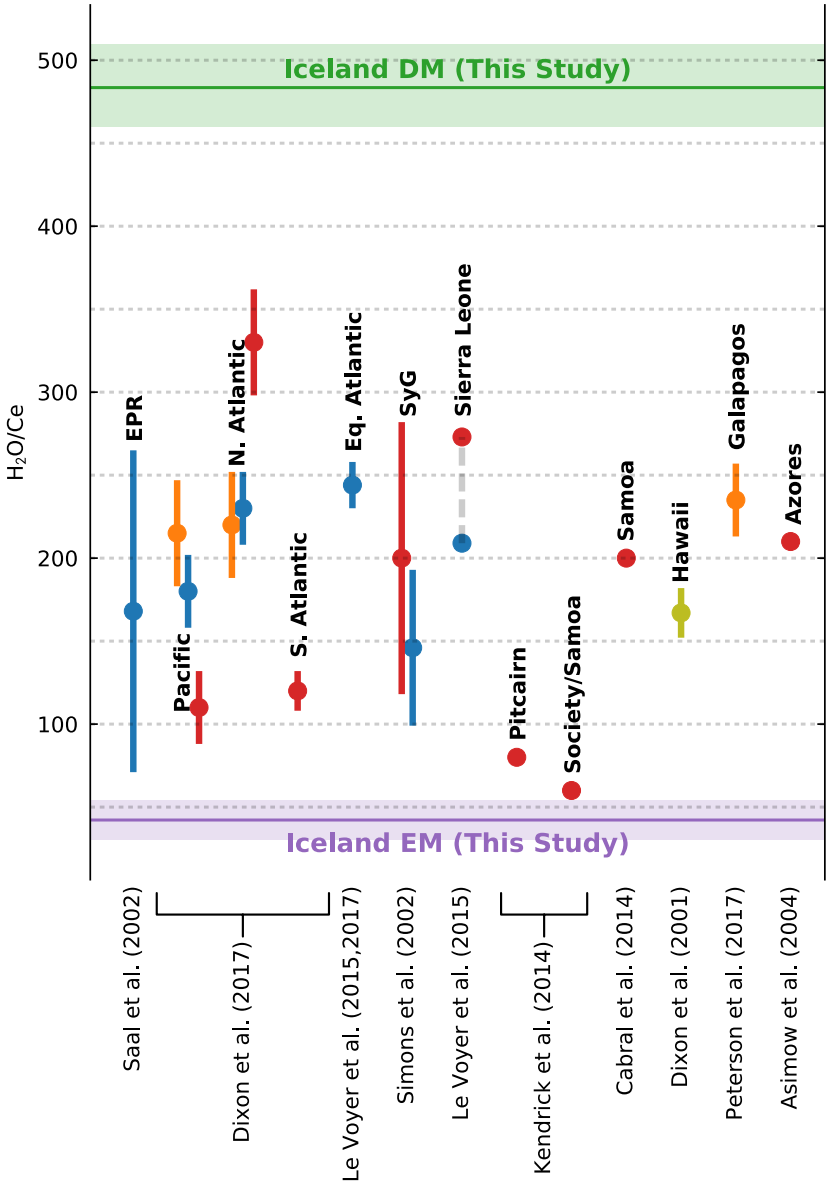

Figure 7.14: Previous estimates of mantle H_2O/Ce ratios, see Figure 1.5 for more information. The H_2O/Ce ratios of the depleted mantle component and enriched mantle component beneath Iceland are calculated from the estimated H_2O/La ratios and the La/Ce ratios of the depleted mantle (Workman and Hart, 2005) and subduction altered MORB (**?**). The bounds shown are the 25% and 75% confidence intervals.

by Le Voyer et al. (2017) and Gibson and Richards (2018). However, the enriched mantle H_2O concentration falls much lower than any of the previous estimates. This might reflect extremely efficient dehydration in a hot subduction zone (Kerrick and Connolly, 2001).

It might be expected that the depleted plume component should have H_2O/La ratio distinct from the ambient upper mantle beneath the Reykjanes Ridge (e.g. Fitton et al., 2003). However, the data from both the submarine Reykjanes Ridge glasses and on-land Iceland eruptions requires only one depleted component. The presence of H_2O/La heterogeneity between different depleted components may be revealed by a more comprehensive study.

The low H_2O concentrations inferred for the enriched component in the Iceland mantle plume, compared with the H_2O concentrations estimated elsewhere, provides further support for the anomalously high melt production beneath Iceland not being caused by unusually 'wet' mantle (e.g. Bonath, 1990). This is consistent with the arguments presented in Chapter 3 for an elevated temperature in the Icelandic mantle.

7.6 Diffusive homogenisation of plume H_2O?

In three of the four inversions for mantle H_2O concentrations in Section 7.3.2, the calculated H_2O concentrations of the depleted and enriched components are similar and have overlapping probability density distributions (Figures 7.7–7.9). Additionally, the concentration of H_2O calculated in the enriched mantle component is significantly lower than many previous estimates from other locations, whilst the H_2O concentration calculated for the depleted component is higher (Figure 7.15).

One possible explanation for this observation is diffusive homogenisation of H_2O between mantle components during residence in the mantle (Cabral et al., 2014; Workman et al., 2006). H^+ has been shown to diffuse extremely rapidly through olivine, with a diffusivity of $\sim 10^{-10}$ m^2s^{-1} at 1000°C (e.g Mackwell and Kohlstedt, 1990). Figure 7.16 shows the timescale of diffusive H^+ homogenisation as a function of heterogeneity size, for diffusivities from 10^{-8}–10^{-12} m^2s^{-1}.

The presence of large amplitude isotope and trace element heterogeneity within individual eruptions in Iceland (e.g Maclennan, 2008b; Winpenny and Maclennan, 2014) demonstrates the length scale of the Icelandic mantle is heterogeneous on a length scale smaller than 100 km. The timescale of plume ascent from the lower mantle is on the order of 100 Ma (Steinberger and Antretter, 2006). Assuming the diffusivity of H^+ through the minerals of the lower mantle is a similar magnitude to olivine, heterogeneities $<$10 km might be expected to partially homogenise their H_2O concentrations. If heterogeneities have a length scale $<$1 km, extensive homogenisation could take place in the upper mantle.

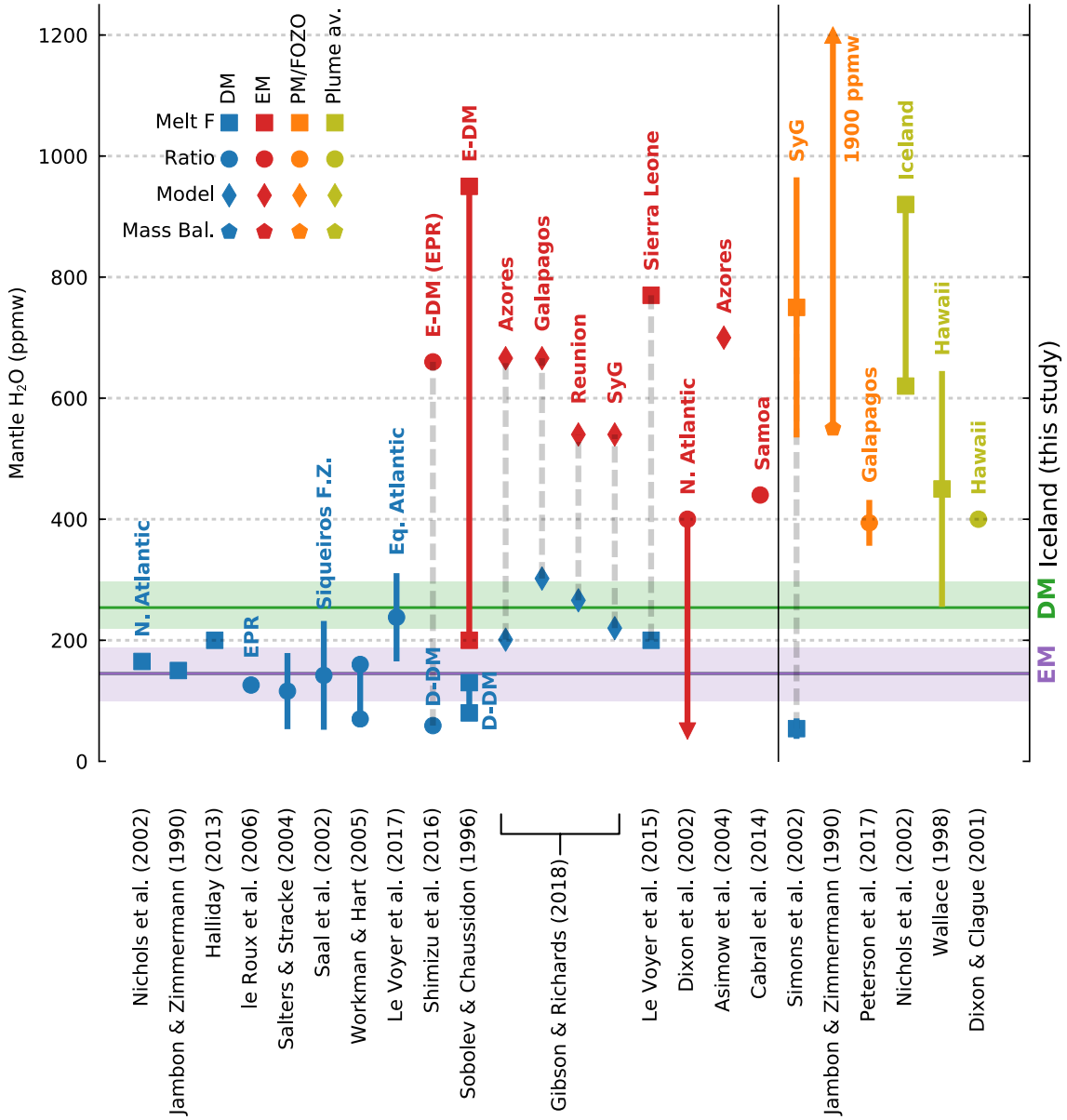

Figure 7.15: Compilation of previous estimates of mantle H_2O concentrations, see Figure 1.4 for more information. The horizontal lines show the H_2O concentrations estimated for the depleted and enriched mantle components beneath Iceland. The shading shows the 25% and 75% confidence intervals.

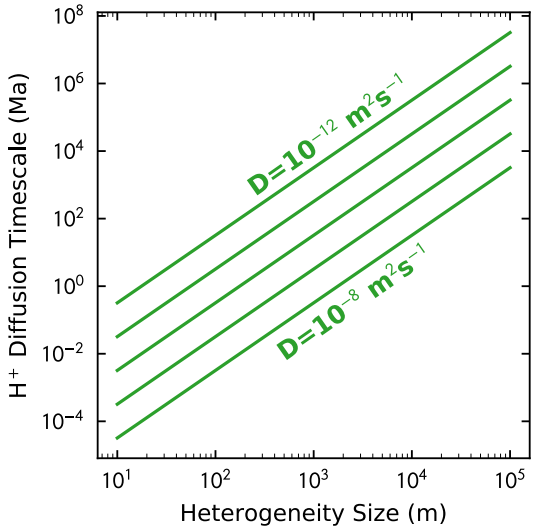

Figure 7.16: The timescale for diffusion to reduce H_2O concentration contrasts between slab-like mantle heterogeneities, of variable size, by a factor of $1/e$. The timescale, τ, is calculated with $\tau = a^2/(\pi^2 D)$ where D is the H^+ diffusivity. Each line represents a different diffusivity, in the plausible range for diffusion in olivine.

If the mantle components have diffusively re-equilibrated during residence in the mantle, this effect should be most pronounced on Iceland, and decay along the length of the Reykjanes ridge as the ambient upper mantle increasingly contributes to melting. However, the H_2O/La systematics of both the Reykjanes glasses and on-land Iceland melt inclusions are adequately matched by a single depleted component. If diffusive homogenisation of H_2O in mantle plumes is an important process, then it is unclear why previous studies have found distinct H_2O concentrations in the mantle components underlying single volcanic centres (Figure 1.4).

Diffusive equilibration of H_2O concentrations may also take place during melt transport through the mantle. The efficiency of diffusive re-equilibration will depend on the length scale and spacing of channels and melt velocity. Channels of width 3 mm to 100 m have been seen in the Oman ophiolite (Braun and Kelemen, 2002), and extrapolation of the observed power-law relationship suggests channels up to 3.5 km wide may be present beneath spreading ridges. The velocity of melt transport through the mantle remains uncertain: ^{230}Th disequilibrium suggests velocities $\sim$1 m yr^{-1} (Kelemen et al., 1997a), whilst the increase in volcanic activity coinciding with deglaciation in Iceland suggests melt transport velocities of $\sim$50 m yr^{-1} (Jull and McKenzie, 1996). The coincidence of small scale channelisation and slow melt transport may allow H_2O equilibration (Figure 7.16).

7.7 Summary

In this chapter I have quantified the heterogeneity of H_2O/La in the Icelandic mantle. I demonstrated estimates of primary magmatic H_2O/La ratios from melt inclusions from on-land Iceland and submarine glasses from the Reykjanes Ridge covary with indices of mantle enrichment, i.e. radiogenic

isotopes and trace element ratios. Though the difference in H_2O/La ratios between the depleted and enriched mantle components are large, they imply similar mantle H_2O concentrations. Only when the enriched mantle component is assumed to be implausibly rich in La do the calculations imply H_2O concentrations similar to that inferred for other enriched sources globally. The low H_2O concentrations in the enriched component may reflect its derivation from an efficiently dehydrated subducted slab. Alternatively, the similarity of H_2O concentrations in the depleted and enriched components may reflect diffusive homogenisation of H_2O during solid-state transport in the mantle, or melt transport following melting.

Chapter 8

Summary

In this thesis I have presented new chemical data which characterises the volatile budgets of primitive magmas from four geochemically diverse Icelandic eruptions (Chapter 2). By developing new statistical tools (Chapter 4) I have robustly assessed the effect magma degassing and mixing has exerted on the dataset, allowing me to isolate the signal of mantle volatile heterogeneity. Combining simple mixing models with a Bayesian Monte-Carlo inversion scheme I placed new quantitative constraints on the carbon and water distribution in the Icelandic plume (Chapters 6 and 7). With a novel combination of geophysical, geochemical and petrological observations I have identified the temperature of the Icelandic plume and its mineralogical heterogeneity (Chapter 3). In this Chapter I assess how the volatile and mineralogical heterogeneity might coincide, and the implications this may have for the development of Earth's deep volatile cycles.

8.1 Are mantle volatile and lithological heterogeneity related?

Volatile heterogeneity might be expected to coincide with lithological heterogeneity in two ways: the volatile storage capacity of the minerals from which the lithology is composed (Bercovici and Karato, 2003), and the varied histories of recycling and melt extraction the lithologies represent (e.g. Dixon et al., 2017; Hauri et al., 2018). In Section 6.6.2 I estimated the CO_2 concentration varies between 38–5900 ppmw in the Icelandic mantle. This range in mantle CO_2 concentration exceeds the likely storage capacity of the silicate mineral assemblage in any mantle lithology (Rosenthal et al., 2015), but could be stored as diamond or graphite instead (e.g. Dasgupta and Hirschmann, 2010). In Chapter 7 I estimated that the range of H_2O concentrations in the Icelandic mantle to be 145–591 ppmw, much lower than the mantle's storage capacity (e.g. Hauri et al., 2006; Hirschmann

et al., 2005). It therefore seems unlikely that the mantle's storage capacity of either H_2O or CO_2 exerts any control on mantle H_2O or CO_2 heterogeneity.

In Chapter 3, following Shorttle et al. (2014), I argued for the presence of three lithological components in the Icelandic mantle: lherzolite, pyroxenite and harzburgite. Shorttle and Maclennan (2011) demonstrated the lherzolitic component is associated with chemically depleted magmas, and the pyroxenite component with enriched magmas. This association between mineralogy and trace-element and isotope geochemistry is unsurprising; many authors have argued the geochemical enrichment observed in Icelandic basalts derives from recycled oceanic crust in mantle source (e.g. Hanan and Schilling, 1997; Kitagawa et al., 2008; Kokfelt et al., 2006; Peate et al., 2009; Thirlwall et al., 2004). The moderate CO_2/Ba and low H_2O/La ratios of the enriched mantle component are therefore most likely to reflect subduction zone processing (e.g. Dixon et al., 2017; Kelemen and Manning, 2015).

Harzburgitic mantle is a product of extensive melt extraction from peridotite. Considerable quantities of mantle harzburgite should, therefore, have been generated by melting beneath mid-ocean ridges (e.g. Kelemen et al., 1995). Direct geochemical evidence of harzburgite in the Icelandic mantle is comparatively limited (Shorttle et al., 2014), though Nb–Zr–Y systematics and radiogenic Hf-isotopes reveal a depleted mantle component distinct from that sampled along most of the mid-Atlantic ridge (Fitton et al., 1997, 2003; Kempton et al., 2000). Stracke et al. (2011) demonstrated Hf-isotopes in abyssal peridotites correlate with major and trace element indices of melt depletion, indicating the distinct plume depleted component may reflect particularly refractory mantle (Shorttle et al., 2014).

Though harzburgite might contribute a small amount to depleted melt production, it has not been possible to deconvolve volatile heterogeneity between this harzburgitic component and the depleted lherzolite component. The lack of a harzburgite signal may arise from its negligible contribution to the magmatic volatile and trace element budget, owing to extensive prior melt depletion. The lithology hosting the primordial noble gases in the Icelandic mantle is unclear. Decoupling of $^3He/^4He$ from the lithophile trace elements, radiogenic isotopes and major elements (Starkey et al., 2009), prevents direct identification of its source mineralogy in the same manner as the depleted and enriched components (Shorttle and Maclennan, 2011). In the calculations performed in Chapter 6 the primordial mantle component is assumed to have the same chemistry as either bulk silicate Earth or a moderately depleted FOZO-like source (e.g Stracke et al., 2005).

This leaves both the harzburgite lithological component without an estimate for its volatile budget, and the primordial geochemical component without a lithological host. A natural question is whether the primordial component is hosted in harzburgite, with a direct magmatic correspondence being obscured by the melting process.

8.1.1 Harzburgite as the primordial volatile reservoir?

Models of mantle heterogeneity have previously been proposed that place the high $^3He/^4He$ component in extremely refractory, trace element poor, mantle domains (Albarède, 2008; Ballmer et al., 2017). These harzburgitic domains may then supply He to magmas either by diffusion or by melting themselves. Any melts generated from the harzburgite will be extremely depleted in trace elements relative to the melts of typical lherzolite or pyroxenite components. The harzburgite could then contribute a substantial mass of He, dominating the $^3He/^4He$ ratio, whilst having barely any influence on the lithophile trace elements and isotope ratios.

These models therefore offer a mechanism for generating the often observed decoupling between $^3He/^4He$ and the lithophile radiogenic isotope ratios (Condomines et al., 1983; Starkey et al., 2009). Albarède (2008) suggested He diffuses into refractory mantle domains over the lifetime of the Earth, where it remains unsampled by mantle melting in all but the hottest melting regions. Ballmer et al. (2017) suggested that refractory lower mantle bridgmanite cumulates can be preserved throughout the lifetime of the Earth. They argue the mechanical strength of bridgmanite (Yamazaki and Karato, 2001) can prevent substantial mixing by mantle convection, providing a mechanism to isolate a chemical reservoir as required by noble gas observations (Allègre et al., 1983; Harrison et al., 1999).

The results presented in Chapter 6 demonstrate the high $^3He/^4He$ mantle component also has high CO_2/Ba and CO_2/Nb ratios. Prior melt extraction will have removed the majority of the harzburgite's original CO_2 and Ba budgets, suggesting the high source CO_2/Ba may reflect extremely low source CO_2 and Ba concentrations. However, it is unclear how the harzburgite would have acquired such high CO_2/Ba; if it were a result of fractionation during melting the CO_2/Nb ratio would be extremely low (Rosenthal et al., 2015). Though Albarède (2008) shows that He can diffuse into harzburgite domains over the lifetime of the Earth, carbon is unlikely to diffuse sufficiently quickly for the harzburgite to gain high CO_2/Ba and CO_2/Nb ratios by the same mechanism. Alternatively, metasomatic addition of small quantities of carbonated fluids or melts (e.g. Green and Wallace, 1988) could quickly increase both the CO_2/Ba and CO_2/Nb ratios of harzburgite, though it might also be expected to fractionate other trace element ratios (e.g Brenan et al., 1995; Dasgupta et al., 2009; Green et al., 1992; Stalder et al., 1998; Sweeney et al., 1995).

If the refractory component in the Icelandic mantle was instead derived from a bridgmanite cumulate, as suggested by Ballmer et al. (2017), this source may never have experienced melt extraction and its volatile and trace element budget will be primordial. Experimental bridgmanite–melt trace element partitioning data suggest a bridgmanite cumulate will be extremely depleted in the LREEs, Ba, Nb, U and Th relative to the magma it crystallised from (Corgne et al., 2005; Walter et al., 2004). Noble-gas solubility experiments on bridgmanite by Shcheka and Keppler (2012) suggest bridgmanite could incorporate >0.1 wt% He, though its partition coefficient for He remains unknown. The low U and Th

concentration means radiogenic production of ^{4}He will be small in a bridgmanite cumulate, making it an attractive host for the high ^{3}He/^{4}He mantle reservoir.

Assuming a bridgmanite cumulate formed from a magma ocean with a composition close to bulk silicate Earth (BSE), its Ba and CO_2 concentrations can be estimated. Using a partition coefficient of $D_{\mathrm{Ba}}^{\mathrm{Bg/Liq}} = 0.01$ (Corgne et al., 2005), and a BSE Ba concentration of 6.85 ppmw (Palme and O'Neill, 2003), the calculated cumulate Ba concentration is 0.0685 ppmw. Combining this Ba concentration with the calculated primordial (PM) endmember CO_2/Ba ratio of 900 (Section 6.6.2) suggests a cumulate CO_2 concentration of $\sim$60 ppmw. Therefore, assuming the PM component is derived from a refractory cumulate reduces the inferred CO_2 concentration by two orders of magnitude, placing it lower in CO_2 concentration than the depleted mantle (106 ± 18 ppmw).

If the primordial mantle component has such a low CO_2 concentration, the high CO_2 contents inferred in mantle plumes by other authors (Anderson and Poland, 2017; Boudoire et al., 2018; Marty, 2012; Trull et al., 1993) might suggest mantle carbon is predominantly hosted in recycled components, favouring the upper-end of the enriched mantle estimates in Chapter 6. High carbon concentrations in recycled components would favour the argument made for extensive CO_2 recycling into the deep mantle by Hirschmann (2018), based on the mantle CO_2/Ba ratio being higher than the exosphere CO_2/Ba ratio. Large CO_2 inventories in recycled components is hard to reconcile with the extensive slab decarbonation predicted by Kelemen and Manning (2015) using chemical models. However, the hypotheses developed here regarding the primordial component will remain conjectural until a comprehensive understanding of the behaviour of He and the other noble gases in the Icelandic melting region can be developed.

8.2 The water content of the primordial component

A primordial mantle component is not required to explain the observed H_2O/La systematics (Chapter 7), despite its importance in understanding the CO_2/Ba systematics of the same datasets (Chapter 6). If the primordial component resides in a harzburgitic component, as suggested in Section 8.1.1, the lack of a primordial mantle H_2O/La signal could arise from this component contributing only a small mass fraction of H_2O and trace elements to the magmas. A signal may only be apparent in the CO_2/Ba systematics because the primordial CO_2/Ba is so different from the depleted and enriched components, whilst the H_2O/La ratio of the primordial component may be hidden if it is close to the ratios of the other components.

Identifying the primordial CO_2/Ba signal relies on the apparent coupling between ^{3}He/^{4}He and CO_2/Ba. CO_2, He and Ba are all expected to behave extremely incompatibly during melting (e.g.

Brooker et al., 2003; Rosenthal et al., 2015; Workman and Hart, 2005), whilst H_2O and La are slightly more compatible (e.g. Hauri et al., 2006; Workman and Hart, 2005). If melts separate from the mantle matrix at extremely low melt fractions, decoupling of H_2O and He could occur, though most geochemical trends are best explained by the deepest melts being largely homogenised (Rudge et al., 2013). Alternatively, if the first melts generated are carbonatitic (e.g. Dasgupta and Hirschmann, 2010), their extremely low viscosity (Dobson et al., 1996) may allow them to migrate through the melting region independently before mixing with silicate melts. This process might be apparent in the ratios of the most incompatible elements, including Rb, Th and U, elements that were not measured in this study.

It is also possible that the apparent co-variation of CO_2/Ba with $^{143}Nd/^{144}Nd$ and $^{3}He/^{4}He$ in Iceland has occurred by chance and does not reflect a real mantle signal. The presence of a mantle signal can only be confirmed with significantly more melt inclusion datasets from primitive Icelandic eruptions, but is an obvious avenue for future research.

8.3 The role of the mantle in global volatile cycles

In Section 6.6.2 the primordial component in the Iceland plume was calculated to contain 5900^{+560}_{-520} ppmw CO_2. If this CO_2 concentration is representative of the primordial mantle globally, this result could imply a significant fraction of Earth's CO_2 budget remains in the deep Earth. However, the proportion of the mantle represented by the primordial component remains highly uncertain (e.g. Porcelli and Ballentine, 2002).

If the primordial component is representative of most of the lower mantle, then a significant quantity of Earth's carbon budget has remained in the mantle and has never been outgassed. In contrast, if the primordial component represents a smaller reservoir, perhaps the "large low shear velocity provinces" (LLSVPs) imaged by seismic tomography at the base of the mantle (e.g. Trampert et al., 2004), the contribution of such carbon rich domains to the Earth's total CO_2 budget may be marginal. The balance of CO_2 retained in the mantle and outgassed in the primordial Earth may have had a significant impact on the development of the Earth's climate and oceans (e.g. Kasting, 1993). In order to constrain the importance of the retention of primordial volatiles in Earth's mantle the volume of the primordial reservoir must be identified.

Though the importance of the primordial reservoir in the early evolution of the planet remains uncertain, the primordial reservoir may have been an important source of carbon to the Earth's surface during the Phanerozoic. If mantle plumes entrain significant quantities of primordial carbon-rich mantle, the resulting volcanism may be associated with extreme CO_2 outgassing. Large fluxes of CO_2

during the emplacement of large igneous provinces (LIPs) could be an important contributor to global the climatic changes that often accompany LIP volcanism (e.g. Wignall, 2001).

Despite the magnitude of the CO_2 flux from the primordial mantle to the atmosphere being largely unconstrained, it is clear this mantle reservoir is losing CO_2 to the surface. Whether this has resulted in the CO_2 budget of the exosphere increasing through time depends on the magnitude of CO_2 recycling. Though I have quantified the constraints that currently exist for the CO_2 budget of the recycled component in the Iceland plume, the uncertainties are too large to identify whether there is a significant return CO_2 flux to the deep Earth from the surface.

If the low H_2O content of the recycled component in the Iceland plume is representative of its H_2O budget following deep recycling, it would suggest H_2O transfer from the slab to the overlying mantle wedge during recycling was efficient. The recycled component sampled by Icelandic basalts may have been derived from an intermediate–hot slab (Kerrick and Connolly, 2001). The high H_2O contents in the depleted component, relative to other estimates of depleted mantle H_2O concentration, suggests greater global heterogeneity in the depleted mantle H_2O budget than previously thought (Section 1.2).

As discussed in Section 7.6, the similar H_2O concentrations in the depleted and enriched mantle components might reflect diffusive re-equilibration during mantle transport. If diffusive re-equilibration has occurred, the primary H_2O concentration of the enriched component may have been considerably higher, similar to previous estimates for recycled mantle components (Section 1.2). If significant H^+ diffusion occurred between mantle components, the $^3He/^4He$ ratios of the mantle components might also be homogenised (Hart et al., 2008) as the diffusivities of H^+ and He are similar (e.g. Delon et al., 2018; Trull and Kurz, 1993). Diffusive re-equilibration of $^3He/^4He$ ratios in the Iceland plume may explain the decoupling of $^3He/^4He$ from other isotope systems (Starkey et al., 2009), the long wavelength $^3He/^4He$ spatial variation, and comparatively little small scale $^3He/^4He$ variability (e.g. Harðardóttir et al., 2018).

However, if this hypothesis is true, it is an unavoidable conclusion that the observed covariation of CO_2/Ba with $^3He/^4He$ (Chapter 6) is likely a product of chance. The high $^3He/^4He$ would be distributed between mantle components and would no longer correspond uniquely to the component with high CO_2/Ba. However, even in the presence of local $^3He/^4He$ and CO_2/Ba decoupling, if the high CO_2/Ba signal is seen only in locations with high $^3He/^4He$ then the co-variation may still be meaningful. If this process is important, the approach taken in Chapter 6 would need to be applied with more care.

8.4 Conclusion

In this thesis I have presented new major, trace, and volatile element data from melt inclusions from four geochemically diverse eruptions in Iceland. By applying new statistical treatments for volatile-trace element systematics I developed, I have shown degassing and mixing processes can be robustly filtered for in large melt inclusion datasets. Using observed covariations of CO_2/Ba and H_2O/La ratios with indices of mantle heterogeneity I have placed the first quantitative constraints on the CO_2 and H_2O concentrations in the depleted and recycled components of the Icelandic plume, and the CO_2 concentration in the primordial component. Using a novel combination of geophysical, geochemical and petrological observations I place new bounds on the mineralogical heterogeneity in the Icelandic plume, and discuss how this might coincide with the observed volatile heterogeneity. In order for further progress to be made in understanding the distribution of volatile elements in the Icelandic mantle, and how they behave during mantle, a substantially larger melt inclusion dataset is required.

References

Aghaei, O., Nedimović, M. R., Carton, H., Carbotte, S. M., Canales, J. P., and Mutter, J. C. (2014). Crustal thickness and moho character of the fast-spreading East Pacific rise from 9° 42'N to 9° 57'N from poststack-migrated 3-D MCS data. *Geochemistry, Geophysics, Geosystems*, 15(3):634–657.

Aigner-Torres, M., Blundy, J., Ulmer, P., and Pettke, T. (2007). Laser ablation ICPMS study of trace element partitioning between plagioclase and basaltic melts: an experimental approach. *Contributions to Mineralogy and Petrology*, 153(6):647–667.

Albarède, F. (2008). Rogue mantle helium and neon. *Science*, 319(5865):943–945.

Allègre, C. J. (1987). Isotope geodynamics. *Earth and Planetary Science Letters*, 86(2-4):175–203.

Allègre, C. J. and Condomines, M. (1982). Basalt genesis and mantle structure studied through Th-isotopic geochemistry. *Nature*, 299(5878):21.

Allègre, C. J., Hofmann, A., and O'Nions, K. (1996). The argon constraints on mantle structure. *Geophysical Research Letters*, 23(24):3555–3557.

Allègre, C. J., Staudacher, T., Sarda, P., and Kurz, M. (1983). Constraints on evolution of earth's mantle from rare gas systematics. *Nature*, 303(5920):762.

Allègre, C. J. and Turcotte, D. L. (1986). Implications of a two-component marble-cake mantle. *Nature*, 323(6084):123.

Alt, J. C., Schwarzenbach, E. M., Früh-Green, G. L., Shanks III, W. C., Bernasconi, S. M., Garrido, C. J., Crispini, L., Gaggero, L., Padrón-Navarta, J. A., and Marchesi, C. (2013). The role of serpentinites in cycling of carbon and sulfur: seafloor serpentinization and subduction metamorphism. *Lithos*, 178:40–54.

Anderson, K. R. and Poland, M. P. (2017). Abundant carbon in the mantle beneath Hawai'i. *Nature Geoscience*, 10(9):704.

Asimow, P. D., Dixon, J., and Langmuir, C. (2004). A hydrous melting and fractionation model for mid-ocean ridge basalts: Application to the mid-atlantic ridge near the azores. *Geochemistry, Geophysics, Geosystems*, 5(1).

Asimow, P. D., Langmuir, and CH (2003). The importance of water to oceanic mantle melting regimes. *Nature*, 421(6925):815.

Aubaud, C., Hauri, E. H., and Hirschmann, M. M. (2004). Hydrogen partition coefficients between nominally anhydrous minerals and basaltic melts. *Geophysical Research Letters*, 31(20).

Bali, E., Hartley, M., Halldórsson, S., Gudfinnsson, G., and Jakobsson, S. (2018). Melt inclusion constraints on volatile systematics and degassing history of the 2014–2015 Holuhraun eruption, Iceland. *Contributions to Mineralogy and Petrology*, 173(2):9.

Ballentine, C. J., Van Keken, P. E., Porcelli, D., and Hauri, E. H. (2002). Numerical models, geochemistry and the zero–paradox noble–gas mantle. *Philosophical Transactions*

of the Royal Society of London A: Mathematical, Physical and Engineering Sciences, 360(1800):2611–2631.

Ballmer, M. D., Houser, C., Hernlund, J. W., Wentzcovitch, R. M., and Hirose, K. (2017). Persistence of strong silica-enriched domains in the Earth's lower mantle. *Nature Geoscience*, 10(3):236.

Beattie, P. (1993). Olivine-melt and orthopyroxene-melt equilibria. *Contributions to Mineralogy and Petrology*, 115(1):103–111.

Beattie, P., Ford, C., and Russell, D. (1991). Partition coefficients for olivine-melt and orthopyroxene-melt systems. *Contributions to Mineralogy and Petrology*, 109(2):212–224.

Bercovici, D. and Karato, S.-i. (2003). Whole-mantle convection and the transition-zone water filter. *Nature*, 425(6953):39.

Bergmanis, E. C., Sinton, J., and Rubin, K. H. (2007). Recent eruptive history and magma reservoir dynamics on the southern East Pacific Rise at 17°30'S. *Geochemistry, Geophysics, Geosystems*, 8(12).

Berry, A. J., Stewart, G. A., O'Neill, H. S. C., Mallmann, G., and Mosselmans, J. F. W. (2018). A re-assessment of the oxidation state of iron in MORB glasses. *Earth and Planetary Science Letters*, 483:114–123.

Bianchi, D., Sarmiento, J. L., Gnanadesikan, A., Key, R. M., Schlosser, P., and Newton, R. (2010). Low helium flux from the mantle inferred from simulations of oceanic helium isotope data. *Earth and Planetary Science Letters*, 297(3-4):379–386.

Bizimis, M., Griselin, M., Lassiter, J. C., Salters, V. J., and Sen, G. (2007). Ancient recycled mantle lithosphere in the Hawaiian plume: osmium–hafnium isotopic evidence from peridotite mantle xenoliths. *Earth and Planetary Science Letters*, 257(1):259–273.

Blundy, J. and Wood, B. (2003). Mineral-melt partitioning of uranium, thorium and their daughters. *Reviews in Mineralogy and Geochemistry*, 52(1):59–123.

Bonath, E. (1990). Not so hot "hot spots" in the oceanic mantle. *Science*, 250(4977):107–111.

Bottinga, Y. and Javoy, M. (1990). Mid-ocean ridge basalt degassing: Bubble nucleation. *Journal of Geophysical Research: Solid Earth*, 95(B4):5125–5131.

Boudier, F., Nicolas, A., and Ildefonse, B. (1996). Magma chambers in the Oman ophiolite: fed from the top and the bottom. *Earth and Planetary Science Letters*, 144(1-2):239–250.

Boudoire, G., Rizzo, A. L., Di Muro, A., Grassa, F., and Liuzzo, M. (2018). Extensive CO_2 degassing in the upper mantle beneath oceanic basaltic volcanoes: First insights from Piton de la Fournaise volcano (La Réunion Island). *Geochimica et Cosmochimica Acta*, 235:376–401.

Brandon, A. D., Graham, D. W., Waight, T., and Gautason, B. (2007). ^{186}Os and ^{187}Os enrichments and high-^{3}He/^{4}He sources in the earth's mantle: Evidence from Icelandic picrites. *Geochimica et Cosmochimica Acta*, 71(18):4570 – 4591.

Braun, M. G. and Kelemen, P. B. (2002). Dunite distribution in the Oman ophiolite: implications for melt flux through porous dunite conduits. *Geochemistry, Geophysics, Geosystems*, 3(11):1–21.

Breddam, K. (2002). Kistufell: Primitive melt from the Iceland mantle plume. *Journal of Petrology*, 43(2):345–373.

Breddam, K., Kurz, M. D., and Storey, M. (2000). Mapping out the conduit of the Iceland mantle plume with helium isotopes. *Earth and Planetary Science Letters*, 176(1):45–55.

Brenan, J., Shaw, H., Ryerson, F., and Phinney, D. (1995). Mineral-aqueous fluid partitioning of trace elements at 900°c and 2.0 GPa: Constraints on the trace element chemistry of mantle and deep crustal fluids. *Geochimica et Cosmochimica Acta*, 59(16):3331–3350.

Brooker, R., Du, Z., Blundy, J., Kelley, S., Allan, N., Wood, B., Chamorro, E., Wartho, J.-A., and Purton, J. (2003). The 'zero charge' partitioning behaviour of noble gases during mantle melting. *Nature*, 423(6941):738.

Brown, E. L. and Lesher, C. E. (2014). North Atlantic magmatism controlled by temperature, mantle composition and buoyancy. *Nature Geoscience*, 7(11):820.

Brown, P. J. and Fuller, W. A. (1990). *Statistical analysis of measurement error models and applications: proceedings of the AMS-IMS-SIAM joint summer research conference held June 10-16, 1989, with support from the National Science Foundation and the US Army Research Office*, volume 112. American Mathematical Soc.

Buchner, J., Georgakakis, A., Nandra, K., Hsu, L., Rangel, C., Brightman, M., Merloni, A., Salvato, M., Donley, J., and Kocevski, D. (2014). X-ray spectral modelling of the AGN obscuring region in the CDFS: Bayesian model selection and catalogue. *Astronomy & Astrophysics*, 564:A125.

Bucholz, C. E., Gaetani, G. A., Behn, M. D., and Shimizu, N. (2013). Post-entrapment modification of volatiles and oxygen fugacity in olivine-hosted melt inclusions. *Earth and Planetary Science Letters*, 374:145–155.

Cabral, R. A., Jackson, M. G., Koga, K. T., Rose-Koga, E. F., Hauri, E. H., Whitehouse, M. J., Price, A. A., Day, J., Shimizu, N., and Kelley, K. A. (2014). Volatile cycling of H_2O, CO_2, F, and Cl in the HIMU mantle: A new window provided by melt inclusions from oceanic hot spot lavas at Mangaia, Cook Islands. *Geochemistry, Geophysics, Geosystems*, 15(11):4445–4467.

Canil, D. (1990). Experimental study bearing on the absence of carbonate in mantle-derived xenoliths. *Geology*, 18(10):1011–1013.

Canil, D. and Scarfe, C. M. (1990). Phase relations in peridotite + CO_2 systems to 12 GPa: implications for the origin of kimberlite and carbonate stability in the earth's upper mantle. *Journal of Geophysical Research: Solid Earth*, 95(B10):15805–15816.

Carmichael, I. S. E. (1964). The petrology of Thingmuli, a Tertiary volcano in eastern Iceland. *Journal of Petrology*, 5(3):435–460.

Cartigny, P., Pineau, F., Aubaud, C., and Javoy, M. (2008). Towards a consistent mantle carbon flux estimate: Insights from volatile systematics (H_2O/Ce, δD, CO_2/Nb) in the north atlantic mantle (14°N and 34°N). *Earth and Planetary Science Letters*, 265(3-4):672–685.

Chauvel, C. and Hémond, C. (2000). Melting of a complete section of recycled oceanic crust: trace element and Pb isotopic evidence from Iceland. *Geochemistry, Geophysics, Geosystems*, 1(2).

Chiodini, G., Cioni, R., Guidi, M., Raco, B., and Marini, L. (1998). Soil CO_2 flux measurements in volcanic and geothermal areas. *Applied Geochemistry*, 13(5):543–552.

Clarke, W. B., Beg, M., and Craig, H. (1969). Excess ^{3}He in the sea: Evidence for terrestrial primordial helium. *Earth and Planetary Science Letters*, 6(3):213–220.

Class, C. and Goldstein, S. L. (2005). Evolution of helium isotopes in the Earth's mantle. *Nature*, 436(7054):1107.

Condomines, M., Grönvold, K., Hooker, P., Muehlenbachs, K., o'Nions, R., Oskarsson, N., and Oxburgh, E. (1983). Helium, oxygen, strontium and neodymium isotopic relationships in Icelandic volcanics. *Earth and Planetary Science Letters*, 66:125–136.

Coogan, L., Saunders, A., and Wilson, R. (2014). Aluminum-in-olivine thermometry of primitive basalts: evidence of an anomalously hot mantle source for large igneous provinces. *Chemical Geology*, 368:1–10.

Corgne, A., Liebske, C., Wood, B. J., Rubie, D. C., and Frost, D. J. (2005). Silicate perovskite-melt partitioning of trace elements and geochemical signature of a deep perovskitic reservoir. *Geochimica et Cosmochimica Acta*, 69(2):485–496.

Cottrell, E. and Kelley, K. A. (2011). The oxidation state of Fe in MORB glasses and the oxygen fugacity of the upper mantle. *Earth and Planetary Science Letters*, 305(3):270–282.

Craig, H., Clarke, W., and Beg, M. (1975). Excess ^{3}He in deep water on the East Pacific Rise.

Earth and Planetary Science Letters, 26(2):125–132.

Danyushevsky, L. V., Eggins, S. M., Falloon, T. J., and Christie, D. M. (2000). H_2O abundance in depleted to moderately enriched mid-ocean ridge magmas; Part I: Incompatible behaviour, implications for mantle storage, and origin of regional variations. *Journal of Petrology*, 41(8):1329–1364.

Danyushevsky, L. V., McNeill, A. W., and Sobolev, A. V. (2002). Experimental and petrological studies of melt inclusions in phenocrysts from mantle-derived magmas: an overview of techniques, advantages and complications. *Chemical Geology*, 183(1-4):5–24.

Danyushevsky, L. V. and Plechov, P. (2011). Petrolog3: Integrated software for modeling crystallization processes. *Geochemistry, Geophysics, Geosystems*, 12(7).

Darbyshire, F. A., Bjarnason, I. T., White, R. S., and Flóvenz, Ó. G. (1998). Crustal structure above the iceland mantle plume imaged by the ICEMELT refraction profile. *Geophysical Journal International*, 135(3):1131–1149.

Darbyshire, F. A., Priestley, K. F., White, R. S., Stefánsson, R., Gudmundsson, G. B., and Jakobsdóttir, S. S. (2000). Crustal structure of central and northern Iceland from analysis of teleseismic receiver functions. *Geophysical Journal International*, 143(1):163–184.

Dasgupta, R. (2013). Ingassing, storage, and outgassing of terrestrial carbon through geologic time. *Reviews in Mineralogy and Geochemistry*, 75(1):183–229.

Dasgupta, R. and Hirschmann, M. M. (2006). Melting in the Earth's deep upper mantle caused by carbon dioxide. *Nature*, 440(7084):659.

Dasgupta, R. and Hirschmann, M. M. (2010). The deep carbon cycle and melting in earth's interior. *Earth and Planetary Science Letters*, 298(1-2):1–13.

Dasgupta, R., Hirschmann, M. M., McDonough, W. F., Spiegelman, M., and Withers, A. C. (2009). Trace element partitioning between garnet lherzolite and carbonatite at 6.6 and 8.6 GPa with applications to the geochemistry of the mantle and of mantle-derived melts. *Chemical Geology*, 262(1-2):57–77.

Dasgupta, R., Jackson, M. G., and Lee, C.-T. A. (2010). Major element chemistry of ocean island basalts—conditions of mantle melting and heterogeneity of mantle source. *Earth and Planetary Science Letters*, 289(3-4):377–392.

Dasgupta, R., Mallik, A., Tsuno, K., Withers, A. C., Hirth, G., and Hirschmann, M. M. (2013). Carbon-dioxide-rich silicate melt in the Earth's upper mantle. *Nature*, 493(7431):211.

Davies, G. F. (1977). Whole-mantle convection and plate tectonics. *Geophysical Journal International*, 49(2):459–486.

Debaille, V., Trønnes, R. G., Brandon, A. D., Waight, T. E., Graham, D. W., and Lee, C.-T. A. (2009). Primitive off-rift basalts from Iceland and Jan Mayen: Os-isotopic evidence for a mantle source containing enriched subcontinental lithosphere. *Geochimica et Cosmochimica Acta*, 73(11):3423–3449.

Deer, W., Howie, R., and Zussman, J. (1997). An introduction to the rock-forming minerals.

Deines, P. (2002). The carbon isotope geochemistry of mantle xenoliths. *Earth-Science Reviews*, 58(3-4):247–278.

Delon, R., Demouchy, S., Marrocchi, Y., Bouhifd, M. A., Barou, F., Cordier, P., Addad, A., and Burnard, P. G. (2018). Helium incorporation and diffusion in polycrystalline olivine. *Chemical Geology*, 488:105–124.

Dixon, J. E., Bindeman, I., Kingsley, R., Simons, K., Le Roux, P., Hajewski, T., Swart, P., Langmuir, C., Ryan, J., Walowski, K., et al. (2017). Light stable isotopic compositions of enriched mantle sources: resolving the dehydration paradox. *Geochemistry, Geophysics, Geosystems*, 18(11):3801–3839.

Dixon, J. E. and Clague, D. A. (2001). Volatiles in basaltic glasses from Loihi Seamount, Hawaii: Evidence for a relatively dry plume component. *Journal of Petrology*, 42(3):627–654.

Dixon, J. E., Leist, L., Langmuir, C., and Schilling, J.-G. (2002). Recycled dehydrated lithosphere observed in plume-influenced mid-ocean-ridge basalt. *Nature*, 420(6914):385.

Dixon, J. E., Stolper, E., and Delaney, J. R. (1988). Infrared spectroscopic measurements of CO_2 and H_2O in Juan de Fuca Ridge basaltic glasses. *Earth and Planetary Science Letters*, 90(1):87–104.

Dixon, J. E. and Stolper, E. M. (1995). An experimental study of water and carbon dioxide solubilities in mid-ocean ridge basaltic liquids. Part II: applications to degassing. *Journal of Petrology*, 36(6):1633–1646.

Dobson, D. P., Jones, A. P., Rabe, R., Sekine, T., Kurita, K., Taniguchi, T., Kondo, T., Kato, T., Shimomura, O., and Urakawa, S. (1996). In-situ measurement of viscosity and density of carbonate melts at high pressure. *Earth and Planetary Science Letters*, 143(1-4):207–215.

Duncan, M. S. and Dasgupta, R. (2017). Rise of Earth's atmospheric oxygen controlled by efficient subduction of organic carbon. *Nature Geoscience*, 10(5):387.

Eguchi, J. and Dasgupta, R. (2018). A CO_2 solubility model for silicate melts from fluid saturation to graphite or diamond saturation. *Chemical Geology*, 487:23–38.

Eiler, J. M., Schiano, P., Kitchen, N., and Stolper, E. M. (2000). Oxygen-isotope evidence for recycled crust in the sources of mid-ocean-ridge basalts. *Nature*, 403(6769):530.

Elkins, L., Scott, S., Sims, K., Rivers, E., Devey, C. W., Reagan, M., Hamelin, C., and Pedersen, R. (2016). Exploring the role of mantle eclogite at mid-ocean ridges and hotspots: U-series constraints on Jan Mayen island and the Kolbeinsey ridge. *Chemical Geology*, 444:128–140.

Elliott, T., Hawkesworth, C., and Grönvold, K. (1991). Dynamic melting of the Iceland plume. *Nature*, 351(6323):201.

Farley, K., Maier-Reimer, E., Schlosser, P., and Broecker, W. (1995). Constraints on mantle ^{3}He fluxes and deep-sea circulation from an oceanic general circulation model. *Journal of Geophysical Research: Solid Earth*, 100(B3):3829–3839.

Faure, G. and Mensing, T. M. (2005). *Isotopes: principles and applications*. Wiley-Blackwell.

Feroz, F. and Hobson, M. (2008). Multimodal nested sampling: an efficient and robust alternative to Markov Chain Monte Carlo methods for astronomical data analyses. *Monthly Notices of the Royal Astronomical Society*, 384(2):449–463.

Feroz, F., Hobson, M., and Bridges, M. (2009). Multinest: an efficient and robust bayesian inference tool for cosmology and particle physics. *Monthly Notices of the Royal Astronomical Society*, 398(4):1601–1614.

Feroz, F., Hobson, M., Cameron, E., and Pettitt, A. (2013). Importance nested sampling and the MultiNest algorithm. *arXiv preprint arXiv:1306.2144*.

Fitton, J., Saunders, A., Norry, M., Hardarson, B., and Taylor, R. (1997). Thermal and chemical structure of the Iceland plume. *Earth and Planetary Science Letters*, 153(3-4):197–208.

Fitton, J. G., Saunders, A. D., Kempton, P. D., and Hardarson, B. S. (2003). Does depleted mantle form an intrinsic part of the Iceland plume? *Geochemistry, Geophysics, Geosystems*, 4(3).

Füri, E., Hilton, D., Halldórsson, S., Barry, P., Hahm, D., Fischer, T., and Grönvold, K. (2010). Apparent decoupling of the he and ne isotope systematics of the Icelandic mantle: The role of He depletion, melt mixing, degassing fractionation and air interaction. *Geochimica et Cosmochimica Acta*, 74(11):3307–3332.

Gaetani, G. A., O'Leary, J. A., Shimizu, N., Bucholz, C. E., and Newville, M. (2012). Rapid reequilibration of H_2O and oxygen fugacity in olivine-hosted melt inclusions. *Geology*, 40(10):915–918.

Gale, A., Dalton, C. A., Langmuir, C. H., Su, Y., and Schilling, J.-G. (2013a). The mean composition of ocean ridge basalts. *Geochemistry, Geophysics, Geosystems*, 14(3):489–518.

Gale, A., Laubier, M., Escrig, S., and Langmuir, C. H. (2013b). Constraints on melting processes and plume-ridge interaction from comprehensive study of the FAMOUS and North Famous segments, Mid-Atlantic Ridge. *Earth and Planetary Science Letters*, 365:209–220.

Gast, P. W. (1968). Trace element fractionation and the origin of tholeiitic and alkaline magma types. *Geochimica et Cosmochimica Acta*, 32(10):1057–1086.

Ghiorso, M. S., Hirschmann, M. M., Reiners, P. W., and Kress III, V. C. (2002). The pMELTS: A revision of MELTS for improved calculation of phase relations and major element partitioning related to partial melting of the mantle to 3 GPa. *Geochemistry, Geophysics, Geosystems*, 3(5):1–35.

Ghiorso, M. S. and Sack, R. O. (1995). Chemical mass transfer in magmatic processes IV. A revised and internally consistent thermodynamic model for the interpolation and extrapolation of liquid-solid equilibria in magmatic systems at elevated temperatures and pressures. *Contributions to Mineralogy and Petrology*, 119(2-3):197–212.

Gibson, S. and Geist, D. (2010). Geochemical and geophysical estimates of lithospheric thickness variation beneath galápagos. *Earth and Planetary Science Letters*, 300(3):275–286.

Gibson, S., Thompson, R., Weska, R., Dickin, A., and Leonardos, O. (1997). Late Cretaceous rift-related upwelling and melting of the Trindade starting mantle plume head beneath western Brazil. *Contributions to Mineralogy and Petrology*, 126(3):303–314.

Gibson, S. A. (2002). Major element heterogeneity in Archean to Recent mantle plume startingheads. *Earth and Planetary Science Letters*, 195(1-2):59–74.

Gibson, S. A. and Richards, M. A. (2018). Delivery of deep-sourced, volatile-rich plume material to the global ridge system. *Earth and Planetary Science Letters*, 499:205–218.

Gill, J., Michael, P., Woodcock, J., Dreyer, B., Ramos, F., Clague, D., Kela, J., Scott, S., Konrad, K., and Stakes, D. (2016). Spatial and temporal scale of mantle enrichment at the Endeavour Segment, Juan de Fuca ridge. *Journal of Petrology*, 57(5):863–896.

Gill, R. (2010). *Igneous rocks and processes: a practical guide*. John Wiley & Sons.

Green, D. and Ringwood, A. (1967). The genesis of basaltic magmas. *Contributions to Mineralogy and Petrology*, 15(2):103–190.

Green, D. H. and Wallace, M. E. (1988). Mantle metasomatism by ephemeral carbonatite melts. *Nature*, 336(6198):459.

Green, T., Adam, J., and Siel, S. (1992). Trace element partitioning between silicate minerals and carbonatite at 25 kbar and application to mantle metasomatism. *Mineralogy and Petrology*, 46(3):179–184.

Gudmundsson, A. (1995). Ocean-ridge discontinuities in Iceland. *Journal of the Geological Society*, 152(6):1011–1015.

Gurenko, A. A. and Chaussidon, M. (1995). Enriched and depleted primitive melts included in olivine from Icelandic tholeiites: origin by continuous melting of a single mantle column. *Geochimica et Cosmochimica Acta*, 59(14):2905–2917.

Gurenko, A. A., Hansteen, T. H., and Schmincke, H.-U. (1996). Evolution of parental magmas of Miocene shield basalts of Gran Canaria (Canary Islands): constraints from crystal, melt and fluid inclusions in minerals. *Contributions to Mineralogy and Petrology*, 124(3-4):422–435.

Gurenko, A. A., Sobolev, A. V., Hoernle, K. A., Hauff, F., and Schmincke, H.-U. (2009). Enriched, HIMU-type peridotite and depleted recycled pyroxenite in the Canary plume: a mixed-up mantle. *Earth and Planetary Science Letters*, 277(3):514–524.

Halliday, A. N. (2013). The origins of volatiles in the terrestrial planets. *Geochimica et Cosmochimica Acta*, 105:146–171.

Hamilton, P., O'Nions, R., Bridgwater, D., and Nutman, A. (1983). Sm-Nd studies of Archaean metasediments and metavolcanics from

West Greenland and their implications for the Earth's early history. *Earth and Planetary Science Letters*, 62(2):263–272.

Hanan, B. B. and Schilling, J.-G. (1997). The dynamic evolution of the Iceland mantle plume: the lead isotope perspective. *Earth and Planetary Science Letters*, 151(1):43–60.

Harðardóttir, S., Halldórsson, S. A., and Hilton, D. R. (2018). Spatial distribution of helium isotopes in Icelandic geothermal fluids and volcanic materials with implications for location, upwelling and evolution of the Icelandic mantle plume. *Chemical Geology*, 480:12–27.

Hardarson, B., Fitton, J., Ellam, R., and Pringle, M. (1997). Rift relocation—a geochemical and geochronological investigation of a palaeo-rift in northwest Iceland. *Earth and Planetary Science Letters*, 153(3):181–196.

Harpp, K. and Geist, D. (2002). Wolf–Darwin lineament and plume–ridge interaction in northern Galápagos. *Geochemistry, Geophysics, Geosystems*, 3(11):1–19.

Harrison, D., Burnard, P., and Turner, G. (1999). Noble gas behaviour and composition in the mantle: constraints from the Iceland plume. *Earth and Planetary Science Letters*, 171(2):199–207.

Hart, S. R. (1984). A large-scale isotope anomaly in the Southern Hemisphere mantle. *Nature*, 309(5971):753.

Hart, S. R., Hauri, E. H., Oschmann, L. A., and Whitehead, J. A. (1992). Mantle plumes and entrainment: Isotopic evidence. *Science*, 256(5056):517–520.

Hart, S. R., Kurz, M. D., and Wang, Z. (2008). Scale length of mantle heterogeneities: Constraints from helium diffusion. *Earth and Planetary Science Letters*, 269(3-4):508–517.

Hartley, M. E., Bali, E., Maclennan, J., Neave, D. A., and Halldórsson, S. A. (2018). Melt inclusion constraints on petrogenesis of the 2014–2015 Holuhraun eruption, Iceland. *Contributions to Mineralogy and Petrology*, 173(2):10.

Hartley, M. E., Maclennan, J., Edmonds, M., and Thordarson, T. (2014). Reconstructing the deep CO_2 degassing behaviour of large basaltic fissure eruptions. *Earth and Planetary Science Letters*, 393:120–131.

Hartley, M. E., Neave, D. A., Maclennan, J., Edmonds, M., and Thordarson, T. (2015). Diffusive over-hydration of olivine-hosted melt inclusions. *Earth and Planetary Science Letters*, 425:168–178.

Harvey, J., Gannoun, A., Burton, K. W., Rogers, N. W., Alard, O., and Parkinson, I. J. (2006). Ancient melt extraction from the oceanic upper mantle revealed by Re–Os isotopes in abyssal peridotites from the Mid-Atlantic ridge. *Earth and Planetary Science Letters*, 244(3):606–621.

Hauri, E., Gaetani, G., Green, T., et al. (2004). Partitioning of H_2O between mantle minerals and silicate melts. *Geochim. Cosmochim. Acta*, 68:A33.

Hauri, E. H., Gaetani, G. A., and Green, T. H. (2006). Partitioning of water during melting of the earth's upper mantle at H_2O-undersaturated conditions. *Earth and Planetary Science Letters*, 248(3-4):715–734.

Hauri, E. H., Maclennan, J., McKenzie, D., Gronvold, K., Oskarsson, N., and Shimizu, N. (2018). CO_2 content beneath northern Iceland and the variability of mantle carbon. *Geology*, 46(1):55–58.

Hayes, J. M. and Waldbauer, J. R. (2006). The carbon cycle and associated redox processes through time. *Philosophical Transactions of the Royal Society of London B: Biological Sciences*, 361(1470):931–950.

Heinonen, J. S., Jennings, E. S., and Riley, T. R. (2015). Crystallisation temperatures of the most Mg-rich magmas of the Karoo LIP on the basis of Al-in-olivine thermometry. *Chemical Geology*, 411:26–35.

Hekinian, R., Chaigneau, M., and Cheminée, J. (1973). Popping rocks and lava tubes from the Mid-Atlantic Rift Valley at 36°N. *Nature*, 245(5425):371.

Helo, C., Longpré, M.-A., Shimizu, N., Clague, D. A., and Stix, J. (2011). Explosive eruptions at mid-ocean ridges driven by CO_2-rich magmas. *Nature Geoscience*, 4(4):260.

Helz, R. T. and Thornber, C. R. (1987). Geothermometry of Kilauea Iki lava lake, Hawaii. *Bulletin of volcanology*, 49(5):651–668.

Hemond, C., Arndt, N. T., Lichtenstein, U., Hofmann, A. W., Oskarsson, N., and Steinthorsson, S. (1993). The heterogeneous Iceland plume: Nd-Sr-O isotopes and trace element constraints. *Journal of Geophysical Research: Solid Earth*, 98(B9):15833–15850.

Hemond, C., Condomines, M., Fourcade, S., Allegre, C., Oskarsson, N., and Javoy, M. (1988). Thorium, strontium and oxygen isotopic geochemistry in recent tholeiites from Iceland: crustal influence on mantle-derived magmas. *Earth and Planetary Science Letters*, 87(3):273–285.

Hemond, C., Hofmann, A. W., Vlastelic, I., and Nauret, F. (2006). Origin of MORB enrichment and relative trace element compatibilities along the mid-Atlantic Ridge between 10° and 24°N. *Geochemistry, Geophysics, Geosystems*, 7(12).

Herzberg, C. (2004). Partial crystallization of mid-ocean ridge basalts in the crust and mantle. *Journal of Petrology*, 45(12):2389–2405.

Herzberg, C. (2010). Identification of source lithology in the Hawaiian and Canary Islands: Implications for origins. *Journal of Petrology*, 52(1):113–146.

Herzberg, C. (2011). Basalts as temperature probes of Earth's mantle. *Geology*, 39(12):1179–1180.

Herzberg, C. and Asimow, P. (2015). PRIMELT 3 MEGA. XLSM software for primary magma calculation: Peridotite primary magma MgO contents from the liquidus to the solidus. *Geochemistry, Geophysics, Geosystems*, 16(2):563–578.

Herzberg, C., Vidito, C., and Starkey, N. A. (2016). Nickel–cobalt contents of olivine record origins of mantle peridotite and related rocks. *American Mineralogist*, 101(9):1952–1966.

Hilton, D., Grönvold, K., O'Nions, R., and Oxburgh, E. (1990). Regional distribution of ^{3}He anomalies in the Icelandic crust. *Chemical Geology*, 88(1-2):53–67.

Hilton, D., Gronvold, K., Sveinbjornsdottir, A., and Hammerschmidt, K. (1998). Helium isotope evidence for off-axis degassing of the Icelandic hotspot. *Chemical Geology*, 149(3-4):173–187.

Hirose, K. and Kushiro, I. (1993). Partial melting of dry peridotites at high pressures: determination of compositions of melts segregated from peridotite using aggregates of diamond. *Earth and Planetary Science Letters*, 114(4):477–489.

Hirschmann, M. M. (2000). Mantle solidus: Experimental constraints and the effects of peridotite composition. *Geochemistry, Geophysics, Geosystems*, 1(10).

Hirschmann, M. M. (2018). Comparative deep earth volatile cycles: The case for C recycling from exosphere/mantle fractionation of major (H_2O, C, N) volatiles and from H_2O/Ce, CO_2/Ba, and CO_2/Nb exosphere ratios. *Earth and Planetary Science Letters*, 502:262–273.

Hirschmann, M. M., Aubaud, C., and Withers, A. C. (2005). Storage capacity of H_2O in nominally anhydrous minerals in the upper mantle. *Earth and Planetary Science Letters*, 236(1-2):167–181.

Hirschmann, M. M. and Dasgupta, R. (2009). The H/C ratios of Earth's near-surface and deep reservoirs, and consequences for deep Earth volatile cycles. *Chemical Geology*, 262(1-2):4–16.

Hirschmann, M. M., Kogiso, T., Baker, M. B., and Stolper, E. M. (2003). Alkalic magmas generated by partial melting of garnet pyroxenite. *Geology*, 31(6):481–484.

Hirschmann, M. M. and Stolper, E. M. (1996). A possible role for garnet pyroxenite in the origin of the "garnet signature" in MORB. *Contributions to Mineralogy and Petrology*, 124(2):185–208.

Hirth, G. and Kohlstedt, D. L. (1996). Water in the oceanic upper mantle: implications for rheology, melt extraction and the evolution of the lithosphere. *Earth and Planetary Science Letters*, 144(1-2):93–108.

Hjartarson, Á. and Sæmundsson, K. (2014). Geological map of Iceland, bedrock. 1: 600,000. *Iceland GeoSurvey, Reykjavík*.

Hoffman, N. and McKenzie, D. (1985). The destruction of geochemical heterogeneities by differential fluid motions during mantle convection. *Geophysical Journal International*, 82(2):163–206.

Hofmann, A. W. and White, W. M. (1982). Mantle plumes from ancient oceanic crust. *Earth and Planetary Science Letters*, 57(2):421–436.

Hole, M. J. and Millett, J. (2016). Controls of mantle potential temperature and lithospheric thickness on magmatism in the north Atlantic Igneous Province. *Journal of Petrology*, 57(2):417–436.

Holland, T. and Powell, R. (1998). An internally consistent thermodynamic data set for phases of petrological interest. *Journal of metamorphic Geology*, 16(3):309–343.

Holland, T. J., Green, E. C., and Powell, R. (2018). Melting of peridotites through to granites: a simple thermodynamic model in the system KNCFMASHTOCr. *Journal of Petrology*.

Holland, T. J., Hudson, N. F., Powell, R., and Harte, B. (2013). New thermodynamic models and calculated phase equilibria in NCFMAS for basic and ultrabasic compositions through the transition zone into the uppermost lower mantle. *Journal of Petrology*, 54(9):1901–1920.

Iacono-Marziano, G., Morizet, Y., Le Trong, E., and Gaillard, F. (2012). New experimental data and semi-empirical parameterization of H_2O–CO_2 solubility in mafic melts. *Geochimica et Cosmochimica Acta*, 97:1–23.

Ito, K. and Kennedy, G. C. (1967). Melting and phase relations in a natural peridotite to 40 kilobars. *American Journal of Science*, 265(6):519–538.

Jackson, D. and Somers, K. (1991). The spectre of 'spurious' correlations. *Oecologia*, 86(1):147–151.

Jacobsen, S. B. and Wasserburg, G. J. (1979). The mean age of mantle and crustal reservoirs. *Journal of Geophysical Research: Solid Earth*, 84(B13):7411–7427.

Jakobsson, S. P. (1972). Chemistry and distribution pattern of recent basaltic rocks in Iceland. *Lithos*, 5(4):365–386.

Jambon, A., Weber, H., and Braun, O. (1986). Solubility of He, Ne, Ar, Kr and Xe in a basalt melt in the range 1250–1600°C. geochemical implications. *Geochimica et Cosmochimica Acta*, 50(3):401–408.

Jambon, A. and Zimmermann, J. L. (1990). Water in oceanic basalts: evidence for dehydration of recycled crust. *Earth and Planetary Science Letters*, 101(2-4):323–331.

Javoy, M. and Pineau, F. (1991). The volatiles record of a "popping" rock from the mid-atlantic ridge at 14°N: chemical and isotopic composition of gas trapped in the vesicles. *Earth and Planetary Science Letters*, 107(3-4):598–611.

Javoy, M., Pineau, F., and Allègre, C. J. (1982). Carbon geodynamic cycle. *Nature*, 300(5888):171.

Javoy, M., Pineau, F., and Iiyama, I. (1978). Experimental determination of the isotopic fractionation between gaseous CO_2 and carbon dissolved in tholeiitic magma. *Contributions to Mineralogy and Petrology*, 67(1):35–39.

Jenkins, J., Cottaar, S., White, R. S., and Deuss, A. (2016). Depressed mantle discontinuities beneath Iceland: Evidence of a garnet controlled 660 km discontinuity? *Earth and Planetary Science Letters*, 433:159–168.

Jenkins, J., Maclennan, J., Green, R. G., Cottaar, S., Deuss, A., and White, R. S. (2018). Crustal formation on a spreading ridge above a mantle plume: receiver function imaging of the Icelandic crust. *Journal of Geophysical Research: Solid Earth*, 123(6):5190–5208.

Jennings, E. S. and Holland, T. J. (2015). A simple thermodynamic model for melting of peridotite in the system NCFMASOCr. *Journal of Petrology*, 56(5):869–892.

Jennings, E. S., Holland, T. J., Shorttle, O., Maclennan, J., and Gibson, S. A. (2016). The composition of melts from a heterogeneous mantle and the origin of ferropicrite: application of a thermodynamic model. *Journal of Petrology*, 57(11-12):2289–2310.

Jian, H., Singh, S. C., Chen, Y. J., and Li, J. (2017). Evidence of an axial magma chamber beneath the ultraslow-spreading Southwest Indian Ridge. *Geology*, 45(2):143–146.

Jones, E., Oliphant, T., and Peterson, P. (2014a). {SciPy}: open source scientific tools for {Python}.

Jones, M., Wanless, V., Soule, S., Kurz, M., Mittelstaedt, E., Fornari, D., Curtice, J., Klein, F., Le Roux, V., Brodsky, H., et al. (2019). New constraints on mantle carbon from Mid-Atlantic Ridge popping rocks. *Earth and Planetary Science Letters*, 511:67–75.

Jones, S. M., Murton, B. J., Fitton, J. G., White, N. J., Maclennan, J., and Walters, R. (2014b). A joint geochemical–geophysical record of time-dependent mantle convection south of Iceland. *Earth and Planetary Science Letters*, 386:86–97.

Jull, M. and McKenzie, D. (1996). The effect of deglaciation on mantle melting beneath Iceland. *Journal of Geophysical Research: Solid Earth*, 101(B10):21815–21828.

Karson, J. (2017). The iceland plate boundary zone: Propagating rifts, migrating transforms, and rift-parallel strike-slip faults. *Geochemistry, Geophysics, Geosystems*, 18(11):4043–4054.

Kasting, J. F. (1993). Earth's early atmosphere. *Science*, 259(5097):920–926.

Katz, R. F. and Rudge, J. F. (2011). The energetics of melting fertile heterogeneities within the depleted mantle. *Geochemistry, Geophysics, Geosystems*, 12(10).

Katz, R. F., Spiegelman, M., and Langmuir, C. H. (2003). A new parameterization of hydrous mantle melting. *Geochemistry, Geophysics, Geosystems*, 4(9).

Kawakami, Y., Yamamoto, J., and Kagi, H. (2003). Micro-raman densimeter for CO_2 inclusions in mantle-derived minerals. *Applied spectroscopy*, 57(11):1333–1339.

Keiding, J., Trumbull, R., Veksler, I., and Jerram, D. (2011). On the significance of ultramagnesian olivines in basaltic rocks. *Geology*, 39(12):1095–1098.

Kelemen, P., Hirth, G., Shimizu, N., Spiegelman, M., and Dick, H. (1997a). A review of melt migration processes in the adiabatically upwelling mantle beneath oceanic spreading ridges. *Philosophical Transactions of the Royal Society of London A: Mathematical, Physical and Engineering Sciences*, 355(1723):283–318.

Kelemen, P. B., Koga, K., and Shimizu, N. (1997b). Geochemistry of gabbro sills in the crust-mantle transition zone of the oman ophiolite: Implications for the origin of the oceanic lower crust. *Earth and Planetary Science Letters*, 146(3-4):475–488.

Kelemen, P. B. and Manning, C. E. (2015). Reevaluating carbon fluxes in subduction zones, what goes down, mostly comes up. *Proceedings of the National Academy of Sciences*, page 201507889.

Kelemen, P. B., Matter, J., Streit, E. E., Rudge, J. F., Curry, W. B., and Blusztajn, J. (2011). Rates and mechanisms of mineral carbonation in peridotite: natural processes and recipes for enhanced, in situ CO_2 capture and storage. *Annual Review of Earth and Planetary Sciences*, 39:545–576.

Kelemen, P. B., Shimizu, N., and Salters, V. J. (1995). Extraction of mid-ocean-ridge basalt from the upwelling mantle by focused flow of melt in dunite channels. *Nature*, 375(6534):747.

Keller, T., Katz, R. F., and Hirschmann, M. M. (2017). Volatiles beneath mid-ocean ridges: Deep melting, channelised transport, focusing, and metasomatism. *Earth and Planetary Science Letters*, 464:55–68.

Kempton, P., Fitton, J., Saunders, A., Nowell, G., Taylor, R., Hardarson, B., and Pearson, G. (2000). The Iceland plume in space and time: a Sr–Nd–Pb–Hf study of the North Atlantic rifted margin. *Earth and Planetary Science Letters*, 177(3):255–271.

Kerr, A. C., Saunders, A. D., Tarney, J., Berry, N. H., and Hards, V. L. (1995). Depleted mantle-plume geochemical signatures: No paradox for plume theories. *Geology*, 23(9):843–846.

Kerrick, D. and Connolly, J. (2001). Metamorphic devolatilization of subducted oceanic metabasalts: implications for seismicity, arc magmatism and volatile recycling. *Earth and Planetary Science Letters*, 189(1-2):19–29.

Kitagawa, H., Kobayashi, K., Makishima, A., and Nakamura, E. (2008). Multiple pulses of the mantle plume: evidence from Tertiary Icelandic lavas. *Journal of Petrology*, 49(7):1365–1396.

Klein, E. M. and Langmuir, C. H. (1987). Global correlations of ocean ridge basalt chemistry with axial depth and crustal thickness. *Journal of Geophysical Research: Solid Earth*, 92(B8):8089–8115.

Klöcking, M., White, N., and MacLennan, J. (2018a). Role of basaltic magmatism within the Parnaíba cratonic basin, NE Brazil. *Geological Society, London, Special Publications*, 472:SP472–4.

Klöcking, M., White, N., Maclennan, J., McKenzie, D., and Fitton, J. (2018b). Quantitative relationships between basalt geochemistry, shear wave velocity, and asthenospheric temperature beneath western North America. *Geochemistry, Geophysics, Geosystems*, 19(9):3376–3404.

Koga, K., Hauri, E., Hirschmann, M., and Bell, D. (2003). Hydrogen concentration analyses using SIMS and FTIR: comparison and calibration for nominally anhydrous minerals. *Geochemistry, Geophysics, Geosystems*, 4(2).

Kogiso, T., Hirose, K., and Takahashi, E. (1998). Melting experiments on homogeneous mixtures of peridotite and basalt: application to the genesis of ocean island basalts. *Earth and Planetary Science Letters*, 162(1-4):45–61.

Kogiso, T., Hirschmann, M., and Pertermann, M. (2004). High-pressure partial melting of mafic lithologies in the mantle. *Journal of Petrology*, 45(12):2407–2422.

Kogiso, T., Hirschmann, M. M., and Frost, D. J. (2003). High-pressure partial melting of garnet pyroxenite: possible mafic lithologies in the source of ocean island basalts. *Earth and Planetary Science Letters*, 216(4):603–617.

Kogiso, T., Tatsumi, Y., and Nakano, S. (1997). Trace element transport during dehydration processes in the subducted oceanic crust: 1. Experiments and implications for the origin of ocean island basalts. *Earth and Planetary Science Letters*, 148(1-2):193–205.

Kokfelt, T. F., Hoernle, K., Hauff, F., Fiebig, J., Werner, R., and Garbe-Schoenberg, D. (2006). Combined trace element and Pb-Nd–Sr-O isotope evidence for recycled oceanic crust (upper and lower) in the Iceland mantle plume. *Journal of Petrology*, 47(9):1705–1749.

Koleszar, A., Saal, A., Hauri, E., Nagle, A., Liang, Y., and Kurz, M. (2009). The volatile contents of the Galapagos plume; evidence for H_2O and F open system behavior in melt inclusions. *Earth and Planetary Science Letters*, 287(3):442–452.

Koornneef, J. M., Stracke, A., Bourdon, B., and Grönvold, K. (2012). The influence of source heterogeneity on the U–Th–Pa–Ra disequilibria in post-glacial tholeiites from Iceland. *Geochimica et cosmochimica acta*, 87:243–266.

Kurz, M. D., Jenkins, W. J., Hart, S. R., and Clague, D. (1983). Helium isotopic variations in volcanic rocks from Loihi Seamount and the Island of Hawaii. *Earth and Planetary Science Letters*, 66:388–406.

Lambart, S., Laporte, D., and Schiano, P. (2009). An experimental study of pyroxenite partial melts at 1 and 1.5 GPa: Implications for the major-element composition of mid-ocean ridge basalts. *Earth and Planetary Science Letters*, 288(1-2):335–347.

Le Maitre, R. W., Streckeisen, A., Zanettin, B., Le Bas, M., Bonin, B., and Bateman, P. (2005). *Igneous rocks: a classification and glossary of terms: recommendations of the International Union of Geological Sciences Subcommission on the Systematics of Igneous Rocks*. Cambridge University Press.

le Roux, P. J., Shirey, S. B., Hauri, E. H., Perfit, M. R., and Bender, J. F. (2006). The effects of variable sources, processes and contaminants on the composition of northern EPR MORB (8–10°N and 12–14°N): evidence from volatiles (H_2O, CO_2, S) and halogens (F, Cl). *Earth and Planetary Science Letters*, 251(3):209–231.

Le Voyer, M., Cottrell, E., Kelley, K. A., Brounce, M., and Hauri, E. H. (2015). The effect of primary versus secondary processes on the volatile content of MORB glasses: An example from the equatorial mid-atlantic ridge (5°N–3°S). *Journal of Geophysical Research: Solid Earth*, 120(1):125–144.

Le Voyer, M., Kelley, K., Cottrell, E., and Hauri, E. (2017). Heterogeneity in mantle carbon content from CO_2-undersaturated basalts. *Nature communications*, 8:14062.

Lee, P. M. (2012). *Bayesian statistics: an introduction*. John Wiley & Sons.

Liu, C.-Z., Snow, J. E., Hellebrand, E., Brügmann, G., Von Der Handt, A., Büchl, A., and Hofmann, A. W. (2008). Ancient, highly heterogeneous mantle beneath Gakkel ridge, Arctic Ocean. *Nature*, 452(7185):311.

Lundstrom, C., Sampson, D., Perfit, M., Gill, J., and Williams, Q. (1999). Insights into mid-ocean ridge basalt petrogenesis: U-series disequilibria from the Siqueiros Transform, Lamont Seamounts, and East Pacific Rise. *Journal of Geophysical Research: Solid Earth*, 104(B6):13035–13048.

Maaløe, S. and Jakobsson, S. P. (1980). The pt phase relations of a primary oceanite from the Reykjanes peninsula, Iceland. *Lithos*, 13(3):237–246.

Mackwell, S. J. and Kohlstedt, D. L. (1990). Diffusion of hydrogen in olivine: implications for water in the mantle. *Journal of Geophysical Research: Solid Earth*, 95(B4):5079–5088.

Maclennan, J. (2008a). Concurrent mixing and cooling of melts under iceland. *Journal of Petrology*, 49(11):1931–1953.

Maclennan, J. (2008b). Lead isotope variability in olivine-hosted melt inclusions from Iceland. *Geochimica et Cosmochimica Acta*, 72(16):4159–4176.

Maclennan, J. (2017). Bubble formation and decrepitation control the CO_2 content of olivine-hosted melt inclusions. *Geochemistry, Geophysics, Geosystems*, 18(2):597–616.

Maclennan, J. (2019). Mafic tiers and transient mushes: evidence from Iceland. *Philosophical Transactions of the Royal Society A*, 377(2139):20180021.

Maclennan, J., McKenzie, D., and Gronvöld, K. (2001a). Plume-driven upwelling under central Iceland. *Earth and Planetary Science Letters*, 194(1):67–82.

Maclennan, J., McKenzie, D., Grönvold, K., Shimizu, N., Eiler, J., and Kitchen, N. (2003a). Melt mixing and crystallization under Theistareykir, northeast Iceland. *Geochemistry, Geophysics, Geosystems*, 4(11).

Maclennan, J., McKenzie, D., Gronvöld, K., and Slater, L. (2001b). Crustal accretion under northern Iceland. *Earth and Planetary Science Letters*, 191(3):295–310.

Maclennan, J., McKenzie, D., Hilton, F., Gronvöld, K., and Shimizu, N. (2003b). Geochemical variability in a single flow from northern Iceland. *Journal of Geophysical Research: Solid Earth*, 108(B1).

Macpherson, C. G., Hilton, D. R., Day, J. M., Lowry, D., and Grönvold, K. (2005). High-$^3He/^4He$, depleted mantle and low-$\delta^{18}O$, recycled oceanic lithosphere in the source of central Iceland magmatism. *Earth and Planetary Science Letters*, 233(3):411–427.

Mallik, A. and Dasgupta, R. (2012). Reaction between MORB-eclogite derived melts and fertile peridotite and generation of ocean island basalts. *Earth and Planetary Science Letters*, 329:97–108.

Manga, M. (2010). Low-viscosity mantle blobs are sampled preferentially at regions of surface divergence and stirred rapidly into the mantle. *Physics of the Earth and Planetary Interiors*, 180(1-2):104–107.

Marty, B. (1995). Nitrogen content of the mantle inferred from N_2–Ar correlation in oceanic basalts. *Nature*, 377(6547):326.

Marty, B. (2012). The origins and concentrations of water, carbon, nitrogen and noble gases on earth. *Earth and Planetary Science Letters*, 313:56–66.

Marty, B. and Dauphas, N. (2003). The nitrogen record of crust–mantle interaction and mantle convection from archean to present. *Earth and Planetary Science Letters*, 206(3):397–410.

Marty, B. and Tolstikhin, I. N. (1998). CO_2 fluxes from mid-ocean ridges, arcs and plumes. *Chemical Geology*, 145(3):233–248.

Marty, B. and Zimmermann, L. (1999). Volatiles (He, C, N, Ar) in mid-ocean ridge basalts: Assesment of shallow-level fractionation and characterization of source composition. *Geochimica et Cosmochimica Acta*, 63(21):3619–3633.

Matzen, A. K., Baker, M. B., Beckett, J. R., and Stolper, E. M. (2013). The temperature and pressure dependence of nickel partitioning between olivine and silicate melt. *Journal of Petrology*, 54(12):2521–2545.

Matzen, A. K., Baker, M. B., Beckett, J. R., Wood, B. J., and Stolper, E. M. (2017a). The effect of liquid composition on the partitioning of Ni between olivine and silicate melt. *Contributions to Mineralogy and Petrology*, 172(1):3.

Matzen, A. K., Wood, B. J., Baker, M. B., and Stolper, E. M. (2017b). The roles of pyroxenite and peridotite in the mantle sources of oceanic basalts. *Nature Geoscience*, 10(7):530.

McDonough, W. F. and Sun, S.-S. (1995). The composition of the earth. *Chemical geology*, 120(3-4):223–253.

McGovern, P. J. and Schubert, G. (1989). Thermal evolution of the Earth: effects of volatile exchange between atmosphere and interior. *Earth and planetary science letters*, 96(1-2):27–37.

McKenzie, D. (1984). The generation and compaction of partially molten rock. *Journal of petrology*, 25(3):713–765.

McKenzie, D. (1985). ^{230}Th ^{238}U disequilibrium and the melting processes beneath ridge axes. *Earth and Planetary Science Letters*, 72(2-3):149–157.

McKenzie, D. (2000). Constraints on melt generation and transport from U-series activity ratios. *Chemical Geology*, 162(2):81–94.

McKenzie, D. and Bickle, M. (1988). The volume and composition of melt generated by extension of the lithosphere. *Journal of petrology*, 29(3):625–679.

McKenzie, D. and O'Nions, R. (1991). Partial melt distributions from inversion of rare earth element concentrations. *Journal of Petrology*, 32(5):1021–1091.

McKenzie, D. and O'Nions, R. K. (1995). The source regions of ocean island basalts. *Journal of petrology*, 36(1):133–159.

McKenzie, D., Stracke, A., Blichert-Toft, J., Albarède, F., Grönvold, K., and O'Nions, R. K. (2004). Source enrichment processes responsible for isotopic anomalies in oceanic island basalts 1. *Geochimica et Cosmochimica Acta*, 68(12):2699–2724.

Métrich, N., Zanon, V., Créon, L., Hildenbrand, A., Moreira, M., and Marques, F. O. (2014). Is the 'Azores hotspot' a wetspot? Insights from the geochemistry of fluid and melt inclusions in olivine of Pico basalts. *Journal of Petrology*, 55(2):377–393.

Michael, P. (1995). Regionally distinctive sources of depleted MORB: Evidence from trace elements and H_2O. *Earth and Planetary Science Letters*, 131(3-4):301–320.

Michael, P. J. and Graham, D. W. (2015). The behavior and concentration of CO_2 in the suboceanic mantle: inferences from undegassed ocean ridge and ocean island basalts. *Lithos*, 236:338–351.

Moore, J. G. (1965). Petrology of deep sea basalt near Hawaii. *American Journal of Science*, 263(1):40–52.

Moore, J. G. (1979). Vesicularity and CO_2 in mid-ocean ridge basalt. *Nature*, 282(5736):250.

Murton, B. (1995). RSS Charles Darwin Cruise 80, 01 September to 01 October 1993. *The PETROS programme: geologic sampling and bathymetric surveying of the Reykjanes Ridge between*, 57.

Murton, B. J., Taylor, R. N., and Thirlwall, M. F. (2002). Plume–ridge interaction: a geochemical perspective from the Reykjanes Ridge. *Journal of Petrology*, 43(11):1987–2012.

Neave, D. A., Maclennan, J., Edmonds, M., and Thordarson, T. (2014). Melt mixing causes negative correlation of trace element enrichment and CO_2 content prior to an Icelandic eruption. *Earth and Planetary Science Letters*, 400:272–283.

Neave, D. A. and Putirka, K. D. (2017). A new clinopyroxene-liquid barometer, and implications for magma storage pressures under Icelandic rift zones. *American Mineralogist*, 102(4):777–794.

Neave, D. A., Shorttle, O., Oeser, M., Weyer, S., and Kobayashi, K. (2018). Mantle-derived trace element variability in olivines and their melt inclusions. *Earth and Planetary Science Letters*, 483:90–104.

Nichols, A., Carroll, M., and Höskuldsson, A. (2002). Is the Iceland hot spot also wet? Evidence from the water contents of undegassed submarine and subglacial pillow basalts. *Earth and Planetary Science Letters*, 202(1):77–87.

Nicholson, H., Condomines, M., Fitton, J. G., Fallick, A. E., Grönvold, K., and Rogers, G. (1991). Geochemical and isotopic evidence for crustal assimilation beneath Krafla, Iceland. *Journal of Petrology*, 32(5):1005–1020.

O'Nions, R., Hamilton, P., and Evensen, N. (1977). Variations in $^{143}Nd/^{144}Nd$ and $^{87}Sr/^{86}Sr$ ratios in oceanic basalts. *Earth and Planetary Science Letters*, 34(1):13–22.

Öskarsson, N., Helgason, Ö., and Steinthórsson, S. (1994). Oxidation state of iron in mantle-derived magmas of the Icelandic rift zone. *Hyperfine Interactions*, 91(1):733–737.

Ozima, M. and Podosek, F. A. (2002). *Noble gas geochemistry*. Cambridge University Press.

Palme, H. and O'Neill, H. S. C. (2003). Cosmochemical estimates of mantle composition. *Treatise on geochemistry*, 2:568.

Parai, R. and Mukhopadhyay, S. (2012). How large is the subducted water flux? New constraints on mantle regassing rates. *Earth and Planetary Science Letters*, 317:396–406.

Parks, M. M., Caliro, S., Chiodini, G., Pyle, D. M., Mather, T. A., Berlo, K., Edmonds, M., Biggs, J., Nomikou, P., and Raptakis, C. (2013). Distinguishing contributions to diffuse CO_2 emissions in volcanic areas from magmatic degassing and thermal decarbonation using soil gas ^{222}Rn–$\delta^{13}C$ systematics: Application to Santorini volcano, Greece. *Earth and Planetary Science Letters*, 377:180–190.

Pearson, D., Brenker, F., Nestola, F., McNeill, J., Nasdala, L., Hutchison, M., Matveev, S., Mather, K., Silversmit, G., Schmitz, S., et al. (2014). Hydrous mantle transition zone indicated by ringwoodite included within diamond. *Nature*, 507(7491):221.

Pearson, D., Canil, D., and Shirey, S. (2003). Mantle samples included in volcanic rocks: xenoliths and diamonds. *Treatise on geochemistry*, 2:568.

Peate, D. W., Baker, J. A., Jakobsson, S. P., Waight, T. E., Kent, A. J., Grassineau, N. V., and Skovgaard, A. C. (2009). Historic magmatism on the Reykjanes peninsula, Iceland: a snap-shot of melt generation at a ridge segment. *Contributions to Mineralogy and Petrology*, 157(3):359.

Peate, D. W., Breddam, K., Baker, J. A., Kurz, M. D., Barker, A. K., Prestvik, T., Grassineau, N., and Skovgaard, A. C. (2010). Compositional characteristics and spatial distribution of enriched Icelandic mantle components. *Journal of Petrology*, 51(7):1447–1475.

Perfit, M. R., Fornari, D., Ridley, W., Kirk, P., Casey, J., Kastens, K., Reynolds, J., Edwards, M., Desonie, D., Shuster, R., et al. (1996). Recent volcanism in the Siqueiros transform fault: picritic basalts and implications for MORB

magma genesis. *Earth and Planetary Science Letters*, 141(1-4):91–108.

Pertermann, M. and Hirschmann, M. M. (2003). Partial melting experiments on a MORB-like pyroxenite between 2 and 3 GPa: Constraints on the presence of pyroxenite in basalt source regions from solidus location and melting rate. *Journal of Geophysical Research: Solid Earth*, 108(B2).

Peterson, M., Saal, A., Kurz, M., Hauri, E., Blusztajn, J., Harpp, K., Werner, R., and Geist, D. (2017). Submarine basaltic glasses from the Galapagos Archipelago: determining the volatile budget of the mantle plume. *Journal of Petrology*, 58(7):1419–1450.

Phipps Morgan, J. (2001). Thermodynamics of pressure release melting of a veined plum pudding mantle. *Geochemistry, Geophysics, Geosystems*, 2(4).

Pineau, F. and Javoy, M. (1983). Carbon isotopes and concentrations in mid-oceanic ridge basalts. *Earth and Planetary Science Letters*, 62(2):239–257.

Plank, T. (2014). The chemical composition of subducting sediments. *Treatise on geochemistry*, 4:607–629.

Porcelli, D. and Ballentine, C. J. (2002). Models for distribution of terrestrial noble gases and evolution of the atmosphere. *Reviews in Mineralogy and Geochemistry*, 47(1):411–480.

Poreda, R., Schilling, J., and Craig, H. (1986). Helium and hydrogen isotopes in ocean-ridge basalts north and south of Iceland. *Earth and Planetary Science Letters*, 78(1):1–17.

Prytulak, J. and Elliott, T. (2009). Determining melt productivity of mantle sources from ^{238}U–^{230}Th and ^{235}U–^{231}Pa disequilibria; an example from Pico Island, Azores. *Geochimica et Cosmochimica Acta*, 73(7):2103–2122.

Putirka, K. (2008a). Excess temperatures at ocean islands: Implications for mantle layering and convection. *Geology*, 36(4):283–286.

Putirka, K. (2016). Rates and styles of planetary cooling on Earth, Moon, Mars, and Vesta, using new models for oxygen fugacity, ferric-ferrous ratios, olivine-liquid Fe-Mg exchange, and mantle potential temperature. *American Mineralogist*, 101(4):819–840.

Putirka, K. D. (2005). Mantle potential temperatures at Hawaii, Iceland, and the mid-ocean ridge system, as inferred from olivine phenocrysts: Evidence for thermally driven mantle plumes. *Geochemistry, Geophysics, Geosystems*, 6(5).

Putirka, K. D. (2008b). Thermometers and barometers for volcanic systems. *Reviews in mineralogy and geochemistry*, 69(1):61–120.

Putirka, K. D., Perfit, M., Ryerson, F., and Jackson, M. G. (2007). Ambient and excess mantle temperatures, olivine thermometry, and active vs. passive upwelling. *Chemical Geology*, 241(3-4):177–206.

Qin, Z., Lu, F., and Anderson, A. T. (1992). Diffusive reequilibration of melt and fluid inclusions. *American Mineralogist*, 77(5-6):565–576.

Regelous, M., Hofmann, A., Abouchami, W., and Galer, S. (2003). Geochemistry of lavas from the Emperor Seamounts, and the geochemical evolution of Hawaiian magmatism from 85 to 42 Ma. *Journal of Petrology*, 44(1):113–140.

Roeder, P. and Emslie, R. (1970). Olivine-liquid equilibrium. *Contributions to mineralogy and petrology*, 29(4):275–289.

Rosenthal, A., Hauri, E., and Hirschmann, M. (2015). Experimental determination of C, F, and H partitioning between mantle minerals and carbonated basalt, CO_2/Ba and CO_2/Nb systematics of partial melting, and the CO_2 contents of basaltic source regions. *Earth and Planetary Science Letters*, 412:77–87.

Rudge, J. F., Maclennan, J., and Stracke, A. (2013). The geochemical consequences of mixing melts from a heterogeneous mantle. *Geochimica et Cosmochimica Acta*, 114:112–143.

Saal, A., Hart, S., Shimizu, N., Hauri, E., and Layne, G. (1998). Pb isotopic variability in melt inclusions from oceanic island basalts, Polynesia. *Science*, 282(5393):1481–1484.

Saal, A. E., Hauri, E. H., Langmuir, C. H., and Perfit, M. R. (2002). Vapour undersaturation in primitive mid-ocean-ridge basalt and the volatile content of Earth's upper mantle. *Nature*, 419(6906):451.

Sæmundsson, K. (1979). Outline of the geology of Iceland. *Jokull*, 29:7–28.

Sæmundsson, K. (1991). Geology of the Krafla system. *The Natural History of Lake Myvatn*, pages 24–95.

Sæmundsson, K., Hjartarson, Á., Kaldal, I., Sigurgeirsson, M., Kristinsson, S., and Vikingsson, S. (2012). Geological map of the Northern volcanic zone, Iceland. *Northern part*, 1(100.000).

Saemundsson, K., Jóhannesson, H., Hjartarson, Á., Kristinsson, S. G., and Sigurgeirsson, M. (2010). Geological map of southwest Iceland, 1: 100.000. *Iceland GeoSurvey*.

Salters, V. J. and Stracke, A. (2004). Composition of the depleted mantle. *Geochemistry, Geophysics, Geosystems*, 5(5).

Samuel, H. and Farnetani, C. G. (2003). Thermochemical convection and helium concentrations in mantle plumes. *Earth and Planetary Science Letters*, 207(1-4):39–56.

Sarafian, E., Gaetani, G. A., Hauri, E. H., and Sarafian, A. R. (2017). Experimental constraints on the damp peridotite solidus and oceanic mantle potential temperature. *Science*, 355(6328):942–945.

Sarda, P. and Graham, D. (1990). Mid-ocean ridge popping rocks: implications for degassing at ridge crests. *Earth and Planetary Science Letters*, 97(3-4):268–289.

Schilling, J.-G., Kingsley, R., Fontignie, D., Poreda, R., and Xue, S. (1999). Dispersion of the Jan Mayen and Iceland mantle plumes in the Arctic: A He-Pb-Nd-Sr isotope tracer study of basalts from the Kolbeinsey, Mohns, and Knipovich ridges. *Journal of Geophysical Research: Solid Earth*, 104(B5):10543–10569.

Schipper, C. I., Le Voyer, M., Moussallam, Y., White, J. D., Thordarson, T., Kimura, J.-I., and Chang, Q. (2016). Degassing and magma mixing during the eruption of Surtsey Volcano (Iceland, 1963–1967): the signatures of a dynamic and discrete rift propagation event. *Bulletin of Volcanology*, 78(4):33.

Schneider, C. A., Rasband, W. S., and Eliceiri, K. W. (2012). NIH Image to ImageJ: 25 years of image analysis. *Nature methods*, 9(7):671.

Shaw, A. M., Behn, M. D., Humphris, S. E., Sohn, R. A., and Gregg, P. M. (2010). Deep pooling of low degree melts and volatile fluxes at the 85°E segment of the Gakkel Ridge: Evidence from olivine-hosted melt inclusions and glasses. *Earth and Planetary Science Letters*, 289(3):311–322.

Shcheka, S. S. and Keppler, H. (2012). The origin of the terrestrial noble-gas signature. *Nature*, 490(7421):531.

Shimizu, K., Saal, A. E., Myers, C. E., Nagle, A. N., Hauri, E. H., Forsyth, D. W., Kamenetsky, V. S., and Niu, Y. (2016). Two-component mantle melting-mixing model for the generation of mid-ocean ridge basalts: implications for the volatile content of the Pacific upper mantle. *Geochimica et Cosmochimica Acta*, 176:44–80.

Shishkina, T., Botcharnikov, R., Holtz, F., Almeev, R., and Portnyagin, M. V. (2010). Solubility of H_2O-and CO_2-bearing fluids in tholeiitic basalts at pressures up to 500 MPa. *Chemical Geology*, 277(1-2):115–125.

Shishkina, T. A., Botcharnikov, R. E., Holtz, F., Almeev, R. R., Jazwa, A. M., and Jakubiak, A. A. (2014). Compositional and pressure effects on the solubility of H_2O and CO_2 in mafic melts. *Chemical Geology*, 388:112–129.

Shorttle, O. (2015). Geochemical variability in MORB controlled by concurrent mixing and crystallisation. *Earth and Planetary Science Letters*, 424:1–14.

Shorttle, O. and Maclennan, J. (2011). Compositional trends of Icelandic basalts: Implications for short–length scale lithological heterogeneity in mantle plumes. *Geochemistry, Geophysics, Geosystems*, 12(11).

Shorttle, O., Maclennan, J., and Jones, S. (2010). Control of the symmetry of plume-ridge interaction by spreading ridge geometry. *Geochemistry, Geophysics, Geosystems*, 11(7).

Shorttle, O., Maclennan, J., and Lambart, S. (2014). Quantifying lithological variability in the mantle. *Earth and Planetary Science Letters*, 395:24–40.

Shorttle, O., Maclennan, J., and Piotrowski, A. M. (2013). Geochemical provincialism in the Iceland plume. *Geochimica et Cosmochimica Acta*, 122:363–397.

Shorttle, O., Moussallam, Y., Hartley, M. E., Maclennan, J., Edmonds, M., and Murton, B. J. (2015). Fe-XANES analyses of Reykjanes Ridge basalts: Implications for oceanic crust's role in the solid Earth oxygen cycle. *Earth and Planetary Science Letters*, 427:272–285.

Shorttle, O., Rudge, J. F., Maclennan, J., and Rubin, K. H. (2016). A statistical description of concurrent mixing and crystallization during MORB differentiation: implications for trace element enrichment. *Journal of Petrology*, 57(11-12):2127–2162.

Sides, I., Edmonds, M., Maclennan, J., Swanson, D., and Houghton, B. (2014). Eruption style at Kīlauea volcano in Hawai'i linked to primary melt composition. *Nature Geoscience*, 7(6):464.

Sigmarsson, O. and Halldórsson, S. A. (2015). Delimiting Bárðarbunga and Askja volcanic systems with Sr-and Nd-isotope ratios. *Jökull*, 65:17–27.

Simons, K., Dixon, J., Schilling, J.-G., Kingsley, R., and Poreda, R. (2002). Volatiles in basaltic glasses from the Easter-Salas y Gomez Seamount Chain and Easter Microplate: Implications for geochemical cycling of volatile elements. *Geochemistry, Geophysics, Geosystems*, 3(7):1–29.

Sims, K. W., Maclennan, J., Blichert-Toft, J., Mervine, E. M., Blusztajn, J., and Grönvold, K. (2013). Short length scale mantle heterogeneity beneath Iceland probed by glacial modulation of melting. *Earth and Planetary Science Letters*, 379:146–157.

Skovgaard, A. C., Storey, M., Baker, J., Blusztajn, J., and Hart, S. R. (2001). Osmium–oxygen isotopic evidence for a recycled and strongly depleted component in the Iceland mantle plume. *Earth and Planetary Science Letters*, 194(1):259–275.

Slater, L., McKenzie, D., Grönvold, K., and Shimizu, N. (2001). Melt generation and movement beneath Theistareykir, NE Iceland. *Journal of Petrology*, 42(2):321–354.

Sleep, N. H. (1984). Tapping of magmas from ubiquitous mantle heterogeneities: an alternative to mantle plumes? *Journal of Geophysical Research: Solid Earth*, 89(B12):10029–10041.

Sleep, N. H. (2009). Stagnant lid convection and carbonate metasomatism of the deep continental lithosphere. *Geochemistry, Geophysics, Geosystems*, 10(11).

Smith, P. M. and Asimow, P. D. (2005). Adiabat_1ph: A new public front-end to the MELTS, pMELTS, and pHMELTS models. *Geochemistry, Geophysics, Geosystems*, 6(2).

Sobolev, A. (1996). Melt inclusions in minerals as a source of principle petrological information. *Petrology*, 4(3):209–220.

Sobolev, A., Gurenko, A., and Shimizu, N. (1994). Ultra-depleted melts from Iceland: data from melt inclusion studies. *Mineral Mag A*, 58:860–861.

Sobolev, A. V. and Chaussidon, M. (1996). H_2O concentrations in primary melts from supra-subduction zones and mid-ocean ridges: implications for H_2O storage and recycling in the mantle. *Earth and Planetary Science Letters*, 137(1-4):45–55.

Sobolev, A. V., Hofmann, A. W., Brügmann, G., Batanova, V. G., and Kuzmin, D. V. (2008). A quantitative link between recycling and osmium isotopes. *Science*, 321(5888):536–536.

Sobolev, A. V., Hofmann, A. W., Kuzmin, D. V., Yaxley, G. M., Arndt, N. T., Chung, S.-L., Danyushevsky, L. V., Elliott, T., Frey, F. A., Garcia, M. O., et al. (2007). The amount of recycled crust in sources of mantle-derived melts. *science*, 316(5823):412–417.

Sobolev, A. V., Hofmann, A. W., Sobolev, S. V., and Nikogosian, I. K. (2005). An olivine-free mantle source of Hawaiian shield basalts. *Nature*, 434(7033):590.

Sohn, R. A. (2013). A method for inverting ratio–ratio data to estimate end-member compositions in mixing problems. *Chemical Geology*, 352:63–69.

Spandler, C. and O'Neill, H. S. C. (2010). Diffusion and partition coefficients of minor and trace elements in San Carlos olivine at 1,300°C with some geochemical implications. *Contributions to Mineralogy and Petrology*, 159(6):791–818.

Spice, H. E., Fitton, J. G., and Kirstein, L. A. (2016). Temperature fluctuation of the Iceland mantle plume through time. *Geochemistry, Geophysics, Geosystems*, 17(2):243–254.

Spiegelman, M. and Kelemen, P. B. (2003). Extreme chemical variability as a consequence of channelized melt transport. *Geochemistry, Geophysics, Geosystems*, 4(7).

Stachel, T. (2001). Diamonds from the asthenosphere and the transition zone. *European Journal of Mineralogy*, 13(5):883–892.

Stalder, R., Foley, S., Brey, G., and Horn, I. (1998). Mineral-aqueous fluid partitioning of trace elements at 900–1200°C and 3.0–5.7 GPa: new experimental data for garnet, clinopyroxene, and rutile, and implications for mantle metasomatism. *Geochimica et Cosmochimica Acta*, 62(10):1781–1801.

Starkey, N. A., Stuart, F. M., Ellam, R. M., Fitton, J. G., Basu, S., and Larsen, L. M. (2009). Helium isotopes in early Iceland plume picrites: Constraints on the composition of high ^{3}He/^{4}He mantle. *Earth and Planetary Science Letters*, 277(1):91–100.

Steinberger, B. and Antretter, M. (2006). Conduit diameter and buoyant rising speed of mantle plumes: Implications for the motion of hot spots and shape of plume conduits. *Geochemistry, Geophysics, Geosystems*, 7(11).

Stolper, E. and Asimow, P. (2007). Insights into mantle melting from graphical analysis of one-component systems. *American Journal of Science*, 307(8):1051–1139.

Stolper, E. and Holloway, J. R. (1988). Experimental determination of the solubility of carbon dioxide in molten basalt at low pressure. *Earth and Planetary Science Letters*, 87(4):397–408.

Stracke, A., Bizimis, M., and Salters, V. J. (2003a). Recycling oceanic crust: Quantitative constraints. *Geochemistry, Geophysics, Geosystems*, 4(3).

Stracke, A., Hofmann, A. W., and Hart, S. R. (2005). FOZO, HIMU, and the rest of the mantle zoo. *Geochemistry, Geophysics, Geosystems*, 6(5).

Stracke, A., Snow, J. E., Hellebrand, E., Von Der Handt, A., Bourdon, B., Birbaum, K., and Günther, D. (2011). Abyssal peridotite Hf isotopes identify extreme mantle depletion. *Earth and Planetary Science Letters*, 308(3):359–368.

Stracke, A., Zindler, A., Salters, V. J., McKenzie, D., Blichert-Toft, J., Albarède, F., and Grönvold, K. (2003b). Theistareykir revisited. *Geochemistry, Geophysics, Geosystems*, 4(2).

Stuart, F. M., Lass-Evans, S., Fitton, J. G., and Ellam, R. M. (2003). High ^{3}He/^{4}He ratios in picritic basalts from Baffin Island and the role of a mixed reservoir in mantle plumes. *Nature*, 424(6944):57.

Su, Y. (2003). Global MORB chemistry compilation at the segment scale. *Ph. D. Thesis, Department of Earth and Environmental Sciences, Columbia University*.

Sverjensky, D. A., Harrison, B., and Azzolini, D. (2014). Water in the deep Earth: the dielectric constant and the solubilities of quartz and corundum to 60 kb and 1200°C. *Geochimica et Cosmochimica Acta*, 129:125–145.

Sweeney, R., Prozesky, V., and Przybylowicz, W. (1995). Selected trace and minor element partitioning between peridotite minerals and carbonatite melts at 18–46 kb pressure. *Geochimica et Cosmochimica Acta*, 59(18):3671–3683.

Syracuse, E. M., van Keken, P. E., and Abers, G. A. (2010). The global range of subduction zone thermal models. *Physics of the Earth and Planetary Interiors*, 183(1-2):73–90.

Tackley, P. J. (1998). Thermo-chemical basal boundary layer: D"? *The core-mantle boundary region*, page 231.

Tenner, T. J., Hirschmann, M. M., Withers, A. C., and Hervig, R. L. (2009). Hydrogen partitioning between nominally anhydrous upper mantle minerals and melt between 3 and 5 GPa and applications to hydrous peridotite partial melting. *Chemical Geology*, 262(1-2):42–56.

Thirlwall, M., Gee, M., Taylor, R., and Murton, B. (2004). Mantle components in Iceland and adjacent ridges investigated using double-spike Pb isotope ratios. *Geochimica et Cosmochimica Acta*, 68(2):361–386.

Thomson, A., Kohn, S., Bulanova, G., Smith, C., Araujo, D., Walter, M., et al. (2014). Origin of sub-lithospheric diamonds from the Juina-5 kimberlite (Brazil): constraints from carbon isotopes and inclusion compositions. *Contributions to Mineralogy and Petrology*, 168(6):1081.

Thomson, A. and Maclennan, J. (2012). The distribution of olivine compositions in Icelandic basalts and picrites. *Journal of Petrology*, 54(4):745–768.

Thomson, A. R., Walter, M. J., Kohn, S. C., and Brooker, R. A. (2016). Slab melting as a barrier to deep carbon subduction. *Nature*, 529(7584):76.

Thordarson, T. and Höskuldsson, Á. (2014). *Iceland*. Dunedin Academic Press Ltd.

Trampert, J., Deschamps, F., Resovsky, J., and Yuen, D. (2004). Probabilistic tomography maps chemical heterogeneities throughout the lower mantle. *Science*, 306(5697):853–856.

Trela, J., Gazel, E., Sobolev, A. V., Moore, L., Bizimis, M., Jicha, B., and Batanova, V. G. (2017). The hottest lavas of the Phanerozoic and the survival of deep Archaean reservoirs. *Nature Geoscience*, 10(6):451.

Trela, J., Vidito, C., Gazel, E., Herzberg, C., Class, C., Whalen, W., Jicha, B., Bizimis, M., and Alvarado, G. E. (2015). Recycled crust in the Galápagos plume source at 70 Ma: Implications for plume evolution. *Earth and Planetary Science Letters*, 425:268–277.

Trull, T. and Kurz, M. (1993). Experimental measurements of ^{3}He and ^{4}He mobility in olivine and clinopyroxene at magmatic temperatures. *Geochimica et cosmochimica acta*, 57(6):1313–1324.

Trull, T., Nadeau, S., Pineau, F., Polve, M., and Javoy, M. (1993). C-He systematics in hotspot xenoliths: Implications for mantle carbon contents and carbon recycling. *Earth and Planetary Science Letters*, 118(1-4):43–64.

Tucker, J. M., Mukhopadhyay, S., and Gonnermann, H. M. (2018). Reconstructing mantle carbon and noble gas contents from degassed mid-ocean ridge basalts. *Earth and Planetary Science Letters*, 496:108–119.

Turcotte, D. and Schubert, G. (2014). *Geodynamics*. Cambridge University Press.

Ulrich, M., Hémond, C., Nonnotte, P., and Jochum, K. P. (2012). OIB/seamount recycling as a possible process for E-MORB genesis. *Geochemistry, Geophysics, Geosystems*, 13(6).

Van der Hilst, R. D., Widiyantoro, S., and Engdahl, E. (1997). Evidence for deep mantle circulation from global tomography. *Nature*, 386(6625):578.

van Keken, P. E., Hauri, E. H., and Ballentine, C. J. (2002). Mantle mixing: The generation, preservation, and destruction of chemical heterogeneity. *Annual Review of Earth and Planetary Sciences*, 30(1):493–525.

Van Westrenen, W., Blundy, J., and Wood, B. (1999). Crystal-chemical controls on trace element partitioning between garnet and anhydrous silicate melt. *American Mineralogist*, 84(5-6):838–847.

Vidito, C., Herzberg, C., Gazel, E., Geist, D., and Harpp, K. (2013). Lithological structure of the Galápagos plume. *Geochemistry, Geophysics, Geosystems*, 14(10):4214–4240.

Vink, G. E. (1984). A hotspot model for Iceland and the Vøring Plateau. *Journal of Geophysical Research: Solid Earth*, 89(B12):9949–9959.

Walker, J. C., Hays, P., and Kasting, J. F. (1981). A negative feedback mechanism for the long-term stabilization of Earth's surface temperature. *Journal of Geophysical Research: Oceans*, 86(C10):9776–9782.

Wallace, P. J. (1998). Water and partial melting in mantle plumes: Inferences from the dissolved H_2O concentrations of Hawaiian basaltic magmas. *Geophysical Research Letters*, 25(19):3639–3642.

Walter, M., Kohn, S., Araujo, D., Bulanova, G., Smith, C., Gaillou, E., Wang, J., Steele, A., and Shirey, S. (2011). Deep mantle cycling of oceanic crust: evidence from diamonds and their mineral inclusions. *Science*, page 1209300.

Walter, M., Nakamura, E., Trønnes, R., and Frost, D. (2004). Experimental constraints on crystallization differentiation in a deep magma ocean. *Geochimica et Cosmochimica Acta*, 68(20):4267–4284.

Walter, M. J. (1998). Melting of garnet peridotite and the origin of komatiite and depleted lithosphere. *Journal of Petrology*, 39(1):29–60.

Wan, Z., Coogan, L. A., and Canil, D. (2008). Experimental calibration of aluminum partitioning between olivine and spinel as a geothermometer. *American Mineralogist*, 93(7):1142–1147.

Wanamaker, B., Wong, T.-F., and Evans, B. (1990). Decrepitation and crack healing of fluid inclusions in San Carlos olivine. *Journal of Geophysical Research: Solid Earth*, 95(B10):15623–15641.

Wanless, V., Behn, M., Shaw, A., and Plank, T. (2014). Variations in melting dynamics and mantle compositions along the Eastern Volcanic Zone of the Gakkel Ridge: insights from olivine-hosted melt inclusions. *Contributions to Mineralogy and Petrology*, 167(5):1005.

Wanless, V. D. and Shaw, A. M. (2012). Lower crustal crystallization and melt evolution at mid-ocean ridges. *Nature Geoscience*, 5(9):651.

Wanless, V. D., Shaw, A. M., Behn, M. D., Soule, S. A., Escartin, J., and Hamelin, C. (2015). Magmatic plumbing at Lucky Strike volcano based on olivine-hosted melt inclusion compositions. *Geochemistry, Geophysics, Geosystems*, 16(1):126–147.

Warren, J. M. (2016). Global variations in abyssal peridotite compositions. *Lithos*, 248:193–219.

Watson, S. (1993). Rare earth element inversions and percolation models for Hawaii. *Journal of Petrology*, 34(4):763–783.

Watson, S. and McKenzie, D. (1991). Melt generation by plumes: a study of Hawaiian volcanism. *Journal of Petrology*, 32(3):501–537.

Werner, R., Schmincke, H.-U., and Sigvaldason, G. (1996). A new model for the evolution of table mountains: volcanological and petrological evidence from Herdubreid and Herdubreidartögl volcanoes (Iceland). *Geologische Rundschau*, 85(2):390.

White, R. and McKenzie, D. (1989). Magmatism at rift zones: the generation of volcanic continental margins and flood basalts. *Journal of Geophysical Research: Solid Earth*, 94(B6):7685–7729.

White, R. S., McKenzie, D., and O'Nions, R. K. (1992). Oceanic crustal thickness from seismic measurements and rare earth element inversions. *Journal of Geophysical Research: Solid Earth*, 97(B13):19683–19715.

White, W. M. and Hofmann, A. W. (1982). Sr and Nd isotope geochemistry of oceanic basalts and mantle evolution. *Nature*, 296(5860):821.

Wignall, P. B. (2001). Large igneous provinces and mass extinctions. *Earth-science reviews*, 53(1):1–33.

Winpenny, B. and Maclennan, J. (2011). A partial record of mixing of mantle melts preserved in icelandic phenocrysts. *Journal of Petrology*, 52(9):1791–1812.

Winpenny, B. and Maclennan, J. (2014). Short length scale oxygen isotope heterogeneity in the icelandic mantle: Evidence from plagioclase compositional zones. *Journal of Petrology*, 55(12):2537–2566.

Wood, B. J. and Blundy, J. D. (1997). A predictive model for rare earth element partitioning between clinopyroxene and anhydrous silicate melt. *Contributions to Mineralogy and Petrology*, 129(2-3):166–181.

Woodhead, J. D. and McCulloch, M. T. (1989). Ancient seafloor signals in Pitcairn Island lavas and evidence for large amplitude, small length-scale mantle heterogeneities. *Earth and Planetary Science Letters*, 94(3-4):257–273.

Workman, R. K. and Hart, S. R. (2005). Major and trace element composition of the depleted MORB mantle (DMM). *Earth and Planetary Science Letters*, 231(1):53–72.

Workman, R. K., Hauri, E., Hart, S. R., Wang, J., and Blusztajn, J. (2006). Volatile and trace elements in basaltic glasses from Samoa: Implications for water distribution in the mantle. *Earth and Planetary Science Letters*, 241(3):932–951.

Wyllie, P. J. and Huang, W.-L. (1975). Influence of mantle CO_2 in the generation of carbonatites and kimberlites. *Nature*, 257(5524):297.

Yamazaki, D. and Karato, S.-i. (2001). Some mineral physics constraints on the rheology and geothermal structure of Earth's lower mantle. *American Mineralogist*, 86(4):385–391.

Yasuda, A., Fujii, T., and Kurita, K. (1994). Melting phase relations of an anhydrous mid-ocean ridge basalt from 3 to 20 GPa: Implications for the behavior of subducted oceanic crust in the mantle. *Journal of Geophysical Research: Solid Earth*, 99(B5):9401–9414.

Yaxley, G. M. and Green, D. H. (1998). Reactions between eclogite and peridotite: mantle refertilisation by subduction of oceanic crust. *Schweiz. Mineral. Petrogr. Mitt*, 78(2):243–255.

Zindler, A., Staudigel, H., and Batiza, R. (1984). Isotope and trace element geochemistry of young pacific seamounts: implications for the scale of upper mantle heterogeneity. *Earth and Planetary Science Letters*, 70(2):175–195.

Zou, H. (2007). *Quantitative geochemistry*. Imperial college press.

Appendix A

Modelling melting behaviour along the Reykjanes Ridge.

In Chapter 7 I presented the results of two models. The first model calculates the effect of progressive depletion in an enriched pyroxenite fraction in the mantle Southwards along the ridge, in order to capture the essential predictions of a 'plume-outflow' model. The second model provides a simple calculation to simulate the effect of diminishing active upwelling along the ridge, in addition to progressive pyroxenite depletion. Neither model is expected to make quantitative predictions, but instead is designed to illustrate qualitatively the effects pyroxenite depletion and active upwelling might have. Here I present the mathematical formulation used to calculate these results.

A.1 Progressive pyroxenite depletion

The mass fraction of pyroxenite in the mantle, ϕ_{Px} is assumed to decrease away from Iceland according to exponential decay:

$$\phi_{\mathrm{Px}}(x) = \phi^0_{\mathrm{Px}} \exp\left(-\frac{x}{\lambda}\right) \tag{A.1}$$

where x is the distance away from Iceland, λ is the lengthscale of pyroxenite decay, and ϕ^0_{Px} is the mass fraction of pyroxenite at $x = 0$. Assuming batch melting of both the lherzolite and pyroxenite to produce melts with trace element concentrations of C_l^{Lz} and C_l^{Px}, the mixed melt will have a trace element concentration, C_l, of:

$$C_l = C_l^{\mathrm{Lz}}(1 - m_{\mathrm{Px}}) + C_l^{\mathrm{Lz}} m_{\mathrm{Px}} \tag{A.2}$$

where the mass fraction of pyroxenite melt, m_{Px}, is given by:

$$m_{\mathrm{Px}} = \frac{\phi_{\mathrm{Px}} F_{\mathrm{Px}}}{(1-\phi_{\mathrm{Px}})F_{\mathrm{Lz}} + \phi_{\mathrm{Px}} F_{\mathrm{Px}}} \tag{A.3}$$

F_{Lz} and F_{Px} are the melt fractions of the lherzolite and pyroxenite. The batch melting equation relates the concentration of an element in the melt, C_l^{Px} and C_l^{Lz}, to the source concentration, C_s^{Px} and C_s^{Lz}, to the element's partition coefficient, D, and the melt fraction:

$$C_l^{\mathrm{Px}} = \frac{C_s^{\mathrm{Px}}}{D(1-F_{\mathrm{Px}}) + F_{\mathrm{Px}}} \qquad C_l^{\mathrm{Lz}} = \frac{C_s^{\mathrm{Lz}}}{D(1-F_{\mathrm{Lz}}) + F_{\mathrm{Lz}}} \tag{A.4}$$

For melt fractions typical for melting beneath mid-ocean ridges, $\sim$0.2 (Chapter 3), $D \ll F$ for the most incompatible elements, we therefore make the approximation $D \to 0$:

$$C_l^{\mathrm{Px}} = \frac{C_s^{\mathrm{Px}}}{F_{\mathrm{Px}}} \qquad C_l^{\mathrm{Lz}} = \frac{C_s^{\mathrm{Lz}}}{F_{\mathrm{Lz}}} \tag{A.5}$$

Combining Equations A.2 and A.5:

$$C_l(x) = \frac{\phi_{\mathrm{Px}}(x) C_l^{\mathrm{Px}} + (1-\phi_{\mathrm{Px}}(x))\, C_l^{\mathrm{Lz}}}{(1-\phi_{\mathrm{Px}}(x))\, F_{\mathrm{Lz}} + \phi_{\mathrm{Px}}(x) F_{\mathrm{Px}}} \tag{A.6}$$

A.2 Diminishing active upwelling

For convenience I use a normalised co-ordinate system for the pressure, P in the melting region, where $z = 1$ is the onset of decompression melting, $P = P_0$, and $z = 0$ is the termination of melting, $P = P_{\max}$:

$$z = \frac{P - P_0}{P_{\max} - P_0} \tag{A.7}$$

In models of passive corner-flow decompression melting, when melts are mixed they are weighted, w according to:

$$w \propto z \tag{A.8}$$

in order to account for the greater mass of mantle seeing the lowest degrees of decompression prior to moving horizontally away from the ridge axis. Active upwelling increases the mass flux of mantle through the deepest parts of the melting region. To account for this we increase the weighting according to:

$$w(z) = z + \mu \exp\left(-\lambda_w (1-z)\right) \tag{A.9}$$

where μ parameterises the amplitude of active upwelling, and λ_w parameterises its decay lengthscale in z. We model the amplitude of active upwelling decaying exponentially with distance from Iceland:

$$\mu(x) = \mu_0 \exp\left(-\frac{x}{\lambda_\mu}\right) \tag{A.10}$$

where $\mu_0 = \mu(x = 0)$ and λ_μ is the decay lengthscale in x. Combining Equations A.9 and A.10 yields:

$$w(x,z) = z + \mu_0 \exp\left(-\frac{x}{\lambda_\mu}\right) \exp\left(-\lambda_w(1-z)\right) \tag{A.11}$$

To maintain simplicity, the melt fraction is modelled as a function of depth using a exponential function:

$$F_{\mathrm{Lz}}(z) = F_{\mathrm{Lz}}^{\max} \exp\left(-\lambda_F^{\mathrm{Lz}} z\right) \qquad F_{\mathrm{Px}}(z) = F_{\mathrm{Px}}^{\max} \exp\left(-\lambda_F^{\mathrm{Px}} z\right) \tag{A.12}$$

The variation in melt composition, C_l^{Px} and C_l^{Lz}, with depth is modelled using the batch melting equation (Equation A.4). The melts are mixed according to:

$$C_l = \frac{\sum_{i=0}^{n} w_i \left(\Delta F_i^{\mathrm{Lz}}(1-\phi_{\mathrm{Px}}) C_i^{\mathrm{Lz}} + \Delta F_i^{\mathrm{Px}} \phi_{\mathrm{Px}} C_i^{\mathrm{Px}}\right)}{\sum_{i=0}^{n} w_i \left(\Delta F_i^{\mathrm{Lz}}(1-\phi_{\mathrm{Px}}) + \Delta F_i^{\mathrm{Px}} \phi_{\mathrm{Px}}\right)} \tag{A.13}$$

where C_i^{Lz} and C_i^{Lz} are the compositions of the ith increments of melt derived from lherzolite and pyroxenite, ΔF_i^{Lz} and ΔF_i^{Px} are the associated increments of melt fraction.

Appendix B

Data compilation Sources

The following sources were used in the compilation of Icelandic whole rock data: Stracke et al. (2003b), Thirlwall et al. (2004), Hemond et al. (1993), Thirlwall et al. (2006), Schilling et al. (1999), Kempton et al. (2000), Debaille et al. (2009), Brandon et al. (2007), Condomines et al. (1983), Kokfelt et al. (2006), Elliott et al. (1991), Breddam (2002), Furman et al. (1991), Gee et al. (1998b), Gee et al. (1998a), Nicholson et al. (1991), Sigmarsson et al. (1992), Steinthorsson et al. (2000), Shorttle et al. (2013), Prestvik et al. (2001), Sims et al. (2013), Sigmarsson et al. (1991), Kuritani et al. (2011), Peate et al. (2009), Peate et al. (2010), Halldorsson et al. (2008), Kitagawa et al. (2008), Hards et al. (1995), Hards et al. (2000), Lacasse et al. (2007), Breddam et al. (2000), Chauvel and Hémond (2000), Poreda et al. (1986), Füri et al. (2010)

The following sources were used in the compilation of chemical measurements on the Reykjanes Ridge glasses: Thirlwall et al. (2004), Murton et al. (2002), Hilton et al. (2000)

The following sources were used in the compilation of MORB H_2O concentrations in Chapter 5: Niu et al. (2001), Pineau et al. (2004), Bézos et al. (2009), Fretzdorff and Haase (2002), Keller et al. (2008), Wanless and Shaw (2012), Kingsley (2002), Kelley et al. (2013), Laschek (1985), Simons et al. (2002), Michael (1988), Michael (1995), Michael and Graham (2015), Lytle et al. (2012), Perfit et al. (1983), Byers et al. (1983), Cushman et al. (2004), Ingle et al. (2010), Machida et al. (2014), Le Voyer et al. (2015), van der Zwan et al. (2017), le Roux et al. (2006), Hays (2004), Hoernle et al. (2011), Murton et al. (2005), Gale et al. (2013a), Cottrell and Kelley (2011), Danyushevsky et al. (2000), Waters et al. (2011), Jenner and O'Neill (2012), Dickey Jr et al. (1977), Eiler et al. (2000), Arevalo and McDonough (2008), Graham et al. (2016), Poreda et al. (1986), Harpp (1995), Bach and Erzinger (1995), Nielsen et al. (2014), Goss et al. (2010), Soule et al. (2012), Jambon et al. (1995), Newsom et al. (1986), Jochum and Verma (1996), Delaney et al. (1978), Perfit et al. (1983).

Berserkjahraun SIMS (1)

id	CO_2	H_2O	Li	B	F	Cl	Sr	Y	Zr	Nb	Ba	La	Ce
A01a		0.05	2.74	3.01	1348	559	184	23.6	196	54.2	290	32.4	63.5
A02a	1976	0.93	3.30	1.26	961	664	337	21.6	100	27.2	188	18.2	41.3
A04a	1522	0.54	6.44	2.02	1209	806	439	25.3	160	38.8	280	29.8	61.6
A04b	1712	0.91	3.56	2.40	786	1015	552	23.4	197	48.5	313	36.5	75.9
A04c	34	0.20	7.60	2.58	1797	883	417	27.3	186	44.9	325	31.7	66.5
A04d	19	0.24	0.91	3.17	2117	969	432	33.2	243	59.8	385	40.6	85.5
A05a	2023	0.92	3.35	1.28	743	599	333	21.0	105	27.4	195	20.3	40.7
A05b	8	0.08	3.55	1.61	1767	656	194	13.7	94	24.4	175	15.8	33.1
A05c	151	0.15	4.52	1.98	1341	738	422	22.6	143	35.2	247	26.1	53.5
A06a	2333	0.87	5.39	1.92	1243	796	451	24.8	156	37.0	279	28.5	58.6
A08b	1997	0.84	3.32	1.30	861	491	284	17.5	94	22.5	155	16.4	34.1
A08c	995	0.12	6.71	1.91	2045	955	435	25.5	153	39.6	302	29.8	62.8
A09a	58	0.27	5.93	2.10	1234	756	428	25.0	173	40.6	295	30.5	63.5
A09c	1829	0.84	3.36	2.10	840	925	508	18.5	181	43.5	281	34.0	70.2
A09d	2354	0.63	2.85	0.89	553	376	224	13.1	75	16.2	118	12.2	25.2
A09e	84	0.24	5.86	1.98	1367	791	415	25.4	167	39.8	287	29.3	61.1
A09f	83	0.30	5.44	2.07	1250	788	414	26.0	177	41.4	297	30.4	63.0
A09h	2104	0.45	5.02	1.95	1256	770	447	24.0	154	36.3	272	27.8	58.9
A11c	71	0.19	2.82	2.04	1346	724	385	24.1	161	37.8	277	28.0	58.6
A12a	1781	0.95	3.33	1.35	677	502	360	21.5	112	24.9	179	19.1	42.0
A13a	1861	0.88	3.22	1.26	809	592	335	18.7	96	23.1	171	16.7	35.5
A13b	1804	0.64	3.10	0.99	1544	719	289	16.5	84	20.2	151	15.0	31.7
A13d	18	0.14	7.00	2.76	1479	821	382	31.0	203	49.6	344	35.8	75.2
A13e	1846	0.96	3.36	1.11	812	497	333	15.2	63	16.9	164	14.7	31.0
A14a	2283	0.97	3.28	1.15	969	603	315	18.1	95	23.9	175	16.7	35.8
B05a	2242	0.97	3.07	1.14	768	533	308	17.6	95	23.0	171	17.0	34.6
B05b	2601	0.78	3.13	1.06	704	509	322	18.2	96	22.6	174	17.5	36.0
B07a	1531	0.67	3.38	1.21	1791	762	331	18.5	102	26.1	202	18.5	39.3
B07b	1920	0.41	3.61	1.69	1024	698	385	20.2	123	32.2	251	23.7	47.8
B07c	1973	0.89	3.40	1.30	923	626	337	18.9	108	27.6	201	19.0	40.2
B07d	2152	0.85	6.59	1.37	650	602	332	21.0	99	24.5	169	18.4	40.1
B07f	1720	0.85	3.71	2.35	936	973	565	21.0	188	49.7	313	36.8	77.4
B07g	1827	1.00	3.48	1.25	877	652	342	19.7	101	25.2	182	18.8	38.7
B08a	1847	0.70	5.07	1.95	1325	862	451	25.1	156	37.5	276	28.0	59.4
B08b	2027	0.87	3.35	1.36	848	639	347	21.0	107	28.6	204	19.6	41.8
B08c	1283	0.58	5.34	1.90	1264	856	446	24.1	152	36.7	271	27.5	58.6
C01a	2076	0.84	3.01	1.27	730	569	336	15.9	103	24.5	180	17.6	37.2
C01b	2069	0.81	2.55	1.38	827	609	347	17.4	108	25.3	187	17.8	38.6
C01c	1276	0.45	2.41	0.82	554	364	204	9.9	59	15.1	114	10.5	23.0
C02a	1293	0.48	5.23	1.99	1235	821	442	24.1	159	38.6	290	29.0	60.5
C02b	1794	0.93	3.33	2.47	766	1027	581	20.3	199	50.6	341	38.8	77.6
C03a	1821	0.72	3.30	2.60	936	1201	538	22.1	256	56.1	325	47.0	101.1
C03b	2098	0.74	3.25	2.85	805	1058	533	20.9	241	42.1	273	41.4	91.9
C04a	2230	0.90	3.31	1.32	775	651	355	21.8	111	28.6	201	20.2	44.2
C05a	1940	0.85	3.19	1.29	810	633	342	20.5	103	26.0	187	19.9	41.9
C05b	2109	0.85	3.47	1.32	885	619	353	21.3	105	27.6	195	19.9	42.0
C05c	2361	0.91	3.33	1.35	859	677	343	19.4	109	28.4	209	19.0	41.6
C05d	2169	0.86	3.43	1.43	880	662	334	20.1	101	26.1	185	18.1	38.9
C05f	2117	0.82	3.59	1.30	805	610	340	19.4	103	25.8	189	19.8	40.9
C05g	2156	0.83	3.47	1.24	714	574	329	19.1	100	24.7	183	18.3	39.0
C05h	2319	0.89	3.44	1.29	757	609	337	20.4	103	26.2	178	17.7	40.3
C06b	141	0.89	2.09	1.32	722	533	311	18.4	101	23.5	164	17.5	36.5
C10a	2446	0.82	3.19	1.30	656	543	326	20.4	101	25.2	181	18.1	37.3
C10b	110	0.11	4.20	1.79	1610	620	411	21.9	133	35.1	253	24.3	51.4
C10f	838	0.57	5.20	2.12	1208	831	445	25.1	154	37.8	269	27.6	58.5
C10g	309	0.30	6.67	2.05	1216	819	441	24.0	156	38.4	282	27.1	59.9
D01a	1603	0.82	3.69	2.67	811	1052	601	25.1	214	56.7	363	39.0	83.1
D01b	1703	0.74	3.54	2.14	697	925	487	20.5	182	46.9	300	31.9	68.1
D02a	158	0.27	5.99	2.24	1690	834	429	25.8	173	43.2	336	30.0	65.9

id	CO2	H2O	Li	B	F	Cl	Sr	Y	Zr	Nb	Ba	La	Ce
D02b	200	0.24	6.60	2.43	1706	901	406	28.5	182	45.2	337	32.9	70.2
D03a	2001	0.79	3.77	1.56	767	681	375	18.4	128	31.8	220	23.1	48.6
E06a	1028	1.01	8.64	2.94	2525	992	478	16.3	105	38.7	540	18.1	34.9
E07a	209	1.13	1.91	1.74	868	319	379	17.8	106	28.1	198	18.9	40.4
E08a	2202	0.87	4.25	1.81	1047	584	431	24.5	143	32.8	238	24.3	52.5
E10e	187	0.50	6.61	2.95	923	561	689	10.9	141	58.7	461	33.1	63.3
E11a	1826	0.95	3.28	1.16	908	424	319	19.3	96	22.9	178	17.6	38.2
E11b	1438	0.75	6.04	2.28	1259	768	476	27.1	195	45.0	336	35.1	74.1
E12a	1604	0.87	3.14	1.11	865	427	308	17.8	97	22.1	172	17.5	38.0
E14a	535	0.22	6.73	2.03	1335	695	469	26.8	176	40.0	307	31.4	68.9
E17e	197	0.29	5.83	1.95	1240	600	435	25.8	172	38.3	296	30.3	64.7
E17g	191	0.39	5.20	2.21	1272	609	433	28.0	190	44.8	329	32.8	71.6
E19a	1879	0.89	3.73	1.45	747	459	388	20.4	122	26.4	204	21.2	46.0
E19b	134	0.13	7.44	2.14	1605	571	440	26.0	175	39.0	297	31.2	65.7
E21a	2127	0.79	3.14	0.77	816	290	198	16.2	58	13.6	105	11.2	23.7
F06a	986	0.69	8.51	3.62	2355	967	494	28.6	212	66.5	494	40.6	78.7
F08b	1292	0.98	3.62	2.65	955	697	561	30.6	263	51.1	280	46.8	106.1
F10a	1345	0.78	4.02	3.13	641	1134	570	30.3	323	79.3	479	58.5	130.0
F10b	1044	1.14	3.40	3.56	757	1022	519	32.2	294	72.6	496	52.5	112.1
F10d	163	0.15	7.40	3.08	2310	977	401	36.9	250	62.7	425	45.3	96.3
F11a	983	0.88	7.25	3.23	2081	880	372	30.1	201	50.1	360	32.0	65.2
F11a	1078	0.89	7.17	3.25	2217	929	367	29.5	196	49.9	361	31.5	64.1
F12b	1088	0.82	4.25	1.73	1113	597	418	22.9	147	34.0	258	25.5	54.4
F12d	48	0.21	4.94	2.55	1596	772	398	31.9	214	50.0	353	37.4	79.4
F12d	704	0.12	3.60	1.79	1012	498	478	22.1	153	33.7	279	25.8	55.8
F13a	494	0.85	2.35	1.69	1042	437	413	21.7	125	34.3	255	24.7	53.0
F13a	1180	1.14	3.86	1.54	943	539	386	20.6	114	29.0	217	21.7	46.8
F17a	2210	0.94	3.22	1.20	795	475	338	19.3	108	26.6	204	19.6	42.7
F18a	1834	0.92	3.70	1.53	1066	574	380	22.8	134	30.3	225	23.6	52.0
F21a	258	0.14	4.48	2.37	1616	651	436	28.5	183	44.4	360	34.0	73.1
F24a	2380	1.62	6.83	2.23	2863	832	487	23.7	156	74.6	491	30.2	58.9
F25a	1163	0.39	3.63	2.32	797	940	759	28.1	307	64.6	463	54.0	123.9
F25c	50	0.09	4.65	4.36	2385	953	453	43.1	348	100.2	613	60.7	129.0
F28b	273	1.15	4.24	1.67	1012	572	423	21.2	124	35.1	253	24.0	51.5
F28c	15	0.11	4.30	1.82	1303	649	433	24.1	155	35.4	267	28.2	59.0
F28d	2170	0.80	3.61	1.27	1109	615	373	21.3	113	33.0	218	21.8	46.6
F28e	2051	0.80	3.59	1.35	979	602	386	21.2	114	31.8	234	22.0	45.9
F29a	2261	1.42	7.25	3.92	1966	900	493	24.3	214	74.0	491	36.7	69.5

Berserkjahraun SIMS (2)

id	Pr	Nd	Sm	Eu	Gd	Tb	Dy	Ho	Er	Tm	Yb	Lu
A01a	7.39	31.9	5.73	1.91	4.15	0.760	4.09	0.749	2.07	0.294	2.09	0.265
A02a	4.78	20.7	4.14	1.31	4.74	0.644	4.15	0.704	2.60	0.338	2.30	0.339
A04a	7.88	31.3	6.85	2.66	6.66	0.857	6.10	0.866	2.67	0.309	1.93	0.284
A04b	8.97	40.0	7.36	2.47	6.93	1.028	5.22	0.947	2.65	0.322	2.02	0.287
A04c	7.94	33.9	6.68	2.21	6.56	0.918	5.99	0.957	2.78	0.408	2.67	0.333
A04d	10.17	45.0	7.97	2.84	8.45	1.080	6.80	1.358	3.57	0.487	2.71	0.422
A05a	4.92	23.0	4.85	1.42	4.77	0.515	3.46	0.836	1.98	0.278	2.20	0.399
A05b	3.78	16.7	3.33	0.82	2.47	0.318	2.46	0.362	1.22	0.181	1.12	0.188
A05c	6.42	28.5	5.27	2.08	6.05	0.775	5.28	0.848	2.45	0.412	2.26	0.366
A06a	7.04	31.5	6.01	2.17	6.29	0.802	4.76	0.887	2.81	0.418	2.12	0.301
A08b	4.24	19.9	3.86	1.17	4.74	0.622	3.38	0.522	1.91	0.312	1.74	0.289
A08c	7.39	32.6	6.24	2.29	6.30	0.920	5.53	1.129	2.69	0.304	1.96	0.271
A09a	7.32	35.2	6.60	2.31	7.44	1.003	5.81	1.026	3.52	0.398	2.65	0.312
A09c	8.28	34.1	5.27	1.77	5.63	0.729	4.61	0.694	2.26	0.276	2.30	0.246
A09d	3.27	13.9	2.71	0.99	2.55	0.317	2.88	0.402	1.54	0.204	1.30	0.170
A09e	7.32	29.2	6.73	2.10	6.43	0.941	5.65	1.064	2.86	0.294	1.98	0.353
A09f	7.54	31.9	6.10	2.24	6.26	0.872	6.21		2.64	0.382	2.52	0.366
A09h	7.38	31.5	6.06	1.80	5.80	0.876	4.91	0.974	2.80	0.329	2.59	0.334
A11c	6.79	29.4	6.53	1.89	5.15	0.842	5.11	0.899	2.88	0.363	2.21	0.319

A12a	5.14	24.5	4.04	1.58	4.41	0.786	4.48	0.915	2.56	0.319	2.33	0.298
A13a	4.39	18.8	4.04	1.50	4.48	0.576	4.52	0.739	1.99	0.256	1.71	0.340
A13b	3.79	16.9	3.31	0.93	4.30	0.590	3.08	0.541	1.88	0.267	1.68	0.243
A13d	9.11	39.1	7.70	2.74	8.54	1.077	5.91	1.117	3.43	0.446	2.31	0.374
A13e	3.63	15.7	3.50	1.34	4.07	0.581	2.63	0.581	1.65	0.230	1.35	0.250
A14a	4.45	20.1	3.67	1.45	4.37	0.509	3.78	0.743	1.85	0.255	2.07	0.261
B05a	4.20	20.8	3.50	1.35	3.30	0.580	3.08	0.643	1.71	0.298	2.04	0.261
B05b	4.31	20.6	3.92	1.63	4.52	0.589	3.89	0.828	1.82	0.312	1.58	0.169
B07a	4.63	19.1	3.68	1.29	4.52	0.535	3.89	0.612	1.98	0.295	1.77	0.232
B07b	6.07	25.0	5.09	1.53	3.40	0.805	3.57	0.820	2.16	0.260	2.02	0.327
B07c	4.99	21.2	4.41	1.58	4.98	0.751	3.70	0.771	2.03	0.243	1.49	0.187
B07d	4.49	22.1	4.77	1.60	4.97	0.657	3.63	0.624	2.64	0.322	2.01	0.268
B07f	9.23	38.5	6.63	2.34	5.16	0.773	4.82	0.945	2.17	0.360	2.39	0.297
B07g	4.70	20.0	3.82	1.24	4.74	0.768	4.37	0.648	2.50	0.336	2.12	0.219
B08a	7.18	31.8	5.69	2.16	6.55	0.938	4.92	0.873	2.59	0.323	2.49	0.297
B08b	5.21	24.1	4.78	1.42	4.32	0.692	3.76	0.803	2.54	0.361	2.20	0.318
B08c	7.08	32.4	6.63	1.91	7.02	0.646	5.35	0.970	2.57	0.390	2.62	0.329
C01a	4.45	18.9	4.18	1.04	3.82	0.521	3.94	0.648	1.91	0.217	1.71	0.270
C01b	4.69	21.2	4.58	1.46	3.87	0.520	3.87	0.607	1.85	0.266	1.86	0.205
C01c	2.88	10.8	2.22	0.78	1.87	0.337	1.58	0.411	1.05	0.137	0.64	0.096
C02a	7.03	30.1	5.87	2.14	5.48	0.817	5.08	0.907	2.28	0.266	2.95	0.381
C02b	8.94	38.7	6.98	1.98	8.47	0.712	5.08	0.870	2.30	0.293	1.88	0.292
C03a	11.89	50.6	7.33	2.33	6.99	1.112	5.37	0.854	2.09	0.393	1.93	0.260
C03b	11.01	43.6	6.92	2.07	5.85	0.784	5.10	0.719	2.03	0.325	1.70	0.242
C04a	5.38	24.6	5.00	1.67	5.61	0.711	5.16	0.911	2.48	0.354	2.04	0.313
C05a	5.17	23.9	4.96	1.69	4.98	0.647	4.88	0.841	2.41	0.280	2.40	0.356
C05b	5.16	22.5	4.90	1.60	3.93	0.691	4.98	0.782	2.31	0.346	2.10	0.294
C05c	5.55	22.8	3.99	1.53	3.97	0.584	4.39	0.755	2.22	0.261	2.21	0.294
C05d	4.70	21.4	4.25	1.38	5.39	0.791	4.68	0.844	2.30	0.239	2.55	0.243
C05f	5.01	20.6	4.98	1.61	4.51	0.808	4.05	0.714	1.99	0.295	1.98	0.355
C05g	4.79	20.7	4.07	1.40	5.87	0.651	4.39	0.708	2.26	0.343	1.76	0.253
C05h	6.93	24.7	4.59	1.62	2.26	0.556	3.68	0.847	2.00	0.333	2.11	0.271
C06b	4.58	19.6	3.96	1.47	4.30	0.615	3.94	0.770	2.03	0.258	1.26	0.277
C10a	4.56	21.3	4.14	1.44	4.67	0.611	3.39	0.857	2.87	0.398	2.12	0.209
C10b	5.96	26.5	4.95	1.74	5.33	0.724	4.51	0.877	2.49	0.299	2.19	0.342
C10f	7.18	30.7	6.50	2.17	5.85	0.821	4.53	1.025	2.63	0.393	2.45	0.359
C10g	6.90	32.8	6.22	2.12	6.75	0.877	4.98	0.974	2.74	0.379	2.68	0.343
D01a	9.39	43.1	7.81	2.44	7.09	0.913	5.56	1.013	3.47	0.408	2.42	0.427
D01b	8.02	31.8	5.59	1.80	5.26	0.848	4.70	0.986	2.73	0.307	2.36	0.355
D02a	7.96	33.7	6.41	2.30	6.87	1.017	5.93	1.010	2.83	0.432	2.07	0.363
D02b	8.25	39.0	7.14	2.77	6.20	0.978	4.98	1.217	3.43	0.447	2.93	0.372
D03a	5.87	26.9	5.15	1.56	4.80	0.593	3.78	0.759	1.75	0.256	2.29	0.342
E06a	3.85	17.6	3.97	0.92	4.28	0.552	3.67	0.786	2.01	0.225	1.67	0.229
E07a	4.74	22.8	4.98	1.29	5.35	0.658	3.05	0.718	1.78	0.299	1.98	0.255
E08a	6.39	29.6	6.28	1.71	6.15	0.896	4.48	0.870	2.57	0.389	2.16	0.344
E10e	6.36	24.2	3.63	0.84	3.14	0.393	2.39	0.572	1.40	0.192	1.09	0.168
E11a	4.56	21.3	4.46	1.21	4.26	0.566	3.37	0.716	2.29	0.271	1.90	0.288
E11b	8.42	37.7	7.61	2.19	7.49	0.936	6.04	1.152	3.13	0.379	2.68	0.405
E12a	4.53	21.3	3.72	1.26	4.28	0.561	3.37	0.733	1.97	0.274	1.79	0.232
E14a	8.04	36.4	7.06	2.22	6.45	0.987	6.52	0.997	2.88	0.450	2.61	0.347
E17e	7.52	35.1	7.18	2.04	6.77	0.892	5.28	0.994	3.11	0.367	2.82	0.340
E17g	8.35	37.9	7.56	1.95	7.53	1.086	6.32	1.077	2.97	0.436	2.83	0.370
E19a	5.39	26.2	4.79	1.47	5.27	0.877	4.62	0.711	2.28	0.306	1.82	0.244
E19b	8.03	35.7	6.98	2.05	6.36	0.987	5.90	1.131	2.94	0.414	2.41	0.351
E21a	3.01	14.9	3.08	0.99	3.61	0.520	3.56	0.598	1.75	0.263	1.95	0.244
F06a	8.85	38.7	7.74	1.94	7.84	1.087	5.69	1.258	3.19	0.422	3.10	0.446
F08b	12.24	53.7	9.66	2.49	9.85	1.176	7.91	1.176	3.37	0.509	2.74	0.479
F10a	14.67	65.5	11.24	2.73	8.82	1.183	6.55	1.212	3.30	0.431	2.94	0.404
F10b	12.95	54.0	9.96	2.73	9.07	1.363	6.61	1.305	3.42	0.448	3.03	0.390
F10d	11.67	49.4	9.26	2.69	8.75	1.283	7.97	1.418	3.96	0.509	3.43	0.520
F11a	7.33	33.0	6.69	1.76	7.94	1.020	6.40	1.204	3.40	0.426	3.03	0.401
F11a	7.19	35.4	6.78	1.69	8.03	1.000	5.56	1.165	2.86	0.445	2.96	0.429
F12b	6.55	30.5	5.66	1.80	5.61	0.741	4.87	0.941	2.68	0.398	2.16	0.321

id	Pr	Nd	Sm	Eu	Gd	Tb	Dy	Ho	Er	Tm	Yb	Lu
F12d	9.48	42.3	8.74	2.62	7.58	1.091	6.75	1.247	3.41	0.462	2.84	0.444
F12d	6.50	29.4	5.82	1.63	6.03	0.720	4.53	0.919	2.37	0.357	1.95	0.391
F13a	6.15	26.1	5.17	1.50	5.22	0.708	4.75	0.921	2.30	0.308	2.26	0.376
F13a	5.33	26.7	5.02	1.13	5.59	0.666	4.04	0.807	2.51	0.319	2.13	0.281
F17a	5.19	23.0	4.50	1.31	3.87	0.688	3.77	0.748	1.99	0.304	2.08	0.283
F18a	5.91	28.9	5.53	1.54	5.90	0.779	4.96	0.905	2.43	0.294	1.97	0.289
F21a	8.52	39.2	7.19	2.26	6.61	0.897	5.06	1.124	3.12	0.434	2.56	0.376
F24a	6.59	27.3	5.25	1.01	5.32	0.968	4.59	1.044	2.98	0.370	2.12	0.324
F25a	14.07	60.3	10.16	2.51	9.60	1.360	6.54	1.165	3.24	0.458	2.66	0.377
F25c	14.88	63.6	12.11	3.36	12.01	1.429	8.95	1.746	5.06	0.663	3.79	0.670
F28b	6.00	27.3	5.08	1.28	4.79	0.688	4.12	0.787	2.22	0.322	2.41	0.298
F28c	7.09	32.0	6.61	1.54	5.19	0.905	5.30	0.977	2.60	0.356	2.26	0.347
F28d	5.68	24.5	5.15	1.58	5.29	0.734	4.76	0.888	2.13	0.368	1.89	0.288
F28e	5.52	24.1	5.04	1.37	5.65	0.731	4.91	0.935	2.34	0.354	2.47	0.331
F29a	7.25	30.3	5.57	1.05	5.62	0.739	4.36	1.034	2.75	0.455	2.69	0.362

Berserkjahraun EPMA (glass)

id	SiO_2	MgO	FeO	CaO	Al_2O_3	Na_2O	K_2O	MnO	TiO_2	P_2O_5	Cr_2O_3	NiO	SO_2	Total
A01a	49.7	4.52	12.49	8.9	13.6	2.78	2.18	0.27	4.03	0.97	0.01	0.02	0.01	99.9
A02a	49.5	5.83	6.77	15.3	15.0	1.93	0.55	0.12	2.59	0.26	0.06	0.04	0.21	98.3
A04a	47.4	4.93	9.69	13.1	16.3	2.58	0.95	0.19	2.49	0.42	0.04	0.00	0.30	98.6
A04b	47.3	5.63	7.29	13.8	15.6	2.34	1.04	0.12	3.80	0.45	0.08	0.01	0.29	97.9
A04c	48.0	4.88	11.77	11.7	15.0	2.60	1.17	0.22	2.82	0.51	0.02	0.01	0.06	99.0
A04d	48.5	4.05	13.39	9.6	14.7	3.21	1.57	0.24	3.27	0.58	0.02	0.01	0.09	99.5
A05a	49.7	6.16	6.72	14.6	15.2	1.97	0.67	0.15	2.25	0.23	0.04	0.01	0.25	98.0
A05b	48.4	3.54	11.56	11.3	15.7	2.79	1.34	0.25	3.02	0.49	0.00	0.02	0.04	98.7
A05c	48.3	4.63	8.55	13.7	16.6	2.66	0.86	0.16	2.42	0.36	0.04	0.02	0.07	98.6
A06a	47.9	3.99	8.72	13.1	16.8	2.99	1.02	0.16	2.57	0.37	0.04	0.01	0.31	98.2
A08b	50.4	5.91	6.68	15.9	15.1	1.88	0.55	0.12	1.62	0.21	0.04	0.02	0.23	98.8
A08c	47.4	4.62	10.97	13.0	16.2	2.73	1.29	0.21	2.57	0.35	0.02	0.01	0.25	99.9
A09a	48.9	5.99	10.06	12.1	16.4	2.66	1.11	0.21	2.39	0.39	0.05	0.02	0.12	100.6
A09c	47.9	5.37	7.64	15.0	15.7	1.84	1.02	0.15	3.11	0.39	0.04	0.02	0.31	98.7
A09d	48.7	8.09	6.76	13.6	14.7	2.01	0.65	0.12	1.71	0.21	0.10	0.03	0.27	97.0
A09e	48.6	5.72	10.04	12.4	16.3	2.77	1.12	0.20	2.40	0.42	0.04	0.02	0.12	100.3
A09f	48.3	6.05	10.09	12.3	15.3	2.80	1.09	0.18	2.57	0.42	0.05	0.02	0.10	99.4
A11c	48.6	5.35	9.80	12.3	16.1	2.34	1.05	0.24	2.39	0.42	0.07	0.00	0.11	99.1
A12a	50.3	4.83	6.94	15.0	16.3	2.18	0.66	0.14	2.17	0.31	0.05	0.00	0.28	99.3
A13a	49.1	6.57	7.34	14.8	15.0	1.93	0.62	0.14	2.00	0.22	0.07	0.03	0.26	98.1
A13b	49.9	5.49	7.32	15.5	15.2	1.86	0.61	0.10	2.22	0.22	0.03	0.03	0.25	98.9
A13d	48.3	5.05	11.39	11.2	14.3	2.76	1.42	0.22	3.08	0.50	0.01	0.04	0.10	98.6
A13e	48.6	6.67	7.65	15.2	16.0	1.97	0.61	0.15	1.56	0.12	0.05	0.03	0.24	98.9
A14a	50.0	5.83	6.65	15.8	15.3	1.92	0.64	0.11	1.75	0.23	0.07	0.02	0.29	98.7
B05a	50.2	7.25	6.61	15.0	14.8	2.05	0.61	0.12	1.71	0.20	0.07	0.00	0.24	99.1
B05b	49.5	6.41	6.87	15.1	14.7	1.76	0.50	0.12	2.33	0.21	0.08	0.02	0.21	98.0
B07a	50.1	6.10	7.19	15.4	14.8	1.97	0.65	0.15	1.72	0.19	0.08	0.00	0.26	98.9
B07b	48.7	6.00	8.90	12.6	16.3	2.68	0.93	0.17	2.13	0.30	0.00	0.05	0.27	99.2
B07c	50.3	5.98	7.23	14.9	15.0	2.02	0.64	0.12	1.91	0.24	0.07	0.02	0.26	98.9
B07d	50.4	4.98	6.72	15.3	15.0	2.04	0.59	0.13	2.61	0.22	0.08	0.02	0.28	98.5
B07f	50.1	4.74	7.21	14.7	15.7	2.01	0.96	0.12	3.49	0.43	0.10	0.03	0.27	100.0
B08a	48.8	4.88	9.60	12.8	16.3	2.70	0.96	0.13	2.42	0.35	0.03	0.04	0.30	99.5
B08b	50.0	6.21	6.83	14.6	14.6	1.89	0.64	0.12	2.20	0.25	0.06	0.04	0.26	97.8
B08c	48.0	5.19	9.44	12.7	15.8	2.61	0.93	0.22	2.44	0.34	0.07	0.01	0.26	98.1
C01b	50.4	4.75	6.77	16.2	16.0	1.86	0.68	0.14	2.01	0.24	0.06	0.05	0.25	99.5
C02a	47.7	6.28	10.19	12.4	15.5	2.79	0.94	0.22	2.35	0.34	0.06	0.00	0.26	99.2
C02b	48.6	5.75	6.94	14.0	15.5	2.16	1.09	0.13	3.58	0.42	0.07	0.03	0.30	98.8
C03a	47.7	4.28	6.41	15.1	16.3	1.96	1.14	0.09	3.85	0.71	0.06	0.06	0.38	98.3
C03b	47.6	4.88	7.06	15.2	16.1	2.01	1.01	0.12	3.83	0.69	0.03	0.03	0.32	99.1
C04a	50.8	5.46	6.78	15.2	15.2	2.00	0.67	0.10	2.21	0.27	0.02	0.03	0.25	99.0
C05b	50.6	6.11	7.20	15.3	15.0	1.90	0.57	0.14	2.11	0.22	0.07	0.02	0.26	99.5
C05c	50.6	5.81	6.77	15.0	15.1	2.04	0.70	0.13	1.89	0.24	0.03	0.01	0.26	98.6

id	SiO_2	MgO	FeO	CaO	Al_2O_3	Na_2O	K_2O	MnO	TiO_2	P_2O_5	Cr_2O_3	NiO	SO_2	Total
C05d	50.5	5.79	6.87	15.4	15.2	2.06	0.59	0.12	2.33	0.23	0.06	0.00	0.23	99.5
C05f	50.7	4.01	7.26	15.0	16.3	2.37	0.70	0.15	2.02	0.22	0.08	0.00	0.27	99.3
C10a	50.1	5.97	6.90	15.4	14.9	1.97	0.58	0.10	2.27	0.21	0.07	0.00	0.26	98.8
C10b	50.4	5.64	8.22	13.1	16.4	2.74	0.84	0.17	2.10	0.27	0.03	0.01	0.03	100.1
C10f	50.1	3.20	8.70	13.4	17.6	3.10	1.00	0.20	2.56	0.37	0.02	0.08	0.19	100.6
C10g	48.9	5.75	9.43	12.6	16.2	3.02	0.98	0.18	2.38	0.35	0.03	0.03	0.11	100.2
D01b	50.5	4.05	5.91	13.8	16.9	2.42	1.21	0.18	3.82	0.45	0.06	0.01	0.21	99.8
D02a	48.7	5.42	10.93	11.6	16.1	2.88	1.19	0.18	2.40	0.38	0.07	0.03	0.15	100.2
D02b	47.7	4.32	11.24	12.1	15.3	2.99	1.19	0.19	2.70	0.42	0.02	0.05	0.17	98.7
D03a	49.6	6.56	8.59	14.7	15.1	1.90	0.71	0.18	1.82	0.29	0.08	0.04	0.26	99.9
E10e	48.8	7.46	7.87	13.8	15.8	1.18	0.32	0.21	2.06	0.28	0.00		0.21	98.0
E11a	51.2	4.87	6.15	16.7	16.1	2.00	0.59	0.14	1.63	0.19	0.07	0.01	0.17	99.9
E12a	51.1	6.02	6.41	15.8	15.8	2.01	0.64	0.11	1.55	0.21	0.04		0.15	99.9
E17e	48.2	5.47	9.93	12.5	16.0	2.85	1.09	0.20	2.28	0.39	0.04		0.10	99.2
E17g	48.5	5.59	11.38	11.9	14.5	2.61	1.27	0.23	2.72	0.44		0.02	0.05	99.2
E19a	48.8	4.39	7.84	15.2	16.1	2.12	0.69	0.14	1.76	0.27	0.04	0.03	0.17	97.6
E19b	48.8	4.46	9.97	12.9	16.4	2.97	1.23	0.21	2.37	0.40	0.03	0.03	0.09	100.0
E21a	52.3	4.48	5.70	16.0	15.6	1.91	0.40	0.11	1.20	0.11	0.05	0.04	0.13	98.2
F06a	50.4	4.49	7.82	8.9	17.5	3.76	1.75	0.19	2.91	0.65	0.04	0.01	0.35	98.9
F08b	47.9	4.22	7.18	13.9	16.9	2.85	0.97	0.15	3.81	1.81	0.05	0.01	0.29	100.0
F10a	48.9	3.06	8.34	12.3	17.7	3.01	1.56	0.22	5.20	0.86	0.01	0.00	0.32	101.6
F10b	48.4	4.76	9.24	10.3	17.2	3.42	1.61	0.17	3.92	0.63	0.02	0.01	0.26	100.1
F10d	48.3	5.19	12.62	11.6	13.4	2.46	1.57	0.28	3.32	0.60	0.03	0.01	0.03	99.5
F11a	48.6	6.92	9.49	11.4	15.0	3.15	1.29	0.17	2.84	0.60	0.02	0.03	0.35	100.0
F11a	48.6	6.92	9.49	11.4	15.0	3.15	1.29	0.17	2.84	0.60	0.02	0.03	0.35	100.0
F12b	48.6	6.41	8.26	13.6	16.0	2.60	0.89	0.19	2.39	0.37	0.03	0.03	0.26	99.6
F12d	48.8	5.87	11.92	11.7	14.4	2.62	1.29	0.22	2.78	0.47	0.03	0.03	0.11	100.3
F12d	48.8	5.87	11.92	11.7	14.4	2.62	1.29	0.22	2.78	0.47	0.03	0.03	0.11	100.3
F13a	50.9	6.32	7.43	13.6	15.5	2.00	0.75	0.17	1.73	0.25	0.05	0.02	0.22	98.9
F13a	50.9	6.32	7.43	13.6	15.5	2.00	0.75	0.17	1.73	0.25	0.05	0.02	0.22	98.9
F17a	50.3	6.31	7.16	15.7	15.4	2.08	0.68	0.15	1.73	0.24	0.03	0.02	0.24	100.0
F18a	48.8	6.97	8.22	14.4	15.1	2.19	0.77	0.17	2.10	0.30	0.05	0.01	0.20	99.4
F21a	48.5	5.65	10.22	12.1	15.7	2.68	1.23	0.20	2.34	0.40	0.08	0.02	0.06	99.3
F24a	50.3	6.13	9.58	9.3	15.0	3.43	1.30	0.20	2.22	0.40	0.03		0.27	98.3
F25a	46.6	5.20	9.27	12.7	15.5	2.62	1.09	0.20	3.54	0.63			0.34	97.8
F25c	49.7	3.71	12.31	10.2	13.7	2.90	1.92	0.23	3.67	0.76	0.03	0.00	0.02	99.3
F28b	50.5	4.57	7.61	12.2	17.7	2.49	0.88	0.14	1.95	0.29	0.00	0.03	0.10	98.5
F28c	48.9	5.66	8.92	13.2	16.0	2.62	0.87	0.18	2.23	0.34	0.07	0.03	0.03	99.1
F28d	50.4	3.99	6.23	15.6	16.0	2.22	0.68	0.16	2.00	0.26	0.02	0.03	0.16	97.8
F28e	51.2	4.57	6.24	16.1	16.1	2.29	0.59	0.12	2.30	0.24	0.05	0.04	0.15	100.0
F29a	50.3	6.16	7.70	8.9	16.6	3.70	1.45	0.16	1.91	0.59	0.03	0.01	0.25	97.9

Berserkjahraun EPMA (host)

id	SiO_2	MgO	FeO	CaO	Al_2O_3	MnO	TiO_2	P_2O_5	Cr_2O_3	NiO	Total
A01a	39.9	43.2	17.8	0.29	0.05	0.32	0.02	0.01	0.01	0.19	101.8
A02a	40.7	48.1	10.9	0.32	0.05	0.17	0.02	0.01	0.07	0.26	100.6
A04a	40.0	46.2	12.9	0.31	0.05	0.21	0.01	0.01	0.06	0.24	100.0
A04b	40.6	47.9	10.5	0.30	0.05	0.12	0.01	0.01	0.07	0.31	99.8
A04c	40.3	46.4	12.6	0.32	0.05	0.21	0.02	0.00	0.06	0.24	100.1
A04d	40.1	46.2	12.8	0.32	0.05	0.20	0.01	0.00	0.05	0.27	100.0
A05a	40.8	48.0	10.9	0.31	0.05	0.19	0.02	0.02	0.08	0.26	100.6
A05b	40.5	46.4	12.7	0.32	0.06	0.21	0.01	0.01	0.07	0.25	100.6
A05c	40.5	47.2	11.6	0.31	0.06	0.16	0.01	0.01	0.06	0.28	100.1
A06a	39.8	46.0	12.6	0.32	0.06	0.22	0.01	0.00	0.06	0.26	99.4
A08b	41.0	48.5	10.8	0.35	0.05	0.20	0.01	0.00	0.08	0.29	101.3
A08c	40.3	46.9	12.4	0.31	0.05	0.18	0.01	0.01	0.09	0.27	100.5
A09a	40.6	46.4	13.5	0.29	0.05	0.22	0.01	0.01	0.06	0.22	101.3
A09c	40.5	47.0	12.1	0.33	0.05	0.19	0.01	0.01	0.05	0.27	100.6
A09d	40.9	48.0	11.0	0.36	0.04	0.17	0.01	0.00	0.06	0.27	100.9
A09e	40.6	46.1	13.8	0.30	0.04	0.19	0.01	0.01	0.04	0.23	101.4

id	SiO_2	MgO	FeO	CaO	Al_2O_3	MnO	TiO_2	P_2O_5	Cr_2O_3	NiO	Total
A09f	40.0	46.4	12.6	0.32	0.05	0.22	0.01	0.01	0.08	0.27	99.8
A11c	40.9	46.9	12.8	0.31	0.06	0.24	0.03	0.02	0.07	0.22	101.6
A12a	40.8	47.7	11.5	0.32	0.05	0.20	0.02	0.04	0.04	0.25	101.0
A13a	40.6	47.4	11.4	0.37	0.05	0.20	0.02	0.00	0.07	0.26	100.4
A13b	40.6	47.4	11.4	0.37	0.05	0.20	0.02	0.00	0.07	0.26	100.4
A13d	40.6	47.2	11.8	0.33	0.04	0.23	0.01	0.01	0.03	0.27	100.5
A13e	40.4	47.5	11.5	0.36	0.05	0.19	0.01	0.03	0.05	0.25	100.4
A14a	40.9	48.4	10.5	0.36	0.05	0.17	0.00	0.00	0.07	0.28	100.7
B05a	41.1	48.2	10.6	0.36	0.05	0.17	0.01	0.01	0.06	0.32	100.8
B05b	40.3	47.5	10.6	0.35	0.06	0.20	0.01	0.00	0.06	0.28	99.4
B07a	40.3	47.5	11.1	0.37	0.05	0.19	0.02	0.01	0.03	0.27	99.8
B07b	40.2	46.6	12.0	0.31	0.05	0.18	0.02	0.01	0.06	0.26	99.7
B07c	40.4	47.2	11.5	0.32	0.05	0.20	0.02	0.01	0.08	0.28	100.1
B07d	40.2	47.4	10.8	0.34	0.04	0.21	0.02	0.01	0.07	0.27	99.3
B07f	40.7	48.2	11.3	0.31	0.05	0.18	0.02	0.01	0.06	0.27	101.2
B08a	40.5	46.7	12.9	0.31	0.05	0.21	0.02	0.01	0.07	0.24	101.1
B08b	40.2	47.0	10.8	0.33	0.05	0.18	0.00	0.01	0.07	0.25	98.9
B08c	39.3	44.7	13.6	0.31	0.05	0.23	0.02	0.01	0.03	0.25	98.6
C01b	41.2	48.4	10.6	0.34	0.05	0.19	0.02	0.02	0.07	0.27	101.2
C02a	40.5	47.0	11.2	0.34	0.05	0.17	0.01	0.01	0.05	0.29	99.7
C02b	40.5	47.0	11.2	0.34	0.05	0.17	0.01	0.01	0.05	0.29	99.7
C03a	40.6	47.2	10.8	0.32	0.05	0.18	0.03	0.00	0.06	0.27	99.6
C03b	40.6	47.8	11.0	0.32	0.05	0.20	0.02	0.00	0.08	0.29	100.4
C04a	40.9	47.9	10.9	0.32	0.05	0.21	0.00	0.01	0.06	0.25	100.6
C05b	40.8	47.9	10.9	0.35	0.05	0.19	0.01	0.01	0.06	0.28	100.6
C05c	40.7	48.0	11.0	0.33	0.05	0.18	0.01	0.02	0.06	0.31	100.6
C05d	40.9	48.3	10.6	0.32	0.05	0.22	0.01	0.01	0.06	0.32	100.8
C05f	40.3	46.8	12.0	0.32	0.05	0.19	0.00	0.01	0.05	0.28	100.1
C10a	40.7	48.1	10.7	0.34	0.05	0.15	0.01	0.01	0.06	0.26	100.5
C10b	40.5	46.9	12.1	0.31	0.05	0.23	0.01	0.01	0.06	0.25	100.5
C10f	40.2	46.3	12.4	0.32	0.06	0.20	0.01	0.02	0.07	0.24	99.8
C10g	40.0	46.3	12.6	0.32	0.07	0.22	0.04	0.02	0.07	0.25	99.8
D01b	40.5	47.9	10.8	0.28	0.06	0.19	0.02	0.01	0.08	0.28	100.1
D02a	39.9	45.9	13.3	0.30	0.05	0.22	0.02	0.01	0.08	0.23	100.0
D02b	39.8	45.3	14.4	0.28	0.05	0.22	0.03	0.01	0.02	0.21	100.4
D03a	40.4	46.9	12.6	0.34	0.05	0.23	0.01	0.02	0.06	0.27	100.8
E06a	49.9	15.5	5.8	21.30	5.62	0.14	1.07	0.01	0.66	0.02	100.4
E10e	52.1	17.6	4.8	21.16	3.76	0.13	0.64	0.02	0.42	0.03	100.9
F06a	48.8	14.3	7.0	20.77	5.92	0.16	1.60	0.01	0.44	0.02	99.6
F08b	41.3	48.6	11.8	0.28	0.04	0.19	0.01	0.04	0.05	0.25	102.6
F10a	40.4	45.6	15.0	0.25	0.04	0.26	0.02	0.01	0.01	0.15	101.8
F10b	40.4	45.7	14.8	0.24	0.04	0.26	0.02	0.01	0.00	0.15	101.7
F12b	40.3	47.1	12.7	0.29	0.04	0.19	0.01	0.01	0.05	0.26	100.9
F12d	40.4	46.7	12.7	0.31	0.04	0.19	0.02	0.01	0.03	0.26	100.7
F12d	40.4	46.7	12.7	0.31	0.04	0.19	0.02	0.01	0.03	0.26	100.7
F13a	40.3	48.0	10.9	0.33	0.05	0.17	0.02	0.01	0.06	0.28	100.1
F13a	40.3	48.0	10.9	0.33	0.05	0.17	0.02	0.01	0.06	0.28	100.1
F17a	40.7	48.0	11.2	0.35	0.06	0.19	0.00	0.02	0.08	0.30	101.0
F18a	40.5	47.0	12.9	0.32	0.05	0.20	0.01	0.01	0.05	0.25	101.3
F24a	49.5	14.9	6.8	20.89	5.18	0.15	1.26	0.00	0.57	0.01	99.7
F25a	40.1	45.3	14.3	0.28	0.05	0.24	0.02	0.01	0.05	0.18	100.5
F25c	40.3	46.4	13.2	0.31	0.04	0.25	0.01	0.00	0.05	0.23	100.9
F28b	40.7	47.3	11.9	0.36	0.06	0.19	0.01	0.01	0.07	0.24	100.8
F28c	40.8	47.0	12.6	0.34	0.07	0.19	0.01	0.01	0.07	0.25	101.3
F28d	40.9	48.0	11.1	0.34	0.05	0.20	0.00	0.02	0.07	0.26	101.0
F28e	40.7	48.0	11.2	0.39	0.10	0.18	0.01	0.02	0.05	0.25	100.8
F29a	49.5	15.2	5.5	20.61	5.85	0.14	1.39	0.01	0.93	0.04	99.7

Berserkjahraun Raman

id	p1	p1_err	p2	p2_err	bubble diameter	mi long	mi short	delta	density
A02-ne1					12.4	51.3	23.9		
A02a	1285.05	0.14	1388.89	0.14	17.5	73.4	43.1	103.84	0.578
A04-ne1	1285.88	0.14	1389.1	0.09	15.1	64.6	62.1	103.22	0.303
A04-ne2	1285.98	0.14	1389.15	0.09	6	29.2	23.9	103.17	0.282
A04b					18.6	77.5	66.1		
A05_ne1	1284.5	0.15	1388.13	0.09	25.3	97.1	80.6	103.63	0.483
A05a					21	148	122		
A08-ne1	1286.07	0.06	1389.65	0.04	18.5	71.7	59.3	103.58	0.460
A08b	1284.75	0.08	1388.05	0.05	23	84.8	69.2	103.3	0.337
A09-ne1	1283.96	0.07	1387.41	0.06	34.2			103.45	0.402
A09-ne10	1285.48	0.1	1388.42	0.08	17.3	78.5	75.4	102.94	0.190
A09-ne11	1284.53	0.23	1388.21	0.1	23.8			103.68	0.505
A09-ne2	1284.78	0.07	1388.19	0.05	36			103.41	0.385
A09-ne3	1285.15	0.13	1388.23	0.1	24.3			103.08	0.245
A09-ne4	1284.46	0.71	1388.34	0.15	13.1	64.9	58.2	103.88	0.596
A09-ne5	1285.35	0.15	1388.43	0.11	16.4	75.1	63.6	103.08	0.245
A09-ne6	1284.2	0.28	1388.03	0.12	6.1	37.1	28.5	103.83	0.573
A09-ne7	1285.43	0.12	1388.54	0.08	13.1	70	67.8	103.11	0.257
A09-ne8	1284.46	0.06	1387.8	0.05	9.2	51.3	40.4	103.34	0.354
A09-ne9	1283.89	0.09	1387.58	0.08	38.5			103.69	0.510
A09c	1284.19	0.12	1387.47	0.07	11.1	47.5	39.5	103.28	0.328
A09d	1284.71	0.14	1388.13	0.11	6.7	31.3	25.1	103.42	0.389
A11-ne1	1284.67	0.14	1388.17	0.09	11.4	44.5	46.2	103.5	0.424
A11-ne2	1285.49	0.06	1388	0.15	12.2	67.8	34.9	102.51	0.043
A13-ne1	1286.51	0.1	1389.98	0.08	12.3	52.4	40.7	103.47	0.411
A13a	1286.54	0.05	1389.91	0.08	23.8	97	78	103.37	0.367
A13b	1283.91	0.1	1387.14	0.08	19.3	79.4	68	103.233	0.308
B05a	1286.12	0.24	1389.34	0.13	27.9	118.3	60.8	103.22	0.303
B07-ne1	1285.51	0.18	1388.86	0.14	20.2	96.1	71.4	103.35	0.358
B07-ne2	1284.52	0.07	1388	0.04	20	78.7	63.8	103.48	0.415
B07-ne3	1284.43	0.19	1388.23	0.12	29.2			103.8	0.560
B07c	1284.48	0.07	1387.9	0.05	28.9	96.8	78.8	103.42	0.389
B07f	1284.41	0.07	1387.33	0.05	11.6	52.4	47.9	102.92	0.182
B08-ne1	1283.75	0.23	1387.24	0.17	19.5	76.4	59.6	103.49	0.420
B08-ne2	1283.84	0.08	1387.3	0.07	19.5	80.4	59.6	103.46	0.407
B08-ne3	1284.01	0.11	1387.37	0.1	16.5	65.3	39.3	103.36	0.363
B08-ne4	1284.06	0.12	1387.01	0.17	6.8	29.8	20.2	102.95	0.194
B08-ne5	1283.71	0.09	1387.32	0.06	14.6	60.9	39.2	103.61	0.474
B08-ne6	1284.31	0.08	1387.56	0.06	15.4	63	50.1	103.25	0.315
B08-ne7	1283.86	0.1	1387.35	0.05	31.2			103.49	0.420
C01-ne1	1284.78	0.15	1387.81	0.11	16.4	69.3	50	103.03	0.225
C01a	1284.69	0.12	1387.96	0.09	12.9	59	58.7	103.27	0.324
C01b	1284.09	0.14	1387.84	0.11	6	37.3	32.8	103.75	0.537
C02b-1	1284.24	0.14	1387.51	0.1	12.6	74.7	55.8	103.27	
C02b-1	1284.08	0.1	1387.26	0.08	11.3	103.2	0.28	755.50	
C02b-1	1284.69	0.07	1387.5	0.05	10	102.8	0.14	523.60	0.324
C03a	1284.3	0.15	1387.61	0.09333	5.6	45.7	46.3	103.31	0.340
C03b	1285.49	0.06	1388	0.15	12.2	67.8	34.9	102.51	0.043
C04-ne1	1284.56	0.07	1387.92	0.05	21.7	83.7	70	103.36	0.363
C04-ne2	1285.97	0.14	1388.89	0.1	23.2	54.8	40.6	102.92	0.182
C04-ne3	1284.06	0.05	1388.14	0.08	10.9	48.6	30.7	104.08	0.686
C04-ne4	1284.41	0.08	1387.82	0.05	13.9	54.2	49.8	103.41	0.385
C04-ne5	1284.67	0.12	1387.89	0.07	11.6	48.1	50.9	103.22	0.303
C04-ne6	1284.89	0.08	1388.18	0.05	25.1	77.1	89.1	103.29	0.332
C04-ne7	1284.76	0.1	1387.83	0.07	5.8	29.4	15.7	103.07	0.241
C04-ne8	1284.05	0.1	1387.53	0.06	8.9	38.5	24.3	103.48	0.415
C05-ne1	1284.41	0.15	1387.91	0.1	26.7	111.6	99.8	103.5	0.424
C05-ne2	1283.37	0.7	1387.51	0.06	11.6	52.7	44.5	104.14	0.712
C05-ne3	1284.02	0.19	1387.65	0.13	10.7	49.7	33	103.63	0.483
C05-ne4	1284.88	0.09	1388.03	0.07	9.8	48.1	31.5	103.15	0.273
C05b	1284.9	0.14	1387.87	0.12	26.4	105.3	89.4	102.97	0.201
C05c	1284.84	0.16	1387.93	0.12	32.3	101	64	103.09	0.249
C05g	1283.13	0.07	1386.68	0.06	16.3	68.6	63.3	103.55	0.447
C05h	1283.35	0.18	1386.92	0.12	11.6	43.3	40.2	103.57	0.456
C06-ne1	1284.4	0.11	1387.92	0.12	15.9	56.3	47.3	103.52	0.433

id	p1	p1_err	p2	p2_err	bubble diameter	mi long	mi short	delta	CO_2 density
C06-ne2	1284.49	0.13	1388.28	0.1	18.1	71.5	50.8	103.79	0.555
C10-ne1	1286.14	0.11	1389.25	0.09	13.9	35.8	34.3	103.11	0.257
C10-ne2	1285.92	0.14	1389.19	0.11	14.1	44.1	26.6	103.27	0.324
C10-ne3	1285.11	0.17	1388.54	0.13	12.5	54.2	41.1	103.43	0.393
C10-ne4	1285.45	0.14	1389.05	0.12	7	32.1	20.5	103.6	0.469
C10-ne5	1285.27	0.11	1388.65	0.07	12.6	44.5	36.8	103.38	0.371
C10-ne6	1285	0.09	1388.57	0.06	11.1	48.7	44	103.57	0.456
D03-ne1	1283.37	0.19	1387.29	0.1	5.5	28.5	18.1	103.92	0.614
E08a-1	1283.86	0.1	1387.25	0.07	8.7	38.8	29.7	103.39	
E08a-2	1283.61	0.15	1387.16	0.1	9.9	103.35	0.35837	508.047	0.376
E12a	1283.69	0.16	1386.96	0.12	17.5	53.2	48	103.27	0.324
E12b	1284.58	0.1	1387.51	0.095	7.3	48.5	41.7	102.93	0.186
E14a	1283.09	0.24	1386.81	0.13	6.2	41.9	19.1	103.72	0.523
F08b	1283.52	0.02	1386.65	0.02	25.2	75.9	43.1	103.13	0.265
F11a					57.7	255.2	109.5		
F11a					57.7	255.2	109.5		
F13a	1283.85	0.04	1386.92	0.03	51.7	114.9	94.4	103.07	0.241
F17a	1283.88	0.08	1387.16	0.06	36.2			103.28	0.328
F18a	1283.32	0.05	1386.51	0.04	21.8	70.6	59.1	103.19	0.290
F21a					29.3				
F25a	1283.35	0.07	1386.58	0.05	23.9	81.1	60	103.23	0.307
F28d	1283.08	0.08	1386.27	0.06	20.2	76.9	60.1	103.19	0.290
F28e	1282.97	0.09	1386.31	0.07	14.2	62.8	36.7	103.34	0.354
F29a					17.5				
F28_ne4	1282.61	0.09	1386.12	0.06	14.7	64.6	43.5	103.51	0.429
F_002_ne2	1283.67	0.17	1386.87	0.14	18.8		50.8	103.2	0.294
F_002_ne1	1284.59	0.25	1387.73	0.21	18.5		48.1	103.14	0.269
F_002_ne3	1284.17	0.24	1386.95	0.14	13.4		63.5	102.78	0.131
F_002_ne4	1284.44	0.18	1387.41	0.13	9.2	55.5	26.3	102.97	0.201
F25_ne2	1283.3	0.05	1386.53	0.04	12.3	47.9	26.6	103.23	0.307
F25_ne3	1282.66	0.1	1386.16	0.06	10.2	35.7	27	103.5	0.424
F25_ne4	1282.77	0.04	1386.24	0.03	19	47.8	29.4	103.47	0.411
F25_ne5	1282.92	0.07	1386.32	0.05	7.1	28.5	15.2	103.4	0.380
F28_4	1283.72	0.07	1387.08	0.05	10.7	48.2	23.5	103.36	0.363
um-12-1-1	1285.49	0.18	1388.94	0.15	17.1	54	51.2	103.45	0.402
um-D12-1-1	1284.4	0.11	1387.64	0.08				103.24	0.311
um-D15-3-1	1286.11	0.11	1389.36	0.09	12.8	57	42.3	103.25	0.315
um-D20-1-2	1283.49	0.24	1386.9	0.11	9.5	44.6	28.8	103.41	0.385
um-D21-1-4	1283.24	0.08	1386.74	0.07	8.2	24	15.8	103.5	0.424
um-D21-2-1	1283.6	0.11	1387.33	0.05	9.1	30.9	21.8	103.73	0.528
um-D22-2-3	1283.66	0.12	1386.93	0.09	8.6	30.9	24.9	103.27	0.324
um-D24-1-3	1284.4	0.2	1387.58	0.13	13.9	46	32.2	103.18	0.286
ne_177_mi1	1283.58	0.1	1386.64	0.08	22.2			103.06	0.237
ne_177_mi2	1283.18	0.16	1386.3	0.09	16	70.2	50.2	103.12	0.261
ne_177_mi3	0	0	0	0	18.6	87.7	40.1		
ne_182_mi1	1283.93	0.11	1387.06	0.08	9.2	39.8	34.3	103.13	0.265
ne_182_mi2	1283.66	0.06	1386.69	0.05	11.2	46.9	34.9	103.03	0.225
ne_182_mi3	1283.83	0.1	1386.8	0.1	7.2	32.2	25.3	102.97	0.201
ne_182_mi4	0	0	0	0	3.4	16.3	13.9		
E08_ne1	0	0	0	0	10.8	41	37.7		
E09_ne1	0	0	0	0	40	125.6	104.7		
E09_ne2	1283.16	0.23	1386.48	0.15	7.6	35.4	28.7	103.32	0.345
E09_ne3-1	1283.6	0.07	1386.69	0.05	10.9	73.9	35.9	103.09	
E09_ne3-2	1283.61	0.1	1386.65	0.07	7.5	103.04	0.22878	220.893	0.249
E11_ne1	1282.79	0.1	1386.28	0.07	20.7	69.2	64.8	103.49	0.420
E11_ne2	1283.15	0.05	1386.5	0.03	18.9			103.35	0.358
ne_034_1	1284.73	0.05	1387.67	0.03	19.9	44.8	22.6	102.94	0.190
ne_134_1	1283.8	0.15	1386.89	0.11	6.4	40.1	35.4	103.09	0.249
F10_ne1	1282.65	0.04	1386.5	0.03	10.2	32.5	27.8	103.85	0.582
F10_ne2	1284.07	0.19	1387.37	0.14	10.9	54.9	33.8	103.3	0.337
F10_ne3	1284.01	0.06	1387.24	0.04	8.7	38.2	30.6	103.23	0.307
F10_ne4	1283.2	0.05	1386.69	0.03	11.6	34	31.1	103.49	0.420
F10_ne5	1284.4	0.05	1387.52	0.04	6.8	33.8	19.2	103.12	0.261
F08_ne1	1283.52	0.06	1386.6	0.04	11.2	63.2	42.4	103.08	0.245
F08_ne2	0	0	0	0	4.3	19.5	14.6		
F08_ne3	1283.71	0.02	1386.77	0.02	11.9	53.4	34.7	103.06	0.237
F08_ne4	1282.89	0.08	1386.29	0.05	21.6			103.4	0.380
F08_ne5	1283.55	0.13	1386.59	0.12	6.7	29.5	22.1	103.04	0.229

id	p1	p1_err	p2	p2_err	bubble diameter	mi long	mi short	delta	CO_2 density
F08_ne6	1283.99	0.08	1386.94	0.07	18.1	82.1	46.6	102.95	0.194
F08_ne7	1283.64	0.15	1386.78	0.16	12.8	60.7	40.1	103.14	0.269
F08_ne9	1284	0.08	1387.12	0.07	20	63.1	88.5	103.12	0.261
F08_ne10	1282.48	0.1	1386.06	0.06	23.5	102.3	71.1	103.58	0.460
F08_ne11	1282.54	0.1	1386.15	0.06	11.9	47.7	39.9	103.61	0.474
F17_ne1	1284	0.55	1386.93	0.2	7.7	28.2	28.1	102.93	0.186
F_ne1	1283.88	0.05	1386.87	0.04	14.6	89.3	29.7	102.99	0.209
nm_016_mi1	1283.29	0.13	1386.36	0.1	10.9	51.2	24	103.07	0.241
nm_051_mi1	1285.76	0.13	1388.5	0.09	23.5	60.5	32.1	102.74	0.117
nm_051_mi2	1285.41	0.76	1388.87	0.26	18.2	35.1	25.6	103.46	0.407
nm_101_mi1	1283.17	0.13	1386.43	0.09	8.3	29	20.5	103.26	0.320
nm_112_mi1	1283.35	0.04	1386.58	0.03	11.8	39.4	29.3	103.23	0.307
nm_112_mi2-1	1283.42	0.04	1386.65	0.03	7.8	33.6	25.6	103.23	0.307
nm_112_mi2-2	1283.16	0.08	1386.53	0.05	6.3	103.37	0.36707	130.924	0.307
nm_112_mi3	1282.25	0.09	1385.97	0.05	22.3	58.1	36.5	103.72	0.523
nm_140_mi1	1283.4	0.0725	1386.72	0.055	5.4	26.1	18.3	103.323	0.346
nm_140_mi2	1283.19	0.055	1386.59	0.04	7.5	29.3	18.2	103.4	0.380
nm_141_mi2	1282.92	0.05	1386.18	0.04	7	18.8	17.6	103.26	0.320
nm_141_mi3	1283.34	0.32	1386.8	0.1	5.5	22.3	17.4	103.46	0.407
nm_143_mi2	1282.5	0.09	1385.97	0.06	12	44.8	39.5	103.47	0.411
nm_143_mi3	1283.22	0.07	1386.16	0.08	9.9	41.5	23.5	102.94	0.190
nm_147_mi1	1282.72	0.07	1386.02	0.05	11.8	56.2	40.1	103.3	0.337
nm_152_mi1	1283.01	0.13	1386.32	0.09	6.4	23.2	21.1	103.31	0.341
nm_D15-3-1	1286.11	0.11	1389.36	0.09	12.8	57	42.3	103.25	0.315
nm_D20-1-2	1283.49	0.24	1386.9	0.11	9.5	44.6	28.8	103.41	0.385
nm_D21_1-4	1283.24	0.08	1386.74	0.07	8.2	24	15.8	103.5	0.424
nm_D21-2-1	1283.6	0.11	1387.33	0.05	9.1	30.9	21.8	103.73	0.528
nm_D22-2-1	1282.44	0.12	1386.59	0.07	7.2	34.8	25.3	104.15	0.717
nm_D22-2-3	1283.66	0.12	1386.93	0.09	8.6	30.9	24.9	103.27	0.324
nm_D24-1-3	1284.4	0.2	1387.58	0.13	13.9	46	32.2	103.18	0.286

Haleyjabunga SIMS (1)

id	CO_2	H_2O	Li	B	F	Cl	Sr	Y	Zr	Nb	Ba	La	Ce
D01a	512	0.13	2.32	0.41	100	232.2	66.6	11.3	39.3	4.33	25.30	3.90	8.03
D03a	54	0.14	2.42	0.24	82	12.5	34.9	13.7	13.4	0.23	1.60	0.50	1.54
D04a	188	0.15	2.32	0.18	117	14.6	57.9	10.7	22.0	0.53	4.88	1.34	3.07
D05a	897	0.11	2.32	0.19	124	11.9	55.9	10.1	20.5	0.67	4.34	1.14	3.48
D06a	167	0.11	2.49	1.54	77	18.0	39.3	13.0	14.3	0.28	2.48	0.58	1.47
D06b	508	0.15	2.59	0.21	95	20.0	38.7	11.8	13.6	0.45	2.61	0.35	1.22
D07a	404	0.11	2.57	0.13	96	39.6	51.2	11.8	11.1	0.63	4.21	0.65	1.80
D08a	441	0.06	2.85	0.11	152	30.9	47.0	11.4	9.9	0.50	2.94	0.64	1.38
D09a	142	0.12	2.60	0.14	80	6.7	29.4	10.6	10.3	0.08	0.73	0.27	0.98
D10a	326	0.08	2.55	0.13	72	11.3	43.8	10.2	9.5	0.20	2.57	0.40	1.07
D10b	292	0.08	2.58	0.15	88	15.0	37.6	10.2	9.6	0.24	2.31	0.26	1.27
D11a	238	0.07	2.83	0.09	151	2.3	35.5	11.5	8.0	0.10	1.27	0.24	0.89
D12a	390	0.15	2.45	0.11	75	45.5	50.4	9.7	10.3	0.46	3.72	0.50	1.31
D13a	591	0.08	3.57	0.46	119	233.2	57.9	11.5	14.0	6.43	39.13	1.51	2.90
D14a	992	0.10	2.66	0.05	110	7.8	33.0	12.4	11.5	0.14	0.89	0.32	1.20
D15a	521	0.11	2.73	0.14	148	31.0	45.9	11.6	10.5	0.72	3.73	0.43	1.55
D16b	470	0.09	2.49	0.14	102	30.7	51.5	11.6	13.8	0.50	4.60	0.52	1.73
D18a	606	0.13	2.45	0.25	92	21.5	23.8	11.0	9.5	0.66	5.41	0.47	1.09
D20a	572	0.10	2.37	0.24	84	8.4	32.0	12.5	13.7	0.33	1.44	0.47	1.33
D22a	0	0.13	2.60	0.00	142	4.2	85.0	10.5	1.1	0.02	0.83	0.03	0.20
E03a	429	0.12	2.39	0.25	83	174.6	57.5	11.8	24.6	2.86	16.09	2.19	5.49
E04a	558	0.15	2.42	0.31	100	20.6	37.8	11.9	11.1	0.39	2.55	0.51	1.31
E05b	878	0.09	2.47	0.27	101	16.0	34.6	12.0	13.7	0.33	1.96	0.58	1.43
E06a	220	0.12	2.81	0.85	91	7.5	48.3	13.4	15.3	0.15	1.28	0.34	1.43
E07b	403	0.14	2.39	0.15	102	58.4	50.8	11.5	10.4	0.48	3.71	0.63	1.62
E08a	679	0.14	2.21	0.28	76	35.6	39.2	11.1	14.2	0.85	7.79	0.68	1.64
E09a	275	0.15	2.79	0.14	118	7.8	48.5	11.5	13.4	0.30	1.99	0.43	1.32
E10a	259	0.19	2.40	0.20	125	12.3	34.7	12.6	14.7	0.07	1.15	0.32	0.96

id	CO_2	H_2O	Li	B	F	Cl	Sr	Y	Zr	Nb	Ba	La	Ce
E11a	399	0.13	2.41	0.45	84	265.2	62.9	11.3	34.2	5.54	25.74	4.02	8.76
E11b	388	0.14	2.57	0.48	88	288.5	62.5	11.3	34.6	5.28	26.67	4.08	8.33
E12a	557	0.11	2.49	0.37	109	48.5	70.9	11.7	26.5	1.46	12.26	1.41	3.56
E13a	70	0.10	2.60	0.39	111	6.5	42.7	13.1	16.2	0.08	0.23	0.29	1.38
E14a	568	0.08	2.24	0.35	100	118.0	26.3	10.1	18.2	4.53	27.40	0.73	1.59
E14b	446	0.13	2.22	0.47	85	177.7	24.5	10.1	28.5	7.44	33.55	0.45	2.42
E15a	424	0.06	3.08	0.11	133	41.5	47.4	10.6	11.4	0.49	4.24	0.58	1.50
E165a	385	0.04	2.62	0.34	98	47.8	28.9	11.4	9.4	1.44	7.96	0.39	1.29
E16a	532	0.13	2.53	0.44	102	201.4	79.8	11.3	26.3	5.12	25.87	4.41	6.64
E16b	594	0.12	2.48	0.46	83	163.4	63.6	11.1	40.6	3.42	18.30	3.07	7.34
E17a	419	0.16	2.54	0.16	103	14.9	31.9	10.6	11.1	0.20	1.67	0.54	1.21
E18a	451	0.17	2.42	0.11	103	21.6	44.5	11.1	10.8	0.23	3.48	0.53	1.53
E19a	46	0.06	2.48	0.08	101	1.1	15.6	9.3	12.7	0.06	0.28	0.61	1.26

Haleyjabunga SIMS (2)

id	Pr	Nd	Sm	Eu	Gd	Tb	Dy	Ho	Er	Tm	Yb	Lu
D01a	1.071	5.58	0.817	0.365	1.35	0.246	1.99	0.457	1.03	0.264	1.27	0.246
D03a	0.267	1.30	0.659	0.370	1.54	0.274	2.27	0.474	1.44	0.166	1.28	0.200
D04a	0.551	3.01	1.232	0.441	1.30	0.262	1.93	0.417	1.07	0.193	0.88	0.183
D05a	0.557	2.68	0.878	0.392	1.03	0.215	1.92	0.363	1.41	0.184	1.46	0.157
D06a	0.292	1.92	1.142	0.484	2.12	0.386	2.16	0.562	1.29	0.196	1.29	0.239
D06b	0.204	1.84	0.873	0.398	1.51	0.265	2.52	0.453	1.22	0.180	1.44	0.169
D07a	0.286	1.36	0.988	0.355	1.08	0.282	1.88	0.428	1.55	0.180	1.49	0.133
D08a	0.217	1.70	0.959	0.370	1.26	0.251	1.50	0.452	1.53	0.159	1.30	0.196
D09a	0.204	1.48	0.612	0.362	0.82	0.289	1.53	0.391	1.27	0.158	1.42	0.121
D10a	0.250	1.35	0.736	0.434	0.88	0.243	1.38	0.472	1.24	0.156	1.27	0.172
D10b	0.211	1.81	0.735	0.347	1.25	0.260	2.01	0.433	0.93	0.163	1.26	0.197
D11a	0.150	1.26	0.967	0.229	1.86	0.207	2.32	0.456	0.98	0.155	1.26	0.156
D12a	0.284	1.54	0.753	0.337	1.68	0.274	1.93	0.524	1.27	0.177	1.01	0.154
D13a	0.338	2.37	0.505	0.220	1.48	0.289	1.86	0.471	1.40	0.179	1.11	0.178
D14a	0.266	1.26	1.150	0.385	1.41	0.329	1.84	0.591	1.79	0.248	1.25	0.230
D15a	0.267	1.44	0.688	0.312	1.44	0.266	2.13	0.423	1.26	0.215	1.27	0.166
D16b	0.394	2.01	0.726	0.402	1.03	0.268	1.90	0.406	1.54	0.131	1.28	0.205
D18a	0.218	1.52	0.884	0.324	1.33	0.244	1.21	0.370	1.34	0.151	1.65	0.232
D20a	0.331	1.94	0.827	0.455	1.57	0.321	2.30	0.466	1.46	0.208	1.75	0.192
D22a	0.025	0.16	0.138	0.144	0.57	0.148	1.25	0.381	1.15	0.259	1.55	0.243
E03a	0.638	3.15	0.593	0.386	1.40	0.228	1.74	0.527	1.37	0.161	1.61	0.169
E04a	0.298	1.83	0.942	0.429	1.65	0.261	2.09	0.482	0.98	0.186	1.25	0.198
E05b	0.271	2.53	0.920	0.390	1.24	0.248	2.27	0.428	1.47	0.199	1.34	0.199
E06a	0.326	1.66	0.986	0.467	2.28	0.320	2.86	0.505	1.45	0.208	1.15	0.162
E07b	0.253	2.18	0.677	0.412	1.39	0.254	1.77	0.477	1.18	0.173	1.24	0.197
E08a	0.267	1.98	0.659	0.271	1.19	0.204	1.35	0.438	1.00	0.164	1.15	0.188
E09a	0.245	1.22	0.792	0.350	1.37	0.223	1.96	0.376	1.08	0.183	1.40	0.177
E10a	0.213	2.56	1.117	0.442	1.94	0.327	2.07	0.585	1.42	0.176	1.35	0.261
E11a	1.086	4.58	0.713	0.393	1.26	0.181	1.57	0.519	1.29	0.183	1.57	0.159
E11b	0.897	3.90	0.852	0.283	1.21	0.266	1.75	0.467	1.07	0.203	1.26	0.144
E12a	0.529	3.60	1.157	0.358	1.45	0.228	1.67	0.426	1.56	0.211	0.97	0.214
E13a	0.314	1.83	0.851	0.398	1.58	0.326	2.49	0.393	1.18	0.233	1.37	0.220
E14a	0.356	1.97	0.652	0.300	1.07	0.222	1.39	0.489	1.38	0.173	0.98	0.183
E14b	0.466	2.76	0.885	0.303	1.39	0.230	2.18	0.395	1.09	0.139	1.34	0.121
E15a	0.268	1.54	0.691	0.310	1.14	0.241	1.72	0.431	0.97	0.103	1.23	0.170
E165a	0.241	1.51	0.747	0.293	1.01	0.276	1.88	0.389	1.42	0.133	1.13	0.193
E16a	0.634	2.32	0.825	0.389	1.78	0.253	2.22	0.505	1.16	0.158	1.27	0.123
E16b	1.047	5.57	1.008	0.434	1.61	0.253	1.60	0.426	1.26	0.178	1.46	0.201
E17a	0.200	1.78	0.755	0.397	1.15	0.227	1.70	0.427	1.02	0.205	1.37	0.182
E18a	0.180	1.61	1.047	0.279	1.32	0.259	1.38	0.434	1.40	0.197	1.37	0.214
E19a	0.208	1.31	0.518	0.309	1.51	0.288	1.49	0.365	0.96	0.136	1.02	0.129

Haleyjabunga EPMA (glass)

id	SiO_2	MgO	FeO	CaO	Al_2O_3	Na2O	K2O	MnO	TiO2	P_2O_5	Cr_2O_3	NiO	SO_2	Total
D01a	47.4	12.3	6.88	12.9	15.3	1.29	0.09	0.12	0.63	0.16	0.13	0.04	0.14	97.5
D03a	48.7	12.9	7.74	13.3	15.2	1.39	0.03	0.14	0.48	0.03	0.08	0.05	0.11	100.1
D04a	50.1	12.4	6.50	13.2	15.7	1.73	0.02	0.12	0.49	0.05	0.14	0.08	0.11	100.8
D05a	48.3	12.0	7.39	12.9	14.7	1.26	0.03	0.13	0.62	0.06	0.13	0.04	0.13	97.6
D06a	48.9	12.6	7.25	13.5	15.7	1.56	0.01	0.14	0.50	0.04	0.07	0.07	0.09	100.5
D06b	48.8	11.9	7.14	13.0	15.6	1.51	0.04	0.12	0.42	0.03	0.11	0.03	0.07	98.8
D07a	49.0	12.8	7.16	13.4	15.5	1.32	0.03	0.14	0.46	0.05	0.12	0.07	0.10	100.1
D09a	48.9	12.6	7.14	13.5	15.4	1.42	0.01	0.13	0.40	0.02	0.12	0.08	0.12	99.9
D10a	48.6	12.5	7.37	13.6	15.2	1.24	0.02	0.16	0.38	0.23	0.14	0.04	0.12	99.6
D10b	48.9	12.8	7.54	13.2	15.3	1.26	0.00	0.14	0.34	0.22	0.12	0.09	0.07	100.0
D12a	49.2	12.1	7.15	13.7	15.9	1.25	0.02	0.16	0.45	0.05	0.14	0.06	0.12	100.3
D13a	48.8	12.2	7.75	13.4	15.0	1.35	0.16	0.11	0.43	0.14	0.08	0.01	0.14	99.6
D14a	48.8	12.2	6.50	13.3	15.9	1.52	0.00	0.13	0.43	0.03	0.10	0.04	0.03	99.0
D15a	49.1	12.8	7.59	13.5	15.8	1.40	0.01	0.13	0.39	0.01	0.12	0.05	0.11	101.0
D16b	49.1	12.7	7.11	13.3	15.6	1.36	0.01	0.15	0.51	0.03	0.16	0.07	0.10	100.2
D18a	49.7	13.1	7.35	13.4	15.9	1.42	0.04	0.11	0.44	0.18	0.16	0.08	0.08	102.0
D20a	50.0	13.0	7.06	13.9	14.8	1.38	0.01	0.12	0.46	0.04	0.06	0.06	0.11	100.9
D22a	49.5	13.0	7.41	14.3	15.6	1.02	0.01	0.12	0.16	0.01	0.13	0.07	0.01	101.4
E01a	48.4	12.6	6.93	13.3	15.4	1.31	0.07	0.14	0.41	0.09	0.12	0.06	0.13	99.0
E01a	48.4	12.6	6.93	13.3	15.4	1.31	0.07	0.14	0.41	0.09	0.12	0.06	0.13	99.0
E04a	49.3	12.6	7.46	13.2	15.6	1.46	0.01	0.13	0.46	0.07	0.12	0.09	0.15	100.7
E05b	50.3	12.7	7.52	13.7	15.2	1.38	0.02	0.13	0.46	0.05	0.18	0.06	0.14	101.8
E06a	49.4	12.9	7.20	13.6	15.8	1.54	0.01	0.16	0.54	0.03	0.11	0.07	0.12	101.4
E07b	50.0	12.8	6.93	13.6	15.4	1.34	0.02	0.13	0.43	0.02	0.13	0.07	0.12	101.1
E08a	50.1	12.7	6.83	13.6	15.1	1.54	0.04	0.11	0.45	0.06	0.17	0.04	0.13	100.8
E09a	48.6	12.3	7.39	13.6	15.4	1.55	0.00	0.15	0.42	0.04	0.04	0.08	0.12	99.7
E10a	48.6	12.3	6.54	13.3	15.5	1.65	0.02	0.11	0.52	0.00	0.10	0.05	0.10	98.7
E11a	49.0	12.7	7.09	13.6	15.8	1.32	0.15	0.14	0.38	0.15	0.16	0.05	0.13	100.7
E11b	49.6	12.9	7.18	13.6	15.7	1.43	0.11	0.12	0.38	0.17	0.13	0.06	0.12	101.6
E12a	49.1	12.8	7.00	13.3	14.7	1.38	0.05	0.12	0.55	0.09	0.06	0.05	0.10	99.3
E13a	49.0	12.5	7.07	13.4	16.1	1.57	0.01	0.14	0.45	0.05	0.15	0.08	0.14	100.6
E14a	48.8	12.2	7.32	13.9	15.4	1.35	0.12	0.11	0.42	0.24	0.15	0.04	0.11	100.1
E14b	49.7	12.6	6.84	13.9	15.4	1.38	0.15	0.09	0.44	0.27	0.14	0.06	0.14	101.1
E16a	49.4	12.7	7.10	13.5	15.8	1.47	0.15	0.14	0.41	0.12	0.05	0.07	0.12	101.1
E16b	49.0	15.9	7.04	12.3	14.7	1.33	0.06	0.15	0.51	0.10	0.09	0.03	0.11	101.3
E17a	48.4	12.2	6.95	13.1	15.0	1.41	0.00	0.13	0.46	0.05	0.07	0.04	0.09	98.0
E18a	49.5	12.7	7.01	13.4	15.4	1.43	0.02	0.14	0.48	0.03	0.13	0.06	0.09	100.3
E19a	49.9	12.8	7.48	13.6	15.4	1.48	0.00	0.14	0.37	0.04	0.17	0.08	0.08	101.6

Haleyjabunga EPMA (hosts)

id	SiO_2	MgO	FeO	CaO	Al_2O_3	MnO	P_2O_5	Cr_2O_3	NiO	Total
D01a	40.4	48.6	10.1	0.35	0.05	0.16	0.008	0.06	0.34	100.1
D03a	40.6	48.6	10.6	0.35	0.06	0.19	0.011	0.07	0.32	100.9
D04a	40.5	48.8	9.6	0.33	0.07	0.16	0.002	0.09	0.35	100.0
D05a	40.9	48.4	10.3	0.36	0.04	0.17	0.002	0.04	0.28	100.5
D06a	40.6	48.2	10.4	0.35	0.06	0.15	0.005	0.06	0.31	100.1
D06b	40.4	48.3	10.5	0.36	0.06	0.16	0.000	0.04	0.30	100.1
D07a	40.2	48.1	10.3	0.35	0.05	0.19	0.005	0.06	0.33	99.5
D09a	40.6	48.4	10.3	0.35	0.08	0.15	0.000	0.09	0.32	100.4
D10a	40.5	48.4	10.3	0.36	0.07	0.17	0.068	0.06	0.31	100.3
D10b	40.6	48.6	10.4	0.36	0.06	0.20	0.061	0.06	0.30	100.7
D11a	41.0	48.9	10.5	0.35	0.06	0.20	0.002	0.07	0.31	101.3
D12a	41.3	48.9	10.4	0.35	0.05	0.18	0.007	0.05	0.32	101.5
D13a	40.7	48.0	10.9	0.36	0.06	0.17	0.010	0.06	0.31	100.6
D14a	40.9	48.9	9.9	0.35	0.06	0.16	0.004	0.09	0.32	100.7
D15a	40.8	48.5	10.4	0.34	0.06	0.17	0.004	0.05	0.31	100.6
D16b	41.0	48.6	10.2	0.35	0.05	0.19	0.002	0.04	0.33	100.7

id	SiO_2	MgO	FeO	CaO	Al_2O_3	MnO	P_2O_5	Cr_2O_3	NiO	Total
D18a	40.9	48.6	10.1	0.35	0.07	0.18	0.009	0.06	0.31	100.7
D20a	40.7	48.5	10.1	0.37	0.06	0.19	0.002	0.08	0.25	100.2
D22a	40.7	48.6	10.4	0.35	0.05	0.15	0.005	0.04	0.33	100.7
E01a	40.5	48.5	10.1	0.35	0.05	0.15	0.006	0.08	0.30	100.1
E01a	40.5	48.5	10.1	0.35	0.05	0.15	0.006	0.08	0.30	100.1
E04a	40.5	48.5	10.3	0.35	0.06	0.17	0.006	0.06	0.30	100.3
E05b	40.6	48.6	10.2	0.36	0.06	0.17	0.005	0.08	0.28	100.3
E06a	40.7	48.3	10.3	0.35	0.06	0.17	0.001	0.07	0.30	100.3
E07b	40.6	48.7	10.0	0.35	0.05	0.18	0.005	0.05	0.31	100.3
E08a	40.6	48.6	9.8	0.36	0.07	0.16	0.009	0.09	0.30	100.0
E09a	40.1	48.0	10.6	0.34	0.07	0.18	0.005	0.05	0.31	99.6
E10a	40.7	49.0	9.5	0.34	0.08	0.16	0.003	0.08	0.35	100.2
E11a	40.5	48.4	10.1	0.34	0.05	0.16	0.035	0.06	0.31	100.1
E11b	40.6	48.5	10.1	0.34	0.06	0.17	0.071	0.07	0.32	100.2
E12a	40.4	48.1	10.4	0.35	0.05	0.15		0.04	0.28	99.8
E13a	40.5	48.6	9.8	0.35	0.08	0.13	0.003	0.08	0.32	99.9
E14a	40.5	48.6	9.9	0.37	0.06	0.15	0.017	0.07	0.32	99.9
E14b	40.4	48.4	9.8	0.36	0.05	0.15	0.003	0.08	0.31	99.6
E16a	40.5	48.3	10.2	0.35	0.05	0.17	0.017	0.08	0.29	99.9
E16b	40.4	48.1	10.1	0.35	0.05	0.18	0.009	0.06	0.31	99.6
E17a	40.5	48.0	10.2	0.35	0.06	0.20	0.006	0.06	0.32	99.7
E18a	40.4	48.1	10.3	0.34	0.05	0.16	0.008	0.05	0.31	99.7
E19a	40.6	48.1	10.2	0.34	0.06	0.16	0.006	0.05	0.29	99.8

Haleyjabunga Raman

id	p1	p1 err	p2	p2 err	bubble diameter	Mi long	Mi short	delta	density
D02a	1284.36	0.1	1387.12	0.09	8	40	31	102.76	0.124
D03a					17	50	41		
E01a	1283.89	0.13	1386.78	0.1	8	44	39	102.89	0.171
E01a					5	32	27		
E02a					34	136	95		
E03a	1285.26	0.17	1387.98	0.2	26	101	85	102.72	0.110
E06a	1284.6	0.17	1387.14	0.08	20	96	88	102.54	0.052
E07a					11	64	50		
E07b					15	75	64		
E12a	1284.81	0.17	1387.56	0.16	7	76	41	102.75	0.120
E07a					31	71	69		
HAL_um02					15	80	68		

Heilagsdalsfjall SIMS (1)

id	CO_2	H_2O	Li	B	F	Cl	Sr	Y	Zr	Nb	Ba	La	Ce
A16a	332	0.050	3.24	0.111	76.9	15.1	68.3	15.5	16.8	1.085	8.28	1.014	2.79
A17a	357												
A19a	561	0.063	3.34	0.150	62.1	43.6	72.9	15.5	13.3	0.742	6.03	0.805	2.31
A20a	342	0.051	3.69	0.109	64.2	10.7	66.9	15.7	14.4	0.773	5.49	0.796	2.08
A21a	351	0.051	3.28	0.107	64.7	11.1	66.7	15.1	15.8	0.695	5.19	0.970	2.40
A22a	352	0.049	1.05	0.108	51.4	9.2	63.1	16.0	14.6	0.645	4.76	0.684	2.17
A23a	360	0.051	3.28	0.136	59.4	8.6	65.4	14.7	12.9	0.562	5.53	0.733	2.24
A24a	376	0.051	3.48	0.124	53.7	14.0	48.7	15.6	15.8	1.034	4.58	0.784	2.42
B21a	343	0.047	3.56	0.102	64.5	16.1	82.1	15.6	13.8	0.560	5.05	0.751	2.46
B22a	23	0.050	3.35	0.117	87.9	27.3	69.7	16.2	18.5	1.218	8.67	1.306	3.01
B23a	340	0.049	3.46	0.132	62.6	7.8	56.6	14.9	13.7	0.631	4.49	0.622	2.38
B23b	330	0.051	3.44	0.123	65.5	14.8	59.1	15.5	13.3	0.673	4.59	0.817	1.82
B24a	404	0.053	3.21	0.125	65.8	17.7	68.6	15.4	16.5	0.991	8.57	1.236	2.63
B24b	53	0.051	3.59	0.136	80.1	35.6	70.7	17.4	18.8	1.199	10.66	1.332	3.47
B24e	314	0.050	3.49	0.146	68.9	16.3	76.7	16.6	12.5	0.476	5.20	0.876	2.18
B25a	330	0.048	3.69	0.165	68.9	16.2	64.0	16.8	14.4	0.788	4.61	0.677	2.12
B26a	389	0.051	3.68	0.155	71.4	12.5	58.2	14.6	12.3	0.602	4.38	0.683	1.68

id	CO_2	H_2O	Li	B	F	Cl	Sr	Y	Zr	Nb	Ba	La	Ce
C15a	329	0.073	3.49	0.107	60.8	14.0	62.8	15.2	13.0	0.662	5.22	0.581	2.10
C15b	305	0.065	3.39	0.116	51.6	15.9	58.1	14.1	12.4	0.560	4.34	0.645	1.77
C19a	360	0.065	3.50	0.159	70.5	13.4	47.7	15.7	15.9	0.910	4.49	0.950	2.50
C19b		0.058	3.10	0.132	71.4	12.5	69.4	15.8	17.6	1.069	10.40	1.167	3.20
C19c		0.060	3.24	0.122	72.9	16.3	69.9	16.7	18.5	1.056	9.37	1.247	3.23
Z01a	461	0.079	3.42	0.154	70.5	13.6	63.2	15.6	13.5	0.512	4.91	0.721	2.01
Z01b	323	0.074	3.20	0.167	90.3	13.9	68.9	16.1	17.7	0.975	9.65	1.110	3.44
Z01c	193												
Z01d	136												

Heilagsdalsfjall SIMS (2)

id	Pr	Nd	Sm	Eu	Gd	Tb	Dy	Ho	Er	Tm	Yb	Lu
A16a	0.476	2.62	0.95	0.434	1.23	0.359	2.83	0.556	1.62	0.273	1.44	0.200
A19a	0.300	2.38	1.07	0.509	2.31	0.360	2.47	0.724	1.52	0.240	1.53	0.225
A20a	0.408	2.24	1.27	0.528	1.64	0.482	2.92	0.562	1.90	0.269	2.33	0.231
A21a	0.392	2.38	0.92	0.506	1.79	0.536	3.01	0.549	1.84	0.322	1.56	0.239
A22a	0.378	2.50	1.17	0.655	1.11	0.358	2.73	0.599	2.05	0.221	1.96	0.290
A23a	0.419	3.00	1.18	0.580	1.53	0.348	2.20	0.570	2.04	0.235	1.94	0.221
A24a	0.341	2.59	0.93	0.532	1.56	0.383	2.27	0.520	1.61	0.180	1.86	0.226
B21a	0.360	2.08	1.46	0.545	1.41	0.300	2.64	0.612	1.90	0.217	2.33	0.276
B22a	0.489	3.01	1.38	0.513	1.95	0.309	2.38	0.606	1.80	0.314	2.20	0.259
B23a	0.361	2.71	0.82	0.396	1.76	0.283	2.35	0.584	1.98	0.265	1.69	0.250
B23b	0.334	3.11	1.22	0.388	1.51	0.390	2.70	0.600	1.94	0.238	1.75	0.231
B24a	0.512	2.70	1.05	0.503	1.68	0.432	2.54	0.557	1.97	0.238	2.07	0.249
B24b	0.605	4.03	1.37	0.685	1.79	0.375	2.90	0.678	1.98	0.327	1.79	0.281
B24e	0.390	2.76	1.37	0.572	2.18	0.382	2.68	0.762	1.70	0.299	1.97	0.277
B25a	0.368	2.25	1.16	0.542	1.85	0.516	3.21	0.561	2.13	0.193	2.10	0.215
B26a	0.315	1.73	0.98	0.358	1.61	0.371	2.39	0.531	1.47	0.196	1.68	0.166
C15a	0.280	2.12	1.07	0.452	1.51	0.374	2.79	0.532	1.39	0.229	1.74	0.318
C15b	0.287	2.36	0.71	0.450	1.51	0.225	1.78	0.536	1.94	0.174	1.71	0.205
C19a	0.332	2.64	1.43	0.675	1.92	0.380	2.79	0.581	2.02	0.295	1.94	0.214
C19b	0.473	2.36	1.22	0.475	1.39	0.274	3.04	0.641	1.69	0.306	1.89	0.251
C19c	0.444	2.87	1.08	0.551	1.70	0.400	2.70	0.505	2.01	0.257	1.80	0.345
Z01a	0.339	2.80	1.09	0.518	1.84	0.354	2.56	0.585	1.62	0.221	1.78	0.312
Z01b	0.442	2.72	1.30	0.498	2.10	0.423	2.81	0.534	1.78	0.293	1.96	0.300

Heilagsdalsfjall EPMA (glass)

id	SiO_2	MgO	FeO	CaO	Al_2O_3	Na_2O	K_2O	MnO	TiO_2	P_2O_5	Cr_2O_3	NiO	SO_2	Total
A16a	50.1	8.51	9.53	14.1	16.0	1.64	0.02	0.20	0.67	0.07	0.09	0.03	0.08	101.0
A17a	50.1	7.91	8.98	14.5	16.5	1.78	0.02	0.19	0.75	0.03	0.12	0.01	0.08	100.9
A19a	49.6	6.87	8.41	14.8	16.8	1.57	0.01	0.11	0.71	0.04	0.10	0.05	0.08	99.1
A20a	50.8	8.37	9.06	14.5	16.5	1.62	0.03	0.12	0.73	0.02	0.08	0.03	0.11	101.9
A21a	50.0	8.15	9.06	14.1	16.3	1.72	0.04	0.16	0.75	0.05	0.05	0.05	0.11	100.5
A22a	50.4	8.36	8.92	14.5	16.3	1.61	0.03	0.17	0.72	0.02	0.10	0.04	0.12	101.3
A23a	47.0	14.38	8.61	10.8	13.7	1.88	0.01	0.16	0.54	0.01	0.10	0.03	0.09	97.4
A24a	49.6	8.68	8.34	13.8	15.9	1.58	0.02	0.16	0.61	0.03	0.08		0.12	98.9
B21a	50.1	6.82	8.63	15.2	16.9	1.58	0.01	0.16	0.86	0.01	0.11		0.12	100.6
B22a	49.0	5.29	8.49	14.8	16.6	1.89	0.05	0.19	0.67	0.06	0.07		0.10	97.1
B23a	48.6	8.31	8.47	13.9	15.5	1.65	0.04	0.13	0.60	0.05	0.06	0.04	0.10	97.5
B23b	49.3	8.32	8.79	14.3	16.0	1.63	0.02	0.16	0.67	0.04	0.07	0.04	0.12	99.5
B24a	48.9	7.48	9.12	14.3	15.9	1.61	0.04	0.20	0.67	0.04	0.06		0.13	98.5
B24b	51.1	6.41	9.38	14.6	16.6	1.84	0.05	0.19	0.77	0.04	0.04	0.01	0.06	101.1
B24e	51.0	5.30	8.35	15.7	17.6	1.83	0.02	0.20	0.80	0.04	0.03	0.01	0.17	101.0
B25a	50.8	5.72	7.74	15.1	17.9	2.01	0.04	0.14	0.74	0.04	0.09	0.04	0.14	100.5
B26a	50.1	8.24	8.77	14.8	16.1	1.63	0.03	0.14	0.67	0.02	0.09	0.06	0.15	100.8
C15a	49.2	8.83	8.62	14.2	15.9	1.61	0.00	0.21	0.66	0.04	0.08	0.04	0.16	99.6

id	SiO_2	MgO	FeO	CaO	Al_2O_3	Na_2O	K_2O	MnO	TiO_2	P_2O_5	Cr_2O_3	NiO	SO_2	Total
C15b	48.5	8.68	8.56	14.0	15.8	1.56	0.04	0.14	0.67	0.02	0.06	0.03	0.12	98.1
C19a	49.3	7.98	7.95	14.5	16.1	1.62	0.03	0.15	0.58	0.06	0.06	0.05	0.12	98.5
C19b	48.5	6.46	8.63	13.7	16.2	1.87	0.06	0.13	0.66	0.06	0.07		0.06	96.4
C19c	50.1	7.54	9.74	14.3	16.1	1.69	0.04	0.18	0.74	0.03	0.08	0.04	0.06	100.7

Heilagsdalsfjall EPMA (hosts)

id	SiO2	MgO	FeO	CaO	Al2O3	MnO	P2O5	Cr2O3	NiO	Total
A16a	40.8	47.5	11.6	0.33	0.07	0.20	0.014	0.05	0.28	100.9
A17a	40.9	47.6	11.4	0.33	0.06	0.18	0.002	0.08	0.29	100.8
A19a	40.3	47.9	11.2	0.32	0.06	0.18		0.10	0.30	100.4
A20a	41.0	48.0	11.5	0.33	0.07	0.19	0.006	0.09	0.29	101.5
A21a	40.9	47.6	11.7	0.35	0.06	0.17		0.08	0.28	101.1
A22a	41.0	47.8	11.2	0.34	0.07	0.20	0.007	0.08	0.29	101.0
A23a	40.4	47.3	11.5	0.34	0.06	0.18	0.014	0.08	0.29	100.1
A24a	40.6	47.9	11.1	0.34	0.07	0.19	0.006	0.09	0.31	100.6
B21a	40.6	47.0	11.5	0.34	0.06	0.19	0.003	0.06	0.29	100.1
B22a	40.3	46.0	12.4	0.38	0.06	0.22	0.002	0.06	0.30	99.6
B23a	40.6	47.0	11.2	0.34	0.07	0.18	0.007	0.06	0.32	99.7
B23b	40.6	47.0	11.2	0.34	0.07	0.18	0.007	0.06	0.32	99.7
B24a	40.9	46.7	11.8	0.34	0.06	0.17	0.005	0.06	0.29	100.3
B24b	40.8	46.4	11.9	0.33	0.06	0.19	0.000	0.06	0.28	100.1
B25a	40.5	46.5	11.4	0.34	0.07	0.19	0.004	0.06	0.29	99.3
B26a	40.5	46.2	11.8	0.33	0.06	0.19	0.003	0.06	0.29	99.6
C15a	40.8	47.0	11.4	0.33	0.07	0.17	0.004	0.08	0.32	100.2
C15b	40.8	47.0	11.4	0.33	0.07	0.17	0.004	0.08	0.32	100.2
C19a	40.5	47.2	11.1	0.32	0.07	0.19	0.004	0.07	0.33	99.8
C19b	40.6	46.9	11.2	0.33	0.06	0.19	0.003	0.06	0.30	99.6
C19c	40.5	46.9	11.3	0.33	0.06	0.20	0.007	0.06	0.31	99.7

Stapafell SIMS (1)

id	CO_2	H_2O	Li	B	F	Cl	Sr	Y	Zr	Nb	Ba	La	Ce
A01a	1713	0.36	3.35	0.657	533	167	197	22.8	95.6	15.1	73.8	11.07	25.4
A02a	892	0.43	3.43	0.614	375	119	164	18.5	63.9	8.6	45.6	6.77	15.5
A04a	843	0.40	3.84	0.728	471	162	176	22.3	79.0	11.5	67.8	8.75	21.8
A04b	1598	0.40	3.61	0.678	506	156	183	20.4	85.1	13.1	70.8	9.79	21.5
A04c	1611	0.40	3.47	0.651	522	169	192	21.3	84.0	13.2	74.8	9.74	23.2
A04d	876	0.43	3.73	0.708	468	154	192	22.3	87.3	13.6	72.6	9.80	23.8
A06a	756	0.41	3.23	0.710	569	171	202	21.3	87.3	14.3	77.6	11.09	24.4
A06d	1975	0.40	3.22	0.832	685	223	217	21.9	92.2	16.1	91.3	12.56	28.4
A08a	1006	0.43	2.89	0.724	461	192	198	20.1	86.6	14.2	76.3	11.00	24.2
A09a	594	0.41	3.08	0.734	657	103	237	21.3	60.4	5.5	48.4	5.97	14.8
A10a	630	0.43	3.64	0.216	445	47	143	11.7	31.1	2.3	19.0	2.41	6.7
A11a	1877	0.42	3.21	0.853	598	203	219	21.8	101.6	16.4	92.6	12.51	29.5
A13b	1117	0.41	3.54	0.721	339	164	141	20.7	67.6	13.0	66.8	7.61	16.8
A14b	1349	0.39	3.67	0.716	456	184	130	19.2	66.5	11.4	96.7	6.64	16.5
B01a	1865	0.41	3.00	0.868	438	192	160	14.0	74.3	13.2	69.5	6.97	18.9
B02a	934	0.38	3.39	0.811	566	235	239	21.1	100.1	11.7	82.8	10.46	24.1
B04a	998	0.44	3.28	0.636	593	167	193	20.1	80.6	13.4	74.4	9.48	22.8
B05a	1284	0.44	3.64	0.707	511	197	176	21.6	69.0	9.1	63.8	7.49	17.4
B06a	1131	0.43	3.29	0.666	473	162	170	20.4	74.3	10.6	60.1	8.47	19.5
B06b	1253	0.41	3.34	0.695	485	176	172	21.4	75.8	10.6	60.5	8.84	20.1
B07a	1870	0.42	3.16	0.759	614	182	203	21.5	90.7	14.8	82.9	10.99	25.7
B09a	722	0.42	4.26	0.871	421	216	144	24.6	106.2	14.2	75.9	9.59	23.7
B10a	506	0.43	3.67	0.695	464	205	156	21.1	80.7	11.4	59.8	8.24	19.8
B12a	1757	0.41	3.60	0.789	443	193	203	22.2	106.4	16.3	81.7	12.26	27.4
B13a	1874	0.41	3.20	0.704	490	149	195	21.1	84.2	13.5	77.0	10.50	24.6
B14a	1079	0.41	3.42	0.632	532	172	191	20.7	80.9	12.8	72.7	10.12	23.3
B15a	1100	0.39	3.30	0.665	503	156	186	19.6	82.9	12.6	65.5	9.98	21.6
B16a	1475	0.39	3.56	0.671	438	151	176	20.2	74.6	11.6	65.6	9.37	21.5

id	CO_2	H_2O	Li	B	F	Cl	Sr	Y	Zr	Nb	Ba	La	Ce
B17a	1200	0.42	3.67	0.301	460	35	145	20.4	92.5	2.3	10.0	8.28	24.6
B18a	1567	0.41	3.67	0.680	487	150	186	20.4	78.9	12.9	71.2	9.57	21.1
B19a	1316	0.44	3.44	0.690	592	147	170	21.5	76.6	11.1	62.8	9.08	20.8
B19b	1293	0.44	3.44	0.758	610	158	171	20.8	74.9	11.1	64.0	8.42	19.9
C01a	1632	0.42	3.29	0.870	561	201	212	22.4	106.7	17.0	84.7	12.53	29.7
C03a	679	0.38	3.22	0.377	556	115	99	17.0	42.9	6.1	34.7	5.24	12.2
C04a	1061	0.43	3.17	0.779	488	85	112	16.9	58.3	7.6	24.7	5.37	15.2
C07a	2079	0.47	3.71	0.899	498	207	141	24.0	108.6	15.6	82.5	10.06	23.1
C09a	1675	0.41	3.41	0.791	524	187	201	19.9	90.3	14.5	82.6	11.33	25.0
C09b	1820	0.47	3.76	0.915	596	217	215	22.6	96.4	15.6	88.0	12.04	26.3
C11a	1294	0.43	3.70	0.706	521	149	165	21.3	72.6	10.2	60.4	7.51	19.2
C12a	1132	0.36	3.93	0.727	600	206	200	23.3	94.1	14.6	80.1	10.36	24.8
D23a	1122	0.44	3.90	0.371	553	52	254	18.8	82.7	1.7	14.3	5.09	19.1
D24a	1678	0.45	3.53	0.796	613	382	212	21.0	79.2	11.6	84.4	8.56	20.9
D25a	1432	0.44	4.01	0.507	616	323	166	17.8	50.9	8.5	73.2	6.29	14.0
D25b	1485	0.46	4.18	0.634	626	358	175	17.8	54.3	10.2	85.0	7.43	15.8
D25c	1534	0.49	4.07	0.601	554	332	172	20.5	55.2	9.5	79.5	7.54	17.8
D27a	1726	0.48	3.75	0.825	622	300	207	20.8	90.1	14.7	84.2	10.90	24.7
D28a	1616	0.47	3.63	0.606	626	196	177	20.2	73.3	11.1	64.5	8.26	21.1
D31a	1050	0.48	3.54	0.813	553	245	196	19.9	89.1	13.8	78.1	9.81	23.5
D36a	1018	0.47	3.45	0.321	634	77	128	18.8	66.5	5.2	25.0	4.84	16.1
E21a	994	0.45	4.05	0.877	374	270	160	27.8	139.7	16.6	81.2	10.66	26.2
E22d	1871	0.47	3.59	0.777	665	275	218	21.8	91.1	14.5	88.3	11.30	26.1
E23a	1378	0.48	3.72	0.731	559	253	192	22.4	79.8	11.6	68.4	9.21	20.9
E23b	1558	0.49	3.65	0.701	578	264	194	21.3	75.6	11.3	69.6	9.20	20.9
E24a	1684	0.48	3.76	0.773	574	263	214	22.2	96.7	14.4	85.6	10.59	26.2
E24b	1523	0.47	3.69	0.776	576	295	207	21.5	89.1	14.4	82.5	9.94	24.9
E25b	1297	0.48	3.71	0.695	373	235	174	17.7	62.2	8.1	64.0	6.61	16.3
E25c	1290	0.48	3.35	0.660	661	241	181	21.6	80.2	10.7	65.9	9.00	20.3
E26a	1222	0.46	3.61	0.667	597	209	177	19.9	74.2	11.0	67.1	9.14	19.8
E26b	1508	0.46	3.43	0.827	596	288	207	22.3	105.0	16.5	81.6	11.88	25.3
E27a	731	0.45	3.55	0.678	508	248	158	18.7	74.6	14.8	60.0	7.05	18.6
E28a	1246	0.46	3.74	0.768	599	302	211	22.0	94.5	14.5	83.8	10.64	25.7
E29a	929	0.45	3.82	0.757	527	289	210	23.1	94.6	14.9	84.7	11.31	26.3
E30a	1256	0.47	3.71	0.826	563	265	210	21.9	97.1	15.3	85.0	10.72	25.2
E31a	1371	0.44	3.80	0.762	601	275	198	21.8	87.8	13.9	80.2	9.69	23.1
E31b	1395	0.45	3.76	0.833	552	313	203	22.2	89.8	14.2	82.5	9.87	23.3
E32a	1009	0.45	3.63	0.785	605	290	209	22.5	97.2	15.0	80.2	11.92	26.0
E34a	2142	0.49	3.67	0.881	794	371	242	22.8	106.1	18.0	105.1	13.19	30.5
E35a	1107	0.49	3.69	0.721	587	338	200	18.7	81.5	13.6	83.1	10.19	22.8
E37a	1004	0.45	3.87	0.704	482	206	165	22.8	76.9	10.6	58.6	7.74	18.6
E39b	1401	0.47	4.61	0.631	406	430	143	26.4	106.0	11.1	50.1	10.70	24.2

Stapafell SIMS (2)

id	Pr	Nd	Sm	Eu	Gd	Tb	Dy	Ho	Er	Tm	Yb	Lu
A01a	3.52	18.0	4.31	1.50	5.46	0.677	4.51	0.812	3.24	0.292	2.57	0.333
A02a	2.28	10.5	3.32	1.07	3.09	0.601	3.45	0.654	2.11	0.316	2.03	0.291
A04a	2.91	15.0	3.22	1.17	3.26	0.692	3.62	0.829	2.85	0.338	2.27	0.340
A04b	2.97	14.9	4.15	1.19	3.86	0.668	4.37	0.803	2.68	0.282	2.02	0.270
A04c	3.17	15.3	3.07	1.11	4.01	0.726	4.33	0.884	2.22	0.372	2.52	0.346
A04d	3.15	15.1	3.44	1.22	4.11	0.554	4.74	0.784	2.40	0.340	2.63	0.349
A06a	3.63	15.7	4.15	1.46	3.82	0.647	4.70	0.855	1.97	0.273	1.94	0.322
A06d	3.85	18.2	4.29	1.16	4.34	0.602	4.49	0.886	2.31	0.343	1.88	0.359
A08a	3.27	15.5	3.76	1.41	3.63	0.631	3.45	0.814	2.17	0.285	1.88	0.330
A09a	2.07	11.4	3.03	1.01	3.21	0.669	3.60	0.873	2.64	0.250	2.60	0.334
A10a	1.06	6.1	1.78	0.69	1.76	0.342	1.77	0.402	1.33	0.138	1.66	0.201
A11a	3.72	18.2	4.53	1.38	5.22	0.762	4.90	0.880	2.48	0.326	2.37	0.218
A13b	2.40	12.0	3.26	1.14	3.22	0.558	4.05	0.822	2.35	0.311	1.95	0.255
A14b	2.23	12.3	3.25	1.15	3.08	0.559	3.89	0.756	2.34	0.331	2.14	0.267
B01a	2.47	11.8	2.82	0.79	2.44	0.468	3.19	0.579	1.59	0.240	1.29	0.181
B02a	3.62	17.4	4.19	1.30	3.28	0.548	4.39	0.776	2.38	0.316	1.56	0.265
B04a	2.97	13.7	3.40	1.06	3.39	0.609	4.38	0.808	2.16	0.233	1.61	0.311
B05a	2.23	12.3	3.56	0.97	2.87	0.558	4.48	0.852	2.51	0.306	1.53	0.334
B06a	2.50	12.5	3.57	1.24	3.66	0.659	4.42	0.684	1.94	0.284	2.21	0.256
B06b	2.61	11.5	3.12	1.17	3.54	0.577	3.86	0.785	2.39	0.289	2.15	0.207
B07a	3.05	17.8	4.32	1.30	4.70	0.691	4.65	0.798	2.35	0.251	1.82	0.286

id	Pr	Nd	Sm	Eu	Gd	Tb	Dy	Ho	Er	Tm	Yb	Lu
B09a	3.46	17.1	4.26	1.25	4.06	0.760	4.51	0.930	2.84	0.383	2.62	0.316
B10a	2.74	13.1	3.29	1.11	3.56	0.582	4.81	0.914	2.62	0.385	2.41	0.388
B12a	3.56	18.8	4.10	1.58	5.17	0.787	3.83	0.878	2.43	0.360	2.04	0.279
B13a	3.08	15.6	3.06	1.25	3.56	0.744	3.74	1.011	2.06	0.332	1.98	0.240
B14a	3.06	14.6	3.62	0.98	4.06	0.747	3.22	0.827	2.13	0.346	2.11	0.341
B15a	2.98	14.3	3.61	1.25	3.12	0.595	3.56	0.735	2.38	0.253	1.55	0.259
B16a	2.77	13.7	2.89	1.19	3.90	0.748	4.55	0.822	2.11	0.337	1.93	0.257
B17a	3.31	14.7	3.83	1.21	4.46	0.726	3.90	0.935	2.50	0.361	1.56	0.309
B18a	2.99	13.8	3.15	1.29	3.67	0.537	4.14	0.807	2.05	0.252	2.14	0.238
B19a	2.67	14.3	2.88	1.14	3.31	0.621	4.11	0.922	2.57	0.306	2.21	0.292
B19b	2.82	12.6	3.28	0.96	3.29	0.580	4.01	0.699	2.75	0.361	1.75	0.279
C01a	4.10	20.1	4.43	1.55	5.04	0.664	4.10	0.875	2.20	0.261	2.22	0.350
C03a	1.75	8.5	1.67	0.73	2.54	0.549	3.57	0.629	1.57	0.278	2.06	0.303
C04a	2.25	9.5	3.03	0.77	2.82	0.549	3.42	0.647	1.59	0.311	1.64	0.309
C07a	3.12	16.2	3.62	1.21	4.04	0.689	4.32	0.792	2.61	0.377	2.40	0.293
C09a	3.30	15.0	3.56	1.07	4.23	0.591	3.65	0.770	2.32	0.273	1.54	0.299
C09b	3.40	17.8	3.60	1.40	3.51	0.667	4.61	0.861	2.48	0.269	1.55	0.323
C11a	2.49	12.5	2.73	1.10	3.69	0.690	4.39	0.781	2.15	0.325	1.86	0.338
C12a	3.33	16.2	4.05	1.37	3.85	0.562	3.94	0.982	2.38	0.346	2.53	0.333
D23a	2.78	14.4	3.62	1.15	3.55	0.655	3.59	0.700	2.12	0.389	2.34	0.311
D24a	2.71	14.2	3.02	1.34	3.57	0.560	4.63	0.794	2.38	0.372	2.35	0.349
D25a	1.88	8.9	2.30	0.82	3.08	0.463	2.92	0.710	1.96	0.384	2.14	0.234
D25b	2.03	11.1	2.57	0.76	2.80	0.521	3.31	0.728	2.25	0.302	2.24	0.275
D25c	2.26	10.2	2.37	1.12	3.39	0.625	3.31	0.753	1.93	0.326	2.25	0.342
D27a	3.26	17.6	4.04	1.45	4.26	0.754	3.95	0.848	2.45	0.291	2.39	0.362
D28a	2.75	12.1	2.52	1.01	3.67	0.670	3.65	0.827	2.11	0.385	2.50	0.302
D31a	3.01	15.5	3.61	1.07	4.30	0.622	4.58	0.837	2.11	0.353	1.91	0.393
D36a	2.25	12.0	2.26	1.07	3.22	0.444	2.87	0.771	2.06	0.267	2.20	0.324
E21a	3.97	20.6	5.21	1.52	6.35	0.979	4.98	1.166	2.96	0.359	3.21	0.321
E22d	3.63	16.5	4.03	1.19	4.29	0.766	3.92	0.785	2.38	0.336	2.66	0.329
E23a	3.01	15.0	4.11	1.27	4.41	0.720	3.51	0.873	2.04	0.316	2.25	0.332
E23b	2.87	13.2	3.49	1.22	3.83	0.679	3.84	0.895	2.51	0.364	1.58	0.289
E24a	3.69	17.9	4.01	1.50	4.65	0.739	4.09	0.836	2.95	0.372	2.03	0.288
E24b	3.24	16.8	3.15	1.46	5.61	0.768	4.68	0.720	2.25	0.319	1.99	0.284
E25b	2.11	9.9	2.55	1.13	2.11	0.470	3.04	0.657	1.86	0.265	1.63	0.250
E25c	2.68	13.8	3.53	0.90	3.79	0.641	4.20	0.859	2.45	0.342	2.45	0.309
E26a	2.85	14.5	3.67	1.18	4.30	0.609	3.13	0.757	2.09	0.288	1.57	0.263
E26b	3.46	16.8	4.29	1.17	4.75	0.550	3.84	0.852	2.30	0.338	2.06	0.226
E27a	2.46	12.5	3.44	1.04	3.56	0.495	3.40	0.745	1.84	0.289	1.87	0.288
E28a	3.26	15.4	3.73	1.48	4.13	0.705	3.56	0.805	2.38	0.321	2.20	0.288
E29a	3.75	16.6	4.14	1.47	4.15	0.675	3.95	0.793	2.21	0.333	2.03	0.351
E30a	3.56	15.3	3.53	1.21	4.63	0.635	4.32	0.849	2.50	0.385	2.18	0.299
E31a	3.19	15.3	3.49	1.19	4.56	0.815	4.21	0.897	2.48	0.426	2.10	0.303
E31b	3.13	14.7	4.18	1.21	4.01	0.687	3.65	0.847	2.50	0.345	2.40	0.287
E32a	3.65	16.1	3.72	1.32	4.43	0.695	4.55	0.974	2.38	0.395	2.74	0.340
E34a	3.82	17.8	4.57	1.44	3.85	0.757	4.46	0.992	2.96	0.309	2.46	0.344
E35a	2.95	14.3	3.99	1.14	4.10	0.561	3.37	0.730	2.09	0.310	1.75	0.298
E37a	2.64	12.6	4.57	1.21	3.96	0.550	4.03	0.728	1.96	0.376	2.40	0.330
E39b	3.40	16.5	4.22	1.36	4.54	0.673	4.45	1.010	3.08	0.457	2.90	0.401

Stapafell EPMA (glass)

id	SiO_2	MgO	FeO	CaO	Al_2O_3	Na_2O	K_2O	MnO	TiO_2	P_2O_5	Cr_2O_3	SO_2	Total
A01a	49.2	4.77	9.63	13.5	16.3	2.31	0.30	0.17	1.98	0.29	0.08	0.19	98.7
A02a	50.6	7.51	9.99	12.2	14.6	1.88	0.18	0.16	1.30	0.17	0.03	0.16	98.8
A04a	49.2	7.42	10.59	12.1	14.6	2.06	0.31	0.19	1.59	0.22	0.06	0.15	98.5
A04b	48.7	7.61	10.39	12.3	14.8	2.01	0.27	0.20	1.62	0.24	0.06	0.15	98.3
A04c	49.3	7.89	9.98	12.8	14.9	2.02	0.30	0.16	1.69	0.20	0.08	0.15	99.5
A04d	49.9	7.76	10.25	12.6	15.0	2.03	0.29	0.20	1.69	0.22	0.04	0.15	100.3
A06a	49.1	6.53	8.91	13.7	15.3	1.89	0.31	0.14	1.95	0.24	0.05	0.14	98.4
A06d	49.4	6.35	9.34	13.9	15.4	1.98	0.37	0.19	2.02	0.27	0.10	0.18	99.6
A08a	50.1	6.75	9.13	13.6	16.1	1.88	0.31	0.19	1.86	0.22	0.12	0.15	100.5
A09a	50.5	6.35	9.15	14.2	15.9	1.89	0.19	0.17	1.68	0.18	0.10	0.12	100.4
A10a	48.2	7.83	10.57	13.2	17.2	1.57	0.08	0.19	0.69	0.06	0.04	0.03	99.7
A11a	49.5	7.40	8.83	13.1	15.1	1.86	0.35	0.17	1.97	0.26	0.08	0.13	98.9
A13b	50.6	4.44	10.98	12.9	15.5	2.08	0.28	0.21	1.61	0.20	0.02	0.12	99.1
A14b	49.8	5.45	9.38	12.7	15.3	2.03	0.39	0.21	1.56	0.31	0.06	0.11	97.4

id	SiO_2	MgO	FeO	CaO	Al_2O_3	Na_2O	K_2O	MnO	TiO_2	P_2O_5	Cr_2O_3	SO_2	Total
B01a	49.8	7.35	8.44	13.6	14.7	1.86	0.28	0.15	1.30	0.22	0.07	0.16	98.0
B02a	48.0	6.10	10.28	13.0	15.1	1.93	0.34	0.18	2.34	0.33	0.06	0.19	97.8
B04a	49.9	6.91	9.30	13.6	15.1	1.92	0.32	0.16	1.80	0.24	0.05	0.14	99.5
B05a	50.1	7.60	9.78	12.1	14.7	2.17	0.27	0.20	1.58	0.17	0.04	0.11	98.8
B06a	49.9	6.11	9.81	13.2	15.1	2.06	0.25	0.15	1.64	0.21	0.08	0.13	98.7
B06b	49.6	5.92	9.79	13.3	15.3	2.17	0.26	0.21	1.66	0.20	0.05	0.15	98.6
B07a	49.7	7.73	9.18	13.4	15.0	1.95	0.32	0.18	1.91	0.25	0.10	0.15	99.9
B09a	49.0	6.22	10.67	11.4	14.3	2.15	0.33	0.20	2.30	0.26	0.03	0.19	97.2
B10a	49.4	7.76	9.90	12.7	14.9	2.08	0.27	0.21	1.67	0.55	0.04	0.14	99.7
B12a	49.6	6.40	10.17	12.8	15.9	2.18	0.33	0.18	2.04	0.24	0.04	0.20	100.1
B13a	48.9	7.73	9.39	12.9	14.9	1.97	0.33	0.17	1.73	0.21	0.09	0.19	98.5
B14a	50.1	7.15	9.87	13.3	15.2	2.00	0.31	0.19	1.69	0.24	0.04	0.17	100.3
B15a	47.8	5.99	10.02	13.2	14.9	2.06	0.26	0.21	1.73	0.20	0.05	0.15	96.6
B16a	50.0	5.72	10.20	13.5	15.5	2.22	0.30	0.23	1.68	0.20	0.06	0.16	99.8
B17a	52.1	5.61	9.29	13.5	15.0	2.16	0.06	0.15	1.80	0.08	0.05	0.16	100.0
B18a	48.5	7.25	10.50	12.5	14.7	2.06	0.29	0.23	1.65	0.22	0.05	0.17	98.1
B19a	50.3	7.79	8.65	12.9	15.1	2.13	0.28	0.19	1.59	0.22	0.05	0.18	99.5
B19b	50.4	7.64	8.71	13.0	15.2	2.15	0.26	0.17	1.62	0.18	0.05	0.18	99.5
C01a	49.2	5.53	9.97	13.6	15.6	2.13	0.34	0.21	2.06	0.30	0.08	0.21	99.2
C03a	52.0	6.24	8.55	14.8	14.3	1.45	0.16	0.15	1.11	0.11	0.11	0.10	99.0
C04a	50.1	7.19	8.27	13.1	14.2	1.93	0.12	0.14	1.05	0.17	0.05	0.18	96.5
C09a	48.6	6.60	10.43	13.3	15.6	2.01	0.34	0.20	1.72	0.21	0.06	0.18	99.2
C09b	49.2	9.00	9.96	12.2	15.5	1.95	0.28	0.17	1.62	0.26	0.03	0.18	100.4
C11a	49.1	7.00	9.86	12.6	14.6	2.10	0.27	0.21	1.46	0.14	0.05	0.21	97.6
D23a	50.9	7.70	9.43	12.5	15.2	2.15	0.06	0.14	1.37	0.09	0.04	0.18	99.8
D24a	51.1	6.39	8.84	13.6	15.8	2.07	0.32	0.18	1.49	0.15	0.06	0.22	100.3
D25a	50.0	7.40	10.10	13.0	14.6	1.65	0.26	0.20	0.93	0.11	0.06	0.18	98.5
D25b	51.2	6.50	10.01	13.4	15.0	1.72	0.30	0.19	1.00	0.14	0.08	0.19	99.8
D27a	49.1	6.65	9.59	13.4	15.3	2.12	0.33	0.18	1.72	0.24	0.05	0.27	99.1
D28a	48.8	7.66	9.33	13.0	14.9	2.03	0.23	0.22	1.44	0.16	0.06	0.25	98.1
D31a	49.1	7.73	10.60	13.3	15.3	1.90	0.31	0.19	1.59	0.20	0.10	0.23	100.6
D36a	51.5	7.50	8.84	13.5	14.8	1.93	0.11	0.15	1.24	0.09	0.10	0.20	100.0
E21a	50.3	6.17	10.63	12.0	14.5	2.26	0.33	0.23	2.70	0.50	0.05	0.26	99.9
E22d	49.2	6.92	9.35	13.6	15.0	1.94	0.34	0.15	1.85	0.23	0.08	0.27	99.1
E23a	50.1	6.06	10.10	14.0	15.3	2.08	0.28	0.19	1.64	0.21	0.06	0.26	100.3
E23b	50.3	5.55	9.63	14.0	16.1	2.24	0.31	0.14	1.54	0.18	0.08	0.24	100.3
E24a	49.1	6.91	10.45	13.3	15.1	2.06	0.32	0.18	1.85	0.23	0.06	0.27	99.8
E24b	50.0	6.24	10.30	13.7	15.4	2.04	0.33	0.16	1.76	0.21	0.08	0.28	100.5
E25b	50.4	7.64	10.30	12.4	15.2	1.92	0.26	0.18	1.24	0.13	0.06	0.21	100.0
E25c	48.9	6.53	9.95	13.3	15.2	2.05	0.33	0.20	1.75	0.22	0.05	0.19	98.7
E26a	50.0	7.87	9.49	13.0	14.8	2.11	0.30	0.19	1.52	0.18	0.08	0.21	99.8
E26b	49.1	8.16	9.07	13.2	15.3	2.07	0.30	0.19	1.85	0.27	0.11	0.26	100.0
E27a	48.8	7.32	10.05	12.6	14.7	1.95	0.25	0.17	1.37	0.32	0.05	0.25	97.8
E28a	48.0	6.60	10.79	13.3	15.5	2.03	0.31	0.23	1.74	0.23	0.04	0.24	99.1
E30a	48.8	7.62	10.58	12.9	15.4	2.02	0.31	0.18	1.74	0.21	0.05	0.25	100.1
E31a	49.1	7.02	10.32	13.0	15.0	2.07	0.30	0.22	1.68	0.18	0.03	0.25	99.2
E31b	49.4	6.66	10.35	13.1	15.1	2.05	0.28	0.20	1.69	0.21	0.07	0.26	99.5
E32a	48.9	7.28	10.76	13.1	15.4	2.12	0.27	0.19	1.77	0.22	0.08	0.24	100.3
E34a	49.6	6.61	9.14	14.0	15.7	1.92	0.37	0.16	2.03	0.28	0.08	0.31	100.3
E35a	49.5	7.24	9.93	13.2	15.5	1.96	0.30	0.16	1.45	0.20	0.05	0.20	99.7
E37a	50.4	7.50	10.36	12.5	14.9	2.25	0.25	0.18	1.56	0.17	0.08	0.25	100.4
E39b	50.1	7.14	11.56	11.6	15.1	2.10	0.21	0.24	2.01	0.21	0.04	0.27	100.5

Stapafell EPMA (hosts)

id	SiO_2	MgO	FeO	CaO	Al_2O_3	MnO	P_2O_5	Cr_2O_3	NiO	Total
A01a	40.3	45.6	14.3	0.30	0.05	0.23	0.01	0.05	0.26	101.0
A02a	40.3	45.9	13.9	0.28	0.04	0.21	0.01	0.04	0.25	101.0
A04a	39.9	45.4	14.3	0.29	0.04	0.22	0.02	0.04	0.21	100.5
A04b	39.9	45.4	14.3	0.29	0.04	0.22	0.02	0.04	0.21	100.5
A04c	39.9	45.4	14.3	0.29	0.04	0.22	0.02	0.04	0.21	100.5
A04d	39.9	45.4	14.3	0.29	0.04	0.22	0.02	0.04	0.21	100.5
A06a	40.1	46.8	12.1	0.29	0.05	0.20	0.04	0.08	0.28	99.9
A06d	40.1	46.8	12.1	0.29	0.05	0.20	0.04	0.08	0.28	99.9
A08a	40.4	47.1	12.0	0.28	0.04	0.18	0.01	0.06	0.23	100.4
A09a	40.5	47.2	12.2	0.28	0.05	0.19	0.01	0.06	0.26	100.8
A10a	40.5	45.9	13.9	0.29	0.05	0.22	0.00	0.03	0.24	101.2

id	SiO_2	MgO	FeO	CaO	Al_2O_3	MnO	P_2O_5	Cr_2O_3	NiO	Total
A11a	40.8	47.4	11.7	0.27	0.05	0.17	0.02	0.06	0.29	100.7
A13b	39.7	44.0	16.2	0.27	0.04	0.21	0.01	0.01	0.16	100.6
A14b	39.9	45.6	14.0	0.29	0.04	0.20	0.01	0.07	0.25	100.2
B02a	40.0	45.1	14.2	0.30	0.04	0.23	0.01	0.06	0.23	100.2
B04a	40.2	46.6	12.4	0.29	0.06	0.23	0.02	0.07	0.26	100.1
B05a	39.8	45.1	13.8	0.29	0.04	0.21	0.01	0.05	0.24	99.6
B06a	39.6	45.4	13.6	0.30	0.04	0.21	0.01	0.03	0.26	99.5
B06b	39.6	45.4	13.6	0.30	0.04	0.21	0.01	0.03	0.26	99.5
B07a	40.5	47.0	11.7	0.29	0.05	0.19	0.02	0.05	0.27	100.1
B09a	39.8	43.9	15.8	0.29	0.04	0.24	0.00	0.04	0.22	100.4
B10a	40.2	44.9	13.8	0.30	0.04	0.19	0.01	0.03	0.23	99.8
B12a	40.2	44.6	14.9	0.30	0.05	0.26	0.02	0.05	0.26	100.6
B13a	40.4	46.0	12.8	0.30	0.06	0.21	0.02	0.08	0.28	100.2
B14a	40.3	45.6	13.1	0.30	0.05	0.19	0.01	0.04	0.27	99.9
B15a	40.2	45.2	13.8	0.29	0.04	0.19	0.01	0.04	0.25	100.0
B16a	40.3	45.5	13.8	0.29	0.05	0.23	0.01	0.07	0.25	100.5
B17a	40.1	45.3	14.0	0.28	0.04	0.21	0.00	0.03	0.21	100.1
B18a	40.3	44.8	14.4	0.29	0.04	0.25	0.00	0.03	0.22	100.2
B19a	40.3	46.5	11.8	0.29	0.05	0.18	0.02	0.07	0.31	99.4
B19b	40.5	46.5	12.0	0.28	0.05	0.17	0.01	0.07	0.30	99.9
C01a	40.3	45.5	13.5	0.29	0.05	0.22	0.01	0.06	0.27	100.2
C03a	40.7	46.7	11.9	0.30	0.05	0.18	0.01	0.07	0.33	100.2
C04a	40.5	46.2	12.3	0.29	0.05	0.19	0.00	0.07	0.28	99.9
C07a	39.9	44.9	14.3	0.30	0.05	0.22	0.02	0.07	0.25	100.0
C09a	40.0	44.8	13.9	0.31	0.05	0.23	0.01	0.04	0.25	99.6
C09b	40.1	44.9	13.9	0.30	0.05	0.24	0.01	0.06	0.25	99.8
C11a	40.1	44.8	14.3	0.29	0.04	0.21	0.01	0.05	0.22	100.1
C12a	39.9	44.3	14.3	0.31	0.04	0.26	0.00	0.02	0.22	99.4
D23a	40.1	46.0	13.6	0.29	0.05	0.23	0.01	0.05	0.26	100.7
D24a	40.5	47.4	12.1	0.27	0.04	0.22	0.01	0.07	0.28	100.9
D25a	39.8	45.1	14.6	0.29	0.04	0.22	0.01	0.04	0.27	100.4
D25b	39.9	45.1	14.5	0.30	0.04	0.22	0.02	0.04	0.25	100.4
D25c	39.6	44.9	14.6	0.29	0.05	0.24	0.02	0.02	0.25	100.0
D27a	39.9	45.9	13.6	0.30	0.05	0.20	0.02	0.06	0.28	100.3
D28a	40.3	47.1	12.6	0.29	0.05	0.24	0.01	0.07	0.27	101.0
D31a	39.9	46.1	13.5	0.31	0.05	0.24	0.02	0.05	0.24	100.4
D36a	40.5	47.2	12.1	0.28	0.05	0.21	0.01	0.04	0.30	100.7
E21a	39.8	45.2	14.8	0.27	0.04	0.23	0.02	0.05	0.22	100.7
E22d	40.0	46.2	12.8	0.29	0.05	0.19	0.01	0.08	0.29	100.0
E23a	39.9	45.7	13.5	0.30	0.04	0.22	0.01	0.05	0.24	100.1
E23b	39.9	45.5	13.5	0.29	0.05	0.22	0.01	0.05	0.25	99.8
E24a	39.9	45.5	13.9	0.29	0.05	0.23	0.01	0.06	0.25	100.2
E24b	39.9	45.6	13.8	0.30	0.05	0.21	0.04	0.07	0.26	100.3
E25b	40.2	46.3	12.5	0.27	0.05	0.20	0.01	0.07	0.29	99.9
E25c	40.0	46.7	12.0	0.29	0.05	0.20	0.02	0.08	0.29	99.7
E26a	40.1	46.6	12.1	0.29	0.05	0.22	0.01	0.07	0.32	99.8
E26b	39.9	46.7	12.1	0.28	0.05	0.21	0.01	0.07	0.29	99.6
E27a	39.8	45.1	14.5	0.29	0.05	0.23	0.02	0.04	0.24	100.3
E28a	39.7	45.0	14.7	0.30	0.05	0.27	0.01	0.03	0.24	100.3
E30a	39.6	45.2	14.5	0.29	0.05	0.23	0.02	0.05	0.24	100.1
E31a	40.0	45.2	14.3	0.30	0.05	0.24	0.01	0.04	0.24	100.4
E31b	40.0	45.3	14.2	0.29	0.05	0.22	0.02	0.05	0.25	100.5
E32a	39.7	45.1	14.4	0.31	0.04	0.26	0.01	0.06	0.24	100.2
E34a	40.3	46.9	12.0	0.28	0.05	0.20	0.00	0.10	0.29	100.2
E35a	40.0	45.3	14.1	0.31	0.04	0.23	0.02	0.03	0.25	100.3
E37a	39.9	45.1	14.8	0.30	0.04	0.25	0.01	0.05	0.25	100.7
E39b	39.6	43.9	16.3	0.26	0.04	0.28	0.01	0.03	0.20	100.6

Stapafell Raman

id	p1	p1 err	p2	p2 err	Bubble diameter	mi long	mi short	delta	density
B02a	1282.9	0.06	1386	0.04	8.5	26.7	43.6	103.1	0.253
B04	1282.97	0.24	1386.09	0.04	8.6	33.8	19.6	103.12	0.261
B17	1282.11	0.11	1385.47	0.07	11	38.2	29.9	103.36	0.363
C04a	1282.66	0.05	1385.97	0.04	17.1	99	69.1	103.31	0.341
D28a					32				
D32					7	35	25		
D32					6	27	25		
D32a					6	45	30		
E22b					20				
E33a	1283.22	0.09	1386.49	0.06	40	81	66	103.27	0.324
E39b					11	57	48		
STAP-um01					4	38	27		
STAP-um02					6	28	24		
STAP-um03					5	20	19		
STAP-um04					18	83	58		
STAP-um05					11				
STAP-um06					11	40	35		